SCIENCE • TECHNOLOGY • RESEARCH HIGHLIGHTS • VISIONS •

Dissertation
86

On modeling of the time- or space-averaged gas-solid drag force in fluidized bed conditions

Sirpa Kallio

VTT SCIENCE 86

On modeling of the time- or space-averaged gas-solid drag force in fluidized bed conditions

Sirpa Kallio

Thesis for the degree of Doctor of Science in Technology to be presented with due permission for public examination and criticism in lecture hall 216 at Aalto University School of Engineering, Department of Energy Technology (Espoo, Finland), on the 20th of May 2015 at 12 noon.

ISBN 978-951-38-8246-4 (Soft back ed.)
ISBN 978-951-38-8247-1 (URL: http://www.vtt.fi/publications/index.jsp)

VTT Science 86

ISSN-L 2242-119X
ISSN 2242-119X (Print)
ISSN 2242-1203 (Online)

JULKAISIJA – UTGIVARE – PUBLISHER

Teknologian tutkimuskeskus VTT Oy
PL 1000 (Tekniikantie 4 A, Espoo)
02044 VTT
Puh. 020 722 111, faksi 020 722 7001

Teknologiska forskningscentralen VTT Ab
PB 1000 (Teknikvägen 4 A, Esbo)
FI-02044 VTT
Tfn +358 20 722 111, telefax +358 20 722 7001

VTT Technical Research Centre of Finland Ltd
P.O. Box 1000 (Tekniikantie 4 A, Espoo)
FI-02044 VTT, Finland
Tel. +358 20 722 111, fax +358 20 722 7001

Cover image: Video recording of the CFB pilot at Åbo Akademi University

Grano Oy, Kuopio 2015

Preface

Since late 80's I have worked in different research projects on fluidized bed combustion. The work started as co-operation between my alma mater Åbo Akademi University (ÅA) and Ahlström Oy (later Foster Wheeler Energia Oy which now is a part of Amec Foster Wheeler). Later other universities, VTT Technical Research Centre of Finland and many industries joined in the activities and in 2006 I moved from ÅA to VTT to continue the work. All along the central goal has been to develop tools for numerical modeling of fluidization processes. In these activities, the topic of this thesis i.e. gas-solid drag force has played a significant role. The long time span of the research shows that the modeling task is far from trivial. It also shows the importance of the goal for the industries, which have shown great tenacity in supporting the activities all these years.

I gratefully acknowledge the financial support of Tekes – the Finnish Funding Agency for Innovation, Foster Wheeler Energia Oy, Metso Power Oy, Fortum, Neste Oil Oyj, Etelä-Savon Energia Oy, Numerola Oy, Saarijärven Kaukolämpö Oy, VTT Technical Research Centre of Finland Ltd, Åbo Akademi University, Technical University of Lappeenranta, Technical University of Tampere and University of Jyväskylä for financing the projects that produced the results presented in this thesis.

The invaluable contributions of my co-authors outside VTT are acknowledged. Prof. Timo Hyppänen had a central role in supervising me in the early years of my career and he has been an excellent partner and advisor also in recent years which I warmly thank for. I thank PhD Srujal Shah, prof. Timo Hyppänen and PhD Kari Myöhänen for inviting me to participate in their valuable work on coarse-grained modeling of CFBs. With PhD Kari Myöhänen I have had many fruitful discussions on CFD modeling of fluidized beds and he has helped in many ways over the years which I warmly thank for. Mr Alf Hermanson, Mr Debanga Mondal and Prof. Henrik Saxén and other ex-colleagues at ÅA are thanked for their invaluable contributions and for making me feel that ÅA is still my home.

My colleagues at VTT have made this thesis possible. I thank our Team Leader Lars Kjäldman for his support. My co-authors Mr Veikko Taivassalo, Mr Juho Peltola and Mr Timo Niemi I thank for their major contributions in the modeling work presented in this thesis. Without the push from my nearest co-workers Juho and Timo I would never have written a doctoral thesis. It is like winning a jackpot in

lottery twice over to have gotten these two guys as my colleagues. Besides being professionally extremely valuable as colleagues they are also otherwise of great benefit to me: Juho keeps me in check and is my hard critic while Timo assists me in all imaginable ways and constantly encourages us with his optimism and positive attitude. Although VTT's support for writing a doctoral thesis also had an effect on me, it was Juho and Timo who made me realize how bad an example I am for them and to write this thesis. Thank you, Juho and Timo!

Last but not least I want to thank Prof. Markku Lampinen for supervising me through the process of converting a bunch of papers into a thesis. It was a great pleasure to work with you during this process.

Turku, 29th March 2015

Sirpa Kallio

Academic dissertation

Supervising professor, custos	Prof. Markku Lampinen Aalto University, Helsinki, Finland
Opponent	PhD Stefan Pirker Johannes Kepler Universität, Linz, Austria
Preliminary examiner	Prof. Juray De Wilde Universté catholique de Louvain, Louvain-la-neuve, Belgium
Preliminary examiner	PhD Esa Muurinen Oulu University, Oulu, Finland

List of publications

This thesis is based on the following nine original publications which are referred to in the text as I–IX. The publications are reproduced with kind permission from the publishers.

I Mondal, D.N., Kallio, S., Saxén, H., Length scales of solid clusters in a two-dimensional circulating fluidized bed of Geldart B particles, Powder Technology, 269 (2015) 207–218

II Kallio, S., Taivassalo, V., Hyppänen, T., Towards time-averaged CFD modelling of circulating fluidized beds, 9th Int. Conf. on Circulating Fluidized Beds, Hamburg, 2008.

III Niemi, T., Peltola, J., Kallio, S., Time averaged modeling of BFBs: Analysis of the terms in the momentum equations, In: Proceedings of Fluidization XIV Conference, May 2013, Noordwijkerhout, The Netherlands, pp. 559–566

IV Taivassalo, V., Kallio, S., Peltola, J., On Time-Averaged CFD Modeling of Circulating Fluidized Beds, International Journal of Nonlinear Sciences and Numerical Simulation, 13 (2012) 363–373

V Kallio, S., Peltola, J., Niemi, T., Parametric study of the time-averaged gas–solid drag force in circulating fluidized bed conditions, Powder Technology 257 (2014a) 20–29

VI Kallio, S., Peltola, J., Niemi, T., Modeling of the time-averaged gas–solid drag force in a fluidized bed based on results from transient 2D Eulerian–Eulerian simulations, Powder Technology 261 (2014b) 257–271

VII Kallio, S. , Peltola, J., Niemi, T., Analysis of the time-averaged gas–solid drag force based on data from transient 3D CFD simulations of fluidized beds, Powder Technology 274 (2015) 227–238

VIII Shah, S., Ritvanen, J., Hyppänen, T., Kallio, S., Wall effects on space averaged two-fluid model equations for simulations of gas–solid flows in risers, Chemical Engineering Science 89 (2013) 206–215

IX Shah, S., Myöhänen, K., Kallio, S., Hyppänen, T., CFD simulations of gas–solid flow in an industrial-scale circulating fluidized bed furnace using subgrid-scale drag models, Particuology 18 (2015) 66–75

Author's contributions

Publication I: The author has designed the experimental facility and planned the experiments. The author has participated in the planning of the analysis, in the evaluation of the results and in the preparation of the publication.

Publication II: The author has carried out the transient simulation and done the analysis of results in co-operation with the co-authors. The author has been the principal writer of the publication, in co-operation with the co-authors.

Publication III: The author has supervised the transient simulation and the analysis of the results. The author has participated in the preparation of the publication.

Publication IV: The author has carried out the transient CFD simulations, time-averaging of the results and participated in the development of the closure models. The author has participated in the evaluation of the results and in the preparation of the publication.

Publications V, VI, VII: The author has carried out most of the transient CFD simulations and carried out the analysis of the results in co-operation with co-authors. The author has developed the closures for the drag force. The author has been the principal writer of the publications.

Publication VIII: The author has suggested ways to analyse the results. The author has participated in the evaluation of the results and in the preparation of the publication.

Publication IX: The author has provided the macroscopic model with fitted parameters. The author has participated in the evaluation of the results and in the preparation of the publication.

Contents

List of symbols and abbreviations

a_i	parameter
b_i	parameter
$c_{\varepsilon,i}$	parameter for dissipation of Reynolds stress
C_{drag}	drag correction coefficient
$C_{drag,obs}$	observed value of C_{drag}
$C_{drag,pred.}$	predicted C_{drag}
$D_{q,ij}$	term representing turbulent, pressure and molecular diffusion (Reynolds stress transport equation)
d_p	particle diameter
E	prediction error
$F_{q,ij}$	turbulent mass flux (Reynolds stress transport equation)
$G_{q,ij}$	phase interaction term (Reynolds stress transport equation)
g_i	gravitational acceleration in direction i
K_{gs}	inter-phase momentum transfer coefficient
$K_{gs}^{\#}$	corrected drag coefficient
K_{gs}^{*}	inter-phase momentum transfer coefficient calculated on the basis of the time-averaged velocities and volume fractions
$l_{s,i}$	length scale of solid velocity fluctuations
$M_{q,ij}$	term arising from the local-scale turbulence (Reynolds stress transport equation)
N_{in}	number of input variables
p	gas pressure
p_q	pressure of phase q
$P_{q,ij}$	production term (Reynolds stress transport equation)
$S_{s,ij}$	two-phase term (Reynolds stress transport equation)

t	time
T	time interval
$U_{q,i}$	Favre averaged velocity $\langle u_{q,i} \rangle$
$u''_{q,i}$	velocity fluctuation
u_q	velocity of phase q
x_i	input variable
x_k	space coordinate
Δx_{wall}	distance to the wall
z_i	auxiliary variable

Greek symbols

α_q	volume fraction of phase q
δ_{qs}	Kronecker delta
$\varepsilon_{q,ij}$	dissipation term (Reynolds stress transport equation)
ϕ	auxiliary variable
$\bar{\phi}$	average of value of ϕ
ϕ'	fluctuating part.of ϕ
$\langle \phi \rangle$	Favre average of ϕ
μ_g	gas viscosity
$\Pi_{q,ij}$	pressure-strain covariance term (Reynolds stress transport equation)
ρ_q	density of phase q
τ_q	laminar stress of phase q
τ_q^M	local scale turbulent stress of phase q
$\tau_{s,i}$	time scale of the solid velocity fluctuations

Abbreviations

CFD	computational fluid dynamic
CFB	circulating fluidized bed
BFB	bubbling fluidized bed
EMMS	energy minimization multi-scale
2D	two-dimensional
3D	three-dimensional parameter

1. Introduction

1.1 Background

Efficient methods for computational fluid dynamic (CFD) modeling of industrial fluidized beds need to be developed to enhance application of fluidized bed technology. This is also the main goal of the present work. In the past, development of CFD methods has been slowed down by the unfavourable combination of a large process size and small length scales of inhomogeneous suspension structures. In single phase CFD simulations, computational grids with tens or even hundreds of millions of elements are feasible. Multiphase flows are computationally an order of magnitude more demanding and a few millions of cells is usually in practice the limit for a feasible mesh size today. On the other hand, the dimensions of a circulating fluidized bed (CFB) combustion chamber are typically of the order of 10 m X 20 m x 40 m. A mesh of 5 million cells would divide the combustion chamber in cells of 0.123 m^3. Bubbling fluidized beds (BFB) are typically smaller, but even there the feasible mesh spacings would be several centimeters.

The mesh spacing required for simulation of a process depends on the length scales of the structures that need to be resolved by the simulation. Mesh spacings have to be clearly smaller than the smallest structures to be resolved. Thus it is vital to know the length scales over which the relevant properties of the flow field can be approximated as constant in the chosen modelling approach. Moreover, modelers need to specify what scales the simulation should resolve and what scales need to be incorporated in the model by means of closure relations.

Figure 1 illustrates the inhomogeneous flow patterns in bubbling and circulating fluidized beds. Both the images are taken of lab-scale fluidized beds of Geldart B particles. In the case of Geldart A particles, surface forces become important and particles form smaller, more spherical clusters. In the present work the analysis is focused on fluidized beds of B particles. In a BFB, there are fine structures inside the bubbles and, more importantly, the boundaries of bubbles are quite sharp. In a CFB, the solids are mainly travelling in form of clusters and strands of varying length scales. Thus in both cases, solid volume fraction varies significantly over small length scales

.a)

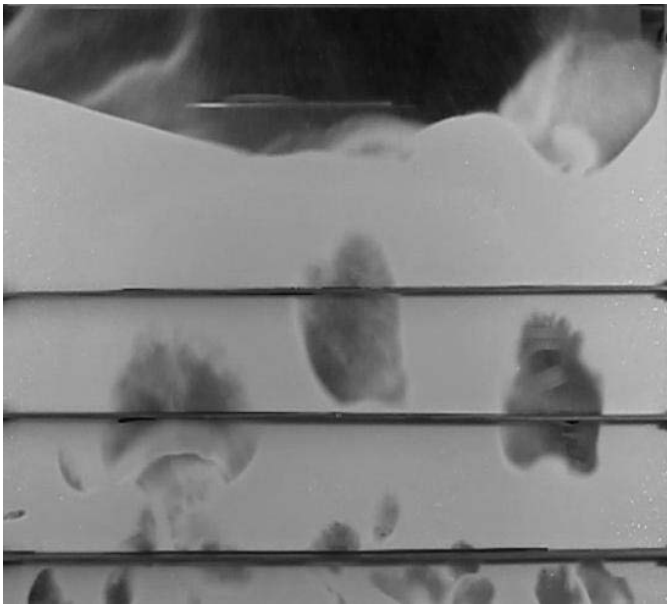

b)

Figure 1. Inhomogeneous flow patterns a) in a BFB and b) in a CFB.

The commonly used Eulerian-Eulerian CFD models based on the kinetic theory of granular flow could be used to produce the fine flow structures of the type seen in Figure 1, but due to the required fine mesh and time resolutions the computational capacity needed to accomplish the task would in practice be orders of magnitude too large in case of industrial applications. Thus alternatives have been sought. One alternative is to use a coarse computational mesh in a transient simulation and special closure relations that account for the flow structures that are not resolved by the coarse mesh (e.g. Lu et al., 2012; Paper IX). Since the results of the transient simulations need to be integrated over a long time period to obtain the

average flow fields, approaches based on steady-state modeling with time-averaged balance equations have been introduced to reduce the computation time (Zeng et al., 2006; Paper IV; O'Brien, 2014).

Similar closure models are needed for both transient coarse-mesh simulations and steady-state simulations. In both cases, it is a common practice to develop closures through averaging results from transient simulations in a fine mesh (Zhang & VanderHeyden, 2002; Milioli et al., 2013; Paper VIII).

1.2 Objectives of the work

The goal of the present work was to evaluate the need for closure relations in transient and steady-state simulations of fluidized beds and to study the applicability of different sub-grid and time-averaged closure models, especially for the gas-solid drag force. Both space-averaged and time-averaged transport equations for mass and momentum are considered in the work and ways to derive closure relations for the equations are developed.

The focus in the work is on gas-solid drag force, which largely determines the vertical distribution of solids in a CFB riser and the mass flow rate of solids leaving the riser. Several models for space- and time-averaged drag force have been suggested in the literature to account for clustering in time- and length scales that are smaller than the lateral and temporal scales resolved by the simulation. Although it seems to be commonly known that the mesh resolution required to describe all relevant cluster sizes depends on the particle size, particle diameter is typically not included as a parameter in the closure relations. Similarly, material properties have commonly been ignored. The present work has as one aim to improve our understanding of the effects of material properties on the drag closures.

Space-averaged transport equations and the related closure laws have so far been a more popular topic of research than time-averaged models. Time-averaged equations rely more on the closure laws used to describe transport of momentum, which has reduced the interest in the development of the approach. However, simulations based on time-averaged models would have clear benefits since the computation time is radically reduced when integration over a long simulation time can be omitted. The present study considers both space- and time-averaged modeling approaches.

The thesis concentrates on CFB conditions. BFB conditions are taken into account only in the analysis of the terms in time-averaged momentum equations and in the analysis and modeling of the time-averaged drag force. Solid phase is in the work assumed to consist of spherical mono-sized particles. Accounting for other particle size distributions and shapes is left outside the scope of the work.

The thesis includes nine papers. Paper I (discussed in Section 2) presents an experimental study of cluster length scales in turbulent and circulating fluidized bed conditions. Paper II (discussed in Section 3) introduces the time-averaging

procedure and evaluates the order of magnitude of the different terms in the solid phase momentum equation in CFB conditions. Paper III (discussed in Section 4) compares the terms in the time-averaged momentum equations in BFB conditions. In Paper IV (discussed in Section 5), closure relations for the time-averaged transport equations are suggested, they are implemented in a CFD software, and tested in the simulation of a small CFB riser. In Paper V (discussed in Section 6), the parameters affecting the time-averaged drag force are analysed on the basis of results from transient two-dimensional simulations of circulating fluidized bed risers. Paper VI (discussed in Section 7) extends the analysis to bubbling fluidized beds and derives closure relations by means of nonlinear regression modeling. In Paper VII (discussed in Section 8) the qualitative analysis is extended to three-dimensional geometries and the significant difference between 2D and 3D results is demonstrated. Paper VIII (discussed in Section 9) presents an analysis of the space-averaged drag force in CFB conditions. In Paper IX (discussed in Section 10), a closure relation for the space-averaged drag force is implemented in a CFD software and used in a transient coarse-mesh simulation of a boiler furnace. Comparisons with results obtained using alternative closure laws are also presented in Paper IX.

2. Paper I: Analysis of cluster length scales in a CFB

In Paper I, length scale distributions of clusters of particles are analyzed both horizontally and vertically from a number of experiments carried out with Geldart B particles in a lab-scale circulating fluidized bed. The height of the riser is 3 m and the width 0.4 m. The distance between the walls is 15 mm, rendering the riser fairly two-dimensional. The experimental unit, located at Åbo Akademi University (in Turku, Finland), is shown in Fig. 2.

The short distance between the walls made it possible to analyze the local solids distribution patterns and cluster length scales in the riser from shadowgraphy images. Videos were recorded from a number of experiments with different bed masses and fluidization velocities. A three-step procedure to analyze the clusters was applied: 1) image thresholding, 2) cluster identification and 3) measurement of length scales. This approach to study cluster sizes differs from the ones presented in the literature, in which cluster length scales are typically determined by measurements with optical probes (Werther, 1999; Zhou et al., 1994). Optical probes are suitable for measurement of the vertical cluster length scales but not of the lateral ones.

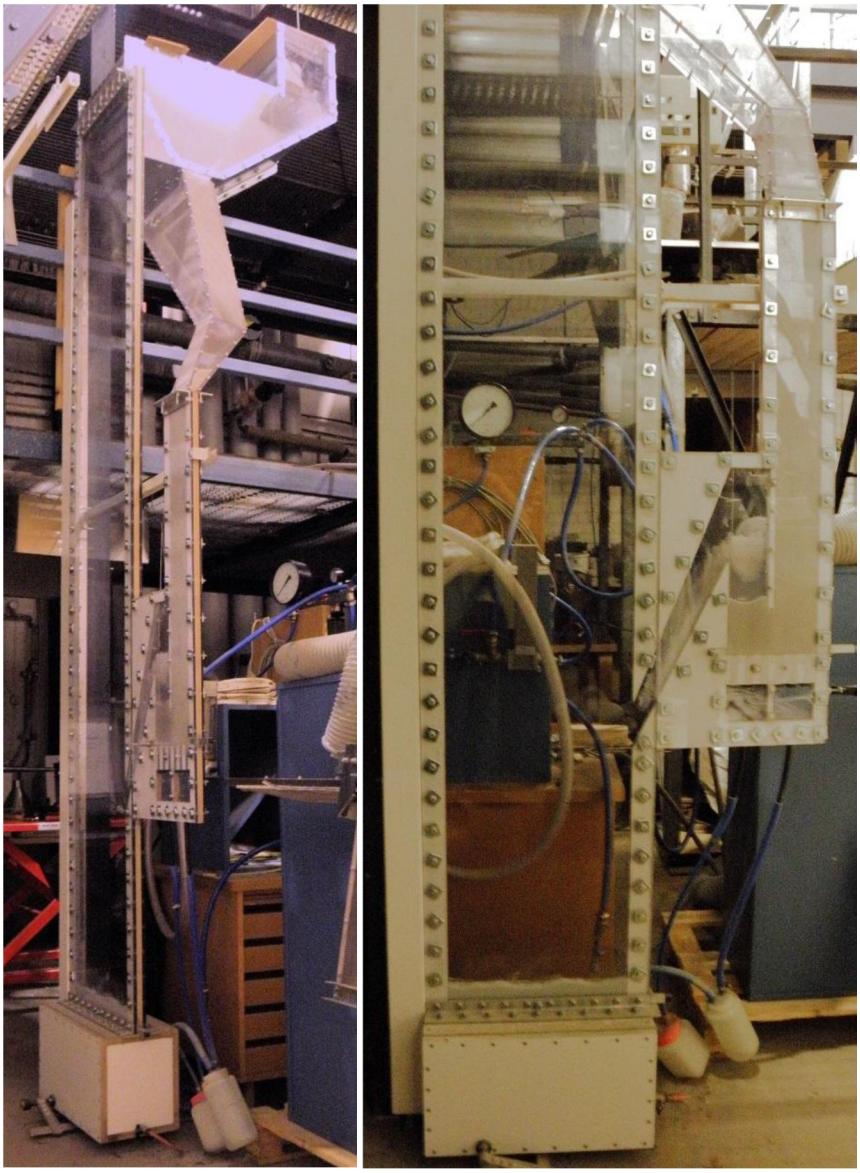

Figure 2. Pseudo-2D fluidized bed at Åbo Akademi University.

In Paper (I), the cluster dimensions were found to be affected by solids loading, superficial gas velocity and the location in the bed. Large length scales were found to be typical for the bottom region, above which on average more narrow clusters were observed. The majority of clusters measured in the upper part of the riser

had a width less than 20 mm. This would indicate that in CFD simulations of circulating fluidized beds the mesh resolution should be finer than 5 mm to accurately reproduce the clusters. A significant fraction, of the order of 10–15 % of the measured cluster widths were below 2 mm. Cluster widths were smaller in the central part of the riser than at the walls. In the center, in some cases even half of the clusters had widths below 6 mm. In the splash zone above the dense bottom section, the most dominant cluster widths were 20–40 mm. Figure 3 shows an example of the distribution of cluster widths at different elevations.

Similar to cluster widths, cluster heights were affected by the bed mass, fluidization velocity and location in the bed. Clusters with heights in the range of 20–40 mm dominated in the entire riser. In the bottom section, the horizontal and vertical dimensions of the clusters were similar but higher up clusters became long and narrow. This indicates that a measurement with an optical probe would probably exaggerate the cluster size.

In the literature, recommendations (Andrews et al., 2005) of CFD mesh spacing equal to or less than ten times the particle diameter have been given on the basis of mesh sensitivity studies. In the cases studied in Paper (I), this would correspond to a mesh spacing of 2.5 mm. On the basis of the analysis of (I), an even finer mesh would seem necessary to resolve the clusters since significant amounts of clusters with dimensions below 2 mm were encountered. Li et al. (2014) showed that the required mesh resolution depends on the property that is analyzed, which would indicate that the finest structures can be unimportant for some macroscopic properties while for other properties they play a significant role.

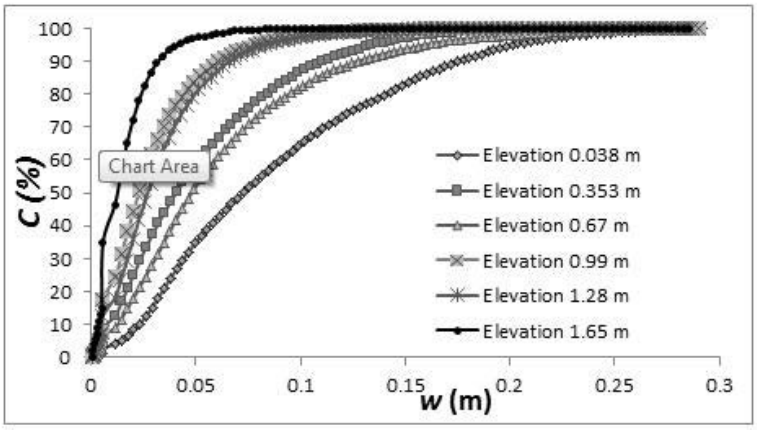

Figure 3. Effect of elevation in the CFB riser on the cluster width distributions at a gas superficial velocity of 2.75 m/s. Vertical axis shows the cumulative percentage of flow area occupied by clusters smaller than the width given on the horizontal axis.

3. Paper II: Analysis of the terms in time-averaged momentum equations in CFB conditions

3.1 Model description

Derivation of time-averaged transport equations, presented in (II), (III) and (IV), is based on integration of the corresponding instantaneous transport equations over time. Following the notation in (IV), the transient multiphase flow equations can be concisely written as

$$\frac{\partial \alpha_q \rho_q}{\partial t} + \frac{\partial \alpha_q \rho_q u_{q,k}}{\partial x_k} = 0 \tag{1}$$

$$\frac{\partial \alpha_q \rho_q u_{q,i}}{\partial t} + \frac{\partial \alpha_q \rho_q u_{q,k} u_{q,i}}{\partial x_k} = -\alpha_q \frac{\partial p}{\partial x_i} + \frac{\partial \alpha_q (\tau_{q,ik} + \tau_{q,ik}^M)}{\partial x_k} + \alpha_q \rho_q g_i + (-1)^{(\delta_{qs}+1)} K_{gs}(u_{g,i} - u_{s,i}) - \frac{\partial p_q}{\partial x_i}\delta_{qs} \tag{2}$$

where α_q is the volume fraction, ρ_q density, u_q velocity, p gas pressure, p_q solid pressure, K_{gs} inter-phase momentum transfer coefficient, δ_{qs} Kronecker delta, τ_q the laminar stress, and τ_q^M the local scale turbulent stress.

These equations are integrated over time. For volume fraction and pressure Reynold's averaging is directly used. In Reynold's averaging the instantaneous flow variables are split into steady and fluctuating parts:

$$\phi = \bar{\phi} + \phi' \tag{3}$$

where $\bar{\phi}$ represents the average value and ϕ' is the fluctuating part. The average value over some time interval T is defined as

$$\bar{\phi} = \frac{1}{T}\int_T \phi \, dt \tag{4}$$

For the velocity the Favre averaging is used. The Favre average is defined as

$$\langle \phi \rangle = \frac{\overline{\alpha_q \phi}}{\overline{\alpha_q}} \tag{5}$$

By denoting the Favre-averaged velocity as $U_{q,i} \equiv \langle u_{q,i} \rangle$, the following averaged flow equations can be derived:

$$\frac{\partial \overline{\alpha_q}}{\partial t} + \frac{\partial \overline{\alpha_q} U_{q,k}}{\partial x_k} = 0 \tag{6}$$

$$\frac{\partial \overline{\alpha_q}\rho_q U_{q,i}}{\partial t} + \frac{\partial \overline{\alpha_q}\rho_q U_{q,k} U_{q,i}}{\partial x_k} = \overline{\alpha_q}\rho_{qm} g_i - \overline{\alpha_q}\frac{\partial \bar{p}}{\partial x_i} - \overline{\alpha_q' \frac{\partial p'}{\partial x_\iota}} + \frac{\partial \overline{\alpha_q \tau_{q,\iota k}}}{\partial x_k}$$
$$+ \frac{\partial \overline{\alpha_q \tau_{q,\iota k}^M}}{\partial x_k} + (-1)^{(\delta_{qs}+1)} \overline{K_{gs}(u_{g,\iota} - u_{s,\iota})} - \frac{\partial \overline{p_q}}{\partial x_i}\delta_{qs} - \frac{\partial \rho_q \overline{\alpha_q u_{q,k}'' u_{q,\iota}''}}{\partial x_k} \qquad (7)$$

The terms on the right hand side in Equation (7) are the gravitation, pressure, pressure fluctuation, laminar and turbulent stress, drag force, solid pressure and so-called Reynolds stress terms. Gravitation and pressure terms can be calculated from the time-averaged basic flow properties whereas for the other terms on the right hand side of Equation (7) closure relations need to be derived.

3.2 Analysis of the terms

As a first step in the derivation of closure relations, an analysis of the different terms should be carried out to evaluate the importance of each term and the actual need of closure relations. Such analysis of the time-averaged equations was carried out in (II) for CFB conditions and in (III) for BFB conditions.

The analysis in (II) was done for a simulation of a CFB cold model with a cross-section of 1 m X 0.25 m and a height 7.3 m. Because of the large size of the unit and the limited computer capacity, the transient simulation used as the basis of the term analysis was carried out in a fairly coarse mesh with mesh spacings of 25 mm and 15 mm in width and depth directions and 46 mm in the vertical direction. To get a realistic solids distribution in the riser, the drag force was adjusted by means of a correction function. The simulation results were compared with measurements and it was concluded that the fluctuations in velocities and volume fractions were well captured in the transient simulation data. Thus the data could be used for qualitative assessment of the orders of magnitude of the different terms in Equation (7). Especially for qualitative analysis of the Reynolds stress components and the gas-solid drag force, this approach is sufficiently accurate. However, for the other terms it is good to verify the results in a simulation with a finer mesh.

According to the analysis in (II), the main terms in Equation (7) to be modeled are in the case of a CFB the average gas-particle drag force and the Reynolds stresses arising from velocity fluctuations. The results show that the correction for the time-averaged gas-particle interaction force should be anisotropic. The normal Reynolds stresses dominate momentum transfer in the horizontal direction and in the bottom bed also in the vertical direction. The shear Reynolds stresses are significant. On basis of the analysis, modeling of the complicated behavior of the Reynolds stresses by means of constant viscosities seems unfeasible and hence alternative approaches such as transfer equations for the Reynolds stress components need to be developed.

In the lateral momentum equation, solid pressure can be important close to the wall. In (II), the coarse mesh probably reduced its effect. In the analysis, the pressure fluctuation term in Eq. (7) was not found important. The analysis has been later repeated in connection to Paper (IV) for smaller geometries, where a finer

mesh could be used. Both solids pressure and the pressure fluctuation term in Eq. (7) were found important and closure relations for these terms were suggested in (IV).

4. Paper III: Analysis of the terms in time-averaged momentum equations in BFB condition

In (III) a similar analysis was carried out for the terms in Eq. (7) in bubbling fluidized bed conditions. The analysis showed that the most important terms in the momentum equations are the gas-solid drag term and the pressure fluctuation term. The solid pressure and the Reynolds stress terms were also found important. Locally also the laminar stress terms that are of minor importance in CFB simulations can become significant in BFBs due to the larger frictional forces. These results are illustrated by Figure 4.

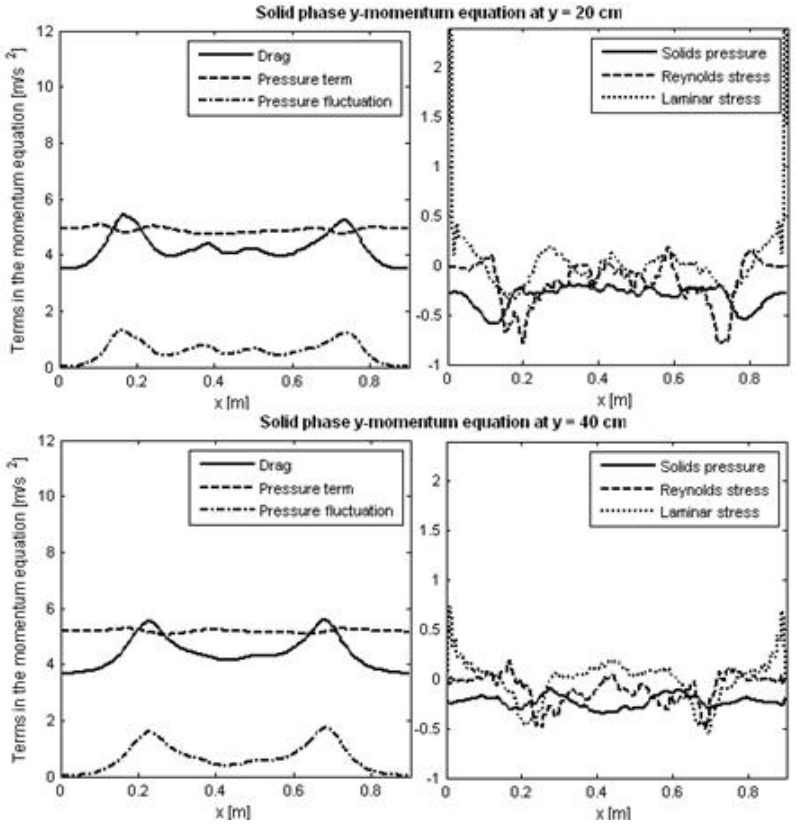

Figure 4. Comparison of terms in the vertical solids momentum equation in BFB conditions.

5. Paper IV: Modeling of flow in a CFB riser using time-averaged transport equations

In Paper (IV), the time-averaged simulation approach for gas-solid flow in a CFB riser and a corresponding CFD model were introduced. Closure models for the drag force, the pressure fluctuation term and solid pressure were derived on the basis of results from 2D simulations carried out with the kinetic theory models in the Fluent 6.3. software. The drag force was modeled as follows:

$$\overline{K_{gs}\left(u_{g,\iota}-u_{s,\iota}\right)} = K_{gs}^{\#}\left(U_{g,i}-U_{s,i}\right) \tag{8}$$

Correlations were developed for $K_{gs}^{\#}$ on the basis of data from transient CFD simulations using the time-averaged velocities and volume fractions as parameters. Tests showed that the vertical drag force was well predicted by the developed closure relation in the main part of the flow domain, and elsewhere the fit was sufficient. Also the fit for the lateral drag force was satisfactory.

The pressure fluctuation term calculated from the transient simulations showed a typical trend as a function of solid volume fraction. The trend somewhat resembled the one for the drag term. A linear relationship was found between the pressure fluctuation term and the variance of solid volume fraction. Thus, this term could easily be added to the drag force and the terms could be modeled together using the observed linear relationship.

The solid pressure term is most significant in the dense wall layer close to the riser bottom. In the lateral momentum balance equation, this term is also important higher up in the vicinity of walls. The solid pressure was modeled by means of a power law function with solid volume fraction as a parameter.

Transport equations for the Reynolds stresses were derived by starting from the instantaneous momentum equations (2) and the time-averaged momentum equations (7). The resulting balance equations can be written as follows

$$\frac{\partial \rho_{qm}\overline{\alpha_q u_{qi}'' u_{qj}''}}{\partial t} + \frac{\partial \rho_{qm} U_{qk}\overline{\alpha_q u_{qi}'' u_{qj}''}}{\partial x_k} = P_{q,ij} + \Pi_{q,ij} + D_{q,ij} + M_{q,ij} - \varepsilon_{q,ij} + G_{g,ij} + F_{q,ij} + \delta_{qs} S_{q,ij} \tag{9}$$

where $P_{q,ij}$ is the production term, $\Pi_{q,ij}$ is the pressure-strain covariance (or redistribution) term, $D_{q,ij}$ represents turbulent, pressure and molecular diffusion, $\varepsilon_{q,ij}$ is the dissipation term, $F_{q,ij}$ is the turbulent mass flux, $M_{q,ij}$ arises from the local-scale turbulence, $G_{q,ij}$ is the phase interaction, and $S_{s,ij}$ is the two-phase term.

Only the production terms $P_{q,ij}$ can be calculated from the basic flow variables during a time-averaged simulation. For all the other terms closure models need to be derived. In (IV), a simpler model for the Reynolds stresses was developed. As the Reynolds stress terms in the gas phase momentum equations are relatively unimportant, only the solid phase stress terms were modeled. Furthermore, transport equations were only solved for the normal components.

The balance equation (9) can be simplified. In (IV), the phase interaction term $G_{s,ii}$ was assumed to be a function of the slip velocity and the fluctuations in solid volume fraction. The diffusion term $D_{s,ii}$ was modeled as follows

$$D_{s,ii} = \frac{\partial}{\partial x_l}\left(c_{Ds,i}\overline{\alpha}_s \rho_{sm} \tau_{s,i} \left\langle u''_{sl} u''_{sl} \right\rangle \frac{\partial \left\langle u''_{si} u''_{si} \right\rangle}{\partial x_l} \right) \qquad (10)$$

where $\tau_{s,i}$ is the time scale of the solid velocity fluctuations. The dissipation term was given by

$$\varepsilon_{s,ii} = c_{\varepsilon,i}\overline{\alpha}_s \rho_{sm} \frac{\left\langle u''_{si} u''_{si} \right\rangle^{2/3}}{l_{s,i}} \qquad (11)$$

where $l_{s,i}$ is the length scale of the solid velocity fluctuations.

A successful steady-state simulation for a 2D test case was presented in (IV). Although the algebraic closure relations used for the other terms than Reynolds stresses were rather simple, the results obtained with the time-averaged Eulerian-Eulerian simulation approach were close to the averages of the results obtained in the transient simulation, see Fig. 5. This proves that although the terms in the solid phase momentum equation, which need to be described by rigorous closure relations, have a dominating role in momentum transport in time-averaged CFD modeling, the approach is feasible and produces realistic results. Later the approach has been successfully extended to 3D simulation of CFB boilers (Taivassalo et al., 2012b; Peltola et al., 2013). These studies also included a description of combustion chemistry and heat transfer.

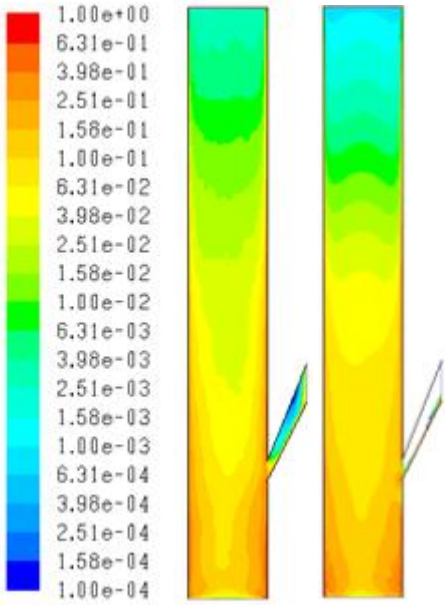

Figure 5. A comparison of the solid volume fraction field obtained from a 2D steady-state simulation of a pseudo-2D CFB (left) and the time-averaged solid volume fraction field from the corresponding transient simulation (right).

6. Paper V: 2D analysis of the time-averaged drag force in CFB condition

The drag correction function applied in Paper (IV) took into account only the solid volume fraction as a parameter. The models presented in the literature for coarse-grained simulation of fluidized beds take into account also the slip velocity and the distance to the wall (Milioli et al., 2013). Even other factors can affect the magnitude of fluctuations in flow properties. To improve our understanding of the requirements for a comprehensive filtered drag law, the effects of material properties on the time-averaged drag force were analysed in (V). The analysis was based on time-averaging the results from transient 2D Eulerian-Eulerian simulations of circulating fluidized beds of Geldart B particles. A large number of 2D simulations were carried out with the kinetic theory of granular flow models (for details of the models, see (VI)) and a selection of the simulations with varying gas viscosities, gas densities, solids densities, particle sizes, riser sizes and mesh spacings were chosen for the analysis. The geometry was a simple riser with straight walls. Although gas density and viscosity in most industrial applications are strongly coupled, their values were changed independently to separate their individual effects. Thus some of the simulations didn't necessarily represent typical CFB conditions as used today.

A mesh with a 12.5 mm resolution was found to be sufficiently fine for the study. This does not mean that all the finest flow structures were resolved by the simulation, but that the scales that have significant influence on the time-averaged drag force were captured and that the statistical properties of the fluctuations in the flow variables were fairly mesh-independent at this mesh resolution.

The closure for the time-averaged drag force was written in the form

$$\overline{K_{gs}\left(u_{g,y}-u_{s,y}\right)} = C_{drag}K_{gs}^{*}\left(U_{g,y}-U_{s,y}\right) \tag{12}$$

where K_{gs}^{*} is the inter-phase momentum transfer coefficient calculated on the basis of the time-averaged velocities and volume fractions using a similar combination of Wen and Yu (1966) and Ergun (1952) drag laws as in the transient simulations. However, instead of using Gidaspow's (1994) drag law implemented in Fluent, a smoother transition between the drag laws, suggested in (III), was used to calculate K_{gs}^{*}. In this model a linear transformation between the Ergun and Wen-Yu models occurs in a solid volume fraction range of 0.4–0.5, which is within the

region recommended by Leboreiro et al. (2008). The coefficient C_{drag} in Equation (12) is a drag correction coefficient, for which a correlation should be developed.

Initial tests of effects of process conditions were first carried out. Tests showed that bed mass, fluidization velocity and riser size have only minor effects on the drag correction coefficient in CFB conditions and they can be omitted from the list of relevant parameters. Since largest range of solid concentrations is obtained at small fluidization velocities simulations at several gas velocities are useful to obtain data from the full range of flow conditions.

Since in models for coarse meshes the lateral distance to the walls has been shown to be an important parameter, it can be assumed to have an effect also on the time-averaged drag force. The distance to the wall was found to have a significant but complicated effect, which was shown to be a result of combined effects with other parameters. To evaluate the combined effect of wall distance and slip velocity, data at a narrow range of wall distances were separated close to the wall and in the central region. Figure 6 shows the values of the drag correction coefficient at these two locations at three studied solid volume fractions as a function of the slip velocity. Clear effects of both slip velocity and wall distance are seen in the figure.

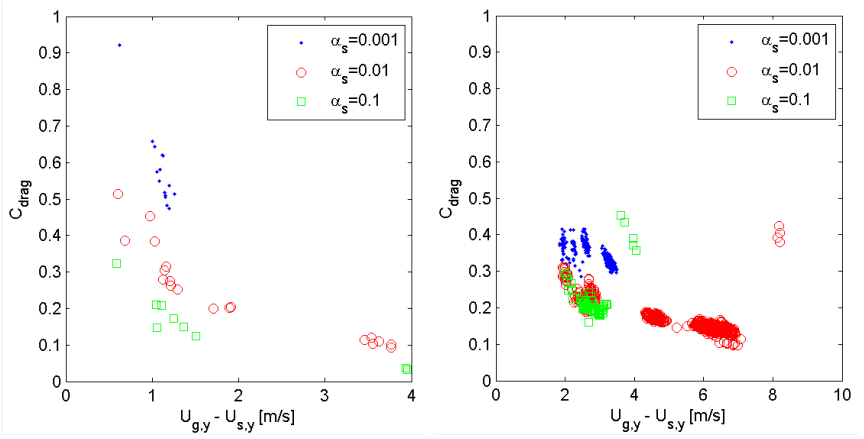

Figure 6. Drag correction coefficient as a function of the slip velocity at three different solid volume fractions in the wall layer (left) and in the central region (right).

The analysis also showed that the effects of material properties cannot easily be lumped together into a single parameter such as the Reynolds number, but they have to be included separately. This is illustrated by Figure 7 in which the drag correction coefficient is plotted with Reynolds number as a parameter.

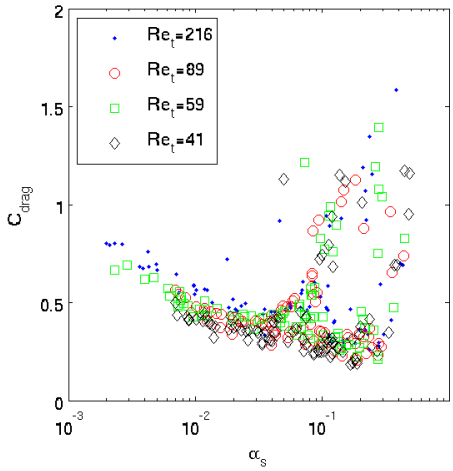

Figure 7. Effect of Reynolds number on the drag correction coefficient, plotted as a function of solid volume fraction.

In Paper (V), a systematic study of the effects of phase properties on the drag correction coefficient C_{drag} was presented. In the literature, no other similar analysis is available. Gas density was shown to have no clear effect on C_{drag} in the range studied in (V), whereas solids density had a positive effect. The effect of gas viscosity was reducing indicating that in hot conditions, the drag force deviates stronger than in cold conditions from what it would be if the suspension would be homogeneous. Also particle size had a significant effect. Clustering tendency seems to be highest in the case of smallest particles. In large fluidized beds there is typically a big difference in the average particle sizes in the bottom bed and in the top region of the riser. Thus even in a single simulation, a correction function that takes the particle size into account would be needed. The effects of solid density, gas viscosity and particle diameter are shown in Fig. 8.

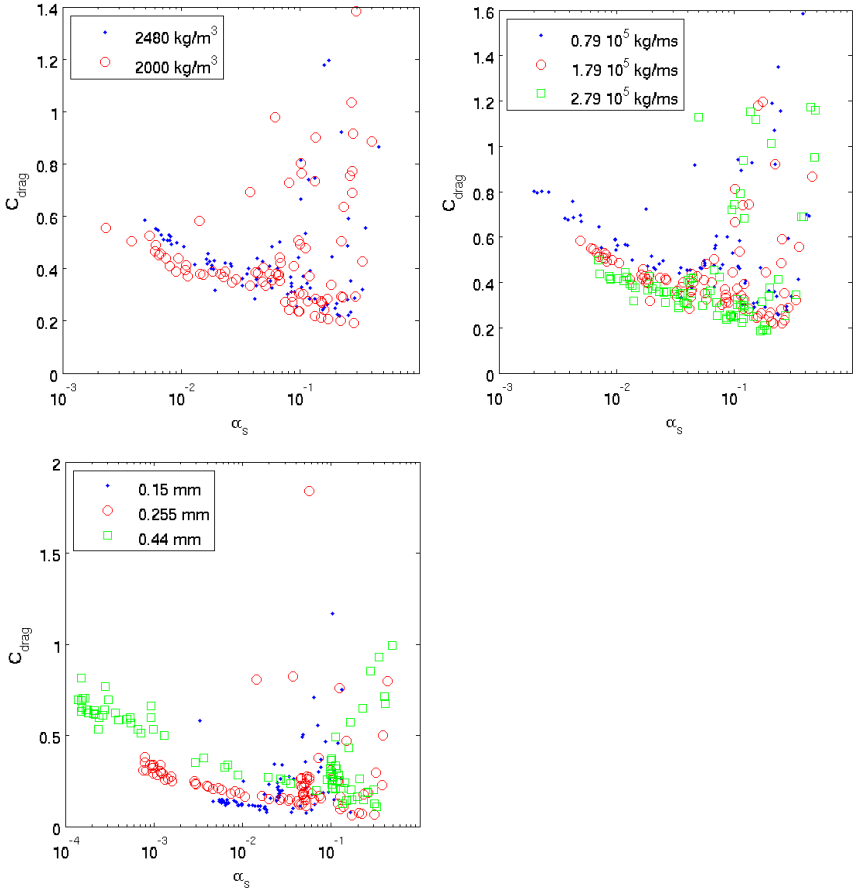

Figure 8. Effects of solid density (top, left), gas viscosity (top, right) and particle diameter (below) on the drag correction coefficient C_{drag}.

According to the results of the study based on 2D CFB data, the main parameters that should be accounted for in a correlation for the time-averaged gas-solid drag force are the solid volume fraction, distance to the wall, slip velocity, solid phase density, particle size and gas phase laminar viscosity. Thus a closure law should be of the form

$$C_{drag} = f(\overline{\alpha_s}, \Delta x_{wall}, |U_g - U_s|, \rho_s, d_p, \mu_g) \quad (13)$$

7. Paper VI: Development of closure relations for the time-averaged drag force in BFB and CFB conditions

No model was developed in Paper (V) since a larger set of data was necessary for model development to cover possible combined effects of different variables. In Paper (VI), the data set was extended to a wider range of conditions, including also bubbling and turbulent fluidized beds, and more cases were added to the data set also from CFB conditions. Data from 69 transient simulations were included in the analysis. All the simulations were carried out with the commercial code ANSYS Fluent v.14 with the Eulerian-Eulerian multiphase approach based on the kinetic theory of granular flow (KTGF).

In (V), only results from CFB conditions were analyzed and it was concluded that fluidization velocity has only a minor effect on C_{drag}. However, when the fluidization velocity significantly reduces from the typical CFB range, the flow pattern drastically changes and instead of being characterized by clusters and strands surrounded by dilute suspension, the voids and bubbles occur inside a dense suspension. This change was in (VI) shown to have a large effect on the average drag force and on C_{drag}.

The C_{drag} values calculated in all the mesh points (excluding the return channel) in a number of cases are displayed as a function of the local average solid volume fraction in Figure 9. A gradual change in the pattern can be observed when the fluidization state changes from BFB conditions (U_0 = 0.5 m/s) to typical CFB riser flow (U_0 =2 m/s). In Paper (V), effects of material properties were evaluated in CFB conditions. In BFB conditions the fluidization state can change when materials change and thus the interpretation of the effects is more difficult than in CFB conditions. Some examples of this kind of analysis are still given in Paper (VI).

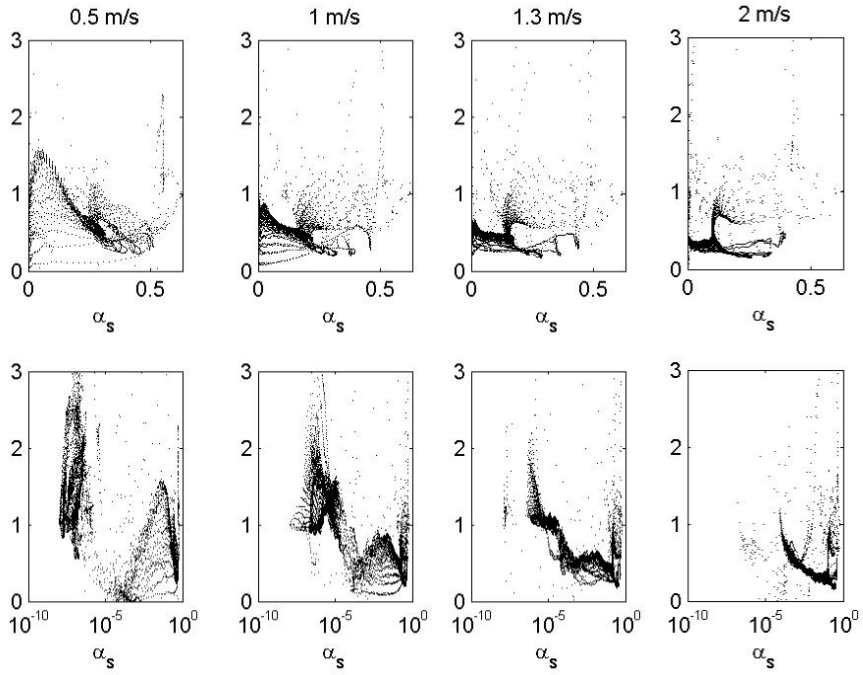

Figure 9. Drag correction coefficient C_{drag} as a function of the solid volume fraction in linear (top) and logarithmic (bottom) scales at fluidization velocities 0.5, 1, 1.3, and 2 m/s.

In (VI), the data from the 69 transient simulations were used as the basis of derivation of closure relations for the gas-solid drag force. Before the data could be used, the data set had to be cleaned. At low fluidization velocities, large scatter is visible in Figure 9 at low solid volume fractions. This scatter originates from the freeboard region, where only occasional clusters or single particles enter. This data was omitted as unreliable. At low slip velocities, the calculated C_{drag} can become excessively large or even negative due to the limited averaging period, which leads to problems when the average drag force is divided by a small inaccurate average slip velocity. Thus all C_{drag} values below zero and above 5 were rejected. The solids return region and the riser exit zone were omitted as non-typical regions. The complexity of the behavior of C_{drag} as a function of solid volume fraction is evident in Fig. 9. An analysis of the reasons behind the large scatter in some regions was carried out in (VI) and the behavior of C_{drag} adjacent to the walls was observed to be completely different from that of the rest of the flow domain. Thus a need for a separate correlation for the wall region was indicated. To simplify the modeling task the region up to 2–5 cm from the wall (depending on the case) was omitted from further analysis. Similarly, in the bottom region, scatter in the data increases as we move towards the air distributor and thus the region from the bottom up to 0.1 m was excluded.

In order to reduce the amount of data to a more manageable quantity without losing relevant information, data used for modeling were randomly picked from each of the simulations. The simulation domain was divided into bottom, side and central regions, from which data were successively picked.

To allow the developed correlation to freely adjust to the input data, a model structure based on a combination of a number of logistic sigmoid functions was used for nonlinear regression. This model structure is commonly used in neural network modeling (Hornik et al., 1989). The model can be written as

$$C_{drag,pred.} = b_0 + \sum_{i=1}^{N_\sigma} b_i \, \sigma(z_i) \tag{14}$$

$$z_i = a_0 + \sum_{i=1}^{N_{in}} a_i \, x_i \tag{15}$$

where a_i and b_i denote model parameters and x_i the N_{in} input variables. The logistic sigmoid function that produces values between 0 and 1 is given by

$$\sigma(z_i) = \frac{1}{1+e^{-z_i}} \tag{16}$$

The input variables considered in this work were the material properties, the solid volume fraction, gas and solid velocities, the slip velocity, the distance from the wall and the elevation, which are readily available in a simulation. Instead of solid volume fraction, the logarithm of solid volume fraction was used as an input parameter which makes it easier to express the steep gradients at low solid concentrations with sigmoid functions.

The model parameters (a_i,b_i) were determined by minimizing the prediction error E

$$E = \sum_{k}^{N_{obs}} \left(C_{drag,obs} - C_{drag.pred}\right)^2 \tag{17}$$

Parameter search was done with the Levenberg-Marquardt (Marquardt, 1963) method. The data used as the basis for modeling was quite limited and not of optimal quality, since only very few combinations of material properties were included. Thus special attention was paid to the robustness of the correlation. The correlation should not produce excessively large or small values in the points that were excluded from the data set used for parameter estimation. Thus some interpolation capabilities were desired. Some of the parameters (a_i,b_i) were fixed to zero to reduce the complexity of the correlation and to improve its robustness. With a larger number of sigmoids and model parameters, prediction accuracy could improve for the actual data set but the correlation's ability to produce reasonable values would deteriorate in conditions that were not included in the simulations carried out so far. Thus demands for robustness and accuracy need to be weighed against each other during the modeling process.

As an initial test, data from 18 simulation cases with the same material properties were chosen for modeling in order to find the necessary parameters for describing the effect of the fluidization state. According to Kallio et al. (2014a), solid volume fraction, wall distance and slip velocity should suffice for the task when material properties are constant. However, a first trial made with these three input

parameters did not produce a satisfactory correlation. Then the height above the air distributor was introduced as the fourth variable and the results clearly improved.

In the next step, material properties were taken as additional inputs and the data from all 69 cases was used during parameter estimation. The results were poor. Next the local gas velocity was added to the set of input parameters. Several different configurations of the model structure were tried with different numbers of sigmoids and parameters. The best developed correlation that was reasonably accurate and at the same time sufficiently robust had 71 parameters. The number of observations (5000) in the data set used in the parameter estimation process was two orders of magnitude larger than the number of parameters. Thus the amount of data can be considered sufficient.

The correlation developed on the basis of the full range of data proved to be far from an optimal fit at low solid concentrations. This is probably due to the difficulties related to trying to model both BFB and CFB conditions with the same correlation. To remedy this problem, a separate correlation was developed on the basis of data collected from CFB riser simulations in regions above 1.5 m height. The set of input variables could in this case be simplified by omitting gas velocity and the elevation. Thus the correlation for the limited dilute region is based on material properties (gas viscosity, solids density, particle size), solid volume fraction, slip velocity and wall distance. Again a number of correlation structures were tried and finally a correlation with acceptable accuracy and robustness was selected. The final correlation had only 14 parameters. As it is, the correlation is not generally usable since it behaves poorly in dense conditions unless it is combined with a correlation that works better in the dense bottom region. Figure 10 shows results obtained with a correlation that by means of linear and bilinear blending functions combines the correlation for dilute conditions in the upper parts of a CFB with the correlation based on the whole data set, which now is used only for the bottom bed and dense conditions. The two parameters that govern the switch from one correlation to the other and determine the value of the blending functions are the solid volume fraction and elevation.

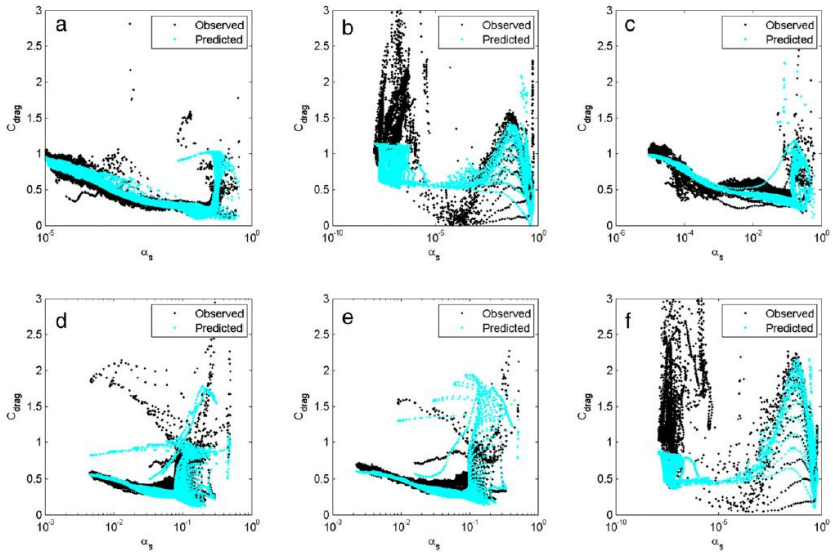

Figure 10. Results obtained in six cases with a model that by means of blending functions combines the drag correlation for dilute CFB conditions with the more general model, which in this model combination is used only for the bottom bed and dense conditions. Figures b and f are from BFB cases, figure c from turbulent fluidization conditions and the rest from CFB cases.

One additional case was simulated in CFB and one in BFB conditions to test the performance and robustness of the correlation. The material properties and the fluid-dynamic conditions of the two test cases were in the middle of the range of conditions in the simulations used for the estimation of the parameters, and thus these two simulations represent a test of the interpolation capabilities of the correlations.

Figure 11 shows a comparison between the observed and predicted C_{drag} values. Data corresponding to the air distributor region (height below 0.1 m), walls (distance from the wall less than 0.02 m), exit region (distance to the exit less than 0.5 m) and the return channel were omitted from the comparison. The freeboard region in the BFB case was also removed from the figure. The results show a good match between the observed and the predicted values, at least qualitatively.

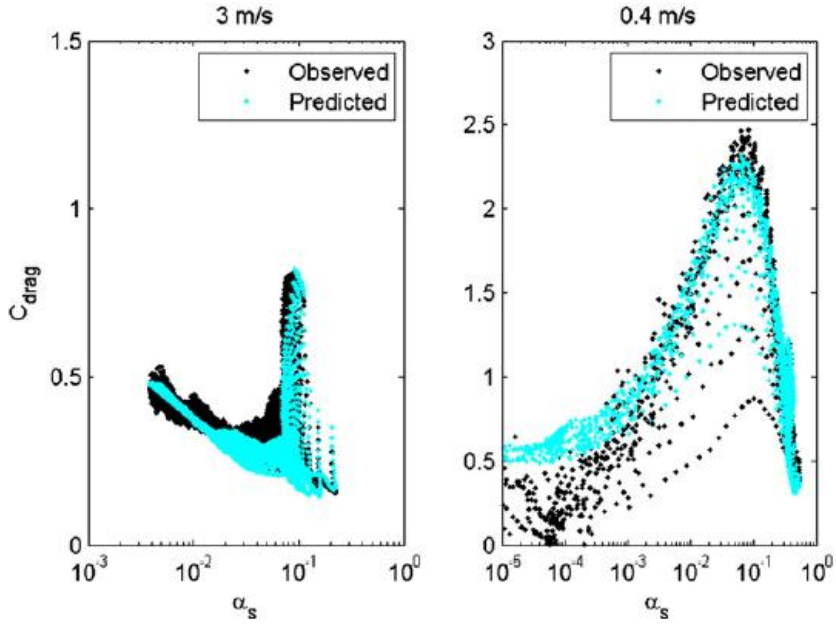

Figure 11. A comparison between observed and predicted C_{drag} values in a CFB (left) and a BFB (right) at conditions that were not included in the data set used for derivation of the correlation for C_{drag}.

Also quantitatively the results are satisfactory, with R=0.84 for the CFB case and R=0.96 for the BFB case, respectively, calculated for the data points shown in Figure 11 (R is defined as the covariance of the two variables divided by the product of their standard deviations). This indicates that the correlation is robust and safe to be used for simulations in the material property and fluid-dynamic ranges included in the 69 transient simulations. An extrapolation to conditions outside the range covered in this work is, however, risky.

The results in (VI) show that a fairly complicated drag correction function is required if the whole range from bubbling and turbulent beds to circulating fluidized beds has to be covered with a single correlation. Before the correlations developed in (VI) can be implemented in a CFD code, steps should be taken to improve their computational performance. The correlations developed contain a large number of model parameters. Many of them may be unnecessary and a superfluous burden for the computations, but no effort was made to check their role in the correlation. Such an investigation should be carried out before implementation. Furthermore the correlation showed behaviors that could be problematic during numerical simulations. The correlations occasionally predicted very small and even negative values and, especially close to the air distributor, excessively high values. Hence upper and lower limits, preferably case specific, should be set for C_{drag} to avoid numerical complications. By definition, C_{drag} should be equal to

unity in the homogeneous flow conditions at very low solids concentrations and at the packing limit. The presented correlations failed to correctly reproduce these limits and thus need to be modified prior to implementation in a CFD code.

8. Paper VII: 3D analysis of the time-averaged drag force in CFB and BFB conditions

The largest uncertainty in the correlations developed in Paper VI comes from the 2D simplification of the transient simulations, which compromises the accuracy of the correlations when applied in steady 3D simulations. In the literature (Esmaili and Mahinpey, 2011; Li et al., 2010), several comparisons of 2D and 3D CFD simulation results have been carried out. The reported significant effects of the dimensionality imply that utilization of 2D simulation data can reduce the accuracy of the developed correlations, when they are applied in 3D simulations. In (VII), data from transient 3D simulations were analyzed. Like in the 2D study, the 3D simulations were restricted to Geldart B particles and the analysis was done only for the vertical drag force component. The geometry was a simple riser with straight walls similar to the one used in the 2D simulations. The simulations covered the full range from bubbling to circulating fluidized bed conditions. Material property values and process conditions were varied to allow analysis of their effects. To save computation time, most of the simulations were carried out with a 12 mm mesh although in some runs a finer mesh was used to allow for grid sensitivity analysis.

As in the 2D study, the transient data from each simulation were time-averaged to determine in each mesh point the average flow properties and the average drag force. Filtering of the data was done at the data collection stage. A minimum limit for the slip velocity magnitude was set at 0.001 m/s and all points with negative C_{drag} were excluded. The data for the solids return channel and the uppermost half meter of the geometry were omitted.

Several of the cases simulated in 2D were simulated in 3D to allow direct comparison. Figure 12 presents comparisons between 2D and 3D simulation results in CFB, TFB (turbulent fluidized bed) and BFB conditions. Figure 12 shows that the 2D simulations produced clearly different trends in BFB, TFB and CFB conditions. No similar significant difference between the fluidization modes can be seen in the 3D results and especially in the dense conditions of the CFB and TFB cases, the general trends in 2D and 3D results radically differ. Quantitatively, the C_{drag} values determined from 2D and 3D simulation data are similar in the dilute CFB conditions and also to some extent in BFB conditions, but in the dense bottom bed of a CFB and in a TFB the 2D results significantly deviate from the 3D results. In

general, the 3D simulations produce higher values of C_{drag} at high solid concentrations. Thus a separate thorough 3D study of the gas-solid drag force, carried out in Paper (VII) is clearly necessary.

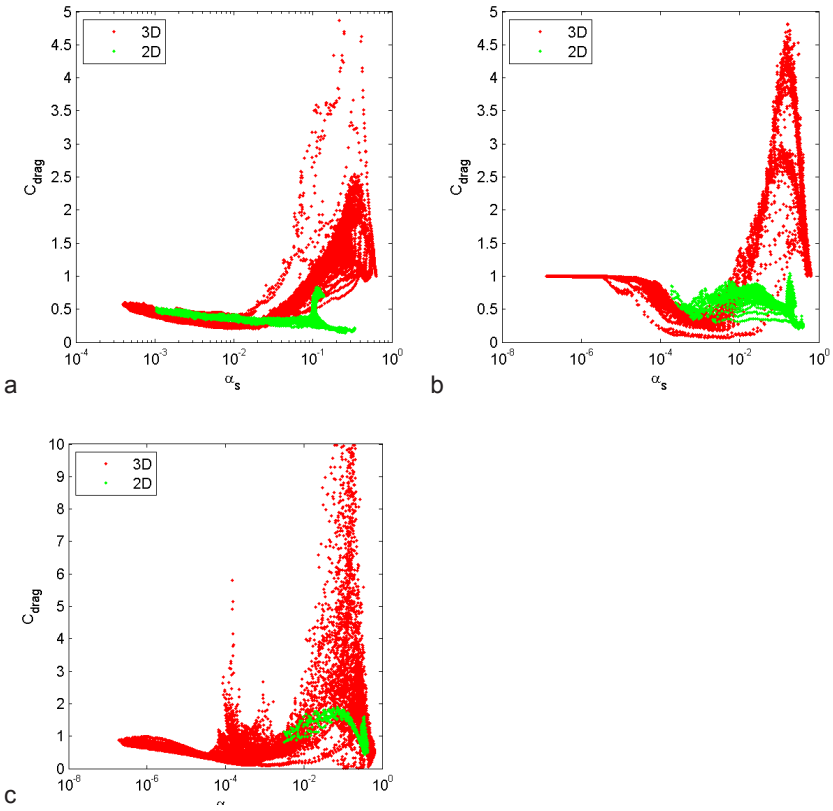

Figure 12. Comparison of C_{drag} determined from transient 3D simulation results with corresponding data from 2D simulations: a) CFB conditions, b) TFB conditions c) BFB conditions.

CFD simulation time depends on the number of computational elements in the mesh. Thus in addition to the mesh resolution, the selected geometry is also important. In the simulations analysed in Fig. 12, the depth direction was small and the geometry corresponded to a pseudo-2D fluidized bed with a core-annular flow structure prevailing only in the width direction. Such geometries have been used in experiments to represent a 2D fluidized bed. To evaluate the applicability of this geometry for analysis of the drag force in 3D geometry, tests with different riser depths were carried out. Figure 13 shows results from two such comparisons in different conditions. In general, the effect of bed depth is relatively small which allows to study parametric effects on the drag force by means of 3D simulations of

pseudo-2D beds. Because of the shorter simulation time, it is thus feasible to carry out a larger number of simulations with wide variation in conditions.

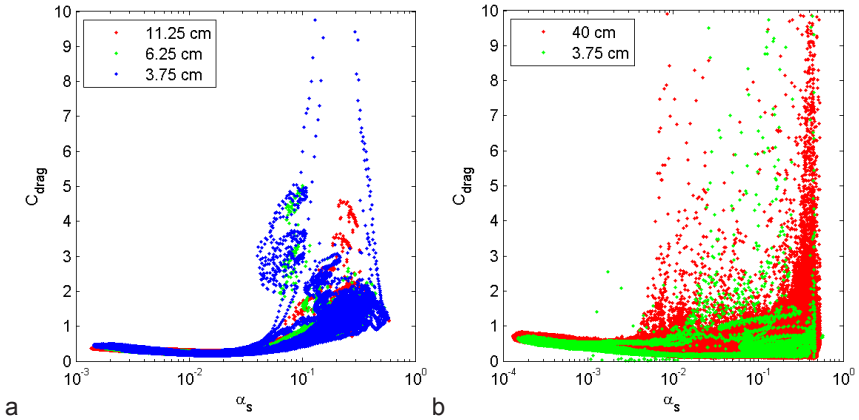

Figure 13. Effect of the depth of the bed a) U_0=2.75 m/s), and b) U_0=5 m/s. μ_g=4.45e-5 kg/m s, ρ_g=0.311 kg/m^3, ρ_s=2480 kg/m^3, d_p=0.255 mm. Riser depth is shown in the legend.

Figure 14 shows C_{drag} in different regions of the 0.4 m deep CFB riser. The riser is divided into four sections: front and back walls, side walls, corners and the middle section. Wall sections are defined as locations where the distance to the wall is below 10 mm while in the corners the distance to walls in both lateral directions is below the 10 mm limit. Close to walls, C_{drag} at solid volume fractions below 0.1 is systematically higher than in the middle region indicating that the suspension is more homogeneous close to a wall.

The data in the middle region of the riser were further split as a function of height. It was shown that the two lower-most control volume layers at riser bottom produced clearly higher C_{drag} values than the rest of the riser volume. A similar division as a function of height was done for the wall layers at front and back walls. Significant scatter of values was also here present in the data.

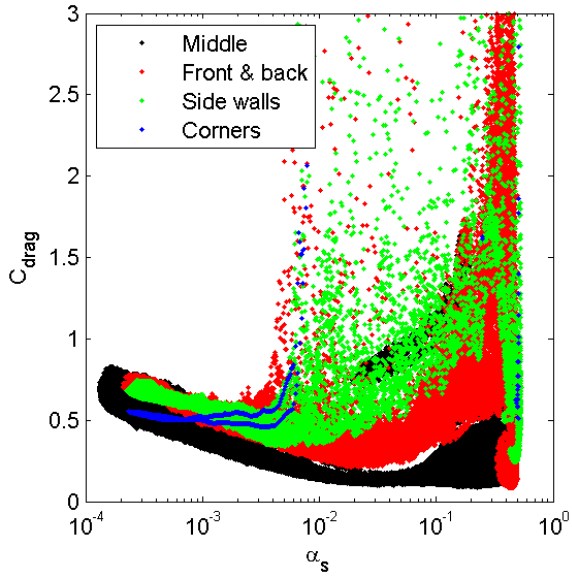

Figure 14. C_{drag} in different geometrical regions in the simulation of a 0.4 m deep CFB riser (μ_g=4.45e-5 kg/m s, ρ_g=0.311 kg/m^3, ρ_g=2480 kg/m^3, d_p=0.255 mm, U_0=5 m/s).

Both slip velocity and the distance to a wall affected the average drag force in the 2D data. Similar analysis was done for the 3D case and a complicated, partly combined effect of the wall distance and slip velocity was detected. Effects of process conditions on the drag correction were also evaluated. Small changes in the fluidization velocity did not affect C_{drag} in any significant way, especially in CFB conditions. In the dense end of the scale the effects of the fluidization velocity were more pronounced.

Not only the fluidization velocity but also the way the air is introduced into the riser affects the flow structure. In Paper (VII), the air distribution didn't show any effect on C_{drag} in CFB conditions whereas in BFB conditions C_{drag} increased when the gas flow was divided to separate nozzles. Thus air distributor design should be taken into account in drag modeling. In practice, this can be difficult in which case the possible effects of the air distributor design should be considered in the interpretation of simulation results as a possible source of inaccuracy. The bed mass determines the range of solid volume fractions occurring in the fluidized bed but it had no significant effect on C_{drag}. However, in dense conditions a small effect was visible. When bed mass increased, the location where a certain average solid volume fraction occurs changed. The differences at any specific value of solid volume fraction could thus, at least partly, be results of changed distance to a wall and to the air distributor.

In the 2D study, solid phase density and particle size were found to affect C_{drag}. Both parameters showed a positive effect, i.e. an increase in both particle size and solid material density increased C_{drag}. In BFB conditions the effect of particle size was similar but the effect of density was not positive in all situations. Similar comparison on the basis of the 3D data is presented in Figures 15 and 16. Figure 15 shows a positive effect of solid density at low solid concentrations and a negative effect in regions of high solid concentration. The effect of particle size, shown in Fig. 16, is of the same nature but even stronger. However, when reduced particle size leads to a change in the fluidization mode, the effect of the particle size is complicated, since the highest values of C_{drag} occur in BFBs and CFBs at different ranges of solid volume fractions, as seen in Fig. 16c.

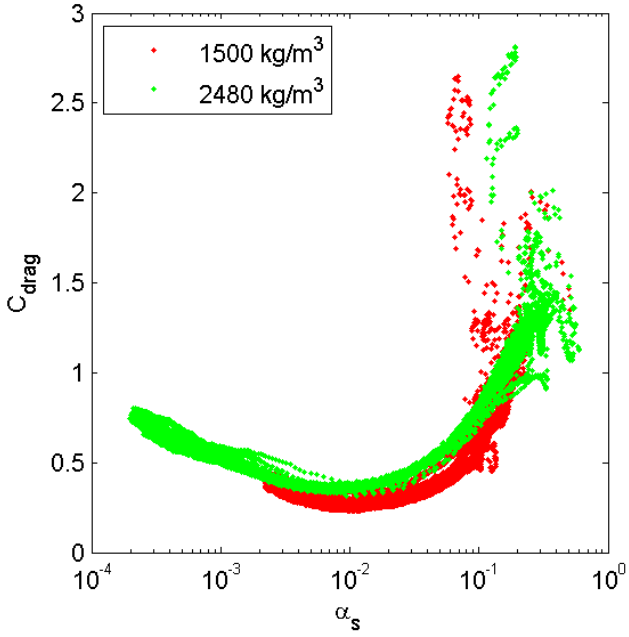

Figure 15. Effect of solid material density on C_{drag} (μ_g=4.45e-5 kg/m s, ρ_g=1.225 kg/m^3, d_p=0.255 mm, U_0=1.3 m/s).

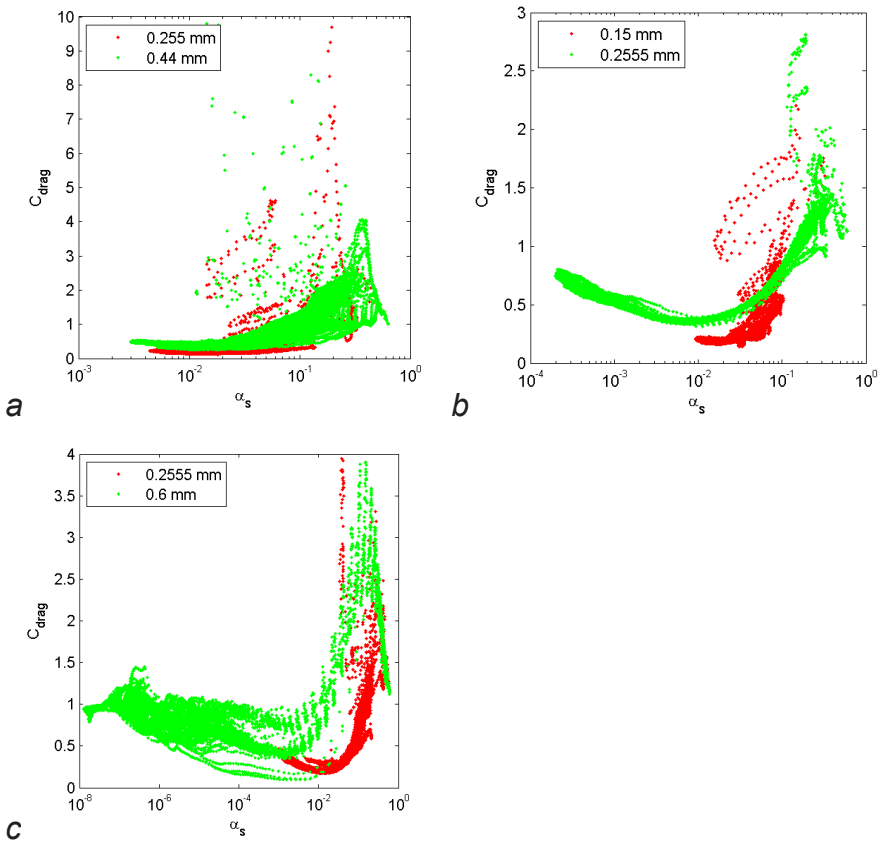

Figure 16. Effect of particle size on C_{drag} in a) Cases 24 and 26 (μ_g=4.45e-5 kg/m s, ρ_g=0.311 kg/m^3, ρ_s=2480 kg/m^3, U_0=5 m/s), b) Cases 21 and 10 (μ_g=4.45e-5 kg/m s, ρ_g=1.255 kg/m^3, ρ_s=2480 kg/m^3, U_0=1.3 m/s), and c) Cases 6 and 2 (μ_g=4.45e-5 kg/m s, ρ_g=0.311 kg/m^3, ρ_s=2480 kg/m^3, U_0=2.75 m/s).

In the 2D study, gas phase density was not found to have any significant effect on the drag correction coefficient. However, the range inside which gas density was varied was quite narrow, i.e. the range typically encountered in fluidization with air at atmospheric pressure. At elevated pressure gas density can be significantly higher. Figure 17 shows two comparisons in which gas density was changed while other parameters were kept constant. When the change in gas density is small, C_{drag} remains unchanged in dilute conditions. At high solid concentrations, a change in gas density produces a clear effect. At the higher gas density of 6 kg/m^3 (Fig. 17a), significant effects on C_{drag} occur in the whole range of solid volume fractions.

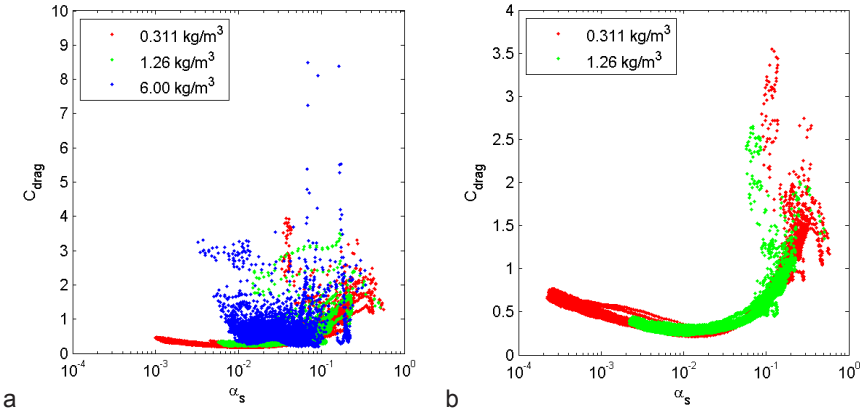

Figure 17. Effect of gas density on C_{drag}. a) μ_g=4.45e-5 kg/m s, ρ_s=2480 kg/m^3, d_p=0.255 mm, U_0=2.75 m/s and b) μ_g=4.45e-5 kg/m s, ρ_s=1500 kg/m^3, d_p=0.255 mm, U_0=1.3 m/s.

The 2D study showed that gas viscosity affects C_{drag} negatively. Same qualitative conclusion can be drawn from the 3D results presented in Fig. 18.

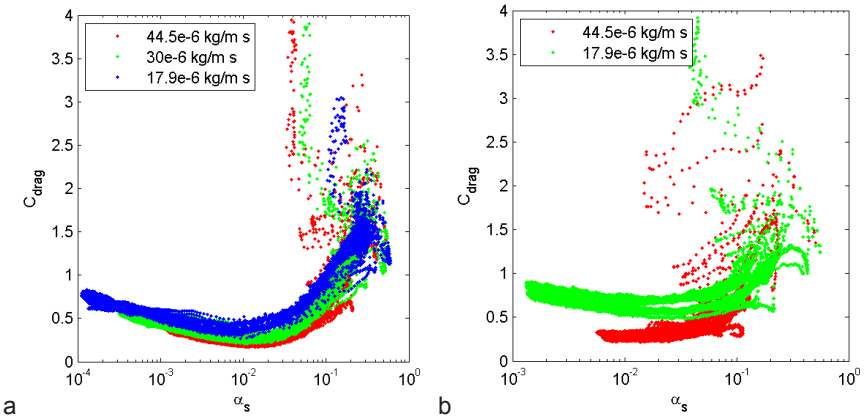

Figure 18. Effect of gas viscosity on C_{drag} in a) Cases 6, 19 and 15 (ρ_g=0.311 kg/m^3, ρ_s=2480 kg/m^3, d_p=0.255 mm, U_0=2.75 m/s) and b) Cases 11 and 20 (ρ_g=1.255 kg/m^3, ρ_s=2480 kg/m^3, d_p=0.255 mm, U_0=5 m/s).

Some of the trends observed in the 2D data were also seen above in the 3D analysis, and especially at low solid concentrations, the results were even quantitatively close to each other. In dense regions the results of the 3D study strongly devi-

ated from the 2D results which confirms that to accurately model gas-solid drag force in a 3D steady state simulation, the drag model has to be based on data from 3D transient simulations.

The 3D parametric study showed that solid volume fraction, particle size, solid density, gas viscosity, the slip velocity between gas and solids and the lateral distance to a wall have significant effects on the drag correction coefficient. At high gas densities typical of pressurized fluidization even the gas density had a significant effect. A general closure model for the time-averaged drag force in a fluidized bed should be based on these variables.

A closure for a very coarse mesh should approach the closure for a time-averaged equation, since a volume average over a distance that is significantly longer than the longest length-scales of the fluctuations should produce the same result as a time average in a single point, when the statistical characteristics over the averaging space and time frame are the same. That would be the case if there would be no spatial gradients in the time-averaged flow field. Although this condition is never exactly met, the gradients in the time-averaged volume fraction and velocities are often small compared to the fluctuations, for example in the center of a large CFB riser. Thus the results obtained for the time-averaged drag force are also indicative for space-averaged drag laws used in coarse mesh simulations.

9. Paper VIII: Analysis of the required closures for the drag force and convection terms in the transient coarse-grained modeling approach

Time-averaged momentum equations rely heavily on the closure relations. In coarse-grained modeling, the largest flow structures can be produced by the transient simulations while the structures of the order of the mesh spacing and smaller need to be accounted for by the closure models. The share of momentum transfer described by closure relations is smaller in coarse–grained models than in steady-state models and it reduces as the computational meshes become finer. When the computer capacity and calculation speed increase in the future, the need for sub-grid closures will thus reduce. Still, since the required mesh spacing in an accurate transient simulation is typically of the order of 2-5 mm, the need for sub-grid closures will remain for a long time.

Many attempts have been made by various research groups for the formulation of closures which could be used in coarse mesh simulations of gas–solid flows in risers (Agrawal et al., 2001; De Wilde, 2007; Igci et al., 2008; Wang and Li, 2007; Yang et al., 2003; Zhang and VanderHeyden, 2002; Igci and Sundaresan, 2011; Igci et al., 2012). Of greatest importance is modeling of the gas-solid drag force and thus it has gained more attention than the other terms. Common to all the suggested sub-grid drag models is that the predicted drag force is reduced from what the drag correlations for a homogeneous suspension would predict in the same flow conditions. In addition to the drag force, the stress terms have attracted attention. A short summary of the work carried out for the derivation of sub-grid closure laws is given in Paper (VIII).

In (VIII), a transient two-dimensional simulation of gas–solid flow in the geometry of the CFB riser of Fig. 2 was performed for a case of Geldart group B particles. The computational mesh was fine enough to allow local space-averaging of the results. Two regions, i.e. the dense bottom bed and the dilute upper section were analyzed. The vertical component of the gas-solid drag force and the normal components of momentum convection were averaged over areas 12.5 x 12.5 mm^2, 25 x 25 mm^2 and 50 x 50 mm^2. A drag correction factor was defined as the ratio between the average drag force in the averaging volume divided by the drag force calculated on the basis of the average flow properties. In very dilute condi-

tions and at the packing limit, where the suspension is nearly homogeneous, the correction factor should approach unity.

In Igci and Sundaresan (2011), the drag correction factor monotonously reduced towards the walls and as the explanation the authors suggested that this trend was due to the increased level of clustering at the wall. In (VIII) a similar trend was seen and an analysis of fluctuations of different flow properties was carried out to find an explanation for the phenomenon. Since the peak in the variance of solids volume fraction is not at the wall, the explanation suggested by Igci and Sundaresan (2011) on the basis of their study of Geldart A particles doesn't hold in the case of Geldart B particles studied in (VIII). The analysis in (VIII) indicated that the reduction in the drag correction factor at the wall is related to the strong fluctuation in the value of the drag coefficient in the wall region.

Figure 19 shows the obtained values of the drag correction factor as a function of the distance to the side wall for the three different averaging areas and for different solid volume fractions. The general reducing trend towards the wall is seen in all the plots. As the filter size increases, the value of the correction factor reduces which is expected.

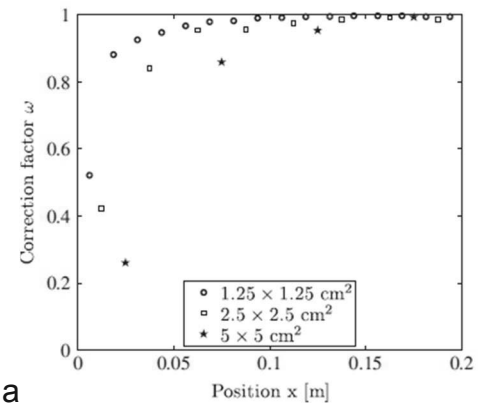

a

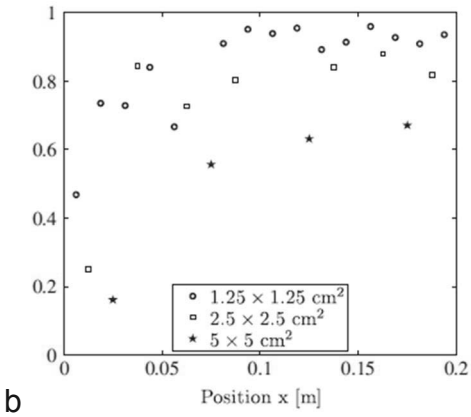

b

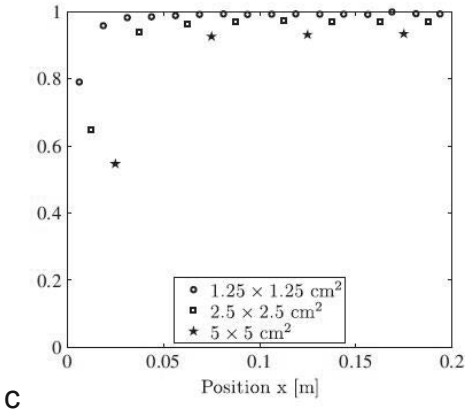

c

Figure 19. Correction factor for the drag force as a function the distance to a wall a) at solids volume fraction 0.01 at 0.175 m height, b) at solids volume fraction of 0.2 at 0.175 m height, c) at solids volume fraction of 0.005 at 2.475 m height.

In (VIII), the normal components of the Reynolds stress show highest values near the wall. Examples of this trend are shown in Fig. 20 for both the horizontal and vertical stress components.

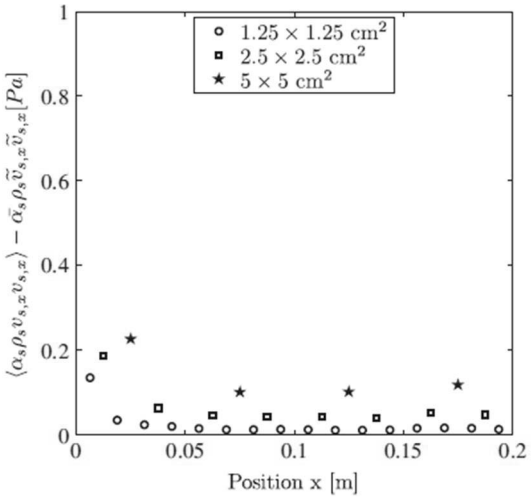

a

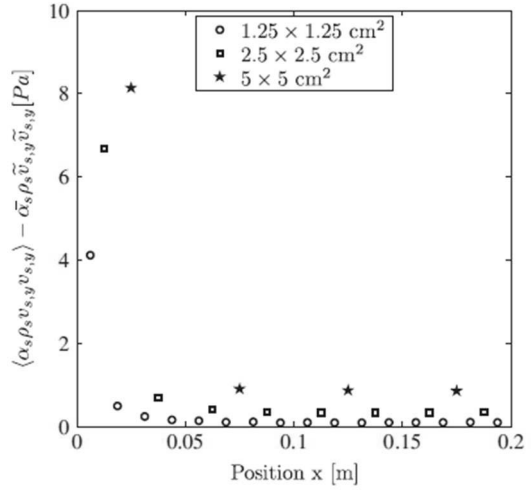

b

Figure 20. a) Horizontal normal Reynolds stress component for different averaging areas at the height of 2.475 m. b) Vertical normal Reynolds stress component for different averaging areas at the height of 2.475 m.

10. Paper IX: Testing of sub-grid closure laws for the gas-solid drag force

On the basis of the results in Paper (VIII), closure relations for gas-solid drag were developed in Paper (IX) for testing in a simulation of the furnace of a commercial CFB boiler. The models were simplified by taking into account the effect of solids volume fraction but not the wall effect. The data from (VIII) for the coarsest averaging area, 50 mm x 50 mm, were selected as the basis for the model.

The simulated furnace was 43 m high and it had a cross-section of 14.3 m x 6.73 m. The solid phase temperature was assumed to be uniform. The incoming gas flows entered the furnace at correct reduced temperatures and the heat transfer equations were solved to obtain a reasonable gas temperature field in the furnace. Solid particles were described to be of a single size of 0.150 mm. The mesh spacings were in the order 0.1–0.3 m.

For comparison, three other drag laws were also applied: Ergun/Wen-Yu drag model, the EMMS (Energy Minimization Multi-Scale, Li et al., 1999) drag model and a macroscopic drag law. Otherwise the models and conditions in the simulations were the same. The Ergun/Wen-Yu drag model is applicable to situations in which homogeneous conditions can be assumed to prevail inside the computational elements while the other models are meant for description of clustering flow.

In the EMMS approach, gas and particles are considered to be either in a dense or a dilute suspension region and the mechanisms of gas–solid interaction are analyzed on different scales. In Lu et al. (2012) and in Zhang et al. (2010), an EMMS-based correction factor was formulated as a function of slip velocity and volume fraction, and it successfully predicted the overall fluidized bed behavior. In (IX), the correction factor was expressed as a function of volume fraction only. The correction factor for the EMMS model was generated from the EMMS software obtained from the Institute of Process Engineering, Chinese Academy of Sciences. A superficial fluidization velocity of 2.66 m/s and solids flux of 5 kg/m^{2}s that correspond to the average conditions in the boiler in question were applied in the calculation of the correction factor. In reality, the superficial gas velocity changes along the furnace height but fortunately the EMMS method is not very sensitive to changes in this parameter and the same correction function could be used for the whole furnace.

The macroscopic drag model used in the simulation was a correlation originally presented by Matsen (1982). It is based on empirical information on the ratio of

the average slip velocity to the terminal velocity of a particle. Matsen (1982) presented model parameters for a case of Geldart group A particles. To use the model for other conditions and Geldart group B particles, the model parameters needed to be changed. Kallio (2005) used the data for Geldart group B particles in two different cases, in addition to Matsen's parameters, to express the model parameters as functions of the Archimedes number. In the simulations of the boiler furnace in Paper (IX), the same expressions were used to calculate the model parameters on the basis of material property values for the boiler in question. Matsen's equations were meant for a one-dimensional steady-state analysis while in this case they were applied for the sub-grid scale in a transient simulation. Although the macroscopic model is thus not designed for transient coarse-mesh modeling, it is useful for comparisons, since it provides a limit for a coarse mesh drag closure.

Figure 21 shows the resulting vertical profiles of the pressure gradient divided by density and gravity. This ratio is in experiments commonly interpreted as the average solid volume fraction. Measurements are also included for comparison. All the tested sub-grid closures improved the results in comparison to the Wen&Yu/Ergun drag model but not enough to match the measurements. The problem with the space-averaged model was probably that the model parameters were determined for a finer mesh resolution than what was used in the present work. Also other parameters such as slip velocity and material properties have effects on the required drag correction and they were ignored in the study. Particle size was smaller than in the 2D transient simulation on the basis of which the correction function was derived. Similarly, gas viscosity was in the furnace simulation higher. According to (VII) both these changes in phase properties should reduce the value of the drag correction coefficient. Similarly, in the EMMS model, slip velocity effects and the effect of gas properties were omitted from the model. Moreover, EMMS doesn't use the mesh resolution as a parameter. These facts can explain the too small correction to the drag force. The macroscopic model produced a too strong correction to the drag force, which was expected.

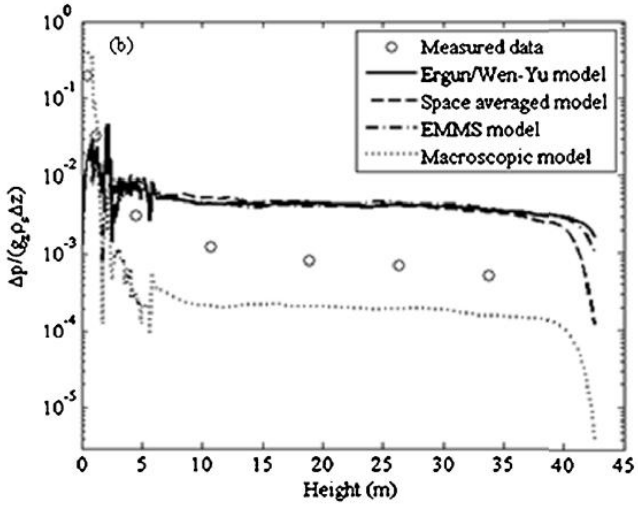

Figure 21. Pressure gradient divided by density and gravity as produced by the simulations with the different drag laws.

Figure 22 shows the lateral profiles of vertical solid velocity at the height of 30 m. Although the solid volume fractions predicted by the different models significantly differ at this elevation, all the models correctly predict a core-annular flow structure.

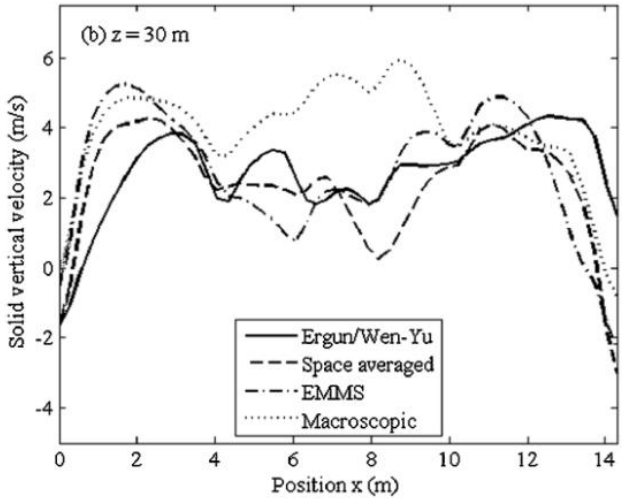

Figure 22. Favre-averaged solid vertical velocity as a function of the lateral position in the furnace predicted by the CFD simulations with different drag laws.

According to the results in (IX), the required correction to the drag force in very coarse meshes lies in between the drag corrections produced by the models presented in the literature and the correction required for steady-state modeling. The space-averaged drag law derived in (IX) and used in the simulation failed probably because its parameters were determined for a finer mesh and for different values of phase properties.

11. Summary of findings

The main results of each included article are listed below.

Paper I: The paper analyzed cluster length scales in a small CFB riser from shadowgraphy images. The method revealed that lateral and vertical length scales drastically differ above the dense bottom region. A large fraction of the measured lateral cluster length scales were smaller than 20–40 mm and, in the center of the riser, a significant fraction of the clusters were narrower than 6 mm. To account for all the significant length scales in a CFD simulation of a CFB, a very fine mesh resolution of the order of 2-5 mm would seem necessary on the basis of the results.

Paper II: The paper compared the orders of magnitude of the different terms in the solid phase momentum equation in CFB conditions. The main terms to be modeled were found to be the average gas-particle drag force and the Reynolds stress. The correction function for the time-averaged drag force was found to be anisotropic. The normal Reynolds stresses dominated momentum transfer in the horizontal direction and in the bottom bed also in the vertical direction. Modelling of the complicated behavior of the Reynolds stress components was shown to require a rigorous closure approach, e.g. transfer equations for the stress components.

Paper III: In the paper, the relative importance of the various terms in the time-averaged momentum equations was determined based on a transient simulation of a BFB. The most important terms were the gas-solid drag term and the pressure fluctuation term arising from the correlation between fluctuations in solid volume fraction and gas pressure. The time-averaged solid pressure and the Reynolds stress terms were also found to be important.

Paper IV: Closure relations for time-averaged two-fluid momentum equations for dense gas-solid riser flow were developed and implemented in a CFD software. A test simulation was carried out. The results showed that the developed model could largely reproduce the average flow field obtained from a transient simulation. Computationally the developed modeling approach was stable and significantly faster than the transient simulation method (by a factor of an order of 1000).

Paper V: Parameters that need to be accounted for in a model for the time-averaged drag force in CFB conditions were studied by analyzing time-averaged results from a number of transient 2D simulations carried out with fairly fine spatial resolution. Solids volume fraction, distance to the wall, gas-solid slip velocity, solid density, particle size and gas phase laminar viscosity were shown to have significant effects on the average drag force.

Paper VI: Closure correlations for the drag correction function were developed by nonlinear regression modelling based on data collected from 69 transient 2D simulations of bubbling, turbulent and circulating fluidized beds. The correlations were given as functions of eight variables: the solid volume fraction, the distance from the nearest wall, the height above the air distributor, the slip velocity between the phases, the gas velocity, the particle size, the solid density and the gas viscosity. The model was improved by combining separate correlations for dense conditions and the bottom region and for the dilute upper part of a CFB riser.

Paper VII: A qualitative analysis of the time-averaged gas-solid drag force in gas-solid fluidized beds was carried out on the basis of a large number of transient 3D simulations of small bubbling, turbulent and circulating fluidized beds. The results significantly differed from corresponding 2D data. The paper showed that even when the third dimension is described with only three nodes in the mesh, the 3D character of the flow is captured in the drag correction coefficient. The analysis showed that solid volume fraction, particle size, solid density, gas viscosity, the slip velocity between gas and solids and the lateral distance to a wall have significant effects on the drag correction coefficient. At high gas densities even the gas density has significant effects.

Paper VIII: In the paper, the vertical component of the gas-solid drag force and the convective term in the space-averaged solid phase momentum equation were analyzed. Their dependence on the averaging length scale, solid volume fraction, and the distance from the wall was presented. Closure models for drag and Reynolds stress were shown to strongly depend on the averaging size. The minimum for the drag correction function and the maximum for Reynolds stress were in all cases found at locations closest to the wall. A clear dependence of the drag correction factor on the distance to the wall was observed.

Paper IX: An industrial scale circulating fluidized bed furnace was modeled using a coarse mesh in a transient simulation. Alternative drag models were tested: the Ergun/Wen-Yu drag model, a subgrid-scale model based on data from Paper (VIII), the EMMS drag model and a macroscopic drag model. All models correctly produced a core-annulus flow structure. None of the models reproduced the measured pressure profile correctly. The macroscopic model assumed too strong clustering whereas the space-averaged and EMMS models applied a too small correction on the drag force given by the Ergun/Wen-Yu drag law.

12. Conclusions

Computational fluid dynamic (CFD) modeling of industrial scale fluidized beds is a challenging task due to the mismatch between a large process size and fine flow structures. In the present work, methods were developed to overcome the problems in order to make it possible to use CFD as a cost-effective tool for development of processes based on the fluidized bed concept.

An analysis of cluster length scales in a CFB riser was carried out and a large fraction of the clusters were shown to be very narrow. On the other hand, images from bubbling fluidized bed show that a steep change in the volume fraction takes place at the bubble borders. Thus in both bubbling and circulating fluidized beds, it is necessary to use a fine mesh resolution if all the significant structures are to be resolved by the simulation. Usually this is not practical in case of large industrial fluidized beds due to the required excessively long simulation times.

Two approaches to tackle the problem caused by a combination of small flow structures and a large process size were discussed in the present work: 1) transient simulation using a coarse computational mesh and subgrid-scale closure relations and 2) a steady-state simulation approach that applies a time-averaged two-fluid model. The biggest benefit of the transient coarse-mesh simulation approach is that the closure laws need to describe a much smaller fraction of the total momentum transfer than what is the case in steady-state modeling. This fraction will reduce with time when more computation power is available. The biggest drawback is that a long simulation is required to obtain the average flow field. An additional complication is that the closure laws have mesh spacing as a parameter, which makes derivation of the models tedious. Steady-state simulations produce the average flow field directly and thus significantly reduce the computation time. Derivation of closure laws for time-averaged momentum equations is, however, time-consuming, since the closure laws need to be fairly accurate.

The analysis of the terms in the time-averaged momentum equations (carried out in (II) and (III)) showed that in the lateral direction Reynolds stress terms dominate momentum transfer and in the vertical direction they are larger than the convection terms in the bottom section of a CFB riser. Especially in the upper parts of a CFB riser, accurate modeling of the drag force is crucial since gas-solid drag is there the largest term in the momentum equations. This explains why so much effort has been put over the years in drag modeling. Closure laws for space-

and time-averaged equations can be derived through averaging the results from transient fine-mesh simulations over appropriate time and length scales. In the present work, both space and time-averaging of the drag force was carried out and parameters affecting the averages were studied by means of a correction coefficient that is the ratio between the average drag force divided by the drag force obtained by combining the Ergun (1952) and Wen and Yu (1966) drag laws. The main parameters affecting the correction function for the time-averaged drag force were found to be the mesh spacing, the distance to the wall, material properties, particle size and the slip velocity between the phases. The elevation in the bed and gas superficial velocity were found to be additional useful parameters in drag modeling.

In the work, both space and time averaged drag laws were used in riser simulations. It was shown that although the requirements on the accuracy of the closure laws are demanding the time-averaged modeling approach is feasible. The application of the space-averaged drag model didn't lead to equally satisfactory results. The reasons behind this failure are related to the mismatch between the conditions in which the model parameters were determined and where they were applied. This discrepancy can be remedied in the future. Similarly, the drag closure function developed for the time-averaged modeling approach needs improvements. It was based on data from 2D simulations. The present work showed that 3D data clearly differ from 2D results, but no model was developed on the basis of the 3D data. The derived correlations also ignored the first few centimeters from the walls and from riser bottom. Separate correlations need to be developed for these regions. In the present work, particles were assumed mono-sized and spherical. Thus further work is required to extend the results of the present work to industrial applications where less ideal conditions prevail. Even with these shortcomings, the work presented in this thesis is a significant step forward in modeling of industrial CFB units.

References

Agrawal, K., Loezos, P.N., Syamlal, M., Sundaresan, S., The role of mesoscale structures in rapid gas-solid flows, J.Fluid Mech. 445 (2001) 151–185

Andrews, A.T., IV, Loezos, P.N., Sundaresan, S., Coarse-grid simulation of gas-particle flows in vertical risers. Industrial & Engineering Chemistry Research 44 (2005) 6022–6037.

De Wilde, J., The generalized added mass revised, Physics of Fluids, 19 (2007) 058103

Ergun, S., Fluid flow through packed columns, Chemical engineering progress, CEP, 48 (1952) 89–94.

Esmaili, E., Mahinpey, N., Adjustment of drag coefficient correlations in three dimensional CFD simulation of gas–solid bubbling fluidized bed, Advances in Engineering Software 42 (2011) 375–386

Gidaspow, D., Multiphase Flow and Fluidization – Continuum and Kinetic Theory Descriptions. Academic Press, ISBN 0-12-282470-9. (1994)

Hornik, K., Stinchcombe, M., White, H., Multilayer feed-forward networks are universal approximators, Neural Networks, 2 (1989) 359–366

Igci, Y., Andrews, A.T., Sundaresan, S., Pannala, S., O'Brien, T., Filtered two-fluid models for fluidized gas–particle suspensions. AIChE J. 54 (2008) 1431–1448.

Igci, Y., Pannala, S., Benyahia, S., Sundaresan, S., Validation studies on filtered model equations for gas–particle flows in risers. Ind. Eng. Chem. Res. 51 (2012) 2094–2103.

Igci, Y., Sundaresan, S., Verification of filtered two-fluid models for gas–particle flows in risers. AIChE J. 57 (2011) 2691–2707.

Kallio, S., Comparison of simulated and measured voidage and velocity profiles and fluctuations in a CFB riser. In K. Cen (Ed.), Proceedings of the 8th International Conference on Circulating Fluidized Beds, 2005. (pp. 105–112). Beijing: International Academic Publishers

Leboreiro, J., Joseph, G.G., Hrenya, C.M., Revisiting the standard drag law for bubbling, gas-fluidized beds. Powder Technology, 183 (2008) 385–400.

Li, J., Cheng, C., Zhang, Z., Yuan, J., Nemet, A., Fett, F.N., The EMMS model – its application, development and updated concepts. Chemical Engineering Science, 54 (1999) 5409–5425.

Li, T., Gel, A., Pennala, S., Shahnam, M. Syamlal, M., CFD simulation of circulating fluidized bed risers, part I: Grid study, Powder Technology 254 (2014) 170–180.

Li, T., Grace, J., Bi, X., Study of wall boundary condition in numerical simulations of bubbling fluidized beds, Powder Technology 203 (2010) 447–457

Lu, B., Zhang, N., Wang, W., Li, J., Extending EMMS-based models to CFB boiler applications, Particuology, 10 (2012) 663–671

Marquardt, D.W., An algorithm for least-squares estimation of nonlinear parameters, J. Soc. Ind. Appl. Math. 11 (1963) 431–441.

Matsen, J. M., Mechanisms of choking and entrainment. Powder Technology, 32 (1982) 21–33.

Milioli, C.C., Milioli, F.E., Holloway, W., Agrawal, K., Sundaresan, S., Filtered Two-Fluid Models of Fluidized Gas-Particle Flows: New Constitutive equations. 59 (2013) 3265–3275

O'Brien, T.J., A multiphase turbulence theory for gas–solid flows: I. Continuity and momentum equations with Favre-averaging, Powder Technology, 265 (2014) 83–87

Peltola, J., Kallio, S., Yang, H., Qiu, X, Li, J., Time-averaged simulation of the furnace of a commercial CFB boiler. 14th International conference on fluidization – From fundamentals to products, Fluidization XIV, 26–31 May 2013, Noordwijkerhout, The Netherlands: Engineering Conferences International. Proceedings Fluidization XIV Conference, Pp. 699–706

Taivassalo, V., Peltola, J., Kallio, S., Time averaged CFD modelling of a circulating fluidized bed combustor. 21st International Conference on Fluidized Bed Combustion, 21FBC, Napoli, Italia, 3–6 June 2012. Napoli, Italia: EnzoAlbanoEditore. 21st International Conference on Fluidized Bed Combustion Proceedings Volume 2 (2012b) 891–898.

Wang, W., Li, J., Simulation of gas–solid two-phase flow by a multi-scale CFD approach – extension of the EMMS model to the sub-grid level. Chem.Eng.Sci. 62 (2007) 208–231.

Wen, C., Yu, Y., Mechanics of fluidization, Chem. Eng. Prog. Symp. Ser., 62 (1966) 100–111.

Werther, J., Measurement techniques in fluidized beds, Powder Technology 102 (1999) 15–36.

Yang, N., Wang, W., Gei, W., Li, J., CFD simulation of concurrent-up gas-solid flow in circulating fluidized beds with structure-dependent drag coefficient. Chemical Engineering Journal 96 (2003) 71–80.

Zeng, Zh.X., Zhou, L.X., A two-scale second-order moment particle turbulence model and simulation of dense gas–particle flows in a riser, Powder Technology (2006) 27–32

Zhang, D.Z., VanderHeyden, W.B., The effects of mesoscale structures on the macroscopic momentum equations for two-phase flows, Int. J. of Multi-phase Flow 28 (2002) 805–822

Zhang, N., Lu, B., Wang, W., Li, J., 3D CFD simulation of hydrodynamics of a 150 MWe circulating fluidized bed boiler. Chemical Engineering Journal 162 (2010) 821–828.

Zou, B., Li, H., Xia, Y., Ma, X., Cluster structure in a circulating fluidized bed, Powder Technology 78 (1994) 173–178.

PAPER I

Length scales of solid clusters in a two-dimensional circulating fluidized bed of Geldart B particles

Powder Technology, 269 (2015) 207–218.

Powder Technology 269 (2015) 207–218

Contents lists available at ScienceDirect

Powder Technology

journal homepage: www.elsevier.com/locate/powtec

Length scales of solid clusters in a two-dimensional circulating fluidized bed of Geldart B particles

Debanga Nandan Mondal [a,*], Sirpa Kallio [b], Henrik Saxén [a]

[a] Thermal and Flow Engineering Laboratory, Åbo Akademi University, Biskopsgatan 8, FI-20500 Åbo, Finland
[b] VTT Technical Research Centre of Finland, Metallimiehenkuja 6, Espoo, P.O. Box 1000, FI-02044 VTT, Finland

ARTICLE INFO

Article history:
Received 27 April 2014
Received in revised form 5 August 2014
Accepted 14 August 2014
Available online 4 September 2014

Keywords:
Circulating fluidized bed
Cluster dimensions
Length scale
Image analysis

ABSTRACT

The flow pattern in a circulating fluidized bed (CFB) is characterized by clusters of particles. The length-scale distribution of solid clusters was analyzed both horizontally and vertically from a number of experiments carried out with Geldart B particles in a two-dimensional circulating fluidized bed. Cluster dimensions were found to be dependent on solid loading, superficial gas velocity and location in the bed. Large length scales were found to be typical for the bottom region, above which more narrow dense clusters are common. The majority of clusters in the upper part of the riser have a width less than 20 mm, which means that in CFD simulations of circulating fluidized beds the mesh resolution should be finer than 5 mm to accurately reproduce the clusters. However, a significant fraction, of the order of 10–15% of the measured cluster widths, was below 2 mm. This is about ten times the particle diameter which is the mesh spacing recommended in the literature for CFD simulation of CFBs. The findings of the study on the width and height distributions of the clusters may also be used as a point of comparison with corresponding measures observed in simulated systems, by which a quantitative validation of CFD results could be made.

1. Introduction

The flow pattern in a circulating fluidized bed (CFB) is characterized by a complicated structure with continuously forming and vanishing clusters of particles. According to Davidson [1] the clusters are particle groups having larger height than width, retaining the primitive structure for a substantial time travel through the CFB riser. For Geldart B particles the shapes of the clusters are obscure and long narrow strands of particles are typical, while Geldart A particles additionally form small, more tightly packed clusters (Cocco et al. [2]).

Computational fluid dynamics (CFD) simulations have become an important tool in the development of CFB processes. To accurately describe the flow patterns, transient simulations should be carried out in a fine computational mesh. In practice, however, computational resources limit the feasible mesh size [3]. Thus it becomes important to understand what length scales of the flow field can be resolved by the simulation and what scales should be covered by sub-grid scale equation closures (see, e.g., Igci et al. [4]). Typically, the thinnest clusters are narrower than the mesh spacing, but their importance is not clear; the share of solids collected in such narrow clusters is not well known.

In case of Geldart A particles, the size of a cluster formed due to cohesive forces can sometimes be easy to measure. For Geldart B particles it is not as easy to define a cluster size, although such attempts have been made [5,6]. Measurements with optical probes can be applied to determine cluster length scales, typically the vertical ones [7,8]. Instead of defining a cluster size the widths and lengths of the particle strands and other regions with high solid content can be analyzed. Many researchers have already observed that the dimensions of clusters vary at different bed locations along with their duration of appearance [9]. It has been noted that clusters at the wall region sustain longer than clusters of the central region. Studies have also shown that in two-dimensional CFBs the solid particle clusters form into streaks [10]. Solid hold-up plays a major role for the cluster shapes. Bai et al. [11] found that higher solid hold-up in solid particle clusters gives rise to a U-shaped form but if the particle density becomes low the particles instead form stands. Furthermore, the dynamic behavior of clusters is very specific to the position and bed properties. Image analysis and evaluation of physical properties of clusters have been undertaken by Rhodes et al. [12] and Lim et al. [13], who inferred that the clusters become elliptical or arched-shaped in vertical front view. Based on experimental evaluations in a pilot-scale CFB, Chew et al. [14,15] stated that for Geldart B particles the local riser position has a very dominant influence on cluster characteristics. These authors also suggested that the physical properties of clusters be dependent on the bed conditions and this influence is more dominant in the upper region of the CFB riser. Their investigations furthermore revealed that higher bed inventory (solid loading) produces U-shaped clusters while lower bed inventory produces more inverted U-shaped structures.

* Corresponding author. Tel.: +358 2 2154439.
E-mail address: dmondal@abo.fi (D.N. Mondal).

http://dx.doi.org/10.1016/j.powtec.2014.08.031
0032-5910/

Cluster dimensions are important in the study of cluster hydrodynamics. In the present study cluster dimensions, both in the vertical and horizontal directions, are studied in a preudo-2D cold CFB rig. Efforts were made to analyze the cluster dimensions at different riser locations to gain an understanding of the influence of specific regions for given bed conditions. Both dilute and dense phase flow structures were studied with appropriate cluster definitions. On the basis of the results, conclusions are finally drawn on the appearance of different-sized clusters in the parts of the bed, on the effect of fluidization conditions and bed loading, as well as on the selection of a suitable mesh resolution in CFD simulation of a circulating fluidized bed.

2. Experimental

In the present work, a cold CFB unit at Åbo Akademi University, Åbo, Finland (Guldén, [16]) was used to study length scales of variations in solid volume fractions (Fig. 1). The height of the riser is 3 m and the width is 0.4 m. The distance between the riser walls is 0.015 m which renders the unit fairly two-dimensional. The air distributor consists of 8 equally spaced air nozzles. The front and back walls are made of polycarbonate plates allowing visual observation and image analysis. In the experiments the bed is illuminated from behind for video recording. The bed material consisted of spherical glass particles with a material density of 2480 kg/m^3. Before the tests, the bed material was sieved to a narrow size range with a Sauter mean diameter of 0.255 mm. The total mass of the bed material was varied between $m = 2.0$ kg and 4.0 kg.

Superficial gas velocities studied were $u = 1.25$ m/s, 1.75 m/s, 2.25 m/s and 2.75 m/s. At the lowest gas velocities solid circulation was minimal and the character of the flow behavior could be classified as turbulent fluidization. However, especially at the highest velocity of 2.75 m/s significant amounts of solids exited the riser and returned to the riser bottom through the solid circulation loop. For the cases with bed masses of 2 kg and 3.3 kg, the measured solid circulation rates per riser cross-sectional area were 24 kg/m^2 s and 47 kg/m^2 s, respectively. A core-annular flow pattern prevailed in these cases along the entire riser height. According to [17] the transport velocity above which fast fluidization state is reached would be for the present case 2.8 m/s, i.e. slightly above the highest velocity used in our study. The measured high circulation rates, the observed core-annular flow structure and the fact that clusters formed below 1.0–1.5 m height were commonly transported up to the riser exit indicate, however, that the flow conditions in our 2D riser were close enough to the conditions in the fast fluidization regime to allow for drawing conclusions on length scales in CFB conditions. Short tests at higher velocities were carried out to visually confirm this but due to the difficulties related to operation of the loop seal and the increased static electricity at higher gas velocities, no long enough videos at higher velocities were recorded for the present analysis.

Fig. 1 illustrates the flow structure at three heights at a superficial gas velocity of 2.75 m/s. The images show long narrow clusters and strands in the upper part of the riser and denser complicated structures further down. At the walls in the bed bottom region wide dense sections occur. The behavior of the CFB at the bed bottom up to 0.73 m, in the middle from 0.73 m to 1.37 m and at the top from 1.37 m to 1.95 m was video recorded in all the experiments. From every test a 3-minute video was analyzed in detail by image processing. To verify that the

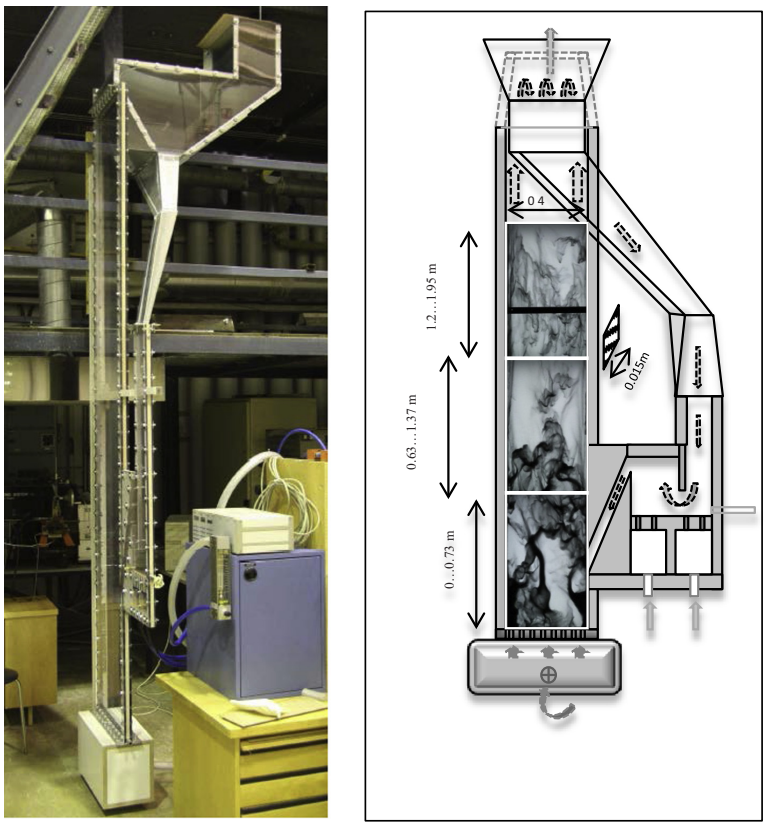

Fig. 1. Left: Photograph of the lab-scale CFB. Right: Functional diagram of the CFB along with experimental images from heights $z = 0.00…0.73$ m, 0.63…1.40 m and 1.40…2.20 m.

analyzed time period is sufficient, part of the study was repeated for a randomly picked 50 s section of one of videos. The calculated statistics for the cluster length scales were compared with corresponding results obtained for the full 3-minute video. No significant differences were detected and thus the 3-minute recording time was considered acceptable for the present analysis. A Canon 7D camera with a 50 mm f/1.8 lens was used for recording videos with shutter speed 1/800, light sensitivity of ISO 100 and an aperture of f/4.

3. Analysis method

Videos were recorded during the experiments at the frame rate of 50 s^{-1}. The videos were then converted to sequential images, after which the individual images were analyzed in MATLAB® in three steps: a) image thresholding, b) cluster identification and c) measurement of length scales. The chosen recording time, 3 min, was considered sufficiently long to produce statistically representative distributions of the measured length scales. This is confirmed by the smoothness of the obtained distribution curves. Only exceptionally, e.g. at low fluidization velocities at high elevations, the number of clusters was locally too small for calculation of statistical properties.

3.1. Image thresholding

To define and separate clusters from the background, the images had to be converted into binary images by using a proper threshold grayscale value. To sustain significant cluster detail, the threshold parameter was determined through an optimization procedure.

The criteria and procedures for treshold selection applied in this work [18–20] are as follows:

- The solid density in the cluster must be significantly higher than in the rest of the suspension. In case of grayscale images the grayscale intensity values inside the clusters must be above the local average intensity values.
- In the tresholding procedure, the image portions having a grayscale value δ above $\overline{\delta} + F\sigma_{\delta}$ are marked as cluster regions. Here σ_{δ} is the standard deviation of local grayscale intensity, $\overline{\delta}$ is the local avarage grayscale intensity and F is a factor to be chosen to produce good separation of clusters.
- Instead of doing the calculation for the whole image at a time, the calculation was also done for variable fractions of the original images to test if it would result in a better separation. The image fraction is thus a small rectangular segment of an image which was used to calculate the local average intensity and its standard deviation. The image segment was moved across the entire image to separate the clusters from the background noise. The selection of this image fraction directly influences the cluster definition and cluster sizes and hence the number of detected clusters.

To select a suitable value of F and a suitable size for the analysis region these two parameters were varied in wide ranges and the number of clusters found in a typical image at bed bottom was calculated. The trade-off between these parameters is illustrated in Fig. 2. When the image is divided into smaller fractions or the value of F is reduced, the tresholding procedure splits the dense regions into a larger number of mainly small clusters. By visual inspection of the produced clusters, compared to the original image, the values for F and analysis region were finally chosen.

The whole image includes 690 pixels, which in Fig. 2 is shown as 190 (690–500). After analysis of the results obtained with different image fractions, it was still decided to take the whole image as the image fraction in the analysis. This choice was made to get more distinct results from the thresholding at a optimum analysis time.

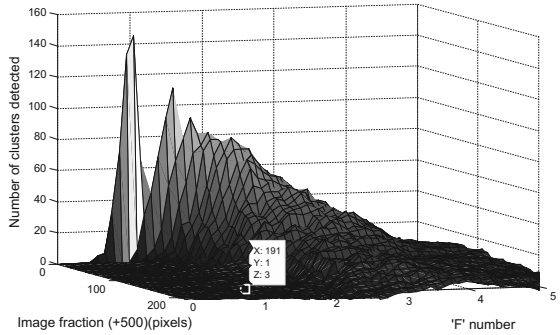

Fig. 2. Trade off between image fraction and parameter F used for the analysis with the corresponding number of clusters obtained from the analysis.

3.2. Cluster identification and determination of the length scale

The threshold was applied on the original images and the cluster boundaries became distinct as shown in Fig. 3. The individual clusters were then represented as polygons.

The length scales of clusters were calculated by measuring the cluster widths and heights at each of the three video recording positions shown in Fig. 1. First, along a particular bed height, the number of all the intersecting cluster sections was calculated. The intersecting cluster sections can be branches of a single cluster or separate clusters. The cluster width, or more specifically cluster branch width, was calculated on the basis of the number of pixels inside the polygon at a particular vertical coordinate.

The selection of a proper value for F is important as the cluster definition depends on it, as can be seen in Fig. 3, which shows the clusters in the bottom section of the riser. Results of the identification procedure higher up in the riser are visualized in Fig. 4.

Fig. 3 illustrates the method in defining and separating the clusters from the background. For $F = 0.5$ the clusters are well defined and the cluster branches are clearly visible. If F is increased to 0.75 or 1.0, the small branches are removed to some extent but also significant large clusters are affected. Considering the trade-off situation it was concluded that $F = 0.5$ is a suitable choice for the image analysis.

The solid hold-up in the clusters higher up in the riser is typically much lower than in clusters in the lower sections. In the upper part of the riser lighter areas must be considered to be clusters and accordingly the cluster dimensions are measured. As shown in Fig. 4a and b the clusters found in the dilute regions of the riser can have dimensions similar to the clusters found in the lower part of the riser. The difference is that solid concentration in the clusters in the upper regions is clearly smaller than in the dense regions at lower elevations. The large dark regions

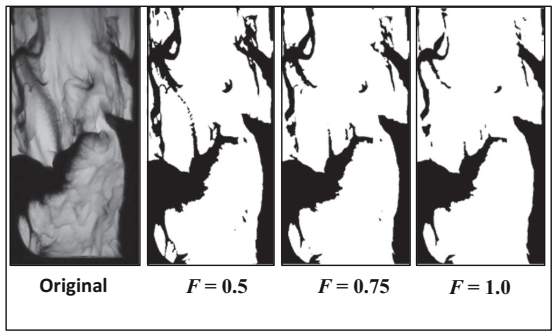

Fig. 3. Defining clusters in an image (Riser: 0 m…0.73 m) with $F = 0.5$, 0.75 and 1.0.

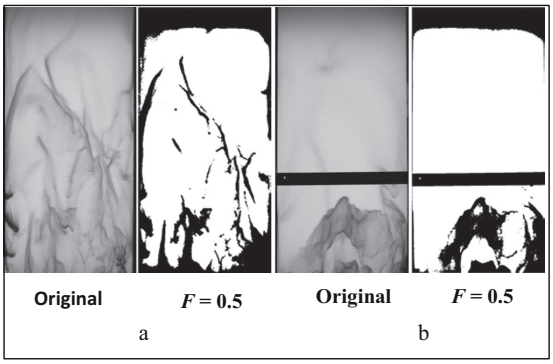

Fig. 4. a. Bed mass $m = 2$ kg, gas velocity $u = 2.25$ m/s, elevation $z = 0.63…1.37$ m. b. $m = 4$ kg, $u = 1.75$ m/s, $z = 1.22…1.95$ m.

seen in the upper part of the figure are caused by non-uniform lighting conditions at the top of the images and these were excluded from the analysis.

4. Results

4.1. Distribution of cluster widths

The cluster branch widths are calculated from the video images for four different bed masses and for four superficial gas velocities at $z =$ 1.28 m, 0.67 m, 0.35 m and 0.038 m. The cumulative cluster branch width distributions for $m = 2.0$ kg, 2.6 kg and 3.3 kg are illustrated in Fig. 5. In each subfigure the horizontal axis shows the cluster branch width, w, and the vertical axis shows the cumulative percentage of cluster area occupied by the respective clusters, C. The superficial gas velocities are $u = 1.25$ m/s (light gray diamonds), 1.75 m/s (gray squares), 2.25 m/s (gray triangles) and 2.75 m/s (black circles).

It is evident that in the bottom-most location ($z = 0.038$ m) clusters with wide branches occupy the majority of the riser area filled by a dense suspension. At low bed mass the gas velocity influences the distribution, but with increased mass the wide clusters become dominant in this region and the effect of gas velocity becomes almost negligible.

At $z = 0.35$ m and $m = 2.0$ kg very narrow clusters of the range 0.005…0.038 m occupy almost 60% of the area at the highest gas velocity ($u = 2.75$ m/s). The general trend of the cluster width at this gas velocity is the same for $m = 2.6$ kg, but larger clusters emerge at lower gas velocities. In fact, the cumulative distribution of cluster branch widths is very similar to what was observed for the lowermost part of the bed, but the effect of gas velocity is stronger here. For $m = 3.3$ kg the horizontal dimension of the clusters become evenly distributed among all the dimension ranges and the portion of wider clusters increases when the velocity changes from u = 2.25 m/s to u = 1.25 m/s. At this bed elevation ($z = 0.35$ m) the bed mass as high as 3.3 kg gives rise to channeling of air through the central portion of the bed, resulting in some wide clusters outside the central zone for all the superficial gas velocities and this is quite evident from the curves. This channeling effect is not prominent for the lower bed masses of 2.0 kg and 2.6 kg and this is the reason their curves show a large number of fine clusters.

Higher up in the riser, $z = 0.67$ m, the clusters become wider. At lower gas velocities (1.25 m/s or 1.75 m/s) almost 50% of the total area is occupied by clusters in the width range 0.02…0.09 m and at the lowest gas velocity the cumulative distribution is almost linear. Overall, on this vertical level the distributions are quite independent of the bed mass, while gas velocity has a strong effect. It should be noted that in the splash zone around $z = 0.67$ m the change in gas velocity influences the cluster dimensions more than on the other elevations.

As for the conditions in the topmost region analyzed ($z = 1.28$ m), it is interesting to note that an increase in velocity can make the cluster branches wider, by contrast to the trend observed for the lower regions of the riser. This is caused by the increase in solid hold-up at higher velocities. It should be mentioned that for the lowest bed mass and gas velocity ($m = 2$ kg, $u = 1.25$ m/s) the number of solid structures in the upper part of the riser was very low which significantly reduces the reliability of the calculated statistics, so this case was omitted from Fig. 5.

Special attention was given to the highest experimental bed mass ($m = 4.0$ kg) since for this there is enough of solids also in the upper part of the riser to facilitate a systematic analysis of the clusters. The distributions of cluster branch widths along with changes in gas velocity and elevation in the CFB riser are illustrated in Figs. 6 and 7. For this big bed mass the bottom-most region of the bed (e.g. bed height z = 0.038 m, not shown in the figure) exhibited no variation of cluster width distribution with changes in gas velocity. This is so because this region is close to the gas entrance into the bed and the major solid bulk remains higher than this elevation, making this region dilute for all the gas velocities and thus the distribution of cluster widths are insensitive to the velocity change.

At $z = 0.35$ m gas velocity has a significant effect. Like in the case of other bed masses higher velocities make the clusters narrower at the bottom. The high bed mass leads to a distinct channeling of the air for the lower superficial gas velocities ($u = 1.25$ m/s, 1.75 m/s, 2.25 m/s). Because of this air channeling a substantial amount of solid bulk remains almost stagnant in this region, giving a high amount of wide clusters for $u = 1.25$ m/s. The dominance of wide clusters is reduced as the gas velocity increases from 1.25 m/s to 2.25 m/s: Almost 50% of total cluster area is occupied by clusters with $w = 0.12…0.20$ m and the extent of channeling is reduced, showing a greater amount of solid transport through this elevation giving rise to narrower cluster structures. At $u = 2.75$ m/s the air channeling almost vanishes and solid transport becomes very rapid; this is the reason why the cluster area is dominated by mostly narrow clusters: almost 60% of the total cluster area is occupied by clusters with w = 0.02…0.10 m.

The splash zone for this bed inventory is located at around $z =$ 0.67 m, and at this height the trend is similar but much less pronounced, showing a dominance of wider clusters at lower gas velocities.

At the highest elevation ($z = 1.28$ m) analyzed, only little variation is seen in the horizontal dimension of the clusters with increasing gas velocity. This can be attributed to the fact that for the gas velocities $u =$ 1.75 m/s…2.75 m/s, the particles are transported upwards in the form of very fine clusters and an increase in gas velocity only increases the number of fine clusters forming along the riser without changing the widths of them.

The effect of elevation along the riser on the cluster branch width distribution is illustrated in Fig. 7 for a bed mass of $m = 4.0$ kg and gas velocity of $u = 2.75$ m/s. The figure clearly indicates that for this bed mass very limited differences of cluster branch widths occur at $z = 0.99…1.28$ m. This can be the consequence of a uniform transport of particles through this region under the studied conditions. Between $z = 0.99$ m and 0.67 m dispersion of solid structures takes place, which explains the slight widening of the observed clusters. The highest elevation studied, $z = 1.65$ m, is already close to the exit. At $u = 2.75$ m/s the solid particles tend to ascend and they do no longer return within the bed, but are transported back through the downcomer. This region gets more dilute making the appearing solid structures narrow.

The influence of bed inventory on the horizontal dimension of solid clusters is shown in Fig. 8. At $z = 0.35$ m (leftmost subpanel) it is evident that increasing the bed mass from $m = 2.0$ kg to 3.3 kg makes the clusters wider. Interestingly, a further increase from $m = 3.3$ kg to 4.0 kg reverses the trend: Operation with the highest bed inventory gives rise to narrower clusters. Visual observation during the experiment reveled that this was caused by channeling of air. A bed mass of $m = 3.3$ kg yields more inverted U-shaped solid structures moving upwards. The solid transportation is more pronounced for this bed mass

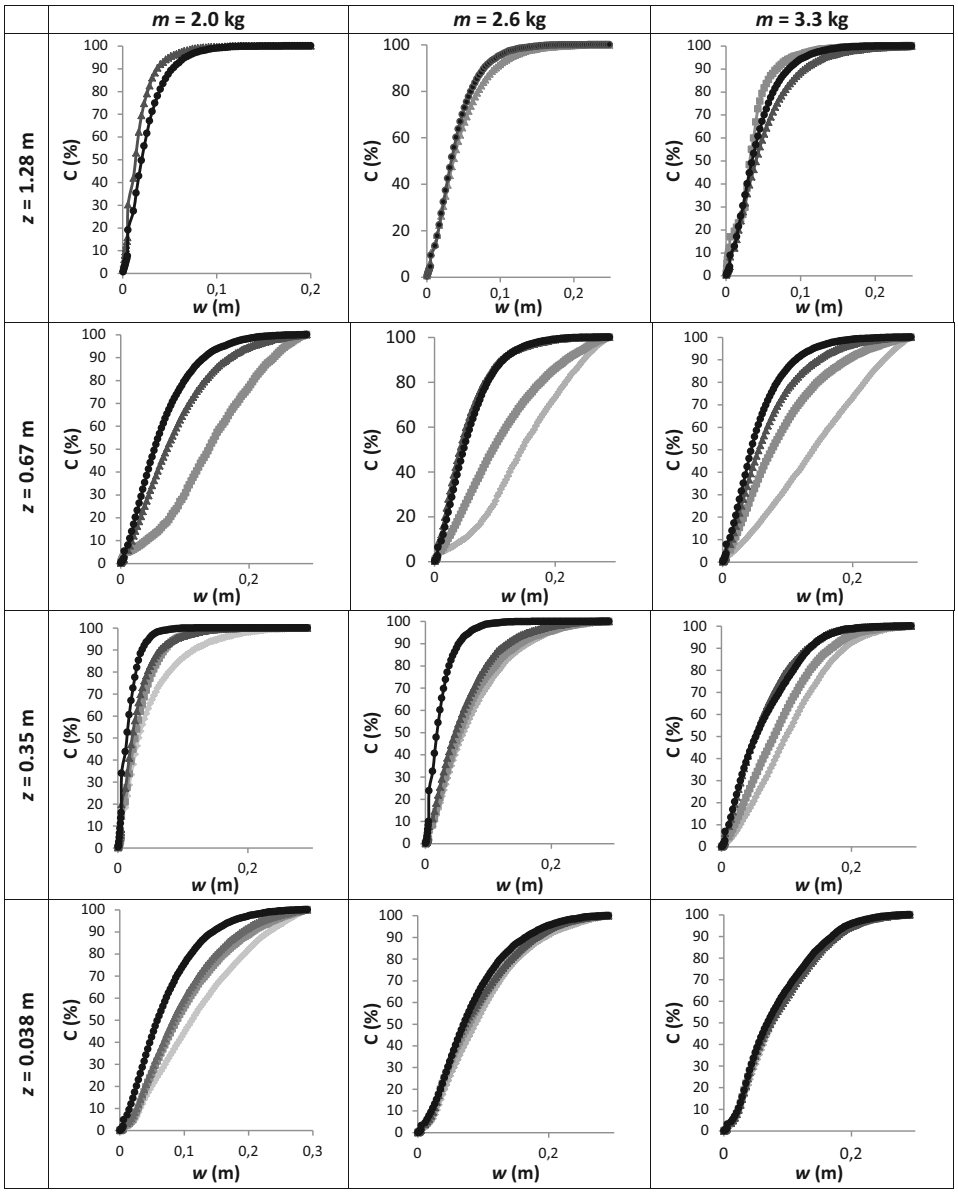

Fig. 5. Effect of superficial gas velocity (•-•-• 2.75 m/s, ▲-▲-▲ 2.25 m/s, ▪—▪—▪ 1.75 m/s, ⋆—⋆—⋆ 1.25 m/s) on the cluster branch width variation in a 2-D CFB with bed masses $m = 2.0$ kg, 2.6 kg and 3.3 kg (going from left to right among the subpanels) and elevations of $z = 1.28$ m, 0.67 m, 0.35 m and 0.038 m (going from top to bottom among the subpanels). Vertical axis shows the cumulative percentage of area occupied by the cluster branch with respective thickness expressed along the horizontal axis.

and the clusters tend to spread out more, giving rise to wider clusters. As the bed mass increases, wider clusters occupy a larger portion of the total cluster-occupied area at $z = 0.99$ m (right subpanel). This is because more bed mass is being carried to this higher region

4.1.1. Horizontal distribution of cluster widths

So far the investigations of cluster branch width distribution have been carried out for vertical positions along the riser, but the cluster branch widths also change along the horizontal direction of the experimental CFB. Therefore, different horizontal regions of the bed were studied.

Fig. 9 shows the width distribution of the clusters along a 10 cm wide central region at different elevations for $m = 4.0$ kg and $u = 2.75$ m/s. The distributions from this narrow central region were analyzed because the high bed mass and superficial gas velocity was observed to give rise to very different trends on the different vertical levels. The clusters in the central region were found to be very thin; a majority of the clusters were much less than 0.1 m wide (which, naturally, was the upper detection limit). The area occupied by comparatively

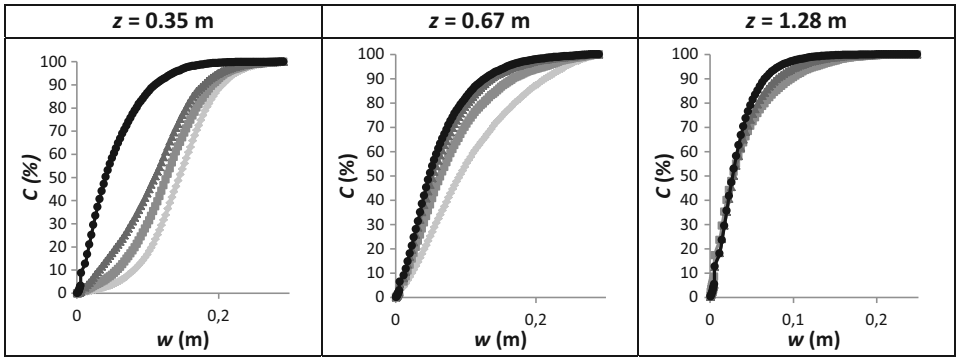

Fig. 6. Effect of gas velocity (•-•-• 2.75 m/s, ▲-▲-▲ 2.25 m/s, ▪—▪—▪ 1.75 m/s, ◦—◦—◦ 1.25 m/s) on the cumulative distribution of cluster branch widths at the riser elevation $z = 0.35$ m (left), $z = 0.68$ m (middle) and $z = 1.28$ m (right). The bed inventory is $m = 4$ kg. Vertical axis shows the cumulative percentage of area occupied by the cluster branch with respective thickness expressed along the horizontal axis.

wider clusters is larger in the bottom bed, and the cumulative distribution is almost linear with respect to the cluster width at the lowest elevation. With an increase in elevation the narrower clusters become predominant in the riser. At the highest elevation ($z = 1.65$ m) cluster branches narrower than 0.006 m represent almost 50% of the total cluster-occupied area. This can be explained from the cluster shape point of view: the clusters in this region are dilute and form narrow strands of particles. Comparing the results of Fig. 9 with those of Fig. 8 it can be concluded that the distribution trends for $z = 0.99$ m and $z = 1.28$ m are similar. It is evident that the majority of the wider clusters for this bed inventory and superficial gas velocity appear outside the central zone, i.e., closer to the side walls.

4.1.2. Summary of cluster width distributions

To summarize the results of the cluster branch width investigation for the 2D CFB, percentages of the total cluster area occupied by clusters branch widths falling within specific ranges are reported in Table 1 and Fig. 10, where the percentages of the total cluster area are given at six different elevations along the riser. The table shows cluster widths up to 0.1 m. Clusters with large widths within this range, e.g. 0.08…0.1 m, become less common with increasing elevation. At the highest elevation (rightmost column) the most dominant cluster branch widths are within the range 0.005…0.01 m and these clusters occupy almost a third of the total cluster area followed by the range 0.01…0.02 m, which occupies a fourth. In the splash zone ($z \approx 0.67$ m) the most dominant widths are 0.02…0.04 m where these clusters occupy a fourth of the total area. It

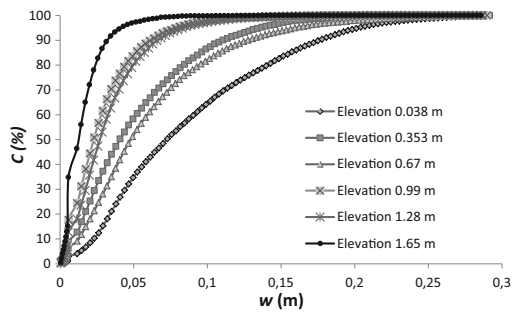

Fig. 7. Effect of elevation along the CFB riser on the cluster branch width distributions for bed inventory of $m = 4$ kg and a gas velocity $u = 2.75$ m/s. Vertical axis shows the cumulative percentage of area occupied by the cluster branch with respective thickness expressed along the horizontal axis.

may be noted that this specific range of widths is a significant contributor in the cluster population at almost all bed elevations studied.

4.2. Cluster branch height distribution

The cluster branch height distributions were calculated at three horizontal locations along vertical lines. The locations were chosen in such a way that typical cluster branch height variations could be extensively evaluated along the horizontal stretch of the riser. Location 1 is along a vertical line 0.025 m from the side wall, Location 2 is at the center of the bed and Location 3 is an intermediate position (roughly midway between the wall and the centerline) 0.28 m from the side wall. Cluster branch heights were calculated along these vertical lines for the three experimental bed sections, i.e., the lower, middle and the higher bed as shown in Fig. 1.

The cumulative distributions of cluster branch heights are illustrated in Figs. 11 (Location 1, wall) and 12 (Location 2, centerline) for bed masses of $m = 2.0$ kg, 2.6 kg and 3.3 kg. The superficial gas velocities are the same as earlier, i.e., $u = 1.25$ m/s, 1.75 m/s, 2.25 m/s and 2.75 m/s.

The region $z = 0.63…1.73$ m is among the most dilute parts of the riser for $m = 2.0$ kg and $u = 1.25$ m/s and 1.75 m/s; the cluster dimensions detected were very much dependent on the cluster definition, so the results for these velocities were omitted from Fig. 10. As described in conjunction with Fig. 4, in these dilute regions the number of clusters is very small and the clusters are extremely dispersed. For $m = 2.0$ kg but for higher gas velocities, the branch height distributions are identical, and the distributions observed for higher bed mass ($m = 2.6$ kg and 3.3 kg) are also alike and quite insensitive to the variation of superficial gas velocity. However, for the lower gas velocities a cluster height of about 0.05 m seems to be more frequent than other heights.

At the lower section of the riser ($z = 0.0…0.73$ m) the gas velocity does not influence the vertical dimensions of the clusters for $m = 3.3$ kg, because falling solid films are always present at the side walls. For lower bed mass, the gas velocity plays a marked influence, and comparatively high clusters (in the range 0.2…0.3 m) frequently appear for $u = 1.25$ m/s.

Fig. 12 illustrates the height distributions of clusters for Location 2, i.e., along the centerline of the bed. The top row, reporting the results for from the upper part ($z = 0.63…1.73$ m) of the bed indicates small vertical dimensions of the clusters. Again, the case with $m = 2.0$ kg and $u = 1.25$ m/s corresponded to very few solid structures and the results were therefore omitted. For $u = 1.75$ m/s about 54% of the cluster area was occupied by clusters of heights 0.078…0.084 m. This can, again, be understood with reference to Fig. 4: In this region the low bed mass and low gas velocity give rise to very few clusters and a very

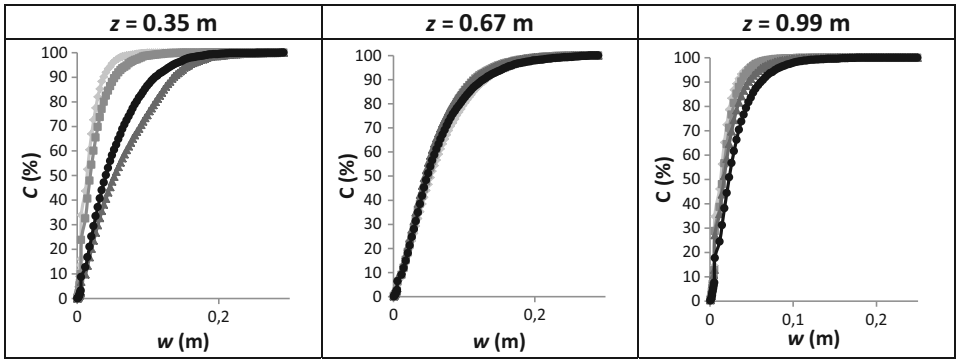

Fig. 8. Cluster branch width distributions with change of bed inventory (•-•-• 4.0 kg, ▲-▲-▲ 3.3 kg, ▪–▪–▪ 2.6 kg, ◦—◦—◦ 2.0 kg) for a gas velocity of u = 2.75 m/s. From left to right: elevations z = 0.35 m, 0.67 m, and 0.99 m. Vertical axis shows the cumulative percentage of area occupied by the cluster branch, *C*, with respective thickness, *w*, expressed along the horizontal axis.

non-uniform distribution of cluster heights. With increased superficial gas velocity the distributions stabilize. The above is a sign of cluster break-down in the central zone. At this height a further increased bed mass yields consistent distributions of the cluster heights. For lower bed elevations ($z = 0.0…0.73$ m), in turn, the changes in the distributions are more monotonic. With increase in velocity a majority of the clusters get shorter and this holds true for all the bed masses. The conditions for $m = 2.6$ kg and, in particular, for $m = 3.3$ kg, are quite insensitive to the gas velocity. It was noticed that a large bed mass in combination with low gas velocities gave rise to air channels, making the cluster heights very similar. With increase in velocity (u = 2.25 m/s and 2.75 m/s) more inverted U-shaped structures moving upwards appeared, and these structures transported more solids, but the vertical dimensions remained close to those found at the lower gas velocities.

Fig. 13 shows a comparison between the cluster branch height distributions for the three horizontal locations for the bed mass of $m = 4.0$ kg. It can be concluded that at the lower bed position the change in superficial gas velocity has a more pronounced effect on the cluster branch height distribution. Location 3, which is between the center and the wall region, shows a significant amount of shorter clusters for the gas velocity of 2.75 m/s: The share of clusters of height 0.12 m or less was about 80%, while the corresponding share was about 48% for the other three gas velocities. The reason behind this behavior is that for a high bed mass the lower velocities (1.25…2.25 m/s) produce distinct channeling of air through the central zone of the bed, keeping the bed mass content in other regions more or less constant. On the other hand, for the gas velocity $u = 2.75$ m/s the central channeling of air vanishes, which gives more uniform turbulence across the bed. Thus, the clusters also get thinner and longer in dimension. These characteristics of cluster formation disappear higher up in the bed, where the four gas velocities gave similar cluster height distributions for each location. The reason is that through this region bed mass is being carried to the higher region and the increase in gas velocity does not affect the vertical dimensions of the particle strands forming.

Finally, for a bed mass of $m = 4.0$ kg and a gas velocity of $u = 2.75$ m/s, the influence of vertical bed elevations on the heights of the cluster branches for the three horizontal locations are reported in Fig. 14. At the wall (Location 1) the cluster heights are seen to distribute linearly over the size range at the lowest portion of the bed (z = 0…0.73 m). Here, the lack of fine clusters can be explained by the large number of falling films along the sidewalls for the high bed mass and superficial gas velocity. As the bed elevation increases the number of finer clusters increases, as the falling films at the side walls are not so dense higher up in the bed; these falling films gradually accumulate solid particles on the way down and become longer at the lower portion of the riser.

From Fig. 14 some observations can be made: Along the side wall at Location 1 an increase in bed elevation seems to shorten the cluster branches. This is also evident for Location 3 midway between the side wall and the center of the bed, but on the contrary the central region of the bed shows opposite trends. The bottom region (elevation up to 0.73 m) shows longer cluster branches than the higher bed elevations (1.22…1.95 m) but shorter cluster branches than in the middle region (0.63…1.37 m).

The cluster height distributions along the center of the riser (Location 2) differ from those of the wall and near-wall regions. At an elevation of 0.63 m…1.37 m, which is vertically the middle portion of the

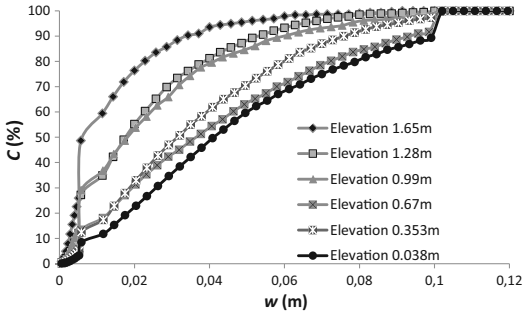

Fig. 9. Effect of elevation on the distribution of cluster branch widths in a 10 cm wide region in the center of the riser for $m = 4$ kg and $u = 2.75$ m/s. Vertical axis shows the cumulative percentage of area occupied by the cluster branch with respective thickness expressed along the horizontal axis.

Table 1
Percentage of the total cluster area occupied by a given range of cluster branch widths at different vertical elevations along the riser ($m = 4$ kg, $u = 2.75$ m/s). The highlighted region is illustrated in Fig. 10.

Cluster branch width (m)	Vertical elevation along the riser (m)					
	0.038	0.35	0.67	0.99	1.28	1.65
0.000…0.002	0.25%	0.679%	0.81%	2.00%	1.74%	5.57%
0.002…0.005	0.92%	2.61%	2.06%	5.64%	3.72%	9.61%
0.005…0.01	2.88%	9.43%	6.23%	16.78%	12.66%	31.22%
0.01…0.02	4.33%	12.5%	9.00%	20.01%	17.54%	25.66%
0.02…0.04	18.46%	25.03%	23.8%	32.14%	34.66%	22.47%
0.04…0.06	16.09%	16.52%	19.3%	13.26%	16.53%	3.88%
0.06…0.08	12.27%	12.17%	13.00%	5.69%	7.47%	1.17%
0.08…0.10	10.32%	7.51%	8.46%	2.52%	2.98%	0.26%
0.01…0.12	7.39%	13.55%	6.04%	1.04%	1.48%	0.09%
0.12…0.16	13.15%	5.95%	6.29%	0.65%	0.97%	0.07%
0.16…0.20	8.75%	1.49%	2.96%	0.22%	0.22%	0%
0.20…0.24	3.56%	0.44%	1.25%	0.04%	0.02%	0%
0.24…0.29	1.73%	0.12%	0.78%	0%	0%	0%

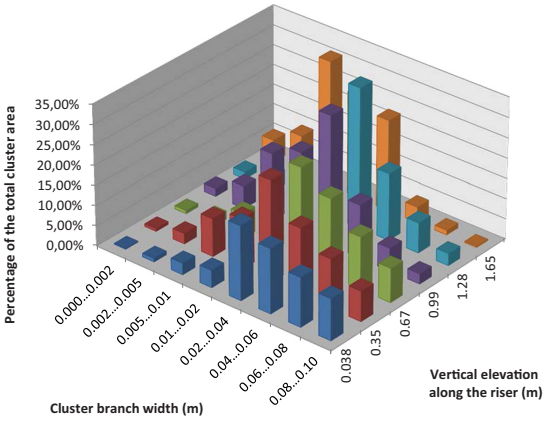

Fig. 10. 3-dimensional histogram plot of Table 1 containing cluster branch width variation from 0 m to 0.1 m which is highlighted in Table 1.

riser, the total cluster area seems to be occupied mostly by the shorter clusters. This is so as the solids are transported upwards through this region in form of fine and short clusters resembling the shape of an inverted "U". Going downwards along the riser the clusters start getting longer and denser. At an elevation of 0…0.73 m the solid structures are more chaotic and they do not have any shape characteristic as above. In the highest region of the riser (1.22…1.95 m) the clusters get elongated and thin along the center of the riser, as can be seen in Fig. 13. The clusters also get more dilute.

The summarizing Table 2 and Fig. 15 for $m = 4.0$ kg and $u = 2.75$ m/s show that clusters of height in the range 0.02…0.04 m occupy a majority of the cluster area throughout the bed with little variations. These clusters are mostly predominant in the higher bed section ($z = 1.22…1.95$ m), particularly at Locations 1 and 3, i.e., other regions than the central zone. Cluster heights in the range 0.04…0.06 m also occupy a significant amount of the cluster area. In comparison with the results of Table 1, it can be clearly stated that in the lower section of the bed ($z = 0.0…0.73$ m) the horizontal cluster dimensions are equal to the vertical dimensions for the more dominant clusters, but higher up in the riser the vertical dimensions exceed the horizontal dimensions.

5. Implications for CFD modeling

The analysis of video images from a cold pilot circulating fluidized bed carried out in the present work has demonstrated that very narrow cluster strands occur practically everywhere in the riser, and that the share of the total cluster area occupied by narrower clusters is significant. Filtering out length scales below 5 mm would result in a significant loss of information. Cluster widths below 5 mm were common in all parts of the riser and need thus to be resolved by the computational mesh. Visual evaluation of video images also indicated that large clusters have similar internal fine structures, particularly in the dilute upper part of the riser. Consequently, to resolve the cluster structures, mesh spacing of the order of 1–2 mm is recommended.

In CFD modeling, it is a common practice to conduct grid convergence studies to evaluate the mesh size required for achieving accurate simulation results. A commonly used rule-of-thumb is that a mesh resolution of 10 particle diameters suffices to produce grid-independent results [21]. For the system studied in the present work it would mean a mesh spacing of 2.5 mm. However, clusters with length scales below 2 mm were commonly found in the center of the riser at the highest elevations, and in a large CFB unit this type of flow patterns are expected to be encountered in the major part of the flow domain. On the basis of the results of the present analysis of length scales, we thus conclude that a much finer mesh than 10 particle diameters may be necessary. Still,

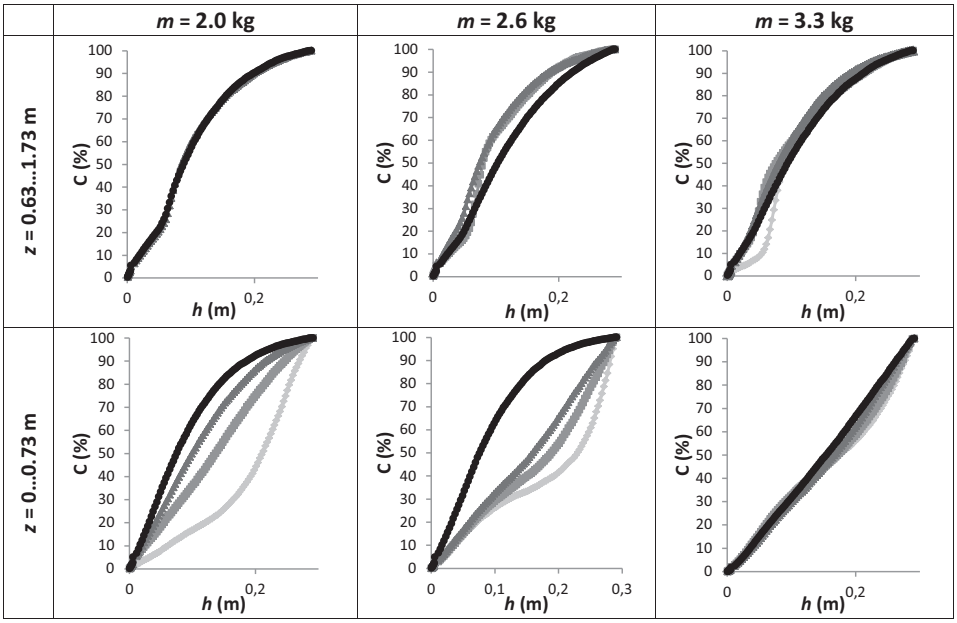

Fig. 11. Cluster branch height distribution at Location 1 for different gas velocities (•-•-• 2.75 m/s, ▲-▲-▲ 2.25 m/s, ▪—▪—▪ 1.75 m/s, ◦—◦—◦ 1.25 m/s): Bed mass increases from left to right ($m = 2.0$ kg, 2.6 kg and 3.3 kg), elevation decreases from top to bottom (z = 0.63 m…1.73 m, 0.0…0.73 m). Horizontal axis represents the cluster branch height and vertical axis the cumulative percentage of the total cluster area occupied by the clusters of respective branch heights.

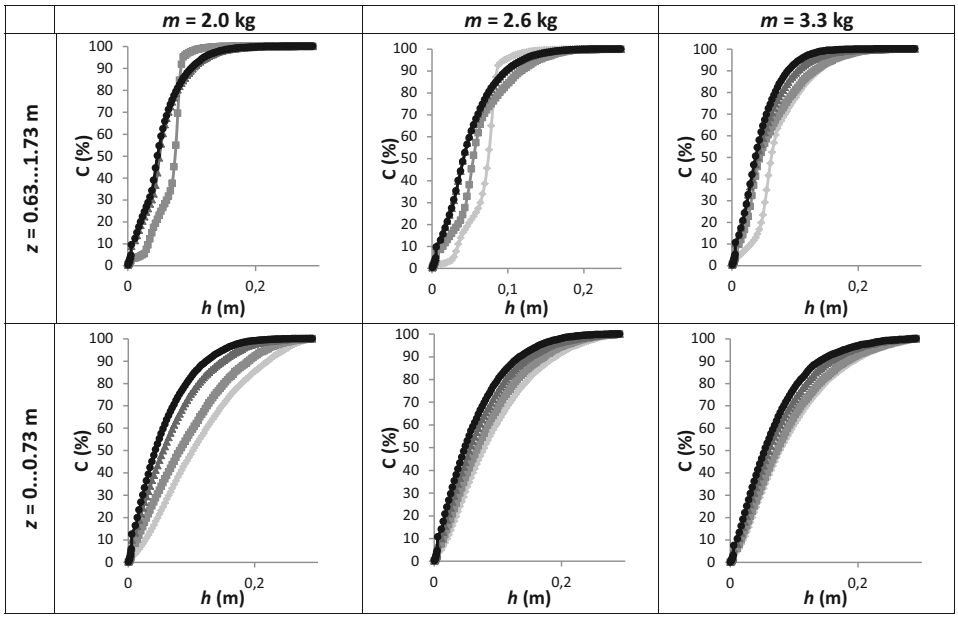

Fig. 12. Cluster branch height distribution at Location 2 for different gas velocities (•-•-• 2.75 m/s, ▲-▲-▲ 2.25 m/s, ▪–▪–▪ 1.75 m/s, ◦—◦—◦ 1.25 m/s): Bed mass increases from left to right ($m = 2.0$ kg, 2.6 kg and 3.3 kg), elevation decreases from top to bottom ($z = 0.63$ m…1.73 m, 0.0…0.73 m). Horizontal axis represents the cluster branch height and vertical axis the cumulative percentage of the total cluster area occupied by the clusters of respective branch heights.

studies of effects of the computational mesh have shown that there is little need to reduce the mesh spacing much beyond the 10-diameters' limit. The produced flow patterns obviously have sufficiently appropriate statistical properties to produce average lateral and vertical velocity, voidage and pressure profiles in general agreement with those encountered in the true processes.

Li et al. [22] demonstrated the complexity of the effects of the computational mesh. The investigators found that the recommended mesh

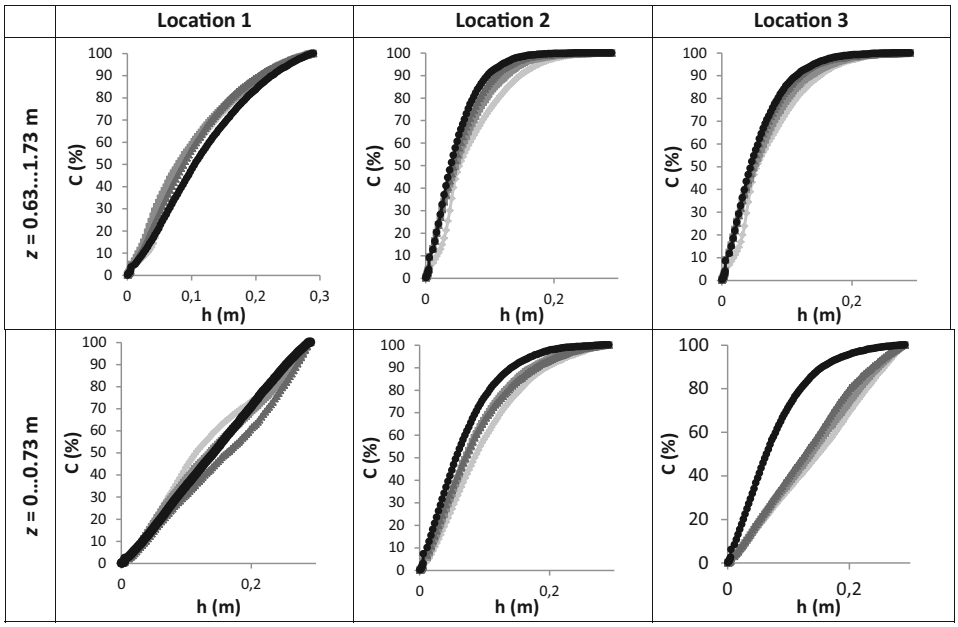

Fig. 13. Cluster branch height distribution for bed mass of $m = 4$ kg at different gas velocities (•-•-• 2.75 m/s, ▲-▲-▲ 2.25 m/s, ▪–▪–▪ 1.75 m/s, ◦—◦—◦ 1.25 m/s). Left to right columns: Location 1, 2 and 3. Vertical bed sections are $\Delta z = 0.63$–1.73 m (top row) and $\Delta z = 0.0$…0.73 m (bottom row). Horizontal axis represents cluster branch height and vertical axis the cumulative percentage of the total cluster area occupied by the clusters of respective branch heights.

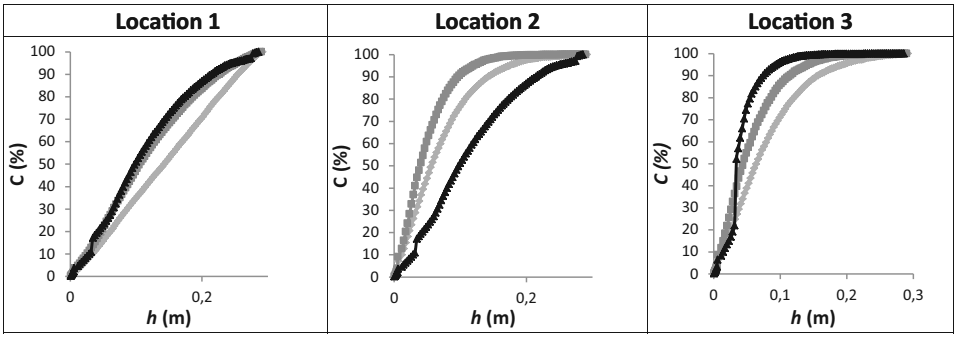

Fig. 14. Cluster branch height distribution in vertical sections (▲-▲-▲ 1.22…1.95 m, ▪–▪–▪ 0.63…1.37 m, ◦—◦—◦ 0…0.73 m) of the bed at three horizontal locations for $m = 4$ kg bed inventory and a gas velocity of $u = 2.75$ m/s. Horizontal axis represents cluster branch height and vertical axis cumulative percentage of the total cluster area occupied by the clusters of respective branch heights.

spacing was dependent on the averaged property they studied. This indicates that different simulation accuracies in a statistical sense are required for evaluation of the different averaged properties. Although the resolution necessary for resolving the true length scales of the clusters is, according to the present authors' study, clearly finer than 10 particle diameters, a coarser mesh may suffice to produce statistically sound flow patterns. The authors also concluded that for different regions in the riser different mesh spacing would be required. This conclusion is supported by our findings: not only the location but also the fluidization conditions, i.e., solid loading and gas velocity, affect the observed length scales.

Instead of carrying out simulations in a fine mesh, the computation burden is commonly reduced by applying a coarse mesh. A description of the flow structures filtered by the mesh by sub-grid closures then becomes necessary. Drag laws for filtered equations can include the cluster size as a parameter. In some models, the particle diameter is replaced by a cluster diameter [23]. The fairly popular filtered drag model EMMS (energy minimization multi-scale) [24] is based on the division of the suspension into dense and dilute regions. It uses the cluster size or a heterogeneity index as a parameter and computes it from empirical equations. The data retrieved from the experiments in the present work could be used to test the accuracy of such correlations for cluster size.

6. Prospects for future work

The particle size used in the present study is typical of CFB boilers. The fact that mesh resolution in a CFD simulation is suggested to be relative to the particle size indicates that particle size has a significant effect on the cluster dimensions. Extension of the experiments to different process conditions (e.g. temperature, pressure, amount of static electricity), solid material densities, and particle sizes and shapes is required in order to further extrapolate the results to the wide field of conditions encountered in fluidized beds.

The present study was carried out in a pseudo-2D unit. The side walls affect the flow by forcing the rising and falling clusters to collide. Although such encounters between clusters take place even in 3D units, the pseudo-2D geometry increases their probability, which can affect the observed length scales. Thus the applicability of the results to 3D cases needs to be evaluated in the future. Cluster length scales can also depend on the size of the riser, but the possible effect of the riser dimensions could not be evaluated in the present study.

Table 2
Fraction of area occupied by clusters with a given range of cluster branch heights at three horizontal locations and three vertical bed sections for $m = 4$ kg and $u = 2.75$ m/s. The highlighted region is illustrated in Fig. 15.

Cluster branch height (m)	Location 1			Location 2			Location 3		
	Vertical elevation along the riser (m)			Vertical elevation along the riser (m)			Vertical elevation along the riser (m)		
	0… 0.73	0.63… 1.37	1.22… 1.95	0… 0.73	0.63… 1.37	1.22… 1.95	0… 0.73	0.63… 1.37	1.22… 1.95
0.000..0.002	0.29%	0.75%	0.90%	0.65%	1.2%	0.90%	0.60%	1.25%	1.08%
0.002…0.005	0.64%	1.24%	1.22%	2.28%	2.74%	1.22%	1.90%	2.75%	2.18%
0.005…0.01	2.1%	2.81%	2.49%	7.11%	9.79%	2.49%	5.87%	7.86%	4.99%
0.01…0.02	2.73%	3.22%	2.67%	8.11%	11.45%	2.67%	6.94%	9.97%	5.07%
0.02…0.04	6.78%	8.85%	12.09%	26.73%	27.24%	12.09%	16.47%	24.72%	48.50%
0.04…0.06	7.64%	10.57%	7.87%	16.92%	19.13%	25.87%	16.14%	17.95%	21.57%
0.06…0.08	8.07%	10.57%	12.71%	13.5%	13.30%	12.71%	13.60%	13.12%	8.49%
0.08…0.1	7.53%	10.18%	11.19%	10.31%	7.7%	11.19%	10.75%	8.78%	4.21%
0.1…0.12	6.2%	7.92%	8.3%	6.49%	3.29%	9.5%	7.32%	4.62%	2.11%
0.12…0.16	14.6%	15.32%	16.61%	9.02%	4.06%	15.42%	11.02%	5.93%	1.43%
0.16…0.2	14.5%	12.25%	7.28%	4.63%	0.89%	10.94%	5.08%	2.21%	0.32%
0.2…0.24	14.6%	9.42%	7.89%	1.38%	0.18%	6.8%	2.65%	0.67%	0.04%
0.24…0.29	14.27%	6.9%	5.76%	0.89%	0.03%	0.17%	1.65%	0.15%	0%

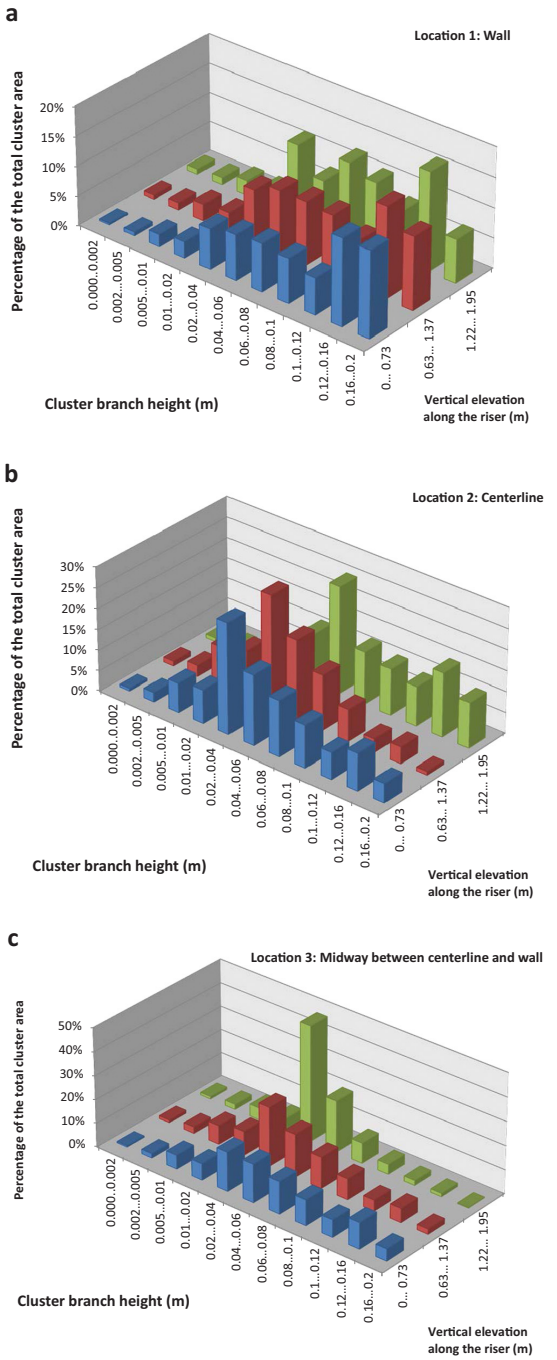

Fig. 15. 3-dimensional histogram plot of the highlighted section of Table 2 for the cluster branch heights observed at the a. wall region, b. central region, c. region midway between centerline and wall.

The results of the present study on the width and height distributions of the clusters will in the forthcoming research be used as a means of verifying CFD simulations of the system by comparing the simulated cluster length scales with the observed ones in different parts of the bed. The differences between simulations and observations can be used to tune parameters in the CFD models or they could guide the investigator in the selection of submodels applied in the complex CFD calculations.

7. Conclusions

In the present study, the length scales of the variations in solid volume fraction in a two-dimensional CFB riser were analyzed from a number of experiments carried out with Geldart B particles with Sauter mean diameter of 0.255 mm. Large length scales are typical for the bottom region above which more narrow dense clusters are common. The narrowest clusters are of the order of a couple of millimeters. A large fraction of solids seems to travel in clusters in the width range around 0.005 m, which means that a mesh spacing of about 1–2 mm should be used in CFD simulations not to lose significant details of the flow structures. In the upper part of the riser the length scales become even smaller and the rule-of-thumb that a mesh spacing of 10 particle diameters suffices in CFD simulations may need to be reconsidered. In the bottom bed the vertical and lateral length scales of the clusters are close to each other, but in the upper part of the riser the vertical dimensions are clearly larger. Thus, measurement of cluster sizes with optical probes, which measure the vertical length scale, can lead to overestimation of cluster dimensions. The study was conducted with a particle size typical of CFB combustors. Extension of the results to other particle sizes and 3D cases should be considered in the future.

Notation

C	cumulative percentage of cluster area
F	cluster separation parameter
h	cluster branch height
u	superficial gas velocity
w	cluster branch width
z	bed elevation
δ	gray scale value
σ_δ	standard deviation

Acknowledgments

The authors gratefully acknowledge the financial support of Tekes, VTT Technical Research Centre of Finland, Åbo Akademi University, Etelä-Savon Energia Oy, Fortum, Metso Power Oy and Numerola Oy, and the support from Saarijärven Kaukolämpö Oy. The invaluable assistance of Mr. Alf Hermanson and Mr. Lassi Karvonen in the laboratory is acknowledged.

References

[1] J.F. Davidson, Circulating fluidised bed hydrodynamics, Powder Technol. 113 (2000) 249–260.
[2] R. Cocco, F. Shaffer, R. Hays, S.B. Reddy Karri, T. Knowlton, Particle clusters in and above fluidized beds, Powder Technol. 203 (2010) 3–11.
[3] J. Peltola, S. Kallio, Estimation of turbulent diffusion coefficients in a CFB on basis of transient CFD simulations, 21st Int. Conf. on Fluidized bed Combustion (FBC 21), Naples, Italy, 2012.
[4] Y. Igci, S. Pannala, S. Benyahia, S. Sundaresan, Validation studies on filtered model equations for gas-particle flows in risers, Ind. Eng. Chem. Res. 51 (2012) 2094–2103.
[5] G.W. Xu, K. Kato, Hydrodynamic equivalent diameter for clusters in heterogeneous gas–solid flow, Chem. Eng. Sci. 54 (1999) 1837–1847.
[6] C. Guenther, R. Breault, Cluster Dynamics in a Circulating Fluidized Bed, US Department of Energy Technology Laboratory, 2007.
[7] J. Werther, Measurement techniques in fluidized beds, Powder Technol. 102 (1999) 15–36.
[8] B. Zou, H. Li, Y. Xia, X. Ma, Cluster structure in a circulating fluidized bed, Powder Technol. 78 (1994) 173–178.
[9] A.K. Sharma, K. Tuzla, J. Matsen, J.C. Chen, Parametric effects of particle size and gas velocity on cluster characteristics in fast fluidized beds, Powder Technol. 111 (2000) 114–122.

[10] U. Arena, A. Cammarota, A. Mazocchella, L. Massimilla, Solids flow structures in a two-dimensional riser of a circulating fluidized bed, J. Chem. Eng. Jpn. 22 (1989) 236–241.
[11] D. Bai, Y. Jin, Z. Yu, Cluster observation in a two-dimensional fast fluidized bed, in: M. Kwauk, H. Hasatani (Eds.), Fluidization '91, Science and Technology, Science Press, Beijing, 1991, pp. 110–115.
[12] M.J. Rhodes, H. Mineo, T. Hirama, Particle motion at the wall of the 305 mm diameter riser of a cold model circulating fluidized bed, in: P. Basu, M. Horio, M. Hasatani (Eds.), Circulating Fluidized Bed Technology, vol. III, Pergamon Press, Oxford, 1990, pp. 171–176.
[13] K.S. Lim, J. Zhou, C. Finley, J.R. Grace, C.J. Lim, C.M.H. Brereton, Cluster descending velocity at the wall of circulating fluidized bed risers, in: M. Kwauk, J. Li (Eds.), Circulating Fluidized Bed Technology, vol. V, Chemical Industry Press, Beijing, 1996, pp. 218–223.
[14] J.W. Chew, R. Hays, J.G. Findlay, T.M. Knowlton, S.B. Reddy Karri, R.A. Cocco, C.M. Hrenya, Cluster characteristics of Geldart Group B particles in a pilot-scale CFB riser. I. Monodisperse systems, Chem. Eng. Sci. 68 (2012) 72–81.
[15] J.W. Chew, R. Hays, J.G. Findlay, T.M. Knowlton, S.B. Reddy Karri, R.A. Cocco, C.M. Hrenya, Cluster characteristics of Geldart group B particles in a pilot-scale CFB riser. II. Polydisperse systems, Chem. Eng. Sci. 68 (2012) 82–93.
[16] M. Guldén, Pilotmodell av en cirkulerande fluidiserad bädd, (M.Sc. Thesis) Åbo Akademi University, Åbo, Finland, 2008. (in Swedish).
[17] H. Bi, L.-S. Fan, On the existence of turbulent regime in gas–solid fluidization, AIChE J. 38 (1992) 297–301.
[18] C.H. Soong, K. Tuzla, J.C. Chen, Experimental determination of cluster size and velocity in circulating fluidized bed, in: J.F. Large, C. Laguerie (Eds.), Fluidization VIII, New York, Engineering Foundation, New York, 1995, pp. 219–227.
[19] K. Tuzla, A.K. Sharma, J.C. Chen, T. Schiewe, K.E. Wirth, O. Molerus, Transient dynamics of solid concentration in downer fluidized bed, Powder Technol. 100 (1998) 166–172.
[20] L.C. Gómez, F.E. Milioli, A numerical simulation analysis of the effect of the interface drag function on cluster evolution in a CFB riser gas–solid flow, Braz. J. Chem. Eng. 21 (2004) 569–583.
[21] A.T. Andrews IV, P.N. Loezos, S. Sundaresan, Coarse-grid simulation of gas-particle flows in vertical risers, Ind. Eng. Chem. Res. 44 (2005) 6022–6037.
[22] T. Li, A. Gel, S. Pennala, M. Shahnam, M. Syamlal, CFD simulation of circulating fluidized bed risers, part I: grid study, Powder Technol. 254 (2014) 170–180.
[23] T. McKeen, T. Pugsley, Simulation and experimental validation of a freely bubbling bed of FCC catalyst, Powder Technol. 129 (2003) 139–152.
[24] B. Lu, W. Wang, J. Li, Eulerian simulation of gas–solid flows with particles of Geldart groups A, B and D using EMMS-based meso-scale model, Chem. Eng. Sci. 66 (2011) 4624–4635.

PAPER II

Towards time-averaged CFD modelling of circulating fluidized beds

9th Int. Conf. on Circulating Fluidized Beds,
Hamburg, 2008.

TOWARDS TIME-AVERAGED CFD MODELLING OF CIRCULATING FLUIDIZED BEDS

Sirpa Kallio[+], Veikko Taivassalo[+], Timo Hyppänen[#]

[+] *VTT Technical Research Centre of Finland, Finland*
[#] *Lappeenranta University of Technology, Finland*

Abstract - In case of large CFBs, steady state CFD simulation can be an attractive alternative for the time-consuming transient simulations. In the present paper, the features of equation closure of a steady state model are evaluated on basis of a transient 3D simulation. The computational results are analysed to determine the averaged flow properties and the main fluctuating components and their correlations. The main terms to be modelled for the steady state approach are, according to this analysis, the average gas-particle drag force and the Reynolds stresses arising from velocity fluctuations. Suggestions for approaches for steady state equation closure in case of industrial CFB applications are discussed.

INTRODUCTION

CFD modelling of circulating fluidized beds is most often done using the kinetic theory model of granular flow and a transient description. The large size of industrial CFBs makes it impossible to resolve the finest flow structures by fine meshes. The practically applicable coarse meshes necessitate development of sub-grid scale closures for the unresolved fluctuations. In transient coarse mesh simulations, the fraction of momentum transfer expressed by the subgrid-scale closures increases in comparison to the momentum transfer expressed by the average velocities and volume fractions as the mesh becomes coarser. An even larger portion of momentum transfer is expressed by closure relations in steady state models. However, there is no large conceptual difference between the steady state and the coarse mesh closure models. Since steady-state simulations should produce the average flow much faster, steady-state simulation can be an attractive alternative for large CFBs.

Several attempts to develop closure models for coarse-mesh and steady-state simulations have been presented in the literature. Closure models are usually based on transient simulations of the detailed flow structures in a fairly small scale. Agrawal et al. (2001), Andrews et al. (2005) and Igci et al. (2006) studied the average drag and stress terms through simulations in small domains with periodic boundary conditions. Zhang and VanderHeyden (2001) discussed the effects of mesh spacing on Reynolds stresses and the drag force. In Zhang & VanderHeyden (2002), they suggest an added-mass force closure for the correlation between fluctuations of the pressure gradient of the continuous phase and fluctuations of solids volume fraction. De Wilde (2007a) analysed the same term from simulations and accounted also for the drag force in the derivation of new closure models that were applied in De Wilde (2007b) for steady state simulation of a riser. Zheng et al. (2006) presented a two-scale Reynolds stress turbulence model for gas-particle flows leaving the parameters undetermined. All the correlation terms resulting from integration over a large volume and/or a long time step have been addressed in the publications listed above. Unfortunately none of these papers consider all features that would be of interest to us when studying steady state modelling of large risers. Anisotropy and the influence of the real CFB geometry are addressed in the present study.

For analysis of requirements for closure relations we have here chosen to simulate a laboratory scale process with a reasonably fine mesh. In this way we have realistic CFB conditions and at the same time we still manage to produce the main fluctuation patterns. The results are validated through comparisons with measurements, which justifies time averaging on the computational results and drawing conclusions on the significance of different terms in the equations as indications for further studies.

DESCRIPTION OF THE NUMERICAL SIMULATIONS

The case studied in Kallio (2006) and in the present paper is a cold model experiment. The particle size in the simulated case is 230 μm and the material density 1800 kg/m^3. The riser height is 7.3 m (coordinate y goes from 0 to 7.3 m) and the cross-section measures 1 m times 0.25 m (x = 0…1 m, z = 0…0.25 m). The average superficial gas velocity above the air distributor is 4 m/s. The local inlet velocities are described by means of a function based on a 2D approximation of the air distributor used in the experiment. The 3D grid of the present study consists of 102400 (40 X 160 X 16) elements and it is refined towards the walls. The time step in the simulation was 5 ms. A time period of several seconds was simulated with 2 ms time

stepping, but since the fluctuation characteristics shown by the results were practically unchanged, the longer time step was chosen.

The transient simulations presented here were conducted by means of the kinetic theory model of the Fluent 6.3.26 CFD software (Fluent, 2006). The solid phase kinetic viscosity was calculated from the model by Syamlal et al. (1993). The k-ε turbulence model used in the simulations was the version modified for multiphase flows ("dispersed turbulence model", Fluent (2006)). First order discretization for time stepping and second order interpolation for spatial discretization were employed.

Since the mesh used here is too coarse to produce the smallest clusters, we have to correct the drag force. The procedure used here for gas-solid drag is the same as used in Kallio (2006). The adjustment of the drag force is based on experimental data from CFBs. Close to the minimum fluidization conditions the drag force is calculated from the Ergun (1952) equation. Elsewhere in dense conditions, an equation based on the two-phase theory of bubbling beds is applied. For more dilute suspensions the drag is calculated from an empirical correlation of an exponential form. The single particle drag law is used in extremely dilute gas-solid suspensions. The voidage function, by which the single particle drag force is multiplied in the drag model, is shown in Fig. 1.

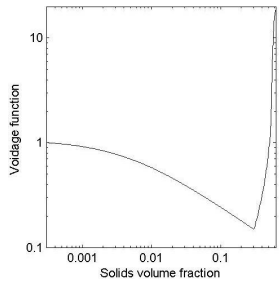

Fig. 1. The voidage function used for d_s=230 μm, ρ_s=1800 kg/m^3, and slip velocity 1 m/s.

To allow us to study the effects of wall friction on the fluctuations, one simulation was carried out using the free slip boundary condition and another one with the partial slip model of Johnson and Jackson (1987) that utilizes a specularity coefficient as a measure of the fraction of collisions which transfer momentum to the wall. To examine the maximum possible wall effects we set the specularity coefficient to one, which is certainly too high a value but useful for our purposes. Fig. 2 shows results obtained with the two models. Wall friction slows down movement of clusters at the walls and as a result the clusters grow and produce a wider wall layer. Solid concentration in the upper parts of the riser increases which is seen in Fig. 2c. No significant change in the fluctuation patterns could be observed. The rest of the analysis of this paper is based on the simulation with the free slip boundary condition, since we have more simulation data from that case. Fig. 3 shows a comparison of the measured and the simulated solid velocities and volume fractions at three different locations in the riser.

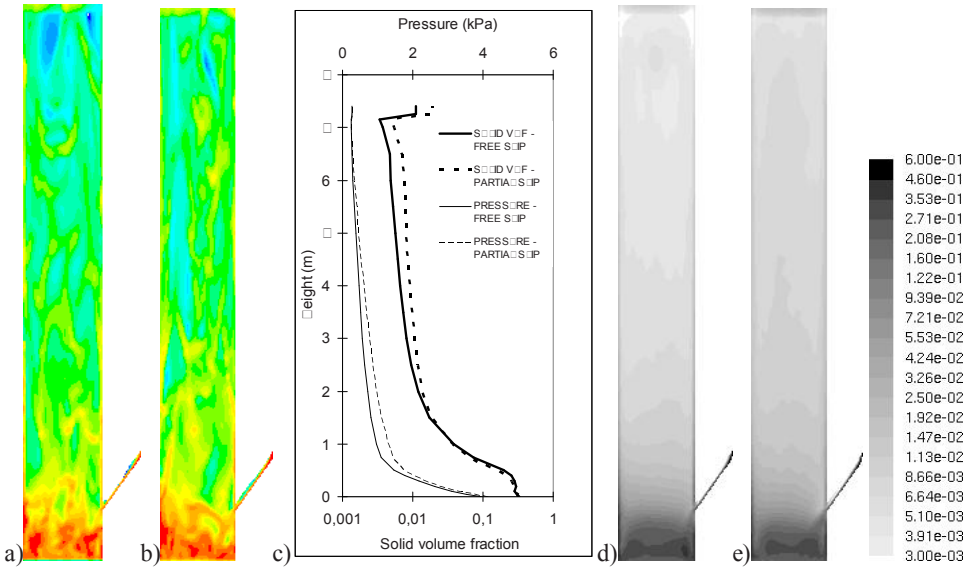

Fig. 2. Instantaneous flow patterns obtained using a) free slip and b) partial slip boundary condition. c) Vertical profiles of the average pressure and voidage distributions in the simulations with free slip and partial slip boundary conditions, respectively. Time-averaged solids volume fraction obtained with d) free slip boundary condition and e) partial slip boundary condition.

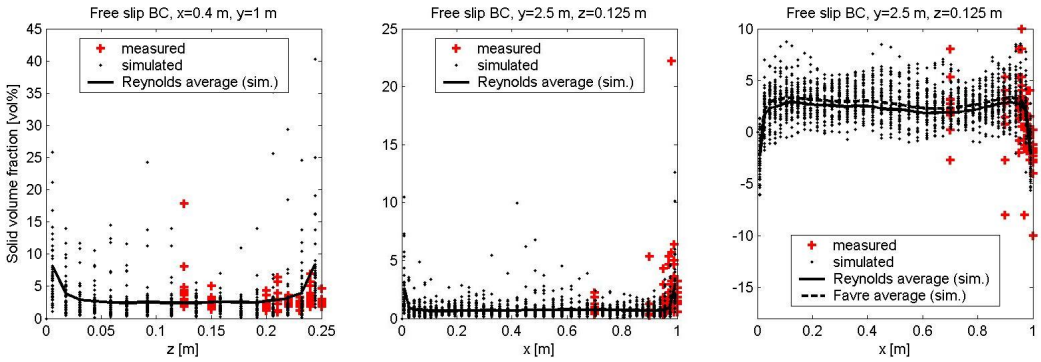

Fig. 3. Comparison between measured and simulated solid velocities and volume fractions along two cross-sectional lines. Vertical coordinate is denoted by y and the horizontal coordinates by x and z, respectively. For additional comparisons, see Kallio (2006).

ANALYSIS OF THE TERMS IN THE TIME-AVERAGED EQUATIONS

Time-averaged momentum equation

The solid phase momentum equation used in the simulations above can be written in the following form:

$$\frac{\partial}{\partial t}(\alpha_s\rho_s\mathbf{u}_s)+\nabla\cdot(\alpha_s\rho_s\mathbf{u}_s\mathbf{u}_s)=-\alpha_s\nabla p-\nabla p_s+\nabla\cdot(\alpha_s\boldsymbol{\tau}_s+\alpha_s\boldsymbol{\tau}_s^t)+\alpha_s\rho_s\mathbf{g}+K_{sf}\left(\mathbf{u}_f-\mathbf{u}_s\right) \tag{1}$$

where the stress terms are as follows:

$$\boldsymbol{\tau}_s=2\mu_s\left(\frac{1}{2}(\nabla\mathbf{u}_s+(\nabla\mathbf{u}_s)^T)\right)+\left(\lambda_s-\frac{2}{3}\mu_s\right)\nabla\cdot\mathbf{u}_s\mathbf{I} \tag{2}$$

Equation (1) will now be time-averaged. For velocities we use Favre averaging and for the rest Reynolds averaging. If a time-average is denoted by < >, we obtain the following equation:

$$\begin{aligned}\nabla\cdot\left(\langle\alpha_s\rangle\rho_s\langle\mathbf{u}_s\rangle\langle\mathbf{u}_s\rangle\right)=&-\langle\alpha_s\rangle\nabla\langle p\rangle+\nabla\cdot\left(\langle\alpha_s\boldsymbol{\tau}_s\rangle+\langle\alpha_s\boldsymbol{\tau}_s^{\,t}\rangle\right)-\langle\nabla p_s\rangle\\&+\langle\alpha_s\rangle\rho_s g+K_{sf}^*\left(\langle\mathbf{u}_f\rangle-\langle\mathbf{u}_s\rangle\right)+S_{\mathrm{Re}}+S_D+S_P\end{aligned} \tag{3}$$

where K_{sf}^* is the drag coefficient calculated from the average flow properties. The three terms resulting from correlations between fluctuations of the flow properties are

Reynolds stress term: $S_{\mathrm{Re}}=-\left[\langle\nabla\cdot(\alpha_s\rho_s\mathbf{u}_s\mathbf{u}_s)\rangle-\nabla\cdot\left(\langle\alpha_s\rangle\rho_s\langle\mathbf{u}_s\rangle\langle\mathbf{u}_s\rangle\right)\right]$ (4)

Solids volume fraction and pressure gradient correlation: $S_P=-\langle\alpha_s\nabla p\rangle+\langle\alpha_s\rangle\nabla\langle p\rangle$ (5)

Drag correction: $S_D=\left\langle K_{sf}(\mathbf{u}_f-\mathbf{u}_s)\right\rangle-K_{sf}^*\left(\langle\mathbf{u}_f\rangle-\langle\mathbf{u}_s\rangle\right)$ (6)

In the following we analyse these terms and the averages of the local stresses from the simulation results and compare them with the other terms in the equations. From the simulation, data was collected at every 4th time step. Simulated time period was 4.5 minutes and hence we have at each studied point data from 13500 time instances.

Stress terms

Several authors (e.g. Agrawal et al. (2001)) have reported that the local stress terms arising from the particle scale phenomena and given in our work by the kinetic theory models are small compared to the stress terms produced by the fluctuating motion of clusters. The same observation was made in our work. The only term that locally has significance is the solid pressure, which in the dense conditions close to walls can be of the same order of magnitude as the leading terms in the horizontal momentum equations. Whether it, even in these situations, has any significant effect on the flow field at large is questionable. Analysis of the gas phase local turbulent stresses showed that they can locally be important in areas of very high shear rates like in the vicinity of the wall layer.

Fig. 4 shows the normal component of the local stress term in comparison with convection term and with the Reynolds stresses arising from meso-scale fluctuations. The curves are for the riser axis and there the local stresses and local solid phase pressure are negligible compared to the other terms. The Reynolds stress terms dominate solids momentum transfer in the horizontal direction throughout the riser height. In the vertical direction momentum equation, Reynolds stresses dominate in the splash zone and close to the exit of the CFB whereas in the rest of the riser convection terms are larger. Gas phase Reynolds stresses arising from meso-scale fluctuations exhibit the same pattern. However, vertical gas momentum transfer is dominated by convection also at the riser bottom. Figure 4c shows a comparison of the normal Reynolds stress components. In the bottom bed region, horizontal stresses are large, but they decrease fast above the bottom bed. Close to the exit there is again an increase in the horizontal Reynolds stress components.

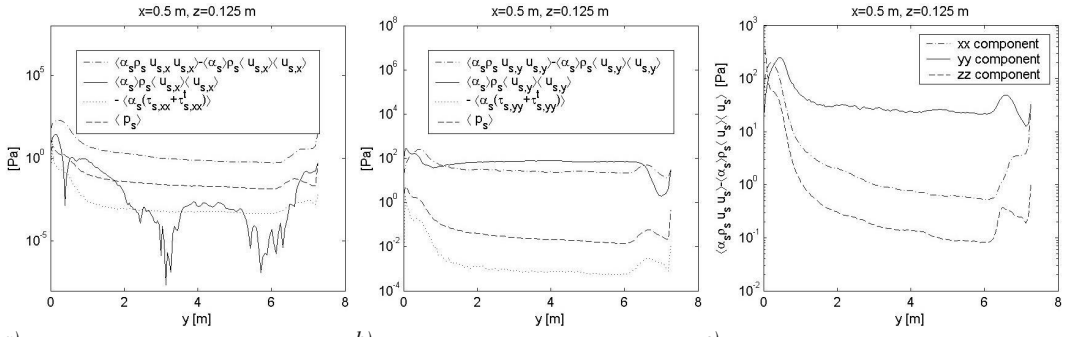

a) *b)* *c)*

Fig. 4. Comparison of convection and normal stress components in the solid momentum equation on the centreline (x=0.5 m, z=0.125 m) as a function of height (u is x-direction and v y-direction velocity component, respectively).

From the data of Fig. 4c it is possible to calculate a bulk viscosity if we use an equation of the same form as equation (2) and assume that bulk viscosity alone is responsible for the normal component of the Reynolds stress. Figure 5 shows that the resulting bulk viscosities are completely different in different directions and, moreover, they change as a function of height.

Similar analysis as for the normal components was also done for the shear stress terms. Both the solid and gas phase shear stress terms are of a similar magnitude as the corresponding convection terms. Determination of the solids viscosity from the data was difficult outside the wall layer. The order of magnitude of solid viscosity was typically 1-30 kg/sm. According to our study, shear stress terms are extremely difficult to express with a single constant viscosity.

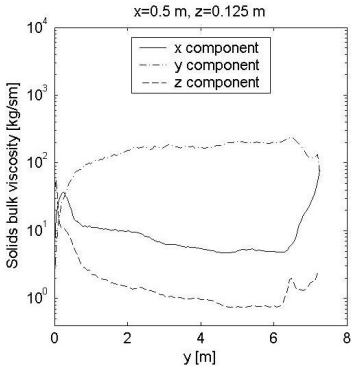

Fig. 5. Solids bulk viscosity calculated from the Reynolds stresses on the centreline (x=0.5 m, z=0.125 m) as a function of height.

Gas-solid interaction

In the literature, the focus in coarse-mesh/steady-state modelling has often been on the terms describing gas-solids interaction, i.e. the drag term and the pressure gradient term. An effective drag coefficient for coarse-mesh/steady-state simulations has been determined by averaging the vertical drag force components from a detailed simulation (see e.g. Igci et al. (2006) and Andrews et al. (2005)). Zhang & VanderHeyden (2002) and De Wilde (2007a) found in their studies surprisingly large effect from the correlation between pressure gradient fluctuations and solids volume fraction fluctuations and derived an added mass type closure for this term. The conditions in those simulations, in which this S_P term was found to be important, were denser than in the major part of a CFB and hence we consider a further analysis necessary.

From our simulation data we have determined the three components of the drag force and S_P and compared them with the other terms in the equation. In Fig. 6 the average drag force is compared with the drag force obtained by inserting the average velocities and solids volume fraction in the same drag model that was used in the transient simulation. In Fig. 6a, the horizontal x component and the vertical y component of the obtained drag force are shown at 0.2 cm height in the riser where dense suspension conditions prevail.

Figures 6b and 6c show the x and y components of the drag force obtained at 4 m height in dilute conditions. At this height the vertical drag force component obtained from the drag law using average flow properties is systematically much higher than the actual average drag between the phases and, consequently, a correction to the drag law seems necessary. The average horizontal force component, however, is fairly well obtained from the drag model used. In the dense bottom bed conditions, the situation looks more complicated and the results do not suggest any systematic correction to the drag law.

The studies in the literature have concentrated on the vertical drag force component. Our results would indicate that the need for corrections to the drag law in the horizontal and vertical directions is not equal. This should be taken in to account in future models, since the drag force is a significant term in both gas phase and solid phase momentum equations. However, as our simulation is conducted in a fairly coarse mesh with a drag law that already includes a correction for the sub-grid scale clusters, our conclusions should be verified in simulations with fine meshes.

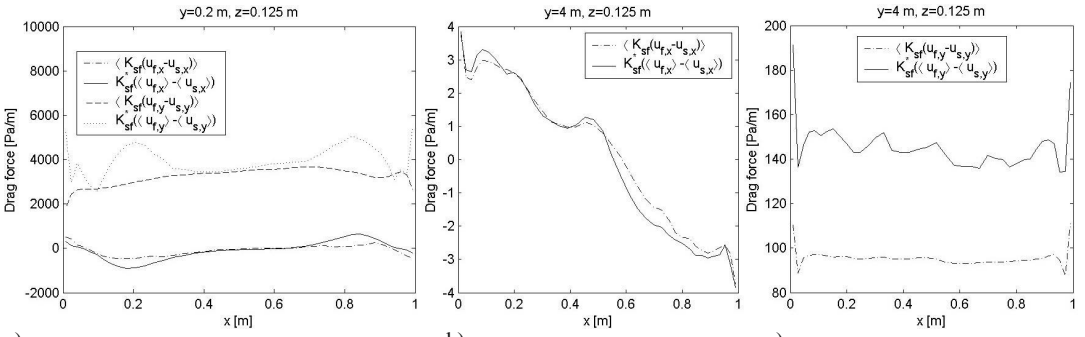

Fig. 6. Average drag force compared with the drag that is obtained with the same model using the average velocities and voidage. a) Horizontal and vertical drag components at z=0.125 m and height y=0.2 m. b) Horizontal drag component at z=0.125 m and y=4 m. c) Vertical drag component at z=0.125 m and y=4 m.

In Fig. 7 the correction S_D to the vertical component of the drag force is compared with the Reynolds stress term S_{Re} and the term S_P (see Eqs. 4-6) at two elevations. At 0.2 m height, i.e. in the bottom bed region, the three terms are roughly of the same order of magnitude. S_P is smallest of the three terms. At 4 m height, the drag correction is the dominating term except in the wall layer, where the Reynolds stress becomes large. The term S_P that other researchers (e.g. Wilde (2007a)) have found important in dense conditions is now practically zero. Similar analysis was carried out for the horizontal terms and the horizontal Reynolds stress was found to be the dominating component throughout the riser.

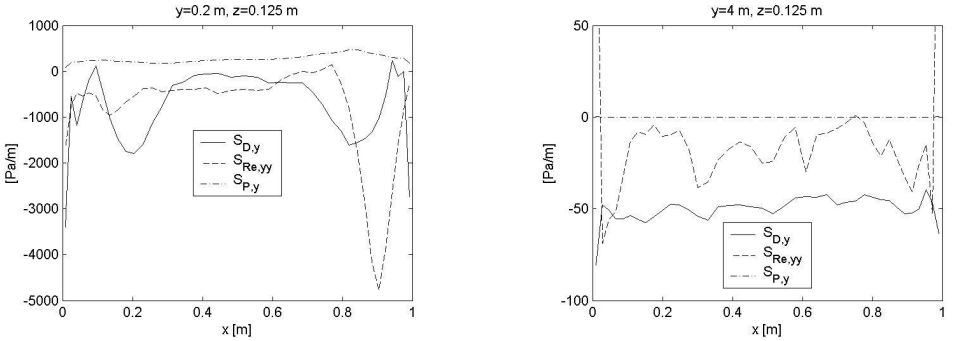

Fig. 7. The different terms in the time-averaged momentum equation. Left: at position z=0.125 m and height y=0.2 m. Right: at position z=0.125 m and height y=4 m.

Our results seem to slightly differ from the ones presented by Zhang & VanderHeyden (2002) and De Wilde (2007a). They found S_P important while we didn't find any region where it would have a dominating effect. One reason for the discrepancy is the lower suspension density of our study. Furthermore, the size of the domain studied was larger in our simulation: it is less likely to find a correlation between the local pressure and local solids content in a large riser where the pressure is determined by flow patterns in the whole riser.

CONCLUSIONS

In case of large CFBs, a steady state CFD simulation can be an attractive alternative for the time-consuming transient simulations. In the present paper, the requirements for equation closure of steady state models were evaluated on basis of a transient 3D simulation. The results were analysed to obtain averaged flow properties and the main fluctuating components and their correlations. The main terms to be modelled for the steady state approach are, according to this analysis, the average gas-particle drag force and the Reynolds stresses arising from velocity fluctuations. According to our analysis of the transient simulation results, the correction for time-averaged gas-particle interaction force should not be isotropic. The normal Reynolds stresses dominate momentum transfer in the horizontal direction and in the bottom bed also in the vertical direction. The shear Reynolds stresses are significant. On basis of the analysis, modelling of the complicated behaviour of the Reynolds stresses by means of constant viscosities seems uncertain and hence alternative approaches such as transfer equations for determining the Reynolds stresses should be considered.

ACKNOWLEDGEMENT

This work was funded by Tekes, VTT Technical Research Centre of Finland, Fortum Oyj, Foster Wheeler Energia Oy, Neste Oil Oyj and Metso Power Oy.

NOTATION

d	diameter [m]
$\mathbf{g}$	gravitational acceleration [m/s^2]
p	pressure [N/m^2]
$u, \mathbf{u}$	velocity [m/s]
K_{sf}	momentum exchange coefficient [kg/sm^3]
S_D	drag correction term (Eq. 6) [kg/m^2·s^2]
S_P	correlation of α_s and ∇p (Eq. 5) [kg/m^2·s^2]
S_{Re}	Reynolds stress term (Eq. 4) [kg/m^2·s^2]
α	volume fraction [-]
λ	second (bulk) viscosity [kg/m·s]
μ	dynamic viscosity [kg/m·s]
ρ	material density [kg/m^3]
$\boldsymbol{\tau}$	stress tensor [N/m^2]

Subscripts

s	solid phase
x,y,z	rectangular coordinates

Superscripts

t	turbulent

Other symbols and operators

∇	gradient operator
$\langle a \rangle$	time average of the variable a

REFERENCES

Andrews, A.T., Loezos, P.N., Sundaresan, S.: Coarse-grid simulation of gas-particle flows in vertical risers, Ind. Eng. Chem. Res. (2005), pp. 6022-6037

Agrawal, K., Loezos, P.N., Syamlal, M., Sundaresan, S.: The role of meso-scale structures in rapid gas-solid flows, J.Fluid Mech. (2001), 445, pp. 151-185

De Wilde, J.: The generalized added mass revised, Physics of Fluids (2007a), 19, 058103

De Wilde, J., Heynderickx, G.J., Martin, G.B.: Filtered gas-solid momentum transfer models and their application to 3D steady-state riser simulations, Chem. Eng. Sci., (2007b) 62, pp. 5451-5457

Ergun, S.: Fluid flow through packed columns, Chem. Eng. Progress (1952), 48, pp. 89-94

Fluent Inc., Fluent 6.3 Users manual (2006)

Igci, Y., Sundaresan, S., Pannala, S., O'brien, T., Breault, R.W.: Coarse-graining of two-fluid models for fluidized gas-particle suspensions, 5th Int. Conf. on CFD in the Process Industries, CSIRO, Melbourne, Australia (2006)

Johnson, P.C., Jackson, R.: Frictional-collisional constitutive relations for granular materials, with application to plane sharing, J. Fluid Mech. (1987), 176, pp. 67-93

Kallio, S.: Characteristics of gas and solids mixing in a CFB determined from 3D CFD simulations, 19th International Conference on Fluidized Bed Combustion, Vienna, Austria, 2006

Zeng, Zh.X., Zhou, L.X.: A two-scale second-order moment particle turbulence model and simulation of dense gas–particle flows in a riser, Powder Tech. (2006), 162, pp. 27-32

Zhang, D.Z., VanderHeyden, W.B.: High-resolution three-dimensional numerical simulation of a circulating fluidized bed, Powder Tech. (2001), 116, pp. 133-141

Zhang, D.Z., VanderHeyden, W.B.: The effects of mesoscale structures on the macroscopic momentum equations for two-phase flows, Int. J. of Multiphase Flow (2002), 28, pp. 805-822

PAPER III

Time averaged modeling of BFBs: Analysis of the terms in the momentum equations

Proceedings of Fluidization XIV Conference, May 2013,
Noordwijkerhout, The Netherlands, pp. 559–566.

Time-averaged modeling of BFBs: Analysis of the terms in the momentum equations

Timo Niemi*, Juho Peltola, Sirpa Kallio
VTT Technical Research Centre of Finland
P.O.Box 1000, FI-02044 VTT, Finland
*T: +358 20 778 5068; F: +358 20 722 7077; E: timo.niemi@vtt.fi

ABSTRACT

Steady state CFD simulation would present an attractive alternative for the computationally demanding transient simulations in the case of large, industrial scale BFBs. In the present paper, the features and relative importance of the various terms appearing in steady state flow equations are analyzed based on a transient simulation. According to this analysis, the most important terms in the momentum equations are the gas-solid drag term and the solid volume fraction and gas pressure fluctuation correlation terms. The solid pressure and the Reynolds stress terms are also found to be important.

INTRODUCTION

Computational fluid dynamics (CFD) combined with the kinetic theory of granular flow (KTGF) has proven to be a useful method for simulating gas-solid flows in bubbling fluidized beds (BFB). Due to the complex nature of the flow in BFBs, the simulations have been typically performed as time-dependent with small time-steps and fine meshes. This kind of an approach is computationally very time consuming and makes larger scale simulations of BFBs challenging.

With single phase flows and recently also with multiphase flows in circulating fluidized beds [1], steady-state CFD modelling approach with time-averaged flow equations has been used to greatly accelerate the simulations. Such an approach would be also attractive for flows in BFBs, but in order to use the time-averaged equations, valid closure models are required. Due to the different nature of the dense flow in BFBs, the relations developed for single phase or more dilute multiphase flows cannot be assumed to hold as such and further development is needed. This development can also help CFB steady-state

modelling, because the bottom region in some CFBs can resemble BFB flow conditions in which closures developed for BFBs would apply.

As a step towards time-averaged modelling of BFBs, in the present study a transient simulation of a lab-scale BFB is performed and time-averaged terms required for steady-state closures are computed. The features and the relative importance of the different terms are analysed and compared to those presented in the literature.

NUMERICAL MODELS

Transient and time-averaged equations

Following the notation by Taivassalo et al [1], the transient multiphase flow equations can be concisely written as

$$\frac{\partial \alpha_q \rho_q}{\partial t} + \frac{\partial \alpha_q \rho_q u_{q,k}}{\partial x_k} = 0 \tag{1}$$

$$\frac{\partial \alpha_q \rho_q u_{q,i}}{\partial t} + \frac{\partial \alpha_q \rho_q u_{q,k} u_{q,i}}{\partial x_k} = -\alpha_q \frac{\partial p}{\partial x_i} + \frac{\partial \alpha_q \left(\tau_{q,ik} + \tau_{q,ik}^M\right)}{\partial x_k} + \alpha_q \rho_q g_i + (-1)^{(\delta_{qs}+1)} K_{gs}(u_{g,i} - u_{s,i}) - \frac{\partial p_q}{\partial x_i}\delta_{qs} \tag{2}$$

where α_q is the volume fraction, $\rho_q$density, u_q velocity, p gas pressure, $p_q$solid pressure, K_{gs} inter-phase momentum transfer coefficient, δ_{qs} Kronecker delta, τ_q the laminar stress, and τ_q^M the local scale turbulent stress.

The steady-state flow equations can be obtained from the transient equations by averaging the equations over time. For the volume fraction and pressure terms the Reynold's averaging can be directly used. In Reynold's averaging the instantaneous flow variables are split into steady and fluctuating parts:

$$\phi = \bar{\phi} + \phi', \tag{3}$$

where $\bar{\phi}$ represents the average value and ϕ' is the fluctuating part. The average value over some time interval T is defined as

$$\bar{\phi} = \frac{1}{T}\int_T \phi \, dt \tag{4}$$

and for the fluctuating part the average vanishes

$$\bar{\phi}' = 0. \tag{5}$$

For the velocity the Favre averaging is used. The Favre average is defined as

$$\langle \phi \rangle = \frac{\overline{\alpha_q \phi}}{\overline{\alpha_q}} \tag{6}$$

By denoting the Favre-averaged velocity as $U_{q,i} \equiv \langle u_{q,i} \rangle$, the following averaged flow equations can be derived:

$$\frac{\partial \overline{\alpha_q}}{\partial t} + \frac{\partial \overline{\alpha_q} U_{q,k}}{\partial x_k} = 0 \tag{7}$$

$$\begin{aligned} \frac{\partial \overline{\alpha_q} \rho_q U_{q,i}}{\partial t} + \frac{\partial \overline{\alpha_q} \rho_q U_{q,k} U_{q,i}}{\partial x_k} &= \overline{\alpha_q} \rho_{qm} g_i - \overline{\alpha_q} \frac{\partial \bar{p}}{\partial x_i} - \overline{\alpha_q' \frac{\partial p'}{\partial x_\iota}} + \frac{\partial \overline{\alpha_q \tau_{q,\iota k}}}{\partial x_k} \\ + \frac{\partial \overline{\alpha_q \tau_{q,\iota k}^M}}{\partial x_k} + (-1)^{(\delta_{qs}+1)} \overline{K_{gs}(u_{g,\iota} - u_{s,\iota})} - \frac{\partial \overline{p_q}}{\partial x_i} \delta_{qs} &- \frac{\partial \rho_q \overline{\alpha_q u_{q,k}'' u_{q,\iota}''}}{\partial x_k} \end{aligned} \tag{8}$$

The terms on the right hand side in equation (8) are the gravitation, pressure, pressure fluctuation, laminar and turbulent stress, drag force, solid pressure and so-called Reynolds stress terms.

Transient simulation parameters

To obtain time averaged terms, transient 3D simulation of a laboratory scale, cold pseudo-2D bubbling fluidized bed was performed. The height of the simulated geometry was 2 m, the width 90 cm and the thickness 1.5 cm. The air was brought to the bed through 9 separate 15x15 mm injectors and the average superficial gas velocity was 0.8 m/s. The simulated bed material had a mean particle size of 656 µm and the particle density was 2480 kg/m^3. Initially the bed was 60 cm high.

At the bottom region of the bed a uniform 5 mm sized 3D mesh was used. To save some computational time, coarser 10 and 20 mm mesh sizes were used above 1.0 and 1.5 meters, but the coarsening was not made in the smallest dimension. Also, during the simulation the bed mass stayed mostly in the fine mesh region, with only some occasional splashes reaching the 10 mm coarser part. All together the mesh had 115080 elements. According to our previous experiences and literature (see [2] and [3]), 5 mm mesh size has been found to give reasonably mesh independent results. Li et al. [3] observed in a 3D simulation of a similar pseudo-2D BFB that the results obtained with three and five elements in the depth direction were close to each other, which supports our selection of mesh spacing.

The simulation was performed with the commercial solver ANSYS Fluent v.14 using the kinetic theory of granular flow (KTFG). The various parameters and sub models for the different terms in the KTFG are presented in Table 1. Except for the interphasial drag term, for all the other terms the implementations provided by Fluent were used. For the drag term the standard Gidaspow [4] model was modified to use linear interpolation between the Ergun [5] and Wen-Yu [6] drag relations to avoid discontinuity. The linear modification is discussed more thoroughly by Leboreiro et al. [7] and Dahl [8]. In the present implementation the linear transformation between the Ergun and Wen-Yu models occurs in a solid

volume fraction range of 0.4-0.5. This range was chosen because it gives a smooth transition and is within the region recommended by Leboreiro et al.

At the boundaries the Johnson-Jackson [9] partial slip boundary condition was used with specularity and restitution coefficients of 0.1 and 0.9 respectively. To obtain sufficiently smooth average values, a time period of 120 s was simulated. The time step was 0.5 ms with first order temporal discretization and for the momentum and volume fraction equations the QUICK scheme was employed.

The time-averaged terms were computed using user defined functions (UDF) and data was collected at every time step. Unfortunately, since the exact way how the gradients are calculated in Fluent has not been provided by ANSYS, those terms in equation (8) that contained derivatives could not be accurately averaged in the firsts few cells near the boundaries of the geometry. Because the mesh had only 3 cells in the depth direction (z-axis), this problem affected the z-components of the derivative terms globally. For this reason, in the following analysis the z-components of the derivative terms are omitted. This has some effect at least on the stress terms, which should be likely larger due to side wall friction. However, in industrial scale 3D BFBs the side walls are further away and the wall effects may not be as large there. Therefore, the error caused by the omitted z-component may not be that significant if the term analysis is applied to larger scale. The same geometry was also simulated with a 2D mesh and the leading terms were same in both cases.

Table 1: The sub models and parameters for the transient simulation.

Submodel or parameter	**Model used**
Granular viscosity	Syamlal, et al. [10]
Granular bulk viscosity	Lun et al. [11]
Frictional viscosity	Schaeffer [12]
Frictional Pressure	Johnson et al. [9]
Granular conductivity	Syamlal, et al. [10]
Solids pressure	Lun et al. [11]
Radial Distribution	Ogawa et al. [13] (Lun et al. in Fluent)
Angle of internal friction	30°
Frictional and packing limits	0.58 and 0.61
Turbulence model	Standard k-epsilon, dispersed

RESULTS

The average and instantaneous solid volume fraction fields from the transient simulation are presented in Figure 1. The simulated case was based on an experimental setup at Åbo Akademi University and it was possible to make qualitative comparison of the results. Overall the simulated flow field has a reasonable resemblance to the experiments, but there is a little bit more channelling in the simulated flow fields.

In Figures 2 and 3 the horizontal profiles of the terms appearing in the vertical (y-axis) and horizontal (x-axis) components of equation (8) are presented. As can be seen from Figure 2, the gas-solid drag term and gas pressure terms are clearly the largest terms in the vertical direction and together they compensate for most of the downward acceleration caused by gravitation. The drag term is relatively smooth through the whole width of the bed, except within the two channels appearing in the flow field. Drag forces are also significant in the horizontal direction, but there they are of the same order as the other major terms.

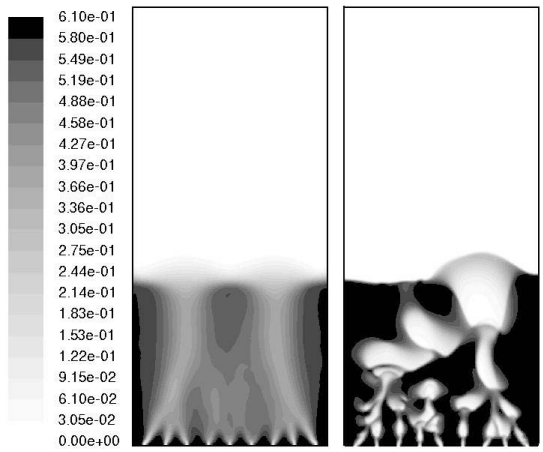

Figure 1: Average and instantaneous solid volume fraction fields.

Next largest term in the vertical direction is the term arising from the correlation between pressure gradient and solids volume fraction fluctuations. This finding supports the earlier, similar conclusions presented in the literature (see eg. De Wilde[14]). The shape of the fluctuation term is very similar to the drag term, but with a clearly smaller magnitude. In horizontal direction this term is small.

The solid pressure term is generally very important in dense flow conditions because it prevents unphysical packing of solid particles. When the particle volume fraction approaches the packing limit this term can grow very large. However, in a fully fluidized bed, as in the present case, the average contribution of this term is relatively small. In industrial scale BFBs there may be larger defluidized regions and within those areas this term can dominate. In the simulated bed there were quite dense regions at the very bottom between the individual air nozzles and there the solid pressure term was large. Also in the horizontal direction this term was significant near the side walls.

From CFBs it is known that, in addition to the drag force, the Reynolds stress terms are dominating both in the vertical and horizontal directions. [15,16] According to present analysis, the Reynolds stresses have a clearly noticeable contribution also here in the more dense flow. However, in this case its magnitude is more comparable to other terms and is for example clearly smaller than the pressure fluctuation term in the vertical direction. In the horizontal direction the Reynolds stress is also significant, but comparable to other terms.

The laminar stress is of the same order as the Reynolds stress, although it is likely that the laminar stress would be larger than what is shown here if the z-component would be included. Laminar stress is mostly concentrated on the dense side wall regions and near the channels. Again, as with the solid pressure term, near the packing limit the frictional contribution to the viscosity is significant and in those conditions the laminar stress can be a leading term. In CFBs laminar stress was found to be less significant. [15]

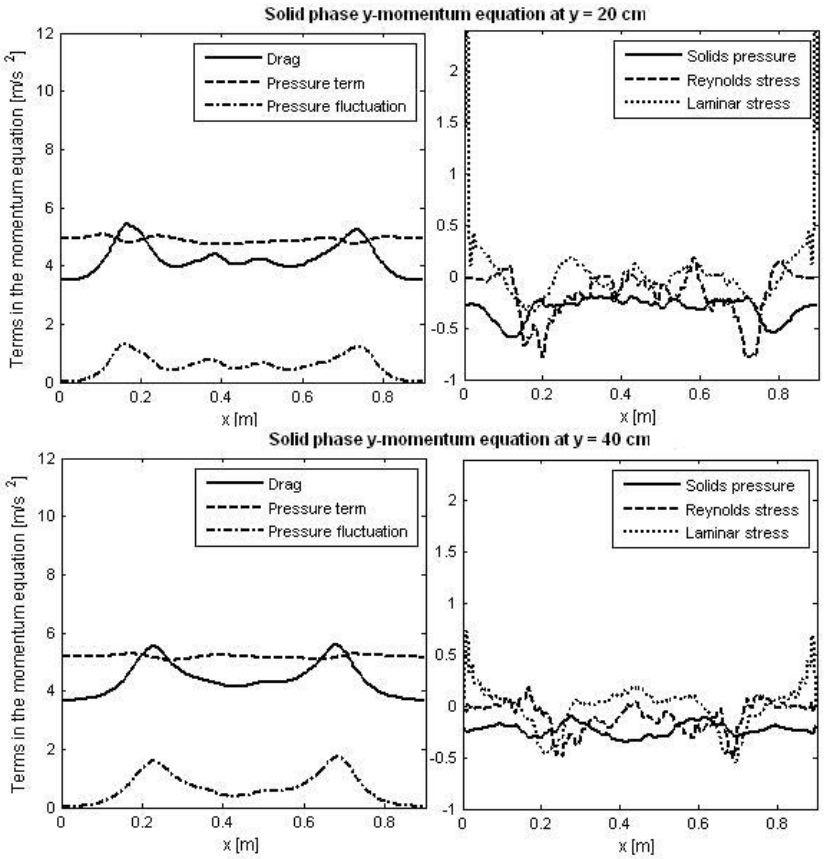

Figure 2: Horizontal profiles of the different terms appearing in the time-averaged vertical solid phase momentum equation for two different heights. The terms are divided with the average solid bulk density to express them as acceleration. Gravitation term (= const. -9.81 m/s^2) was left out from the figure.

Turbulent stress was overall insignificant compared to the other terms both in the vertical and horizontal directions. Convection terms were also quite small, but at the bottom of the bed and near the channels it had some impact.

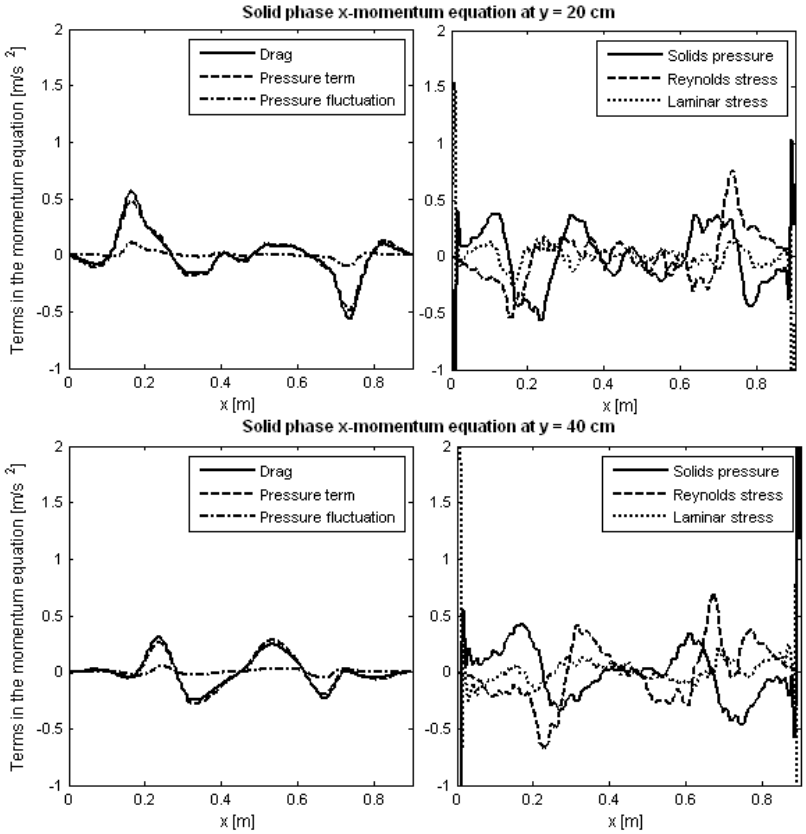

Figure 3: Horizontal profiles of the different terms appearing in the time-averaged horizontal solid phase momentum equation for two different heights.

CONCLUSIONS

Steady state CFD simulation would present an attractive alternative for the computationally demanding transient simulations in the case of large, industrial scale CFBs and BFBs. In the present paper, the features and relative importance of the various terms appearing in steady state flow equations were analyzed based on a transient simulation of a BFB. According to this analysis, the most important terms in the momentum equations are the gas-solid drag term and the solid volume fraction and gas pressure fluctuation correlation terms. The solid pressure and the Reynolds stress terms are also found to be important. Locally also the laminar stress terms that are of minor importance in CFB simulations can become significant in BFBs due to the larger frictional forces. In future more transient simulation data from different cases should be analyzed to gain further insight. Also it would be interesting to perform more thorough comparison of the averaged terms with those from CFB simulations and also with those from turbulent beds.

ACKNOWLEDGMENT

The authors gratefully acknowledge the financial support of Tekes, VTT Technical Research Centre of Finland, Etelä-Savon Energia Oy, Fortum, Metso Power Oy and Numerola Oy, and the support from Saarijärven Kaukolämpö Oy.

NOTATION

g	gravitational acceleration [m/s^2]	ρ	material density [kg/m^3]
K_{gs}	interphase drag coefficient [kg/m^{3}s]	τ	stress tensor [kg/m^3]
p	gas phase pressure [Pa]		
u	velocity [m/s]	Subscripts	
		s	solid phase
Greek letters		g	gas phase
α	volume fraction [-]	q	gas or solid phase
δ	Kronecker delta [-]		

REFERENCES

1. V. Taivassalo, S. Kallio, J. Peltola. *On Time-Averaged CFD Modeling of Circulating Fluidized Beds.* International Journal of Nonlinear Sciences and Numerical Simulation, volume 13, issue 6, 2012. Pages 363–373
2. Teklay Weldeabzgi Asegehegn, Matthias Schreiber, Hans Joachim Krautz, *Influence of two- and three-dimensional simulations on bubble behavior in gas–solid fluidized beds with and without immersed horizontal tubes*, Powder Technology, Volume 219, 2012.
3. Tingwen Li, John Grace, Xiaotao Bi, *Study of wall boundary condition in numerical simulations of bubbling fluidized beds*, Powder Technology, Volume 203, Issue 3, 2010.
4. Gidaspow, D. *Multiphase Flow and Fluidization - Continuum and Kinetic Theory Descriptions.* Academic Press, 1994. ISBN 0-12-282470-9.
5. Ergun, S. *Fluid flow through packed columns.* Chemical engineering progress, CEP, volume 48, 1952. Page 89.
6. Wen, C. and Yu, Y. *Mechanics of fluidization.* Chem. Eng. Prog. Symp. Ser., volume 62, 1966. Pages 100–111.
7. Leboreiro, J., Joseph, G. G., & Hrenya, C. M. *Revisiting the standard drag law for bubbling, gas-fluidized beds.* Powder Technology, volume 183(3), 2008. Pages 385–400.
8. Dahl S.R. and Hrenya C.M., *Size segregation in gas–solid fluidized beds with continuous size distributions,* Chem. Eng. Sci. 60, 2005. Pages 6658–6673.
9. Johnson, P. C. and Jackson, R. Frictional-collisional constitutive relations for granular materials, with application to plane shearing. Journal of Fluid Mechanics, volume 176, 1987. Pages 67-93.
10. Syamlal, M., Rogers, W., and O'Brien, T. J. *MFIX Documentation: Volume 1, Theory Guide.* National Technical Information Service, Springfield, VA, 1993.
11. Lun, C. K. K., Savage, S. B., Jeffrey, D. J., and Chepurniy, N. *Kinetic theories for granular flow: inelastic particles in couette flow and slightly inelastic particles in a general flowfield*. Journal of Fluid Mechanics, volume 140, 1984. Pages 223–256.
12. Schaeffer, D. G. *Instability in the evolution equations describing incompressible granular flow.* Journal of Differential Equations, volume 66(1), 1987. Pages 19-50.
13. Ogawa, S., Umemura, A., and Oshima, N. O*n the Equations of Fully Fluidized Granular Materials*. Journal of Applied Mathematics and Physics (ZAMP), volume 31, 1980. Pages 483-493.
14. De Wilde, J., *The generalized added mass revised*, Physics of Fluids, volume 19(5), 2007.
15. Kallio, S., Taivassalo, V., Hyppänen, T., *Towards time-averaged CFD modelling of circulating fluidized beds,* 9th Int. Conf. on Circulating Fluidized Beds, Hamburg, 2008.
16. L. Zhou and Z. Zeng, *Studies on gas turbulence and particle fluctuation in dense gas-particle flows,* Acta Mechanica Sinica, volume 24(3), 2008. Pages 251–260.

PAPER IV

On Time-Averaged CFD Modeling of Circulating Fluidized Beds

International Journal of Nonlinear Sciences and Numerical Simulation, 13 (2012) 363–373.

 DOI 10.1515/ijnsns-2012-0025 — Int. J. Nonlinear Sci. Numer. Simul. 2012; 13(6): 363–373

Veikko Taivassalo*, Sirpa Kallio and Juho Peltola

On Time-Averaged CFD Modeling of Circulating Fluidized Beds

Abstract: CFD simulations of single-phase flows are regularly performed as steady-state utilizing closure models of varying complexity. On the contrary, dense gas-solid flows are usually computed as time dependent. These simulations commonly require a small time step and a fine mesh resulting in costly and time-consuming computations. In case of large industrial circulating fluidized beds (CFB), the steady-state CFD modeling would be an attractive alternative for the transient simulations, if reliable closure models for the time-averaged transport equations were available. The multiphase closure models developed for time-dependent CFB computations are not as such applicable to the steady-state approach. For instance, the fraction of the momentum transfer expressed by the velocities is significantly smaller in the steady-state models than in the transient ones. Therefore, the steady-state simulations rely more on the closure relations and especially on the models for inter-phase momentum transfer and for the Reynolds stress terms.

Several attempts to develop closure models for coarse-mesh and steady-state simulations have been presented in the literature. In this paper, a novel steady-state simulation approach for a CFB process and a corresponding CFD model are introduced. A successful steady-state simulation for a test case is presented. Compared to the time-dependent simulations, the computing time is reduced by a factor of an order of 1000.

Keywords: CFB, CFD, time-averaged

PACS® (2010). 76T25

***Corresponding author: Veikko Taivassalo:** VTT Technical Research Centre of Finland, P.O. Box 1000, FI-02044 VTT. Finland
E-mail: Veikko.Taivassalo@vtt.fi
Sirpa Kallio: VTT Technical Research Centre of Finland, P.O. Box 1000, FI-02044 VTT. Finland, E-mail: Sirpa.Kallio@vtt.fi
Juho Peltola: VTT Technical Research Centre of Finland, P.O. Box 1000, FI-02044 VTT. Finland, E-mail: Juho.Peltola@vtt.fi

1 Introduction

Today dense gas-solid flows are usually modeled as time dependent. In order to obtain reasonably realistic results, the transient simulations of a gas-solid flow require a small time step and a fine mesh. The reason for this is the complicated flow structure typical of a dense gas-solid flow, which is characterized by large variations of a small length scale in the local solid concentration and large variations even in the gas and solid velocities. Typical flow structures in a circulating fluidized bed (CFB) are illustrated in Fig. 1. The images show particle strands everywhere in the bed. The widths of the narrowest particle strands shown in Fig. 1 are approximately 2 mm.

Since the CFD simulations of fluidized beds demand significant computational resources, especially in the case of large industrial CFB units, steady-state multiphase modeling is an attractive alternative. Unfortunately, the multiphase closure models developed for time-dependent modeling are not as such applicable to steady-state simulations. Furthermore, additional terms resulting from the time-averaging process have to be modeled. The closure models are crucial for the accuracy of the simulations since in steady-state simulations, a larger portion of momentum transfer is governed by closure models than in transient simulations.

Several attempts to develop closure models for coarse-mesh and steady-state simulations have been presented in the literature, e.g. [1–8]. The suggested closure models are based mainly on transient simulations in a fairly small scale. Moreover, none of the suggestions fully cover all the significant terms of the time-averaged multiphase equations. Thus, there is a need to develop a comprehensive time-averaged model for the simulation of dense gas-solid flows.

In the present work, closure models for the time-averaged momentum equations were developed for the CFB riser conditions. Data from a number of transient simulations of cases with varying dimensions, and particle and gas properties were utilized in deriving the closure models. The model has been successfully applied to reproduce the results of the time-dependent simulations for the

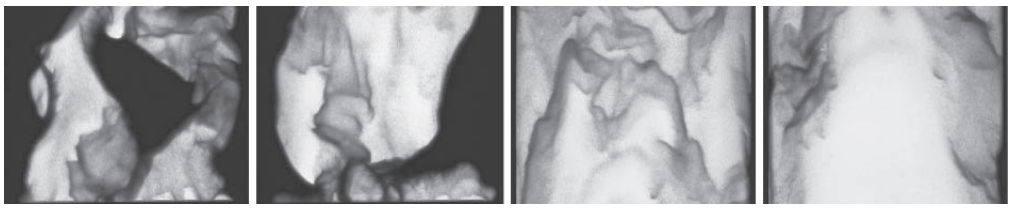

Fig. 1: Images from a 0.4 m wide 2D CFB, illuminated from behind. The two images on the left: at the riser bottom ($y = 0.02–0.33$ m), and the two on the right at $y = 1.14–1.45$ m. The superficial gas velocity is 3.75 m/s and the particle diameter 0.44 mm.

Average solid vof	U_0 (m/s)	d_s (mm)	ρ_s (kg/m³)	ρ_g (kg/m³)	μ_g (kg/ms)	Ar	$u_{s,\infty}$ (m/s)	Re
0.0678	3.75	0.44	2480	1.225	$1.789 \cdot 10^{-5}$	8000	3.3	99

Table 1: Physical parameters in the 2D test case (riser height 3 m and width 0.4 m).

cases studied. Moreover, the model has produced reasonable results for larger and industrial scale CFB units.

This paper concentrates on the verification and validation of the model in a 0.4 m wide and 3 m high 2D CFB case introduced in Table 1. The next section summarizes the time-dependent simulation of the case. The development of the steady-state model is described in Section 3. The results of the time-dependent and steady-state simulations are compared in Section 4. A similar case with 0.385 mm particles was earlier studied experimentally at Åbo Akademi University in a pseudo-2D CFB (distance between walls 0.015 m) [9], where the measurements of voidage and solid phase velocities were conducted as described in [10]. Data from new measurements carried out at the same 2D CFB unit at conditions listed in Table 1 are used in Section 4 for the comparisons with simulation results.

2 Time-dependent simulations

The time-dependent simulation was carried out with the Fluent 6.3.26 CFD software [11]. The computation was based on the Eulerian two-phase and the kinetic theory of granular flow models available in Fluent 6.3.26. The granular temperature was obtained from a partial differential equation using the Syamlal et al. [12] model for the granular conductivity. The solid phase granular viscosity was calculated from the model by Syamlal et al. [12]. The solids bulk viscosity and solids pressure were calculated from the formulas by Lun et al. [13]. The k-ε turbulence model producing the local scale turbulent stress was the version modified for multiphase flows ("dispersed turbulence model", [11]). For gas-particle interaction, a combination of the Wen & Yu [14] (for the voidage above 0.8) and Ergun [15] equations was used. The frictional solids stresses were calculated from the model of Schaeffer [16].

The computational mesh comprises almost 32 000 quadrilateral cells. In the riser section, the mesh is regular with 6.3 mm × 6.3 mm cells.

The air inflow velocity at the bottom was described by a function that reproduces the locations of the eight air inlet orifices in the experimental device. At the walls, the partial slip model of Johnson and Jackson [17] was used for the solid phase with the specularity coefficient equal to 0.001. The free slip boundary condition was used for the gas phase.

The first-order temporal discretization and second-order spatial discretization schemes were employed. The simulation time step was 0.2 ms. After a start-up period of about 10 s in process time, the time-averaged values were computed for a period of about 120 s in process time. Some simulation results are shown in Figs. 5–8. The time-averaged solid-phase velocities and solid-phase volume fractions are compared with the experimental data in Figs. 9–10.

3 Derivation of the time-averaged model

3.1 The transient model

The transient transport equations for gas-solid multiphase flows are used as a basis in the derivation of the corresponding time-averaged equations. The continuity and momentum equations used in transient multiphase simu-

lations can be summarized for a phase of constant density as follows:

$$\frac{\partial \alpha_q}{\partial t} + \frac{\partial \alpha_q u_{q,k}}{\partial x_k} = 0 \tag{1}$$

$$\begin{aligned}\frac{\partial \alpha_q \rho_q u_{q,i}}{\partial t} &+ \frac{\partial \alpha_q \rho_q u_{q,k} u_{q,i}}{\partial x_k} \\ &= -\alpha_q \frac{\partial p}{\partial x_i} + \frac{\partial \alpha_q \tau_{q,ik}}{\partial x_k} + \frac{\partial \alpha_q \tau^M{}_{q,ik}}{\partial x_k} - \frac{\partial p_q}{\partial x_i}\delta_{qs} \\ &+ \alpha_q \rho_q g_i + (-1)^{(\delta_{qs}+1)} K_{gs}(u_{g,i} - u_{s,i})\end{aligned} \tag{2}$$

where α_q is the volume fraction, ρ_q density, $u_{q,i}$ velocity, p pressure, p_s solid pressure, K_{gs} inter-phase momentum transfer coefficient, $\tau_{q,ik}$ the laminar stress, and $\tau^M{}_{q,ik}$ the local scale turbulent stress.

3.2 Time-averaged equations

Time-averaged equations are developed by averaging the corresponding time-dependent equations over time. As an initial step, the instantaneous continuity and momentum equations, Equations (1) and (2), are averaged over time. The time average, also called the Reynolds average, of a variable ϕ is denoted as $\overline{\phi}$. The instantaneous values are thus written as $\phi = \overline{\phi} + \phi'$. This averaging procedure is used for the volume fraction α_q and pressure p.

Assuming constant material densities, the Favre average or phase-weighted average is defined as $\langle \phi \rangle = \alpha_q \phi / \alpha_q$. The Favre averaging is applied to velocities and we denote the average velocity by $U_{q,i} \equiv \langle u_{q,i} \rangle$. For the instantaneous velocity we then have $u_{q,i} = U_{q,i} + u_{q,i}''$.

We obtain now time-averaged continuity and momentum equations for a phase q:

$$\frac{\partial \overline{\alpha}_q}{\partial t} + \frac{\partial \overline{\alpha}_q U_{q,k}}{\partial x_k} = 0 \tag{3}$$

$$\begin{aligned}\frac{\partial \overline{\alpha}_q \rho_q U_{q,i}}{\partial t} &+ \frac{\partial \overline{\alpha}_q \rho_q U_{q,k} U_{q,i}}{\partial x_k} \\ &= \overline{\alpha}_q \rho_q g_i - \overline{\alpha}_q \frac{\partial \overline{p}}{\partial x_i} - \overline{\alpha_q' \frac{\partial p'}{\partial x_i}} + \frac{\partial \overline{\alpha_q \tau_{q,ik}}}{\partial x_k} + \frac{\partial \overline{\alpha_q \tau^M{}_{q,ik}}}{\partial x_k} \\ &+ (-1)^{(\delta_{qs}+1)} \overline{K_{gs}(u_{g,i} - u_{s,i})} - \frac{\partial \overline{p}_q}{\partial x_i}\delta_{qs} - \frac{\partial \rho_q \overline{\alpha_q u_{q,k}'' u_{q,i}''}}{\partial x_k}.\end{aligned} \tag{4}$$

Equation (4) shows that the time-averaging of the transient equations gives rise to a number of new terms to be modeled in the averaged equations because of the correlations between fluctuations in the velocities, voidage, pressure, and local stresses. The terms on the right hand side in Equation (4) are, from the left, the gravitation, pressure, pressure fluctuation, laminar stress, turbulent stress, drag force, solid pressure, and the Reynolds stress terms, respectively. The gravitation and pressure terms can be calculated from the basic average flow properties but for the rest of the terms closure relations have to be developed.

To analyze the requirements for the equation closure, the results from long transient simulations were time-averaged to calculate the terms in Equation (4). In Kallio et al. [18], the three largest terms in the time-averaged momentum equation to be modeled were identified and analyzed from a simulation of a CFB pilot unit. Later on, the findings were confirmed by simulations of the small 2D CFB unit at Åbo Akademi. The largest terms are the drag force, pressure fluctuation and Reynolds stress terms.

In addition to these three terms, a number of other terms in Equation (4) require modeling. These terms are the averages of the laminar and turbulent stress terms and the average solid pressure. The analysis of transient simulations, however, showed that these terms are relatively small in the major part of a CFB riser. In the dense bottom and wall zones, the averages of the local solid stresses and especially of the solid pressure can be significant in the vertical solid phase momentum equation and even elsewhere in the horizontal equation. Thus, closure models are also required for these terms.

3.3 Closure of the time-averaged momentum equation

Closure relations can be derived by analyzing measurements and/or results from transient simulations. In this work, to assist in the equation closure, a large number of transient simulations were conducted with the Fluent [11] software applying the same kinetic theory based hydrodynamic models as in [18] and summarized in Section 2. To validate the models, the simulation results were compared with experimental results [9]. No unexpected significant discrepancies between the results for measurements and simulations were observed as long as the computational mesh in the simulations was fine, i.e., when the mesh resolution was of the order of 5 mm or smaller.

The results from transient simulations were time averaged to obtain the averaged velocities, voidage, pressure and other flow properties as well as the correlation terms resulting from the averaging of the fluctuations. These results were then used in the development of closure

models for the pressure fluctuation, drag force, solid pressure, and Reynolds stress terms in the momentum equation.

The closure models in the following are based on the transient simulation results for the case defined in Table 1. The time-dependent simulation is summarized in Section 2.

3.3.1 The drag term

Typically the largest term in the solid phase momentum equation to be modeled is the gas-solid drag force. In the closure relations developed, the average drag force term is modeled as follows (the notation $\{\phi\}$ refers to a time-average closure model of ϕ)

$$\{\overline{K_{gs}(u_{g,i}-u_{s,i})}\} = K_{gs}^{\star}(U_{g,i}-U_{s,i}) \tag{5}$$

Appropriate correlations were developed for the representative time-averaged inter-phase momentum transfer coefficient $K_{gs}^{\star}$ from the transient simulation data using the time-averaged velocity and volume fraction as parameters. Comparison in Fig. 2 shows that the vertical drag force is well predicted by the developed closure relation in the main part of the flow domain, and elsewhere the fit is sufficient. The fit for the horizontal drag force is also satisfactory.

3.3.2 The pressure fluctuation term

The pressure fluctuation term (the third term on the right hand side in Equation (4)) calculated from the results of the transient simulation showed a typical trend as a function of the solid volume fraction that somewhat resembled the one of the drag term. Instead of plotting the pressure fluctuation term as a function of the solid volume fraction, we analyzed the ratio of it and the corresponding drag component. In all the cases considered, this ratio seems to be a fairly linear function of the volume fraction in a major part of the flow domain. Furthermore, an even better linear correlation was found between the pressure fluctuation term and the variance of the solid volume fraction σ_α (Fig. 3). Thus, this term could easily be added to the drag force and modeled by means of a linear relationship with the equation

$$\left\{\overline{\alpha_q' \frac{\partial p'}{\partial x_i}}\right\} = K_{S_p}\sigma_\alpha \overline{K_{gs}(u_{g,i}-u_{s,i})} \tag{6}$$

A linear function was fitted to the results of the time-dependent simulations for the present simulation case. The coefficient K_{S_p} determined is about 2.5.

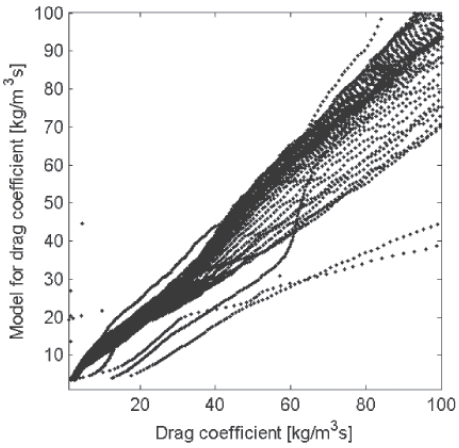

Fig. 2: For the representative time-averaged inter-phase momentum transfer coefficient $K_{gs}^{\star}$ (Equation (5)), the modeled values as a function of the time-averaged values of the time-dependent simulation for cells above the bottom region.

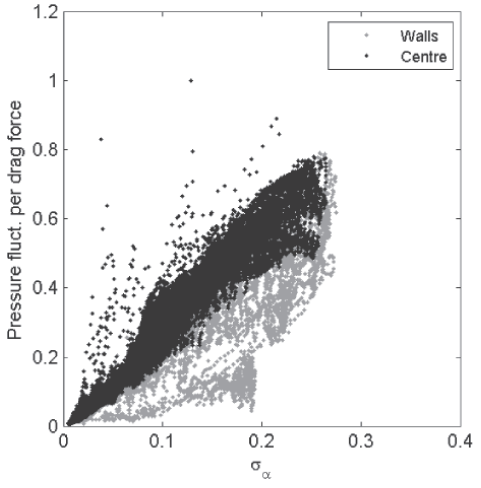

Fig. 3: The ratio of the vertical component of the pressure fluctuation term and the corresponding drag component as a function of the variance of the solid volume fraction σ_α in the computational cells close to walls ("Walls") and elsewhere ("Centre").

3.3.3 Solid pressure

One potentially important term in the momentum equations is the solid pressure. It is most significant in the dense wall layers close to the riser bottom. In the horizontal momentum balance equation, this term is also important at walls along the entire riser height. In the time-dependent simulations, the time-averaged solid pressure was determined for each cell. In Fig. 4, this value is plotted as a function of the time-averaged solid volume fraction for the current case. The solid pressure was modeled using a power law fit

$$\{p_s\} = A\bar{\alpha}_s^B + C\bar{\alpha}_s^D \qquad (7)$$

3.3.4 Reynolds stress terms

In addition to the drag force and the pressure fluctuation term, the Reynolds stresses are significant in most part of the flow domain. Fig. 5 illustrates the complicated character of the solid phase Reynolds stresses in the case considered.

Transport equations for the Reynolds stresses can be derived by starting from the instantaneous momentum equations (2) and the time-averaged momentum equations (4). The resulting balance equations can be expressed as follows (e.g., [19])

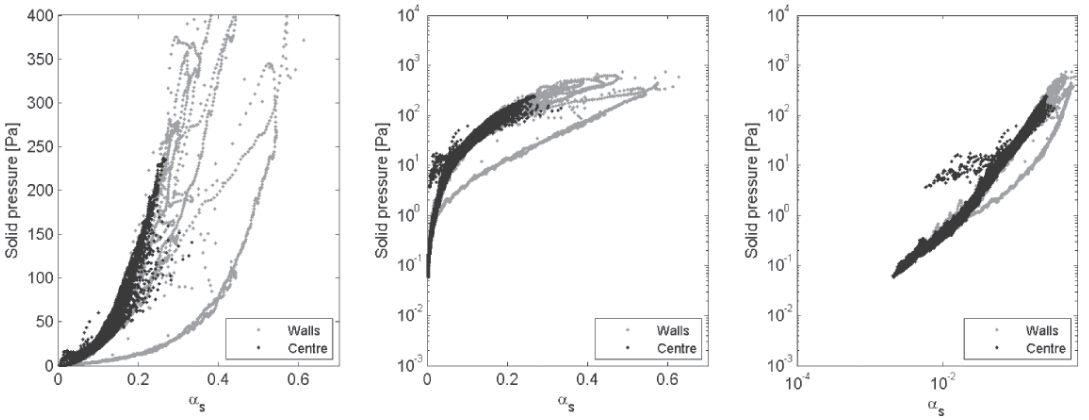

Fig. 4: Time-averaged solid pressure in the time-dependent simulation as a function of the time-averaged solid volume fraction in the computational cells close to walls ("Walls") and elsewhere ("Centre").

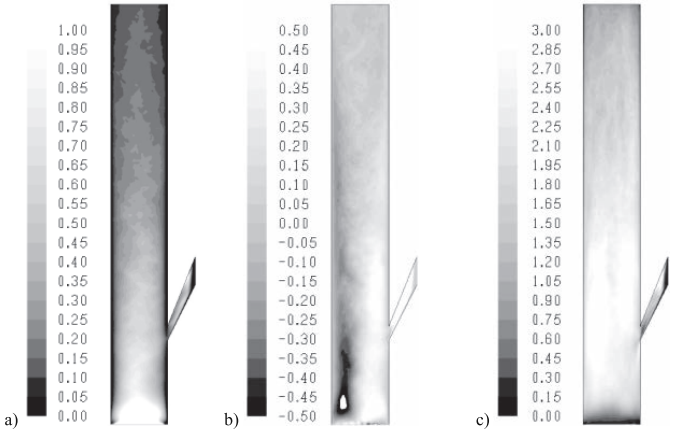

Fig. 5: Mass-weighted time-averaged Reynolds stress components for the solid phase in the time-dependent simulation. a) $\langle u''_{s,x}u''_{s,x}\rangle$, b) $\langle u''_{s,x}u''_{s,y}\rangle$ and c) $\langle u''_{s,y}u''_{s,y}\rangle$. (Unit: m²/s².)

$$\frac{\partial \rho_q \overline{\alpha_q u''_{qi} u''_{qj}}}{\partial t} + \frac{\partial \rho_q U_{qk} \overline{\alpha_q u''_{qi} u''_{qj}}}{\partial x_k} = P_{q,ij} + \Pi_{q,ij} + D_{q,ij} + M_{q,ij} - \varepsilon_{q,ij} + G_{g,ij} + F_{q,ij} + \delta_{qs} S_{q,ij} \quad (8)$$

where $P_{q,ij}$ is the production term, $\Pi_{q,ij}$ is the pressure-strain covariance (or redistribution) term, $D_{q,ij}$ represents the turbulent, pressure and molecular diffusion, $M_{q,ij}$ arises from the local-scale turbulence, $\varepsilon_{q,ij}$ is the dissipation term, $G_{q,ij}$ is the phase interaction, $F_{q,ij}$ is the turbulent mass flux term, and $S_{s,ij}$ is the two-phase term. Only the production term $P_{q,ij}$ can be calculated in a time-averaged simulation directly from the time-averaged flow properties. All the other terms require closure models.

Zhou and Zeng [20] wrote transport equations with closure models for the Reynolds stresses in multiphase flows. Their closure models for the diffusion, pressure strain and dissipation terms are two-phase extensions of the corresponding single-phase closure models. An additional term was included by Zhou and Zeng for the influence of particles on the gas-phase turbulence intensity. The term is called the turbulence enhancement model for the particle wake effect. For dense gas-particle flows, the simulation results of Zhou and Zeng [20] indicate that the particle wake effect both enhances the gas turbulence and amplifies the particle fluctuations.

In the present work, a simpler model for the Reynolds stresses was applied. As the Reynolds stress terms in the gas phase momentum equations are relatively unimportant, only the solid phase stress terms are computed from balance equations. In addition, transport equations are solved only for the normal components.

The balance equations (8) for solid-phase normal components are also simplified on the basis of an analysis of the time-averaged values of the terms on the right hand side in Equation (8). The terms $M_{q,ij}$, $F_{q,ij}$, and $S_{s,ij}$ are ignored as relatively unimportant. The phase interaction term $G_{s,ii}$ is assumed to be a function of the slip velocity and volume fraction fluctuations. The diffusion term $D_{s,ii}$ is modeled with the expression

$$\{D_{s,ii}\} = \frac{\partial}{\partial x_l}\left(c_{Ds,ii} \overline{\alpha}_s \rho_s \tau_{s,i} \langle u''_{sl} u''_{sl} \rangle \frac{\partial \langle u''_{si} u''_{si} \rangle}{\partial x_l} \right) \quad (9)$$

where $\tau_{s,i}$ is the time scale of the solid velocity fluctuations and $c_{Ds,ii}$ is a model parameter. The dissipation term is represented as follows

$$\{\varepsilon_{s,ii}\} = c_{\varepsilon s,ii} \overline{\alpha}_s \rho_s \frac{\langle u''_{si} u''_{si} \rangle^{2/3}}{L_{s,i}} \quad (10)$$

where $L_{s,i}$ is the length scale of the solid velocity fluctuations and $c_{\varepsilon s,ii}$ is a model parameter.

For the gas phase, the Reynolds stresses are evaluated from the corresponding solid phase Reynolds stresses applying correlations based on the data from the time-dependent simulations.

4 Simulations with time-averaged equations – Verification and validation

The time-averaged closure models described above in Section 3.3 were implemented in Fluent 6.3 [11] as user-defined functions. The same mesh that was applied in the transient simulation (Section 2) was also utilized in the steady-state simulations. The same boundary conditions were used on the vertical walls, but the gas inflow was distributed evenly on the bottom.

The main results of the steady-state simulation are presented in Figs. 6–8. In general, the steady-state model is able to reproduce the important features of the CFB flow characteristics including the core-annular flow pattern with internal solid circulation.

Figs. 6–10 compare the results of the steady-state simulations to those of the time-dependent simulations. For most of the quantities and for most of the domain, the agreement is satisfactory. The differences are largest close to the solid particle return and in the bottom section. The largest relative differences are in the horizontal velocities and especially close to the bottom. In this region, the horizontal Reynolds stress term is important (c.f. Fig. 5) and an imperfect modeling of the term results in a discrepancy in the horizontal velocity. On the vertical velocities, the largest downward velocities in the transient simulation results are at some distance from the vertical surfaces (especially at the levels y = 0.8 m and y = 1.2 m in Fig. 9) whereas in the steady-state simulation this phenomena is not observed. This discrepancy is mainly caused by the usage of the same boundary condition of the partial slip model of Johnson and Jackson [17] with the same value of the specularity coefficient. The time-averaged influence of this boundary condition is different for a constant (time-averaged) volume fraction than in the case of a strongly varying volume fraction (transient simulation).

The simulation results are compared with the experimental data in Figs. 9 and 10. Regarding the experimental results, the effect of the front and back walls may have affected the flow at the riser bottom meaning that the flow was not truly two dimensional. Regarding the transient simulations, a most significant discrepancy between the simulation and experimental data is with the horizon-

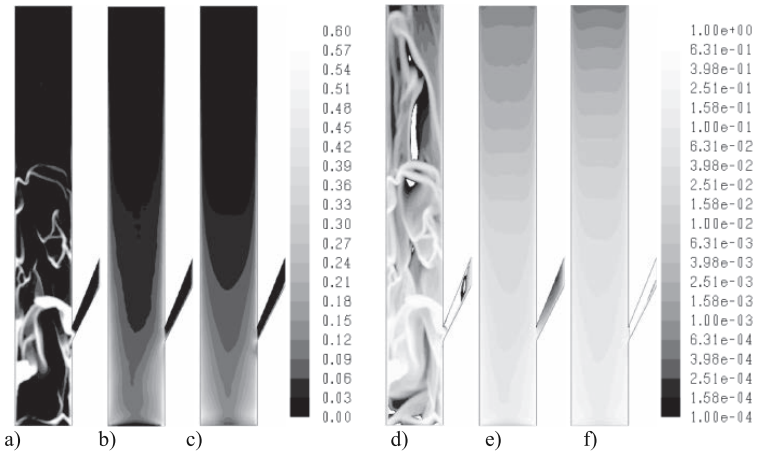

Fig. 6: Computed solid volume fraction. a) and d) instantaneous, b) and e) time-averaged result of the transient simulation, and c) and f) result of the steady-state simulation. In a), b) and c) the contours are on the linear scale given in the middle whereas in d), e) and f) the contours are on the logarithmic scale given on the right.

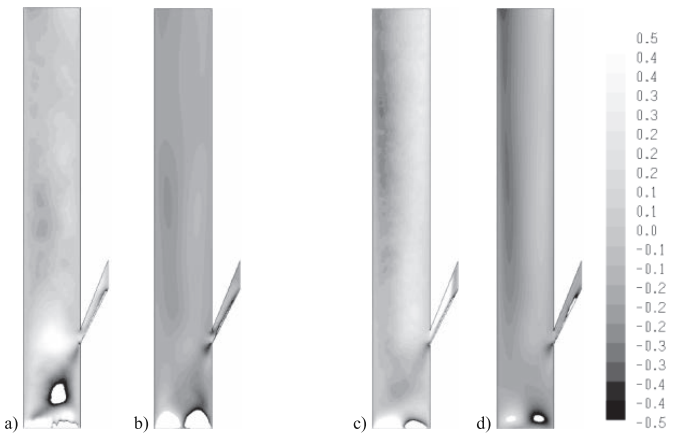

Fig. 7: Computed time-averaged mass-weighted horizontal velocities. a) time-averaged values of the transient simulation for the gas phase, b) steady-state simulation result for the gas phase, and c) time-averaged values of the transient simulation for the solid phase, d) steady-state simulation result for the solid phase.

tal solid phase velocity at 0.4 m height. This discrepancy is likely caused mainly by the fundamental assumption of the two-fluid approach and differences in the solid return.

The agreement of the steady-state simulation results with the experimental data is in general as good as the agreement of the time-dependent simulation data. In fact, a direct comparison of the steady-state simulation and experimental results is not very relevant. Since the time-averaged balance equations and closure models are based on the equations and results of the time-dependent simulation, the time-averaged model should be justified only on the basis of a comparison with the time-dependent simulation. However, by comparing the discrepancies of the results of the steady-state model from those of the time-dependent model, and on the other hand, from experimental data, we are able to evaluate the significance of the approximations of the steady-state model in practical applications as well as the need and relevance of improvements. If a good agreement with the experimental data had been our target, the steady-state model could easily be tuned on a basis of the experimental data.

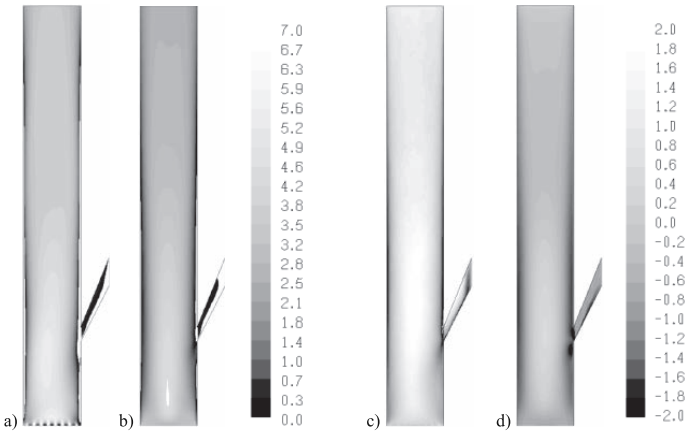

Fig. 8: Computed time-averaged mass-weighted vertical velocities. a) time-averaged values of the transient simulation for the gas phase, b) steady-state simulation result for the gas phase, and c) time-averaged values of the transient simulation for the solid phase, d) steady-state simulation result for the solid phase.

5 Conclusions

A novel closure method for a steady-state simulation of a CFB unit was successfully developed. The time-averaged momentum equations were closed utilizing data from time-dependent simulations and/or experiments. In the closure models, the fluctuations in the solid volume fraction have an important role.

A steady-state simulation of the CFB hydrodynamics was found feasible. The test simulations show that the steady-state model can largely reproduce the time-averaged hydrodynamics of a corresponding time-dependent simulation. The steady-state model also produces many characteristic features of CFBs. Computationally the steady-state model is stable and significantly faster than the time-dependent simulation (by a factor of an order of 1000).

Compared to the time-dependent simulations, the steady-state simulation model is an attractive alternative especially when the reliability of the time-dependent model is questionable, e.g., if the cell size is too large to describe particle strands properly. In the steady-state modeling, individual strands are not described and thus the approach is less sensitive to mesh spacing. The developed simulation model can easily be extended on a basis of experimental and/or transient simulation results to new conditions and scales. After extending the model to varying CFB conditions and all the processes involved in industrial CFBs, CFD simulation could become one stage in the development of new CFB processes. An efficient computational tool would be especially advantageous in designing and applying new CFB-based processes when the process conditions or the process itself are new as in the cases of enriched oxygen combustion, chemical looping combustion and the gasification process for fuel production.

Nomenclature

Ar	Archimedes number
d_s	diameter of the solid phase particles
g_i	gravitational acceleration
K_{gs}	inter-phase momentum transfer coefficient
$K^{\star}_{gs}$	representative time-averaged inter-phase momentum transfer coefficient
p	pressure
p_s	solid pressure
Re	Reynolds number
t	time
u	velocity
$u_{s,\infty}$	terminal velocity of the solid particles
$U_{q,i}$	Favre-averaged velocity, $U_{q,i} \equiv \langle u_{q,i} \rangle$
U_0	superficial gas velocity
x	spatial coordinate
y	vertical spatial coordinate

Greek symbols

α	volume fraction
δ_{qs}	Kronecker delta
μ	viscosity
ρ	density

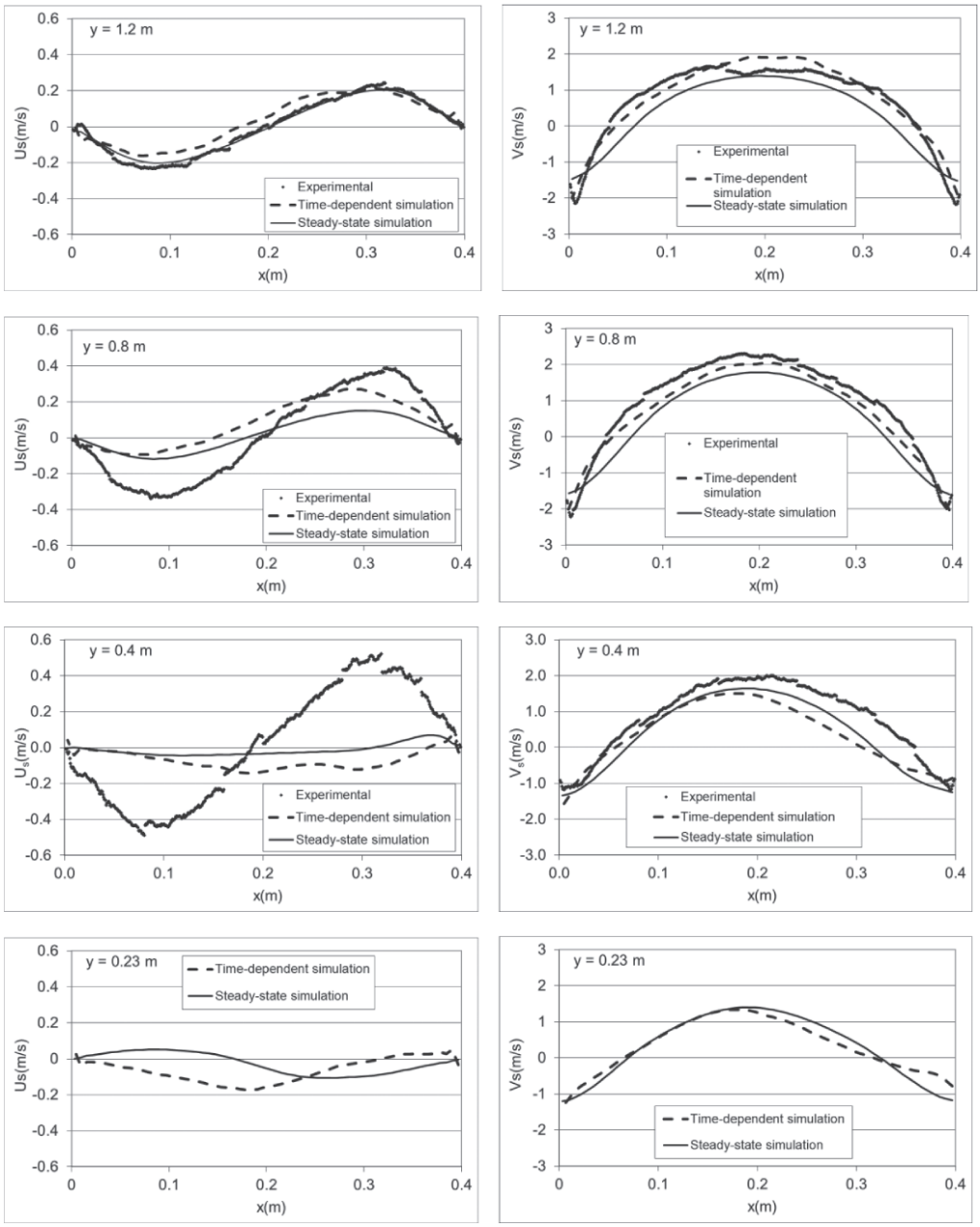

Fig. 9: Experimental and computed time-averaged phase-weighted horizontal (U_s, on the left) and vertical velocities (V_s, on the right) for the solid phase at four height levels ($y = 0.23$ m, $y = 0.4$ m, $y = 0.81$ m and $y = 1.2$ m; riser bottom at $y = 0$).

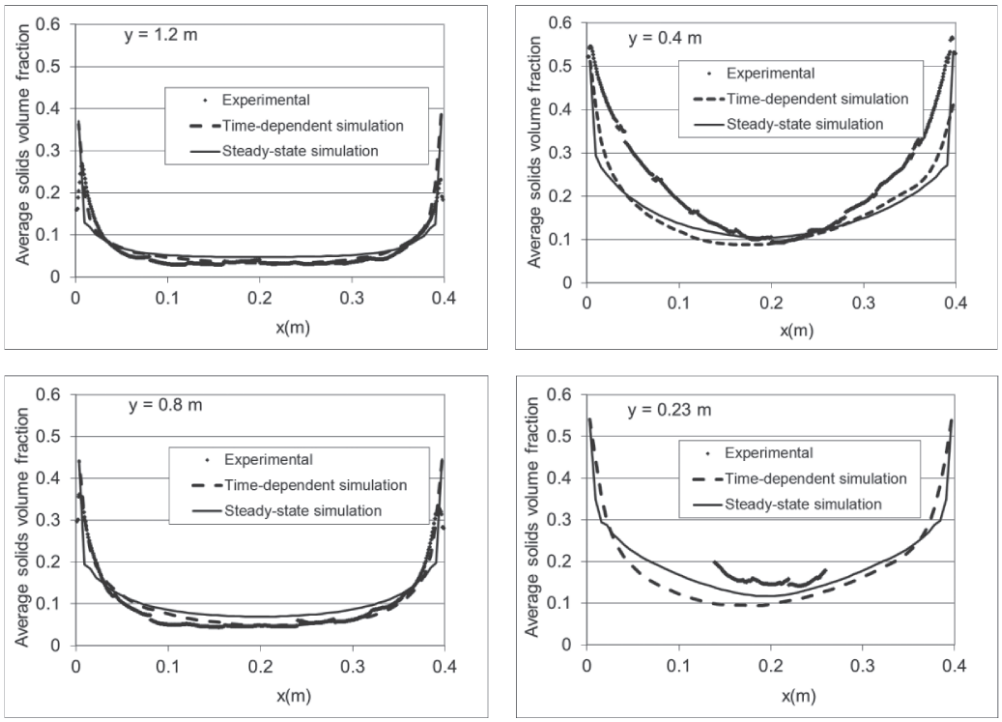

Fig. 10: Experimental and computed time-averaged solid volume fractions at four height levels ($y = 0.23$ m, $y = 0.4$ m, $y = 0.81$ m and $y = 1.2$ m; riser bottom at $y = 0$).

σ_α variance of the solid volume fraction
$\tau_{q,ik}$ laminar stress
$\tau^M{}_{q,ik}$ local-scale turbulent stress
$\tau_{s,i}$ time scale of the solid velocity fluctuations

Subscripts

g gas phase
i coordinate index
j coordinate index
k summation index over the spatial directions
q phase index
s solid phase

Additional notations

$\overline{\phi}$ time average (Reynolds average)
$\langle\phi\rangle$ Favre average or phase-weighted average
$\{\phi\}$ time-average closure model of ϕ
ϕ' fluctuation relative to the time average; $\phi' = \phi - \overline{\phi}$
ϕ'' fluctuation relative to the Favre average; $\phi'' = \phi - \langle\phi\rangle$

Acknowledgements

The authors gratefully acknowledge the financial support of Tekes, VTT Technical Research Centre of Finland, Fortum Oyj, Foster Wheeler Energia Oy, Neste Oil Oyj and Metso Power Oy.

Received: January 23, 2012. Accepted: July 3, 2012.

References

[1] Agrawal, K., Loezos, P.N., Syamlal, M., Sundaresan, S., The role of meso-scale structures in rapid gas-solid flows, J. Fluid Mech. **445**, 151–185.

[2] Andrews, A.T., Loezos, P.N., Sundaresan, S., (2005). Coarse-grid simulation of gas-particle flows in vertical risers, Ind. Eng. Chem. Res. **44**, 6022–6037.

[3] Igci, Y., Sundaresan, S., Pannala, S., O'brien, T., Breault, R.W., (2006). Coarse-graining of two-fluid models for fluidized gas-particle suspensions, 5th Int. Conf. on CFD in the Process Industries, CSIRO, Melbourne, Australia.

[4] Zhang, D.Z., VanderHeyden, W.B., (2001). High-resolution three-dimensional numerical simulation of a circulating fluidized bed, Powder Tech. **116**, 133–141.
[5] Zhang, D.Z., VanderHeyden, W.B., (2002). The effects of mesoscale structures on the macroscopic momentum equations for two-phase flows, Int. J. of Multiphase Flow **28**, 805–822.
[6] De Wilde, J., (2007). The generalized added mass revised, Physics of Fluids **19**, 058103.
[7] De Wilde, J., Heynderickx, G.J., Martin, G.B., (2007). Filtered gas-solid momentum transfer models and their application to 3D steady-state riser simulations, Chem. Eng. Sci. **62**, 5451–5457.
[8] Zheng, Zh.X., Zhou, L.X., (2006). A two-scale second-order moment particle turbulence model and simulation of dense gas–particle flows in a riser, Powder Tech. **162**, 27–32.
[9] Kallio, S., Guldén, M., Hermanson, A., (2009). Experimental study and CFD simulation of a 2D circulating fluidized bed, The 20th Int. Conf. on Fluidized bed combustion. Xi'an, China.
[10] Peltola, J., Kallio, S., Honkanen, M., Saarenrinne, P., (2010). Image based measurement of particle phase Reynolds stresses in a laboratory scale circulating fluidized bed. International Conference on Multiphase Flow (ICMF), University of Florida. Tampa, FL, USA.
[11] Fluent Inc., (2006). Fluent 6.3 User's manual.
[12] Syamlal, M., Rogers, W., and O'Brien, T. J., (1993). MFIX Documentation: Volume 1, Theory Guide. National Technical Information Service, Springfield, VA, DOE/METC-9411004, NTIS/DE9400087. Referenced by Fluent (2006).
[13] Lun, C.K.K., Savage, S.B., Jeffrey, D.J., Chepurniy, N., (1984). Kinetic Theories for Granular Flow: Inelastic Particles in Couette Flow and Slightly Inelastic Particles in a General Flow Field. J. Fluid Mech. **140**, 223–256. Referenced by Fluent (2006).
[14] Wen, C.Y., Yu, Y.H., (1966). Mechanics of fluidization, Chemical Engineering Progress Symposium Series **66**, No. 62, 100–111.
[15] Ergun, S., (1952). Fluid flow through packed columns, Chemical Engineering Progress, **48**, 89–94.
[16] Schaeffer, D.G., (1987). Instability in the evolution equations describing incompressible granular flow, J. Diff. Eq., **66**, 19–50. Referenced by Fluent (2006).
[17] Johnson, P.C., Jackson, R., (1987). Frictional-collisional constitutive relations for granular materials, with application to plane sharing, J. Fluid Mech. **176**, 67–93.
[18] Kallio, S., Taivassalo, V., Hyppänen, T., (2008). Towards time-averaged CFD modelling of circulating fluidized beds, 9th Int Conf. on Circulating Fluidized Beds, Hamburg.
[19] Yoder, D.A., (2005). Algebraic Reynolds Stress Modeling of Planar Mixing Layer Flows. Ph.D. dissertation, University of Cincinnati.
[20] Zhou, L. and Zeng, Z., (2008). Studies on gas turbulence and particle fluctuation in dense gas-particle flows. Acta Mech Sin 24:251–260.

PAPER V

Parametric study of the time-averaged gas–solid drag force in circulating fluidized bed conditions

Powder Technology 257 (2014a) 20–29.

Powder Technology 257 (2014) 20–29

Contents lists available at ScienceDirect

Powder Technology

journal homepage: www.elsevier.com/locate/powtec

Parametric study of the time-averaged gas–solid drag force in circulating fluidized bed conditions

Sirpa Kallio *, Juho Peltola, Timo Niemi

VTT Technical Research Centre of Finland, P.O. Box 1000, FI-02044 VTT, Finland

ARTICLE INFO

Article history:
Received 7 October 2013
Received in revised form 19 December 2013
Accepted 7 February 2014
Available online 14 February 2014

Keywords:
Drag force
Circulating fluidized bed
Time-averaging
Computational fluid dynamics

ABSTRACT

Steady state modeling based on time-averaged transport equations is a computationally efficient method for CFD simulation of large industrial-scale circulating fluidized beds. The feasible alternative for steady state modeling is to carry out transient simulations in a coarse mesh, which would require mesh resolution dependent closure laws and lead to long simulations in order to characterize the average process behavior. These closures could be avoided by simulations with adequate spatial and temporal resolutions, but the required computational effort renders such simulations unfeasible in industrial scale applications in near future. Equation closures for steady state modeling can be developed by time-averaging results from transient simulations. One of the largest terms to be modeled is the time-averaged drag force. In the present work, parameters that need to be accounted for in a model for the time-averaged drag force were studied by analyzing time-averaged results from a number of transient 2D simulations carried out with fairly fine spatial resolution. The analysis was limited to Geldart B particles. In the literature, the solid volume fraction, distance to the wall and the gas–solid slip velocity have been included as parameters in drag correction functions developed for transient coarse-mesh simulations. In the present work, the same parameters are found to have significant effects on the time-averaged gas–solid drag force. Additionally, solid density, particle size and gas phase laminar viscosity are shown to have significant effects on the average drag force. Thus process conditions, which significantly vary inside a CFB, need to be accounted for in the model.

1. Introduction

The flow patterns in a circulating fluidized bed (CFB) are characterized by large spatial and temporal fluctuations in solid concentration as well as in gas and solid velocities. Length scales of these variations can be very small, down to a few particle diameters, which constitutes a difficult challenge for computational fluid dynamic (CFD) simulation of industrial scale CFBs utilized in energy production and conversion processes. Similar computational mesh related spatial resolution challenges are encountered both with Eulerian–Eulerian two-fluid models and with the multi-phase particle-in-cell methods [1]. Resolving the smallest flow structures would require a very fine mesh that would be computationally unfeasible for simulation of typical industrial scale processes. As a result, coarser meshes that filter out the fine sub-grid scale flow structures are commonly used. To account for the filtered information, corrections or sub-grid scale models for the terms in the transport equations should be applied. Such closure models have been proposed in the literature for different terms in the gas and solid phase momentum equations on the basis of theoretical considerations and analysis of results from transient simulations of fairly small geometries with high spatial resolution. As the filtering scale depends on the resolution of the simulation, these closure models should have the resolution as a parameter which complicates derivation of the closure laws. No general closures that would cover all typical conditions in circulating fluidized beds and all terms in the equations have yet been proposed.

To avoid mesh dependence in the closures and to speed up the simulations, steady state modeling has been suggested as an alternative for the transient simulations [2,3]. Transient coarse mesh simulations filter out spatial fluctuations smaller than the mesh spacing and temporal fluctuations shorter than the time step. Steady-state simulation models are derived by time-averaging the transient equations, which filters out all temporal variations in the flow properties. Closures need to be developed to account for the effects of the filtered variations. These closures are of a similar character as the sub-grid closures required for transient coarse mesh simulations. In both cases, the closures describe clustering of particles and fluctuations in flow properties. A closure for a very coarse mesh should approach the closure for a time-averaged equation, since a volume average over a distance longer than the longest length-scales of the fluctuations should produce the same result as a time

* Corresponding author. Tel.: +358 20 7224015.
E-mail address: sirpa.kallio@vtt.fi (S. Kallio).

http://dx.doi.org/10.1016/j.powtec.2014.02.022
0032-5910/

average in a single point, when the statistical characteristics over the averaging space and time frame are the same. That would be the case if there would be no spatial gradients in the time-averaged flow field. Although this condition is never exactly met, the gradients in the time-averaged volume fraction and velocities are often small compared to the fluctuations, for example in the center of a large CFB riser.

To evaluate the need for equation closures, a study of the terms in the time-averaged momentum equations in CFB conditions was carried out by Kallio et al. [4]. One of the largest terms in the momentum equations was the gas–solid drag force, for which several closures have been proposed to describe the effects of clustering of particles. Closures can be derived on experimental basis like what was done by Kallio et al. [5] who applied a drag law that was based on the empirical equations suggested by Matsen [6] for bed expansion in CFB and BFB conditions and on the Ergun [7] equation at the packing limit. In recent years, instead of using empirical correlations as basis, it has been more common to develop models based on transient simulations in fine meshes.

Agrawal et al. [8], Andrews et al. [9], and Igci et al. [10,11] developed closures for the average drag and stress terms through 2D simulations in small domains with periodic boundary conditions and, by volume-averaging the results, they derived closures for the sub-grid scales. In Igci and Sundaresan [12] and Igci et al. [13], wall effects were included in the analysis of a case of Geldart A particles and in the closures that were derived by volume-averaging 2D transient simulation results for the drag force and the normal and shear stresses of the solid phase. Milioli et al. [14] further developed the closures by including the slip velocity between the phases in the equations. Shah et al. [15] studied wall effects on the gas–solid drag force in a case of Geldart B particles through volume-averaging 2D transient simulation results for a small CFB. Zhang and VanderHeyden [16] discussed the effects of mesh spacing on Reynolds stresses and the drag force. In Zhang and VanderHeyden [17], an added-mass force closure was suggested for the correlation between fluctuations of the pressure gradient of the continuous phase and fluctuations of solid volume fraction. De Wilde [18] analyzed the same term from simulations and accounted also for the average drag force in the derivation of new closure models that were applied in De Wilde et al. [19] for steady state simulation of a riser. In addition to models based on measurement data and transient simulation results, closures for the gas–solid drag force have been suggested on the basis of theoretical analysis of clustering flow in dense gas–solid suspensions [20,21]. Common to all the suggested sub-grid and steady-state drag models is that the predicted drag force is reduced from what the homogeneous flow drag correlations would predict in the same flow conditions.

The models presented in the literature often take into account only a small number of factors that can affect the magnitude of fluctuations in flow properties. To improve our understanding of the requirements for a comprehensive filtered drag law, the present study analyzes the effects of material properties on the average drag force applicable to steady state modeling. In addition, the effects of process conditions on the required drag closures are evaluated. The analysis is based on time-averaging the results from transient Eulerian–Eulerian simulations of circulating fluidized beds of Geldart B particles. Since 3D simulations are very time consuming, development of sub-grid closure laws has commonly been carried out by averaging results from 2D simulations. For the same reason, this parametric study is carried out in 2D. Although the observed quantitative effects of the studied parameters cannot be applied to 3D simulations with high accuracy, some implications for further 3D studies and closure development can be derived, since the parameters required for drag correction in 2D should be significant also in 3D geometries. Still, as long as a similar dataset from 3D simulations is not available, the data collected in the present study can be used to derive models for the time-averaged drag force. Furthermore, the results of the present study provide an indication which parameters should be included in the drag correction functions applicable to coarse mesh simulations.

2. Methodology

2.1. Transient simulations

A large number of 2D simulations were carried out for analysis of the required closures for the time-averaged momentum equations. A selection of the simulations with varying gas viscosities, gas densities, solid densities, particle sizes, riser size and mesh spacings was chosen for the present analysis. The geometry is a simple riser with straight walls. A uniform gas inflow is introduced at the bottom and gas and solids exit the riser through the top edge of the simulated domain. Solids that leave the riser are fed back through a return channel located at 0.6–0.7 m height.

The simulations analyzed are listed in Table 1. Although gas density and viscosity in most industrial applications are strongly coupled, here their values were changed independently to separate their individual effects. Thus some of the simulations don't necessarily represent typical CFB conditions as used today.

The numerical simulations were carried out with the commercial code ANSYS Fluent v.14 [22]. The simulations were based on the Eulerian–Eulerian multiphase approach with the kinetic theory of granular flow (KTGF) models. In this study, models available in Fluent v.14 were used and they are listed in Table 2 with references to the corresponding authors.

For the drag term the standard Gidaspow [23] model based on the Ergun [7] and Wen–Yu [24] drag laws was used. For the momentum second order discretization was applied and for the volume fraction equation the QUICK scheme was applied. The time step was 0.001 s for the 12.5 mm and 25 mm meshes and 0.0005 s for the 6.25 mm mesh. For each case, approximately 5 s was simulated before starting to calculate the average values and at least a further 120 s of flow time was simulated to compute the averages. This presented a reasonable compromise between simulation time and accuracy of the average values. Comparisons with measurements have been made earlier for some simulations with the same models in a 0.4 m wide geometry [25]. The measurement and simulation results were in good qualitative agreement and even quantitatively the results were reasonably good considering that the simulations were carried out in 2D. Thus the chosen approach should be sufficiently accurate for the present study.

To allow simulation of a large number of cases in a reasonably short time, most simulations in this work were carried out in a coarse mesh with 12–25 mm spacing. To study effects of the mesh spacing, one simulation was done in a finer 6.3 mm mesh. At the same time, also the time step was halved, i.e., reduced from 0.001 s to 0.0005 s. Fig. 1 shows a comparison of the obtained time-averaged solid volume fraction fields in Cases 1, 3 and 2, where the mesh spacing was 6.3 mm, 12.5 mm and 25 mm, respectively. No significant qualitative change in the solid distribution can be observed. The majority of the simulations analyzed in the present work were carried out in a 2D mesh with 12.5 mm mesh spacing. Although the quantitative results slightly change when the mesh is coarsened, the qualitative results don't show any significant sensitivity to mesh spacing and time step and thus the chosen meshes were considered sufficient for this qualitative parametric study. Some simulations were also carried out in a 50 mm mesh, which produced significantly altered flow patterns. Consequently, simulations with such coarse meshes were omitted from the analysis.

2.2. Time-averaging of the transient simulation results

Time-averaged equations can be developed by averaging the transient equations over time. The instantaneous values are written as a sum of the time-average and a fluctuation: $\phi = \overline{\phi} + \phi'$. Favre averaging is applied on velocities: $U_{q,i} = \overline{\alpha_q u_{q,i}}/\overline{\alpha_q}$, $u_{q,i} = U_{q,i} + u''_{q,i}$. The time-

Table 1
Analyzed cases. Parameters: gas superficial velocity U_0, gas viscosity μ_g, gas density ρ_g, solid density ρ_s, particle diameter d_p, mesh spacing Δx_{mesh}, riser width w, riser height h, terminal velocity v_t, particle Reynolds number at terminal velocity Re_t, average solid volume fraction $\overline{\alpha_s}$, and static pressure at the bottom p_{bot}.

Case	U_0	μ_g	ρ_g	ρ_s	d_p	Δx_{mesh}	w	h	v_t	Re_t	$\overline{\alpha_s}$	p_{bot}
	m/s	kg/m s	kg/m^3	kg/m^3	mm	mm	m	m	m/s	–	%	kPa
1	3.5	1.79E−05	1.225	2480	0.385	6.3	0.4	3	2.85	75	5.38	2.70
2	3.5	1.79E−05	1.225	2480	0.385	25	0.4	3	2.85	75	5.39	2.72
3	3.5	1.79E−05	1.225	2480	0.385	12.5	0.4	3	2.85	75	5.39	2.96
4	3.5	1.79E−05	1.225	2000	0.385	12.5	0.4	3	2.47	65	5.39	2.81
5	3.5	1.79E−05	1.5925	2480	0.385	12.5	0.4	3	2.61	89	5.40	4.24
6	3.5	1.79E−05	0.8575	2480	0.385	12.5	0.4	3	3.22	59	5.39	3.28
7	3.5	2.79E−05	1.225	2480	0.385	12.5	0.4	3	2.45	41	5.39	6.46
8	3.5	7.90E−06	1.225	2480	0.385	12.5	0.4	3	3.61	216	5.39	3.67
9	2.75	4.45E−05	0.3105	2480	0.2555	12.5	0.4	3	1.53	2.7	6.80	4.49
10	2.75	4.45E−05	0.3105	2480	0.2555	12.5	1	7	1.53	2.7	2.97	3.55
11	2.75	4.45E−05	0.3105	2480	0.2555	12.5	3	14	1.53	2.7	1.49	5.04
12	2.75	4.45E−05	0.3105	2480	0.2555	12.5	3	14	1.53	2.7	4.34	12.4
13	2	4.45E−05	0.3105	2480	0.2555	12.5	3	14	1.53	2.7	1.49	4.93
14	5	4.45E−05	0.3105	2480	0.2555	12.5	3	14	1.53	2.7	1.49	5.30
15	5	4.45E−05	0.3105	2480	0.44	12.5	3	14	3.37	10	1.48	4.27
16	5	4.45E−05	0.3105	2480	0.15	12.5	3	14	0.62	0.64	1.48	4.68
17	8	4.45E−05	0.3105	2480	0.2555	12.5	3	14	1.53	2.7	1.48	5.10

averaged continuity and momentum equations for phase q (changes in ρ_{qm} assumed small) can be written as follows [2]:

$$\frac{\partial \overline{\alpha}_q \rho_{qm}}{\partial t} + \frac{\partial \overline{\alpha}_q \rho_{qm} U_{q,k}}{\partial x_k} = 0 \tag{1}$$

$$\begin{aligned}\frac{\partial \overline{\alpha}_q \rho_{qm} U_{q,i}}{\partial t} + \frac{\partial \overline{\alpha}_q \rho_{qm} U_{q,k} U_{q,i}}{\partial x_k} &= \overline{\alpha}_q \rho_{qm} g_i - \overline{\alpha}_q \frac{\partial \overline{p}}{\partial x_i} - \overline{\alpha_q' \frac{\partial p'}{\partial x_i}} + \frac{\partial \overline{\alpha_q \tau_{q,ik}}}{\partial x_k} \\ &+ \frac{\partial \overline{\alpha_q \tau^M_{q,ik}}}{\partial x_k} + (-1)^{(\delta_{qs}+1)} K_{gs}\left(u_{g,i} - u_{s,i}\right) \\ &- \frac{\partial \overline{p}_q}{\partial x_i}\delta_{qs} - \frac{\partial \rho_{qm} \overline{\alpha_q u''_{q,k} u''_{q,i}}}{\partial x_k}.\end{aligned} \tag{2}$$

Here ρ is the density, α volume fraction, p pressure, p_s solid pressure, g gravitational acceleration, K inter-phase momentum transfer coefficient, δ_{gs} Kronecker delta, τ laminar stress, and τ^M local-scale turbulent stress. The time average of a variable φ is denoted by $\overline{\varphi}$ and the fluctuation part by $\varphi' = \varphi - \overline{\varphi}$. In the equations above, u is the instantaneous velocity, U_q is the Favre average or phase-weighted average velocity $U_q = \overline{\alpha_q u_q}/\overline{\alpha_q}$ and $u''_q = u_q - U_q$ is the velocity fluctuation. The gas phase is denoted by g and solid phase by s. The terms on the right hand side in Eq. (2) are the gravitation term, pressure term, pressure fluctuation term, laminar stress, turbulent stress, drag force, solid pressure term, and the Reynolds stress term. The gravitation and pressure terms can be calculated from the basic average flow properties but for the rest of the terms closure relations have to be developed.

In the present study we concentrate on the time-averaged drag force in the vertical (y) direction and utilize for the analysis the time-averaged velocity and volume fraction fields. A closure for the time-averaged drag force can be written in the form.

$$\overline{K_{gs}\left(u_{g,y} - u_{s,y}\right)} = C_{drag} K^*_{gs}\left(U_{g,y} - U_{s,y}\right) \tag{3}$$

where K^*_{gs} is the inter-phase momentum transfer coefficient calculated on the basis of the time-averaged velocities and volume fractions using a similar combination of Wen and Yu [24] and Ergun [7] drag laws as in the transient simulations. However, instead of using Gidaspow's [23] drag law implemented in Fluent, a smoother transition between the drag laws, suggested by Niemi et al. [30], was used to calculate K^*_{gs}. In this model a linear transformation between the Ergun and Wen–Yu models occurs in a solid volume fraction range of 0.4–0.5, which is within the region recommended by Leboreiro et al. [31]. The coefficient C_{drag} in Eq. (3) is a drag correction coefficient, for which a correlation should be developed.

Table 2
The models and parameters used in the simulations.

Submodel or parameter	Model or value used
Granular viscosity	Syamlal et al. [26]
Granular bulk viscosity	Lun et al. [27]
Frictional viscosity	Schaeffer [28]
Granular conductivity	Syamlal et al. [26]
Solids pressure	Lun et al. [27]
Radial distribution	Ogawa et al. [29]
Angle of internal friction	30°
Frictional and packing limit	0.61 and 0.63, respectively
Turbulence model	Standard k − ε, dispersed
Wall boundary condition, gas	No slip
Wall boundary condition, solids	Partial slip, specularity coefficient 0.001

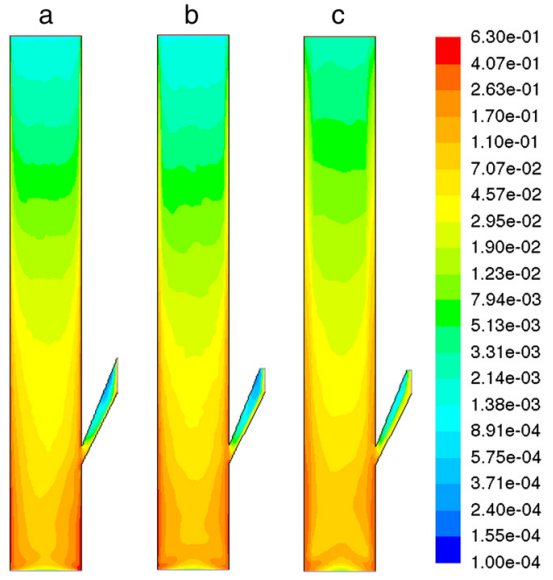

Fig. 1. Time-averaged solid volume fraction in simulations 1 (mesh spacing 6.3 mm), 3 (12.5 mm), and 2 (25 mm).

The value of C_{drag} in each point in the flow field can be calculated from Eq. (3) by time-averaging the drag force, solid volume fraction and gas and solid velocities over the simulation time of a transient simulation. This kind of data was collected for each of the cases listed in Table 1. Some filtering of the data was done at the data collection stage. For very low values of slip velocity, the computed C_{drag} can become unreasonably large due to stochastic nature of the data and finite averaging periods. C_{drag} values above 2.5 were removed from the data. The data for the solid return channel was also omitted from the analysis since the characteristics of the flow are there completely different. Similarly, exit region effects were avoided in the results by excluding the uppermost 20% of the simulated riser volume.

3. Results

3.1. Effect of solid volume fraction

Volume fraction of solid particles, α_s, is the most important parameter affecting the amount of correction that needs to be applied in clustering flow on the customary drag laws derived for homogeneous conditions. For that reason, the drag correction coefficient C_{drag} determined from the transient simulations is in the following plotted as a function α_s with other flow properties as parameters. In the comparisons, one parameter at a time has been varied in the simulations to allow easy comparison.

We start the analysis with Fig. 2 which shows the obtained values for C_{drag} as a function of α_s in all mesh points studied (the simulated domain except the return channel and riser exit region) in each of the cases listed in Table 1. In general we can observe a reduction of the average drag force from what is predicted by the homogeneous flow correlations. In the dilute end of the solid volume fraction scale at α_s values below 0.01 the relationship between C_{drag} and α_s is clear. In this region, C_{drag} for a set of conditions found in a single simulation could be expressed as a function of solid volume fraction only. In the dense regions the relationship is less clear and in an intermediate density range where α_s is of the order of 0.1 there is no correlation between C_{drag} and α_s. High solid concentrations are encountered in the wall layers and in the bottom bed where the flow patterns differ from the ones in the central part of the riser, which explains the different C_{drag} trends at high α_s.

In the dilute conditions, C_{drag} should approach unity since no drag correction needs to be applied for a single particle, i.e. for $\alpha_s \rightarrow 0$. Depending on fluidization conditions, the range of solid volume fractions strongly varies in the different cases in Fig. 2. In Case 10, where fluidization velocity is low, the suspension in the upper part of the riser is so dilute that the expected limit is reached. An interesting phenomenon seen in Fig. 2 is that in the dense suspension areas C_{drag} can also exceed 1. Exactly at packing limit it should go to unity, but in the CFB simulations of the present study the packing limit is not reached in the time-averaged data.

To analyze regional effects in Case 10, data from the riser bottom and wall regions is omitted in Fig. 3 in several steps. Fig. 3 reveals several interesting local effects. The C_{drag} values at around solid volume fraction 0.1 that show no clear correlation with solid content originate from the bottom section below 0.7 m elevation. Characteristic for this region is acceleration of solids from zero upward velocity at the bottom to a higher transport velocity. Fig. 3 also shows that the high values at low solid concentration appear in the near-wall region. The lowest values of C_{drag} originate from a region between 0.05 m and 0.1 m from the wall, which could be related to the location of the edge of the wall layer where both upward and downward movements of solids are common. In general, in the air entrance region the drag force seems to have a very different behavior compared to the rest of the riser and a separate analysis of this region might be necessary.

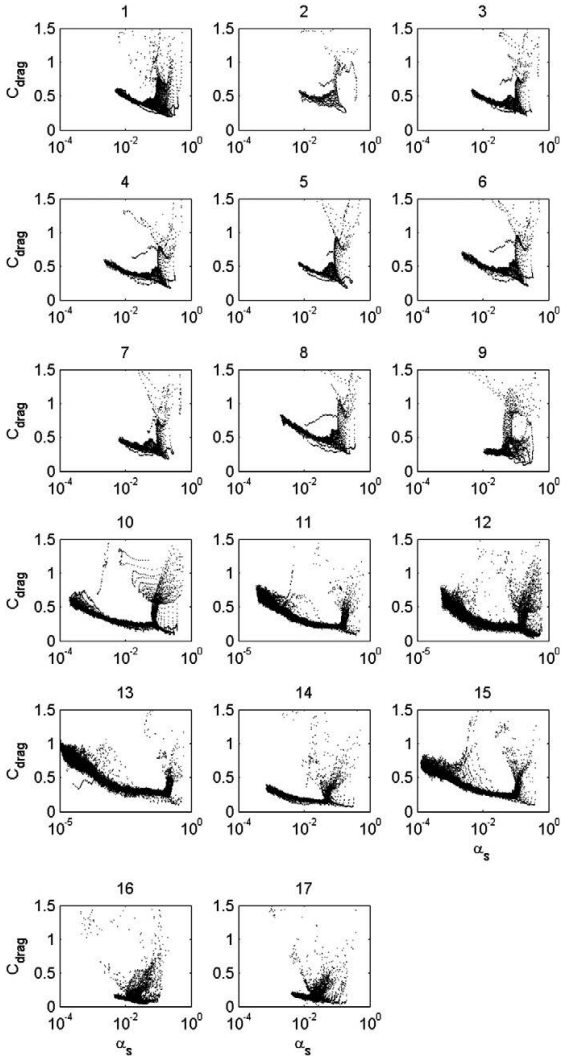

Fig. 2. The values of C_{drag} depicted as a function of α_s in all analyzed points in each of the 17 cases listed in Table 1.

3.2. Effect of mesh spacing

For practical reasons and to allow graphical presentation of the results, the amount of data plotted for comparisons of the different simulations was reduced by randomly picking points from the wall regions, from the bottom bed region and from the rest of the flow field, with different probabilities for the three regions to guarantee that all these regions are well represented in the plots.

Analysis of volume-averaged simulation results has shown [15,12] that in sub-grid closures for coarse mesh simulations, mesh size is an important parameter. It can be assumed that in the development of time-averaged models the mesh could play a role and hence the effect of the mesh that was used in the transient simulations needs to be evaluated.

Fig. 4 shows the effect of mesh spacing in Cases 1, 2 and 3. The same situation is simulated with three different mesh spacings, 6.3 mm,

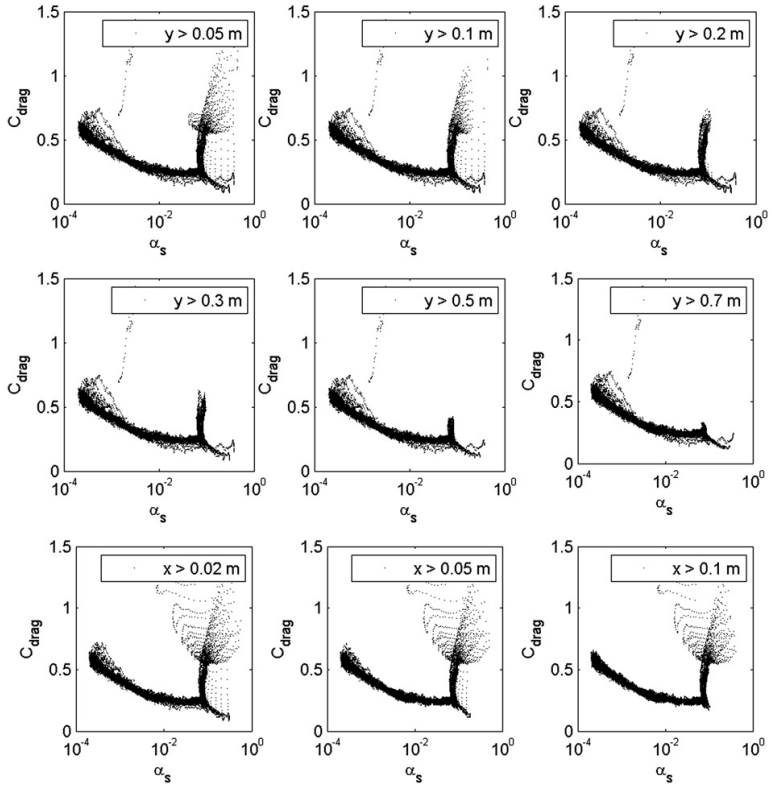

Fig. 3. The values of C_{drag} depicted as a function of α_s in limited regions in the riser in Case 10. In the figure, x is the lateral coordinate and y the vertical coordinate in the riser.

12.5 mm and 25 mm. The two finest meshes in Fig. 4 show practically the same results for C_{drag} whereas the 25 mm mesh has produced slightly higher values. Thus the 12.5 mm mesh can be considered accurate enough for the present analysis. Although Fig. 1 showed that there is a visible difference in the average volume fraction fields obtained with 6.3 mm and 12.5 mm meshes, the very small difference in the produced C_{drag} values indicates that the statistical properties of the fluctuations in the flow variables are fairly mesh independent at this mesh resolution,

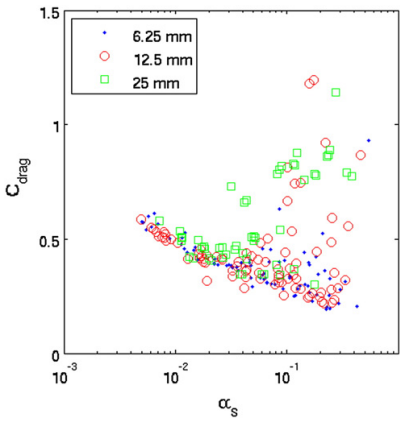

Fig. 4. Effect of mesh spacing on C_{drag} (Cases 1, 3, and 2, respectively, in Table 1).

which is a sufficient condition for accepting the coarser mesh for the analysis of the time-averaged drag force. This does not mean that all the finest flow structures are resolved by the simulation, but that the scales that have significant influence on the time-averaged drag force are captured. Results on C_{drag} obtained with the 25 mm mesh still show qualitatively similar trends and could probably also have been used for parametric studies. However, for derivation of closures, a finer mesh seems necessary.

3.3. Effects of process conditions

In CFBs the flow conditions can vary a great deal even when the temperature is constant and material properties are the same. Bed inventory and fluidization velocity change the voidage and velocity distributions in the process, which could affect solid clustering and hence also the drag correction required. In Fig. 5, results are shown for two simulations with the same gas and solid material properties and fluidization velocity but different solid inventory. The dependence of the drag correction values on the solid volume fraction is practically the same in the two simulations, which means that the bed mass need not to be separately accounted for. Fig. 6 illustrates that the fluidization velocity has no large effect either, although at the two lowest fluidization velocities higher C_{drag} is obtained. The differences can be due to changes in other parameters such as the average slip velocity. Fluidization velocity also affects the range of time-averaged volume fractions in the process. Largest range of solid concentrations is obtained at the small fluidization velocities. To obtain data for deriving a general drag correction function for the full range of flow conditions, simulations at several gas velocities can be necessary.

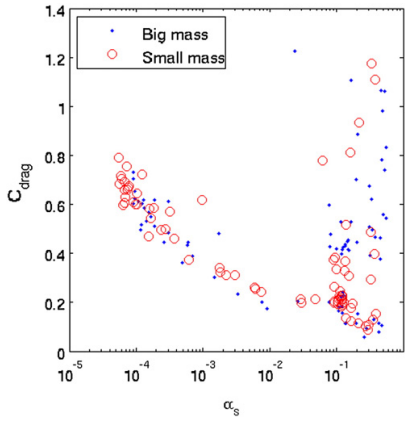

Fig. 5. Effect of bed mass on C_{drag} (Cases 12 and 11, respectively, in Table 1).

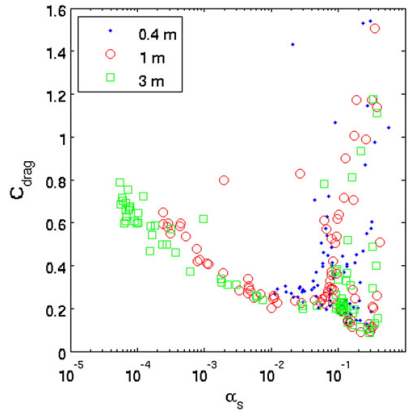

Fig. 7. Effect of riser width on C_{drag} (Cases 9, 10, and 11, respectively, in Table 1).

Riser width and height can also be expected to have an effect on the clustering tendency. Fig. 7 shows results from three simulations where the riser size has varied. A small effect on the drag function is visible in the figure. A bigger correction to the drag force, i.e. a smaller value of C_{drag} was obtained as the riser size was increased. The distance to the walls and the local slip velocity have been shown to have a significant effect in drag corrections required for coarse meshes [13,15] and these could also be behind the observed small effect on C_{drag}.

3.4. Effects of the distance to a wall and the slip velocity

Since in models for coarse meshes the lateral distance to the walls has been shown to be an important parameter, it can be assumed to have an effect also on the time-averaged drag force. In Fig. 8, the drag correction coefficient C_{drag} is plotted as a function of the distance to the wall for three different values of solid volume fraction, 0.001 (data in the range 0.0009–0.0011), 0.01 (0.009–0.011), and 0.1 (0.08–0.12). Wall distance seems to have a complicated effect. In Shah et al. [15] the correction coefficient in the sub-grid scale drag law, determined by volume averaging similar transient simulation results, diminished towards the wall. The same trend is seen in the time-averaged drag force in Fig. 8 in Case 14 for solid volume fraction 0.01, but in several other situations shown in Fig. 8 the trend is opposite. The flow pattern close to the wall can vary greatly depending on process conditions and the vertical position in the riser, which can be the reason behind the differences in the trends seen in Fig. 8.

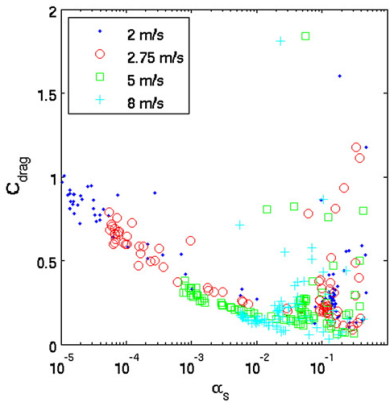

Fig. 6. Effect of fluidization velocity on C_{drag} (Cases 13, 11, 14, and 17, respectively, in Table 1).

Milioli et al. [14] reported that in addition to mesh spacing and the distance to the wall, also the slip velocity between gas and solid phases can play a significant role. The data from Cases 9, 10, 11, 12, 13, 14 and 17, with same material properties but different geometries and fluidization conditions is collected in Fig. 9 where the drag correction coefficient C_{drag} is shown at three solid volume fractions as a function of the lateral distance to a wall and as a function of the local vertical slip velocity component. A big scatter in the data is observed in both plots indicating that neither of these variables alone is capable of explaining the variation in C_{drag} at a fixed solid concentration.

To evaluate the combined effect of wall distance and slip velocity, data at a narrow range of wall distances were separated close to the wall (between 0.01 m and 0.03 m from the wall) and in the central region (distance to wall above 1.2 m). Fig. 10 shows the values of the drag correction coefficient at these two locations at the three studied solid volume fractions as a function of the slip velocity. It is evident that variations in the slip velocity can explain a significant fraction of the scatter visible in Fig. 9. An increase in the slip velocity leads to a lower C_{drag} value. In the central region some points at the two highest volume fractions don't fit the pattern. A closer look into these points showed that they are from the elements closest to the bottom plate. There the flow pattern will differ strongly from the rest of the riser and the drag correlation should perhaps be developed separately.

In the analyzed simulations, the no-slip boundary condition was used for the gas phase and partial slip condition with specularity coefficient 0.001 for the solid phase. Changing the value of the specularity coefficient could somewhat change the voidage and velocity profiles, especially close to the wall, and its effect on the behavior of C_{drag} as a function of the distance to the wall should also be checked in further studies. This was not done in the present work, where the same value as used in the validation study [25] was used in all simulations.

3.5. Effects of gas and solid properties

In the literature, no systematic study of the effects of phase properties on the drag correction coefficient has been presented. The data from the runs listed in Table 1 allows this kind of analysis. Initially in the present study a hypothesis was proposed that drag correction could be expressed as a function of dimensionless numbers such as the Reynolds number. In Fig. 11 results are plotted for Cases 5, 6, 7 and 8 with different Reynolds numbers that are calculated based on the particle terminal velocity. No simple clear trend as a function of the Reynolds number can be observed in these cases were gas density

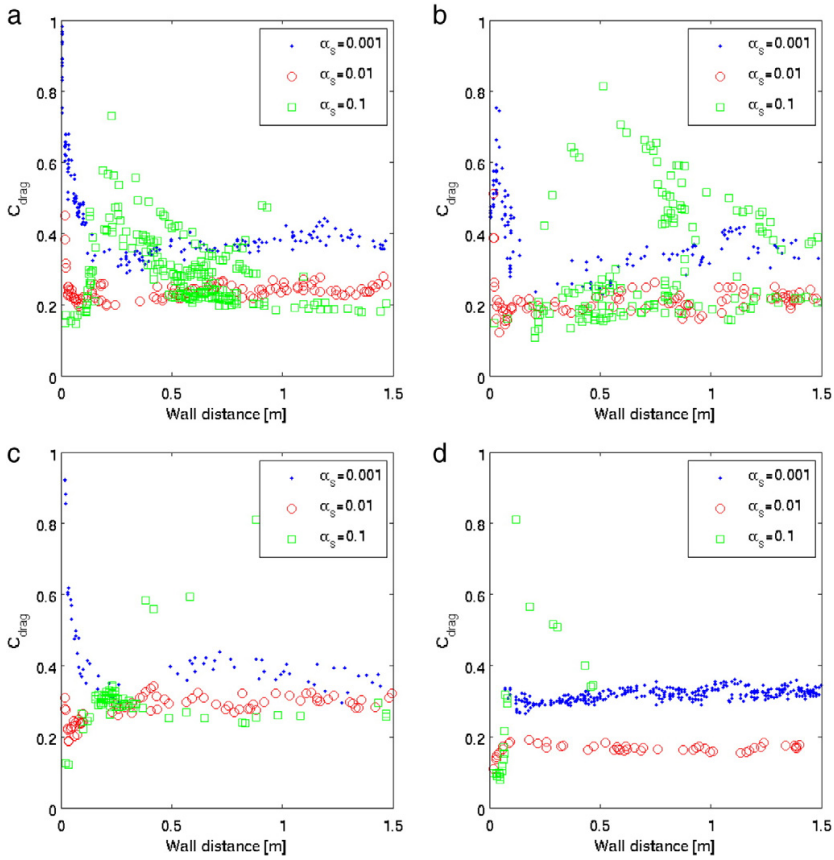

Fig. 8. Effect of the distance to the wall on C_{drag} at different solid volume fractions in Cases 11 (top left), 12 (top right), 13 (bottom left) and 14 (bottom right).

and viscosity varied. Archimedes number, which was also considered as a parameter, gave exactly the same result. Thus the fluid and particle properties need to be separately accounted for.

Fig. 12 shows the effect of varying gas density. It has no clear effect on the drag correction coefficient. According to Fig. 13, solid density has a positive effect on C_{drag}. The effect of gas viscosity is reducing C_{drag} (Fig. 14) indicating that in hot conditions, the drag force deviates stronger than in cold conditions from what it would be if the suspension would be homogeneous. All other properties are the same in the simulations.

Fig. 15 shows that particle size also has a significant effect. Clustering tendency seems to be highest in the case of smallest particles. In large fluidized beds there is typically a big difference in the average particle sizes for the bottom bed and the top of the riser. The largest size in Fig. 15, 0.44 mm, could very well represent the size at bed bottom and the smallest, 0.15 mm, the average size at riser exit. Thus even in a single simulation, a correction function that takes the particle size into account would be needed.

The three phase properties, i.e. solid density, gas viscosity and particle size, which proved to be important for the average drag force, have also a direct effect on the slip velocity. Fig. 10 showed that an increase in slip velocity has a reducing effect on C_{drag}. Thus the possibility that the effect of material properties is due to changes in the slip velocity needs to be considered. This possibility is easily ruled out by studying e.g. the results in Fig. 15. In dilute conditions in the upper part of the riser the slip velocity approaches the terminal velocity of a single particle. Thus we can use the terminal velocities given in Table 1 to indicate the differences in the slip velocity. The terminal velocity increases with particle size and thus C_{drag} in Fig. 15 increases as the slip velocity increases which is opposite to the trend seen in Fig. 10. Thus we can conclude that particle size has an effect separate from that of the slip velocity, which is related to the acceleration of particles while the effect of the particle size is related to changes in the clustering behavior. In a similar way by analyzing Figs. 13 and 14, solid phase density and gas viscosity can be shown to have independent effects.

4. Conclusions

In the present work, parameters affecting the reduction of the average gas–solid drag force in dense gas–solid suspensions due to particle clustering were studied by analyzing time-averaged results from a number of transient simulations carried out in fairly fine meshes. The analysis was limited to Geldart B particles and CFB conditions. The simulations were carried out in 2D, which limits direct quantitative applicability of the results to 2D simulations. Qualitatively, it can be expected that the same parameters that were observed to be important for the average drag force in 2D have also significant effects in 3D geometries. The present results are applicable to time-averaged CFD modeling but not as such to transient coarse mesh simulations. However, since the amount of filtering done by time averaging is similar to the filtering done by a very coarse mesh spacing, the present results indicate that even in coarse mesh closures the parameters that were found to be important in the present work should be considered in development of sub-grid closures.

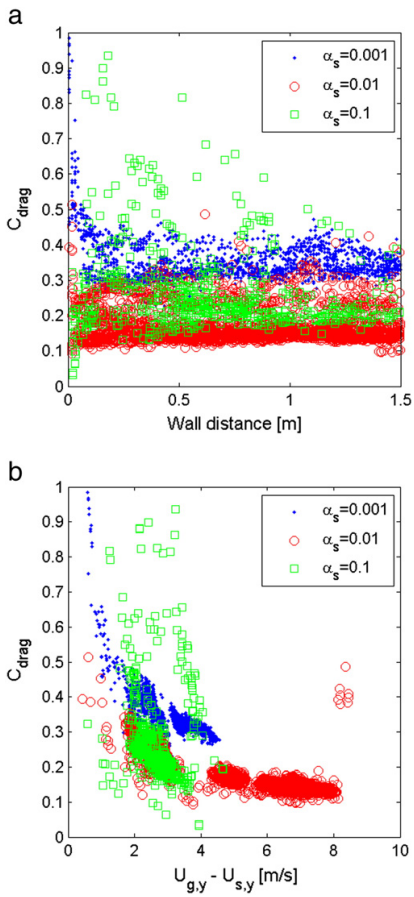

Fig. 9. Summarized data for Cases 9, 10, 11, 12, 13, 14 and 17 at solid volume fractions 0.001, 0.01 and 0.1. a) Drag correction coefficient C_{drag} plotted as a function of the distance to the wall, Δx_{wall}. b) Drag correction coefficient C_{drag} plotted as a function of the slip velocity.

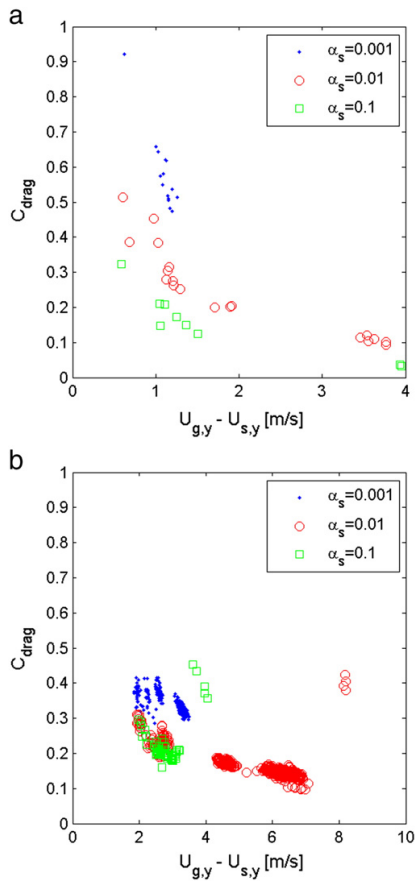

Fig. 10. Summarized data from Cases 9, 10, 11, 12, 13, 14 and 17. Drag correction coefficient C_{drag} plotted as a function of the slip velocity at three different solid volume fractions a) in the wall layer and b) in the central region.

According to the results of the present study, the main parameters that should be accounted for in a relation for the time-averaged gas–solid drag force are the solid volume fraction, distance to the wall, slip velocity, solid phase density, particle size and gas phase laminar viscosity. Thus a closure law should be of the form

$$C_{drag} = f\left(\overline{\alpha_s}, \Delta x_{wall}, \left|U_g - U_s\right|, \rho_s, d_p, \mu_g\right). \quad (4)$$

The distance to the wall has a significant but complicated effect, which was shown to be a result of combined effects with other parameters. Fluidization velocity had an effect on the drag correction but it can probably be at least partly accounted for by including the slip velocity in the model. The present analysis also showed that the effects of material properties cannot easily be lumped together into a single parameter such as a Reynolds number, but they have to be included separately. Within the investigated range, process size and bed mass had no significant effect whereas mesh spacing used in the simulations affected the obtained correction. This implies that drag correction functions can be derived from transient simulations of a small geometry as long as the mesh is fine enough to produce results that are independent of the mesh spacing.

No model was developed in the present study. A wider set of data is necessary for model development to cover possible combined effects of different variables. Only by developing a model we can fully evaluate the extent of the effects of the individual parameters since there can be complicated interactions between them, which weren't studied in the present work.

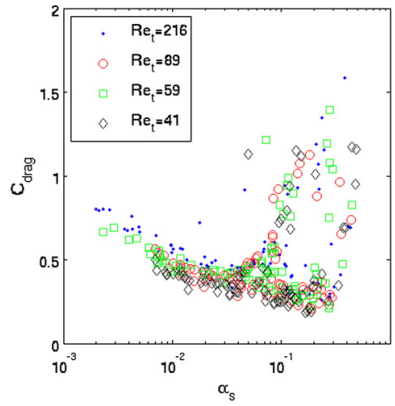

Fig. 11. Effect of Reynolds number (calculated on the basis of particle terminal velocity) on C_{drag} (Cases 8, 5, 6, and 7, respectively, in Table 1). Archimedes numbers for the four cases are 27200, 6900, 3720, and 2180, respectively.

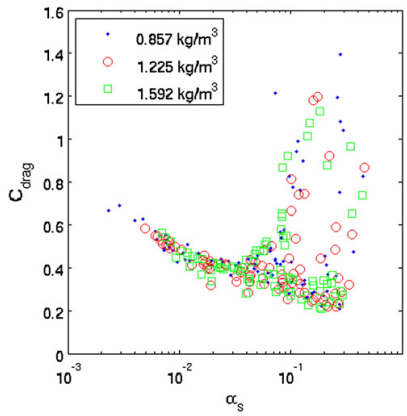

Fig. 12. Effect of gas density on C_{drag} (Cases 6, 3, and 5, respectively, in Table 1).

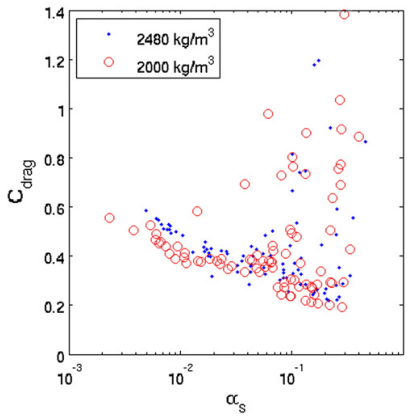

Fig. 13. Effect of solid density on C_{drag} (Cases 3 and 4, respectively, in Table 1).

The models presented in the literature have so far ignored the effects of material properties on the corrections applied on the drag force in coarse mesh and steady state modeling. The present analysis showed that the effects of particle size, solid material density and gas viscosity

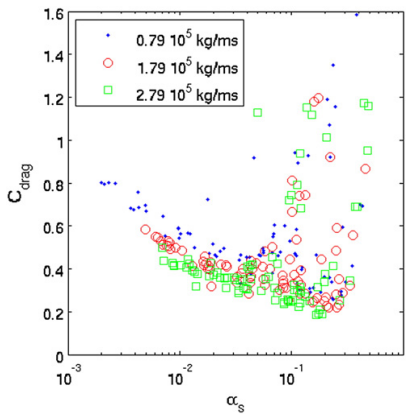

Fig. 14. Effect of gas viscosity on C_{drag} (Cases 8, 3, and 7, respectively, in Table 1).

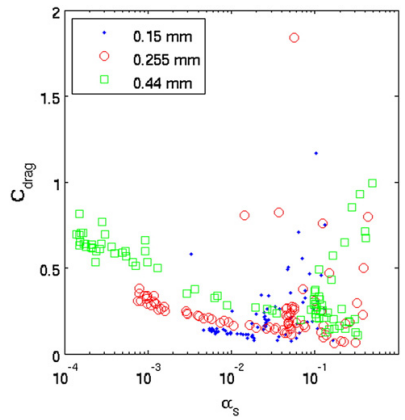

Fig. 15. Effect of particle size on C_{drag} (Cases 16, 14, and 15, respectively, in Table 1).

are significant. Since gas–solid drag strongly affects the vertical distribution of solids in a CFB riser and especially the solid circulation rate, the omission of material property effects from the drag closure significantly reduces the accuracy of the simulations.

Notation

d	diameter
h	height
g	gravitational acceleration
p	pressure
Re	Reynolds number
u	velocity
U	time-averaged velocity
U_0	superficial velocity
v_t	terminal velocity
w	riser width
x	distance
Δx_{mesh}	mesh spacing
Δx_{wall}	distance to wall
K_{qs}	inter-phase momentum transfer coefficient

Greek symbols

α	volume fraction
δ_{qs}	Kronecker delta
μ	viscosity
ρ	density
τ	stress

Subscripts

bot	bottom
k	coordinate k
i	coordinate i
g	gas
p	particle
q	phase q
s	solid
t	related to terminal velocity

Superscripts

M	turbulent
$*$	calculated from time-averaged values

Acknowledgment

The authors gratefully acknowledge the financial support of Tekes, VTT Technical Research Centre of Finland, Etelä-Savon Energia Oy, Fortum, Metso Power Oy and Numerola Oy, and the support from Saarijärven Kaukolämpö Oy.

References

[1] S. Benyahia, S. Sundaresan, Do we need sub-grid scale corrections for both continuum and discrete gas–particle flow models? Powder Technol. 220 (2012) 2–6.
[2] V. Taivassalo, S. Kallio, J. Peltola, On time-averaged CFD modeling of circulating fluidized beds, Int. J. Nonlinear Sci. Numer. Simul. 13 (2012) 363–373.
[3] Zh.X. Zeng, L.X. Zhou, A two-scale second-order moment particle turbulence model and simulation of dense gas–particle flows in a riser, Powder Technol. 162 (2006) 27–32.
[4] S. Kallio, V. Taivassalo, T. Hyppänen, Towards time-averaged CFD modelling of circulating fluidized beds, 9th Int. Conf. on Circulating Fluidized Beds, Hamburg, 2008.
[5] S. Kallio, V. Poikolainen, T. Hyppänen, Mathematical modeling of multiphase flow in a circulating fluidized bed, Report 96-4, Heat Eng. Lab.Åbo Akademi University, Turku, Finland, 1996.
[6] J.M. Matsen, Mechanisms of choking and entrainment, Powder Technol. 32 (1982) 21–33.
[7] S. Ergun, Fluid flow through packed columns, Chem. Eng. Prog. 48 (1952) 89.
[8] K. Agrawal, P.N. Loezos, M. Syamlal, S. Sundaresan, The role of mesoscale structures in rapid gas–solid flows, J. Fluid Mech. 445 (2001) 151–185.
[9] A.T. Andrews, P.N. Loezos, S. Sundaresan, Coarse-grid simulation of gas–particle flows in vertical risers, Ind. Eng. Chem. Res. (2005) 6022–6037.
[10] Y. Igci, S. Sundaresan, S. Pannala, T. O'brien, R.W. Breault, Coarse-graining of two-fluid models for fluidized gas–particle suspensions, 5th Int. Conf. on CFD in the Process Industries, CSIRO, Melbourne, Australia, 2006.
[11] Y. Igci, A.T. Andrews, S. Sundaresan, S. Pannala, T. O'Brien, Filtered two-fluid models for fluidized gas–particle suspensions, AIChE J 54 (2008) 1431–1448.
[12] Y. Igci, S. Sundaresan, Verification of filtered two-fluid models for gas–particle flows in risers, AIChE J 57 (2011) 2691–2707.
[13] Y. Igci, S. Pannala, S. Benyahia, S. Sundaresan, Validation studies on filtered model equations for gas–particle flows in risers, Ind. Eng. Chem. Res. 51 (2012) 2094–2103.
[14] C.C. Milioli, F.E. Milioli, W. Holloway, K. Agrawal, S. Sundaresan, Filtered two-fluid models of fluidized gas–particle flows: new constitutive equations, 59 (2013) 3265–3275.
[15] S. Shah, J. Ritvanen, T. Hyppänen, S. Kallio, Wall effects on space averaged two-fluid model equations for simulations of gas–solid flows in risers, Chem. Eng. Sci. 89 (2013) 206–215.
[16] D.Z. Zhang, W.B. VanderHeyden, High-resolution three-dimensional numerical simulation of a circulating fluidized bed, Powder Technol. 116 (2001) 133–141.
[17] D.Z. Zhang, W.B. VanderHeyden, The effects of mesoscale structures on the macroscopic momentum equations for two-phase flows, Int. J. Multiphase Flow 28 (2002) 805–822.
[18] J. De Wilde, The generalized added mass revised, Phys. Fluids 19 (2007) 058103.
[19] J. De Wilde, G.J. Heynderickx, G.B. Martin, Filtered gas–solid momentum transfer models and their application to 3D steady-state riser simulations, Chem. Eng. Sci. 62 (2007) 5451–5457.
[20] W. Wang, J. Li, Simulation of gas–solid two-phase flow by a multi-scale CFD approach—extension of the EMMS model to the sub-grid level, Chem. Eng. Sci. 62 (2007) 208–231.
[21] X. Wang, F. Jiang, J. Lei, J. Wang, S. Wang, X. Xu, Y. Xiao, A revised drag force model and the application for the gas–solid flow in the high-density circulating fluidized bed, Appl. Therm. Eng. 31 (2011) 2254–2261.
[22] ANSYS Inc., ANSYS FLUENT Theory Guide. Release 14.0, Canonsburg, 2011.
[23] D. Gidaspow, Multiphase Flow and Fluidization — Continuum and Kinetic Theory Descriptions, Academic Press, 1994.
[24] C. Wen, Y. Yu, Mechanics of fluidization, Chem. Eng. Prog. Symp. Ser. 62 (1966) 100–111.
[25] S. Kallio, M. Guldén, A. Hermanson, Experimental study and CFD simulation of a 2D circulating fluidized bed, The 20th Int. Conf. on Fluidized bed combustion. May 18–20, Xi'an, China, 2009.
[26] M. Syamlal, W. Rogers, T.J. O'Brien, MFIX documentation: volume 1, theory guide, DOE/METC-9411004, NTIS/DE9400087, National Technical Information Service, Springfield, VA, 1993.
[27] C.K.K. Lun, S.B. Savage, D.J. Jeffrey, N. Chepurniy, Kinetic theories for granular flow: inelastic particles in couette flow and slightly inelastic particles in a general flow field, J. Fluid Mech. 140 (1984) 223–256.
[28] D.G. Schaeffer, Instability in the evolution equations describing incompressible granular flow, J. Differ. Equ. 66 (1987) 19–50.
[29] S. Ogawa, A. Umemura, N. Oshima, On the equations of fully fluidized granular materials, J. Appl. Math. Phys. (ZAMP) 31 (1980) 483–493.
[30] T. Niemi, J. Peltola, S. Kallio, Time averaged modeling of BFBs: analysis of the terms in the momentum equations, Proceedings Fluidization XIV Conference, May 2013, Noordwijkerhout, The Netherlands, 2013, pp. 559–566.
[31] J. Leboreiro, G.G. Joseph, C.M. Hrenya, Revisiting the standard drag law for bubbling, gas-fluidized beds, Powder Technol. 183 (2008) 385–400.

PAPER VI

Modeling of the time-averaged gas–solid drag force in a fluidized bed based on results from transient 2D Eulerian–Eulerian simulations

Powder Technology 261 (2014b) 257–271.

Powder Technology 261 (2014) 257–271

Contents lists available at ScienceDirect

Powder Technology

journal homepage: www.elsevier.com/locate/powtec

Modeling of the time-averaged gas–solid drag force in a fluidized bed based on results from transient 2D Eulerian–Eulerian simulations

Sirpa Kallio *, Juho Peltola, Timo Niemi

VTT Technical Research Centre of Finland, P.O. Box 1000, FI-02044 VTT, Finland

ARTICLE INFO

Article history:
Received 11 February 2014
Received in revised form 4 April 2014
Accepted 9 April 2014
Available online 18 April 2014

Keywords:
Drag force
Circulating fluidized bed
Time-averaging
Computational fluid dynamics
Empirical modeling

ABSTRACT

In the present paper, the possibilities to cover all fluidization states by a single drag law in steady-state CFD multiphase flow modeling are evaluated. The time-averaged drag force is expressed as the product of the drag force calculated from the traditional drag laws for homogeneous conditions, and a correction function. Closure correlations for the correction function are developed by nonlinear regression modeling based on data collected from 69 transient 2D simulations of bubbling, turbulent and circulating fluidized beds. The correlations are given as functions of eight variables: the solid volume fraction, the distance from the nearest wall, the height above the air distributor, the slip velocity between the phases, the gas velocity, the particle size, the solid density and the gas viscosity. The results indicate that covering all fluidized bed conditions in a single drag correlation is feasible, although fully satisfactory results were not obtained for the surface and freeboard regions of a bubbling fluidized bed (BFB) with correlations that were acceptable in circulating fluidized bed (CFB) conditions. A correlation that covers the whole range of fluidized states is complicated and thus the modeling task could be divided into development of separate correlations for different regions that could be combined into a single correlation by means of blending functions. The validity of this approach was demonstrated by developing a separate correlation for the dilute conditions above a height of 1.5 m in CFB risers. Results show that the accuracy of the predictions significantly improved in dilute CFB conditions where a much simpler correlation with six input variables could be used. The modeling approach is a good starting point for the development of a general drag law for CFD simulations of fluidized beds.

1. Introduction

Steady-state simulation is an attractive alternative for simulations of industrial-scale circulating fluidized bed (CFB) processes [1,2] since the tedious integration over a long time, as applied on transient simulation results, is generally avoided [1]. The clustering of particles in CFB gas–solid flows produces steep local gradients and structures in the solid volume fraction field. In transient simulations, these details have to either be resolved numerically, which requires a fine spatial and temporal resolution, or accounted for by means of closure laws that comprise the effects of the unresolved flow structures. In a steady-state simulation only the statistical properties of the fine structures need to be resolved and thus a coarser mesh suffices, allowing to shorten the simulation time. The equations for steady-state simulations can be derived by time-averaging the transient continuity and momentum equations. The temporal variations in the flow properties are modeled with closure relations that can be derived e.g. through analysis of time-averaged transient simulation results [1].

One of the largest terms in the time-averaged momentum equations is the gas–solid drag force [3]. Since a dense gas–solid flow is characterized by large fluctuations in flow properties, the drag models suitable for homogeneous conditions and used in transient simulations are not applicable in time-averaged modeling. Some attempts have been made to derive a closure for the time-averaged drag force (De Wilde et al. [4,5], Kallio et al. [6] based on Matsen [7]). Typically, the average force is expressed as a product of the drag force calculated from the traditional drag laws for homogeneous conditions (e.g. Wen and Yu [8] and Gidaspow [9] drag laws) and a correction function. In Kallio et al. [10], the parameters that could have significant effects on the correction function in CFB conditions were identified. The analysis was carried out by time-averaging results from 17 transient 2D simulations of CFB risers. The parameters that were shown to be important were the solid volume fraction, the distance from the nearest wall, the slip velocity between the phases, the particle size, the solid material density and the gas viscosity. Kallio et al. studied the qualitative effects of different variables one by one, thus not taking into account the possible combined effects of two or more variables. Still, some complicated joint effects of wall distance and slip velocity were observed. Similarly, the effects of material properties and solid concentration were shown to interact: the correction function values at a specific solid volume fraction

* Corresponding author. Tel.: +358 20 7224015.
E-mail address: sirpa.kallio@vtt.fi (S. Kallio).

http://dx.doi.org/10.1016/j.powtec.2014.04.045
0032-5910/

were significantly affected by changes in the material properties and these effects were different for different ranges of solid concentration. More data are needed if the data are to be used both for extending the models to all relevant conditions and for covering the combined effects of several parameters. To evaluate combined effects of different material properties, several combinations of material property values need to be included in the data. In the present work, data from new simulations are added to the data set of Kallio et al. [10] with the aim to cover a wider range of fluidization conditions. Like the previous study, the present investigation is limited to Geldart B particles [11].

By definition, the correction function for the time-averaged drag force has a value of unity in homogeneous flow conditions. In inhomogeneous conditions it deviates from unity and is typically reduced [10]. The inhomogeneity of a suspension does not necessarily depend only on the local flow properties and the distance from the walls, but may be affected by the formation and the transport of the flow structures, such as clusters, strands and voids. Thus there is the possibility that the efforts to derive a general drag correction function based on the local voidage, velocities and material properties may fail. The goal of the present study is thus to evaluate the possibilities to express a general drag closure law for the time-averaged momentum equation entirely on the basis of the local variables and location.

The results of Kallio et al. [10] indicate that it is not easy to a priori define the functional form of the required closure model. A solution to the problem, presented here, is a nonlinear regression model with a functional form adjusting to the observed behavior. Although the available amount of data is fairly limited, it is sufficient to demonstrate the potential of this modeling approach. In this work, data from 2D simulations are used as the basis for nonlinear empirical modeling of the drag force and the feasibility and the limitations of the approach are discussed. The parameters in the correlations developed in this work are not presented, since due to the 2D simplification and the limited amount of data they should only be considered as a proof of the concept. It would not be advisable to implement them in a CFD model in the present form.

2. Transient Eulerian–Eulerian 2D simulations

In the present work, transient Eulerian–Eulerian CFD simulations in different fluidization conditions are used as the basis for model development. The geometry in all the simulated cases is a simple, rectangular riser with straight walls. A gas inflow is introduced at the bottom and the gas and the solid phase exit the riser through the top edge of the simulated domain. Solids that leave the riser are fed back to the riser at a height of 0.6–0.7 m through a return channel. A schematic of the geometry is presented in Fig. 1. Most of the simulations in this work were carried out in a small geometry with a bed width of 0.4 m, but one fourth of the simulated fluidized beds were larger with widths ranging from 0.9 m to 6 m. A uniform gas inflow rate is applied in most simulations in CFB conditions while in the rest of the CFB simulations air flows in through nozzles, which are either described as separate openings located about 0.05 m from each other or by means of a function that defines the local gas velocity. At lower fluidization rates applied in BFB conditions air is in most simulations introduced through orifices placed about 0.05 m apart from each other to allow for more typical formation of bubbles.

In all the simulation cases a uniform mesh was used. Kallio et al. [10] observed that simulations with a mesh spacing of 12 mm gave nearly the same result for the correction coefficient for the time-averaged drag force as simulations in a finer mesh with 6 mm elements. Li et al. [12] showed that the required mesh resolution varies depending on the property that is studied. For some other properties a finer mesh could be necessary, but for the drag analysis a mesh spacing of 12 mm suffices. Thus to save computation effort, most of the runs presented in this work were carried out with 12-mm and 10-mm mesh resolutions. Kallio et al. [10] also concluded that the riser width, the solid

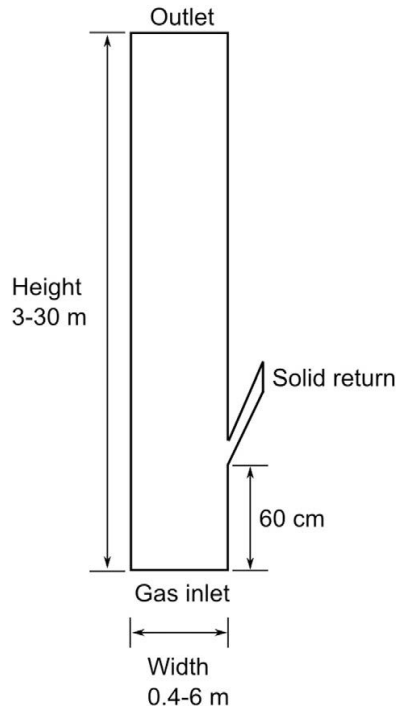

Fig. 1. Geometry in the transient simulations.

inventory and the fluidization velocity have no significant effects on the drag correction function in CFB conditions. However, in bubbling fluidized bed (BFB) conditions, the flow structure is very different and thus the fluidization velocity is likely to have an effect when the fluidization mode changes from BFB to CFB. The set of CFB simulations used in Kallio et al. [10] was therefore extended to cover a wider range of process conditions. The new set includes data also from turbulent fluidized bed (TFB) and bubbling fluidized bed conditions. Because of a wide particle size distribution and a reduced gas velocity at the bottom, the suspension density in the bottom region of an industrial CFB combustor is often relatively high, close to the densities found in turbulent and bubbling bed conditions. Thus a correlation for dense suspensions is required even when the correlation is applied on an industrial CFB process as the goal is to cover the whole riser section of the device.

Data from 69 simulations were included in the analysis. The analyzed cases are listed in Table 1. Although an even larger amount of data would be required in order to fully cover all the possible combinations of the values of the input variables, this data set was considered to be sufficient for the present study, whose aim is to verify the suitability of the proposed modeling approach. To derive a final correlation with higher accuracy, additional simulations in 3D and with a larger set of combinations of material property values should be included in the analysis.

The numerical simulations were carried out with the commercial code ANSYS Fluent v.14 [13] with the Eulerian–Eulerian multiphase approach based on the kinetic theory of granular flow (KTGF). In all the simulations, the solid phase is assumed to consist of monodispersed spherical particles. The multiphase flow equations along with the kinetic theory closure models are listed in Table 2. All the closure models used here are available in Fluent v.14.

The drag term was computed from the Gidaspow [9] drag model, which combines the Ergun [18] and Wen and Yu [8] drag laws. For the momentum equation, a second-order upwind convection scheme was

Table 1
Analyzed cases.

Case	Type	U_0 (m/s)	μ_g (kg/ms)	ρ_g (kg/m^3)	ρ_s (kg/m^3)	d_p (mm)	Δx_{mesh} (mm)	w (m)	h (m)	v_t (m/s)
1	u	2.5	4.45E-05	0.3105	2480	0.2555	12.5	0.4	3	1.53
2	f	3.14	1.79E−05	1.225	2480	0.385	6.25	0.4	3	2.85
3	f	3.5	1.79E−05	1.225	2480	0.385	6.25	0.4	3	2.85
4	u	3.5	1.79E−05	1.225	2480	0.385	6.25	0.4	3	2.85
5	u	3.5	1.79E−05	1.225	2480	0.385	12.5	0.4	3	2.85
6	u	3.5	1.79E−05	1.225	2000	0.385	12.5	0.4	3	2.47
7	u	3.5	1.79E−05	1.5925	2480	0.385	12.5	0.4	3	2.61
8	u	3.5	1.79E−05	1.225	2480	0.385	12.5	1	7	2.85
9	u	3.25	1.79E−05	1.225	2480	0.385	6.25	0.4	3	2.85
10	u	3.75	1.79E−05	1.225	2480	0.44	6.25	0.4	3	3.25
11	u	2.75	4.45E−05	0.3105	2480	0.2555	12.5	0.4	3	1.53
12	f	3.75	1.79E−05	1.225	2480	0.44	12.5	0.4	3	3.25
13	f	2.75	1.79E−05	1.225	2480	0.2555	3.125	0.4	3	1.87
14	f	2.75	4.32E−05	0.324	2480	0.2555	3.125	0.4	3	1.56
15	f	2.75	1.79E−05	1.225	2480	0.2555	3.125	0.4	3	1.87
16	u	2.75	4.45E−05	0.3105	2480	0.2555	12.5	1	7	1.53
17	u	2.75	4.45E−05	0.3105	2480	0.2555	12.5	3	14	1.53
18	u	2.75	4.45E−05	0.3105	2480	0.2555	12.5	3	14	1.53
19	u	2	4.45E−05	0.3105	2480	0.2555	12.5	3	14	1.53
20	u	5	4.45E−05	0.3105	2480	0.2555	12.5	3	14	1.53
21	u	5	4.45E−05	0.3105	2480	0.44	12.5	3	14	3.37
22	u	5	4.45E−05	0.3105	2480	0.15	12.5	3	14	0.615
23	u	5	3.83E−05	0.3986	2480	0.2555	12.5	3	14	1.64
24	u	8	4.45E−05	0.3105	2480	0.2555	12.5	3	14	1.53
25	u	8	4.45E−05	0.3105	2480	0.2555	12.5	3	14	1.53
26	u	8	4.45E−05	0.3105	2480	0.2555	12.5	6	30	1.53
27	o	0.8	1.79E−05	1.225	2480	0.656	5	0.9	2	4.69
28	u	3.5	1.79E−05	1.225	2480	0.001	12.5	0.4	3	6.76
29	u	3.5	1.79E−05	0.8575	2480	0.385	12.5	0.4	3	3.22
30	u	3.5	2.79E−05	1.225	2480	0.385	12.5	0.4	3	2.45
31	u	3.5	7.90E−06	1.225	2480	0.385	12.5	0.4	3	3.61
32	o	0.8	4.45E−05	0.3105	2480	0.656	5	0.9	2	5.5
33	o	0.8	1.79E−05	0.3105	2480	0.656	5	0.9	2	7.67
34	o	0.8	4.45E−05	1.225	2480	0.656	5	0.9	2	3.59
35	u	1.5	1.79E−05	1.225	2480	0.385	12.5	0.4	3	2.85
36	o	0.8	1.79E−05	1.225	2480	0.656	5	0.9	2	4.69
37	o	2.2	1.79E−05	1.225	2480	0.2555	10	0.4	3	1.86
38	o	3.3	1.79E−05	1.225	2480	0.44	10	0.4	3	3.25
39	o	1.8	1.79E−05	1.225	1800	0.2555	10	0.4	3	1.49
40	o	2.75	1.79E−05	1.225	1800	0.44	10	0.4	3	2.63
41	o	0.7	4.45E−05	1.225	2480	0.44	10	0.4	3	2.35
42	o	1.4	4.45E−05	1.225	1800	0.2555	10	0.4	3	0.93
43	o	2.2	4.45E−05	1.225	1800	0.44	10	0.4	3	1.87
44	o	1.8	4.45E−05	1.225	2480	0.2555	10	0.4	3	1.2
45	o	0.5	1.79E−05	1.225	2480	0.2555	10	0.4	3	1.86
46	o	1	1.79E−05	1.225	2480	0.44	10	0.4	3	3.25
47	o	0.6	1.79E−05	1.225	1800	0.2555	10	0.4	3	1.49
48	o	1	1.79E−05	1.225	1800	0.44	10	0.4	3	2.63
49	o	0.8	4.45E−05	1.225	2480	0.44	10	0.4	3	2.35
50	o	0.3	4.45E−05	1.225	1800	0.2555	10	0.4	3	0.931
51	o	0.6	4.45E−05	1.225	1800	0.44	10	0.4	3	1.87
52	o	0.3	4.45E−05	1.225	2480	0.2555	10	0.4	3	1.2
53	o	0.44	1.79E−05	1.225	2480	0.2555	10	0.4	3	1.86
54	o	0.44	1.79E−05	1.225	2480	0.2555	10	0.4	3	1.86
55	o	0.66	1.79E−05	1.225	2480	0.44	10	0.4	3	3.25
56	o	0.4	1.79E−05	1.225	1800	0.2555	10	0.4	3	1.49
57	o	0.3	4.45E−05	0.3105	2480	0.15	10	0.4	3	0.615
58	o	0.3	4.45E−05	0.3105	2480	0.2555	10	0.4	3	1.53
59	o	0.5	4.45E−05	0.3105	2480	0.2555	10	0.4	3	1.53
60	o	0.7	4.45E−05	0.3105	2480	0.2555	10	0.4	3	1.53
61	u	0.7	4.45E−05	0.3105	2480	0.2555	10	0.4	3	1.53
62	o	1	4.45E−05	0.3105	2480	0.2555	10	0.4	3	1.53
63	o	1.3	4.45E−05	0.3105	2480	0.2555	10	0.4	3	1.53
64	o	1.6	4.45E−05	0.3105	2480	0.2555	10	0.4	3	1.53
65	o	2	4.45E−05	0.3105	2480	0.2555	10	0.4	3	1.53
66	o	1.6	4.45E−05	0.3105	2480	0.44	10	0.4	3	3.37
67	o	0.7	4.45E−05	0.3105	1800	0.2555	10	0.4	3	1.15
68	o	1	4.45E−05	1.225	2480	0.2555	10	0.4	3	1.2
69	o	1.6	1.79E−05	0.3105	2480	0.2555	10	0.4	3	2.7

Parameters: gas superficial velocity U_0, gas viscosity μ_g, gas density ρ_g, solids density ρ_s, particle diameter d_p (monodisperse), mesh spacing Δx_{mesh}, riser width w, riser height h, and the terminal velocity of a particle v_t. In the table, 'u' denotes uniform gas inlet velocity, 'o' a distributor with separate nozzles, and 'f' a distributor where the effect of nozzles on the gas velocity profile is given by a function.

Table 2
The models and parameters used in the simulations.

Gas phase (continuity and momentum equations)

$$\frac{\partial}{\partial t}\left(\alpha_g\rho_g\right)+\nabla\cdot\left(\alpha_g\rho_g\boldsymbol{u}_g\right)=0$$

$$\frac{\partial}{\partial t}\left(\alpha_g\rho_g\boldsymbol{u}_g\right)+\nabla\cdot\left(\alpha_g\rho_g\boldsymbol{u}_g\boldsymbol{u}_g\right)=-\alpha_g\nabla p+\nabla\cdot\boldsymbol{\tau}_g+\alpha_g\rho_g\boldsymbol{g}+K_{gs}(\boldsymbol{u}_s-\boldsymbol{u}_g)$$

Solid phase (continuity and momentum equations)

$$\frac{\partial}{\partial t}(\alpha_s\rho_s)+\nabla\cdot(\alpha_s\rho_s\boldsymbol{u}_s)=0$$

$$\frac{\partial}{\partial t}(\alpha_s\rho_s\boldsymbol{u}_s)+\nabla\cdot(\alpha_s\rho_s\boldsymbol{u}_s\boldsymbol{u}_s)=-\alpha_s\nabla p-\nabla p_s+\nabla\cdot\boldsymbol{\tau}_s+\alpha_s\rho_s\boldsymbol{g}+K_{gs}(\boldsymbol{u}_g-\boldsymbol{u}_s)$$

Granular energy equation

$$\frac{3}{2}\left[\frac{\partial}{\partial t}(\alpha_s\rho_s\Theta_s)+\nabla\cdot(\alpha_s\rho_s\boldsymbol{u}_s\Theta_s)\right]=(-p_s\mathbf{I}+\boldsymbol{\tau}_s):\nabla\boldsymbol{u}_s+\nabla\cdot\left(k_{\Theta_s}\nabla\Theta_s\right)-\gamma_{\Theta_s}+\phi_{gs}$$

Diffusion coefficient for granular energy (Syamlal et al. [14])

$$k_{\Theta_s}=\frac{15d_p\rho_s\alpha_s\sqrt{\Theta_s\pi}}{4(41-33\eta)}\left[1+\frac{12}{5}\eta^2(4\eta-3)\alpha_s g_{0,ss}+\frac{16}{15\pi}(41-33\eta)\eta\alpha_s g_{0,ss}\right],\ \text{where}\ \eta=\frac{1}{2}(1+e_{ss})$$

Collisional dissipation of energy [15]

$$\gamma_{\Theta_s}=\frac{12(1+e_{ss}^2)g_{0,ss}}{d_s\sqrt{\pi}}\alpha_s^2\rho_s\Theta_s^{3/2}$$

Energy exchange between the gas and solid phase [15]

$$\phi_{gs}=-3K_{gs}\Theta_s$$

Phase stress–strain tensors

$$\tau_g=\alpha_g\mu_g\left(\nabla\boldsymbol{u}_g+\nabla\boldsymbol{u}_g^T\right)-\frac{2}{3}\alpha_g\mu_g\left(\nabla\cdot\boldsymbol{u}_g\right)\mathbf{I}$$

$$\tau_s=\alpha_s\mu_s\left(\nabla\boldsymbol{u}_s+\nabla\boldsymbol{u}_s^T\right)+\alpha_q\left(\lambda_s-\frac{2}{3}\mu_s\right)(\nabla\cdot\boldsymbol{u}_s)\mathbf{I}$$

Solid shear viscosity $\mu_s=\mu_{s,col}+\mu_{s_{kin}}+\mu_{s,fr}$ [14,16]

$$\mu_s=\frac{4}{5}\alpha_s\rho_s d_s g_{0,ss}(1+e_{ss})\left(\frac{\Theta_s}{\pi}\right)^{\frac{1}{2}}+\frac{\alpha_s\rho_s d_s\sqrt{\Theta_s\pi}}{6(3-e_{ss})}\left[1+\frac{2}{5}(1+e_{ss})(3-e_{ss}-1)\alpha_s g_{0,ss}\right]+\frac{p_s\sin\phi}{2\sqrt{I_{2D}}}$$

Granular bulk viscosity [15]

$$\lambda_S=\frac{4}{3}\alpha_S\rho_S d_s g_{0,ss}(1+e_{ss})\left(\frac{\Theta_s}{\pi}\right)^{1/2}$$

Solids pressure [15]

$$p_s=\alpha_s\rho_s\Theta_s+2\rho_s(1+e_{ss})\alpha_s^2 g_{0,ss}\Theta_s$$

Radial distribution function [17]

$$g_{0,ss}=\left[1-\left(\frac{\alpha_s}{\alpha_{s,\max}}\right)^{\frac{1}{3}}\right]^{-1}$$

Drag model [9], based on Ergun [18] and Wen and Yu [8])

When $\alpha_g > 0.8$:

$$K_{gs}=\frac{3}{4}C_d\frac{\alpha_g\alpha_s\rho_g\left|\boldsymbol{u}_g-\boldsymbol{u}_s\right|}{d_s}a_g^{-2.65}$$

$$C_d=\begin{cases}\frac{24}{Re}\left[1+0.15(\mathrm{Re})^{0.687}\right], Re<1000\\ 0.44, Re\geq 1000\end{cases}$$

$$Re=\frac{\alpha_g\rho_g\left|\boldsymbol{u}_g-\boldsymbol{u}_s\right|d_s}{\mu_g}$$

When $\alpha_g \leq 0.8$:

$$K_{gs}=150\frac{\alpha_s(1-\alpha_g)\mu_g}{\alpha_g d_s^2}+1.75\frac{\rho_g\alpha_s\left|\boldsymbol{u}_g-\boldsymbol{u}_s\right|}{d_s}$$

used and for the volume fraction equation the convection scheme was QUICK. For the pressure–velocity coupling the phase coupled SIMPLE was used. The time step in the first order implicit time-stepping procedure was 0.001 s for the 10 mm and coarser meshes and 0.0005 s for the 6.25 mm and finer meshes. Comparisons [19] with measurements of solids volume fraction profiles, determined from the local gray scale values in video images, have been previously carried out for some of the simulations of a 0.4-m-wide pseudo-2D CFB. The measurement and simulation results were in good qualitative agreement and even quantitatively the results were reasonably good considering that the simulations were carried out in 2D. Thus the chosen transient simulation approach can be considered sufficiently accurate to produce qualitatively representative data for evaluation of the new modeling strategy for filtered gas–solid drag force.

For each case, approximately 5 s was simulated before initialization of the time averaging and at least a further 120 s of flow time was simulated to compute the averages, which is sufficient to guarantee a satisfactory convergence of the time-averaged properties in most of the flow regions. Typical bubbling frequencies in BFBs are of the order of 1–10 Hz [20] and similar fluctuation frequencies are also common in CFBs. Also on this basis the 120-s averaging time can be considered adequate. However, for the very dilute parts of the BFB freeboard region, where bursts of particles only occasionally occur, the averaging period is not sufficient, a limitation that has to be taken into account in the analysis of the simulation results.

3. Analysis and pre-processing of the transient simulation results

3.1. Time averaging

Results from each transient simulation were time-averaged to determine the average flow properties and the average drag force in each computational cell. As in the previous study [10], the analysis was carried out for the dominating, vertical component of the drag force. A closure for the time-averaged drag force can be written in the form

$$\overline{K_{gs}\left(u_{g,y}-u_{s,y}\right)}=C_{drag}K_{gs}^{*}\left(U_{g,y}-U_{s,y}\right) \tag{1}$$

where $u_{g,y}$ and $u_{s,y}$ are the instantaneous gas and solid phase vertical velocity components and $U_{g,y}$ and $U_{s,y}$ the corresponding mass-weighted time-averaged (Favre averaged) velocity components. The coefficient C_{drag} in Eq. (1) is a drag correction coefficient, for which a correlation is to be developed. K_{gs}^{*} is the inter-phase momentum transfer coefficient calculated on the basis of the time-averaged velocities and volume fractions using a combination of Wen and Yu [8] and Ergun [18] drag laws. However, instead of using the combination approach of Gidaspow's [9] drag law a smoother transition between the drag laws, suggested by Niemi et al. [21], was used to calculate K_{gs}^{*}. In this model a linear transformation between the Ergun and Wen–Yu models occurs in a solid volume fraction range of 0.4–0.5, which is within the region recommended by Leboreiro et al. [22].

The value of C_{drag} in each point in the flow field can be calculated from Eq. (1) by time averaging the drag force, the solid volume fraction and the gas and solid velocities over the simulation time of a transient simulation. This kind of data was collected for each of the simulations. A filtering process was carried out on the data collection stage. For very low values of the slip velocity, the computed C_{drag} can become unreasonably large due to the stochastic nature of the data and the finite averaging periods. A maximum limit for C_{drag} was set to 5. Above this level the data were chaotic and the number of observations was small. All negative values were rejected for the same reasons. The data of the solid return channel were also omitted from the analysis since the flow structure in this region significantly deviates from the typical conditions of interest.

3.2. Effects of the fluidization velocity

In the previous study by Kallio et al. [10], only results from CFB simulations were analyzed and it was concluded that fluidization velocity has only a minor effect on C_{drag}. However, when the fluidization velocity significantly reduces from the typical CFB values, the flow pattern drastically changes and instead of being characterized by clusters and strands surrounded by dilute suspension, the flow shows voids and bubbles inside a dense suspension. This change in flow conditions is illustrated in Figs. 2 and 3 for simulations with superficial gas velocity ranging from 0.3 to 2 m/s. The change in flow pattern is expected to have a large effect on the average drag force and on C_{drag}.

The C_{drag} values calculated in all the mesh points (excluding the return channel) are displayed as a function of the local average solid volume fraction in Fig. 4. A gradual change in the pattern can be observed when the fluidization state gradually changes from BFB conditions (cases with $U_0 \leq 0.5$ m/s) to typical CFB riser flow (cases with $U_0 \geq 1.6$ m/s). At high solid concentrations in bubbling bed conditions C_{drag} appears to be independent of the average solid volume fraction α_s. Since the highest α_s values typically occur close to walls and in corners, this behavior can be attributed to wall effects. At approximately $\alpha_s = 0.2 - 0.3$, i.e. typical values inside a bubbling bed, a similar poor coupling between C_{drag} and α_s can be observed. Starting from $\alpha_s = 0.05$, a value corresponding to the zone near bed surface (Fig. 3), C_{drag} first exceeds one and, as α_s decreases, C_{drag} decreases to very low values as α_s approaches 10^{-5}. As α_s is further reduced in the freeboard to

values close to 0 C_{drag} again increases. A large scatter in C_{drag} is visible in the freeboard region at the dilute end of the scale. These very low α_s values represent regions into which only a very limited number of bursts of particles have risen during the 120-s averaging period and consequently the averages are not representative. At high fluidization velocities in CFB conditions C_{drag} shows a clear dependency on α_s, except in the dense end of the scale, which corresponds to the acceleration zone in the bottom bed [10]. At higher superficial velocities, the α_s range in which C_{drag} is almost constant is wider.

Fig. 5 analyses the data from the simulation 65 with the aim to identify the regions from which the different C_{drag} patterns in CFB conditions originate. First, the bottom region up to a height of 0.1 m is removed from the depicted data points. This elimination of data reduces the scattering of C_{drag} at higher α_s values. Next, the regions with a wall distance below selected thresholds (0.01, 0.02 and 0.05 m, respectively) are removed. From the results it can be concluded that the major part of the scattering in the data originates from the wall layer. In particular the values in the grid cells adjacent to the walls show a distinct pattern that completely deviates from the rest of the data.

A similar analysis was carried out in BFB conditions for the simulation 59 whose results are shown in Fig. 6. Removal of the data from the lowermost part below a height of 0.1 m reduces the scatter in the dense end of α_s scale. The large scatter in the dilute end vanishes when data above 0.9 m, corresponding to the freeboard region, is removed. The analysis shown in Fig. 6 demonstrates that low C_{drag} values are found in the regions adjacent to the wall, which are intimately different from the rest of the flow domain.

3.3. Pre-processing of the data

The complexity of the behavior of C_{drag} as a function of solid volume fraction is evident in Fig. 4. In particular, the pattern in the region adjacent to the wall is completely different from that of the rest of the flow domain. Thus a need for a separate correlation for the wall region was indicated. To simplify the modeling task the region up to 2–5 cm from the wall (depending on the case) was omitted from further analysis. Similarly, in the bottom region, scatter in the data increases as we move toward the air distributor and thus the region from the bottom up to 0.1 m was excluded. In BFB simulations, the scatter in the data in dilute conditions is a result of the inadequate averaging period in the freeboard region. Thus freeboard data were also omitted. Since the location of the bed surface varies from case to case, this removal threshold was separately set for each case. As an example, Fig. 7 shows the cleaned data used for modeling in Cases 59, corresponding to typical BFB conditions, and 65, corresponding to typical CFB conditions. Compared to the original data shown in Fig. 6, the scatter in the data has significantly reduced.

3.4. Effect of the air distributor

In some of the simulations, the gas flow entered uniformly through the bottom edge of the computational domain while in others, especially at lower gas velocities, gas was introduced through discrete nozzles separated by 0.05-m space intervals. In CFB conditions, our previous experiences have shown that the type of the gas-flow inlet boundary condition at the bottom plays only a very limited local role. This was also confirmed in the present study by comparing results from Cases 2 and 3 of Table 1 which differ only in the way air enters the bed at riser bottom. In bubbling beds, average bubble size as a function of height is commonly expressed in terms of the initial bubble size, which in turn depends on the nozzle diameter [20]. Thus in BFB conditions, the air distributor design can have a major effect on suspension behavior and hence also on C_{drag}. Fig. 8 illustrates this effect by comparing the C_{drag} values determined from simulations 60 (with orifices) and 61 (uniform gas velocity). Uniform air velocity at the bottom leads to C_{drag} values closer to unity in the solid concentration range corresponding to the center of the bed, which suggests more uniform flow conditions when no orifices are used. The effect of the air distributor design is thus clear, implying that in the bubbling bed region the drag correction function should take into account the effect of the air distributor design. In the present study, most of the BFB data have been obtained with the aforementioned air distributor. In industrial BFBs and CFBs air distributor designs differ from the present simple one. This represents a possible source of inaccuracy, if a drag law based on the results of the present work would be applied in such industrial applications.

3.5. Parametric effects

In Kallio et al. [10] effects of material properties on C_{drag} in CFB conditions were analyzed. Particle size was found to have an increasing effect on C_{drag} while gas viscosity had a reducing effect. The effect of solid density was clear but less straightforward. In BFB conditions, a change in

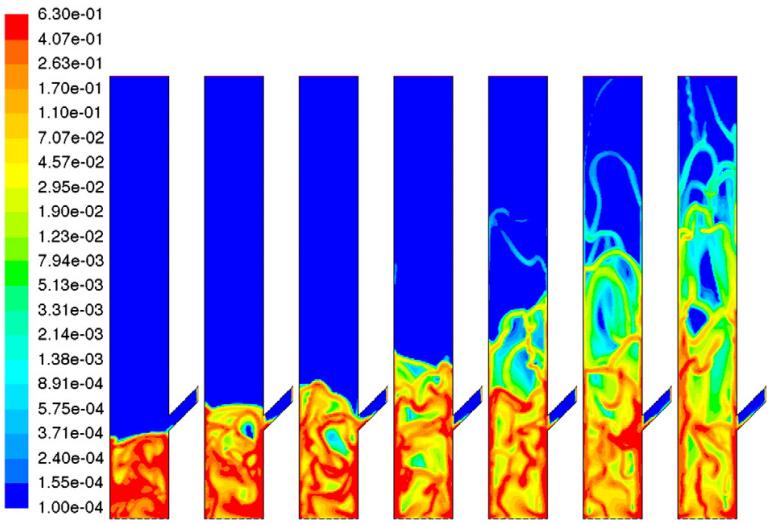

Fig. 2. Instantaneous solid volume fraction fields in simulations (from the left) 58, 59, 60, 62, 63, 64 and 65 at fluidization velocities 0.3, 0.5, 0.7, 1, 1.3, 1.6 and 2 m/s, respectively.

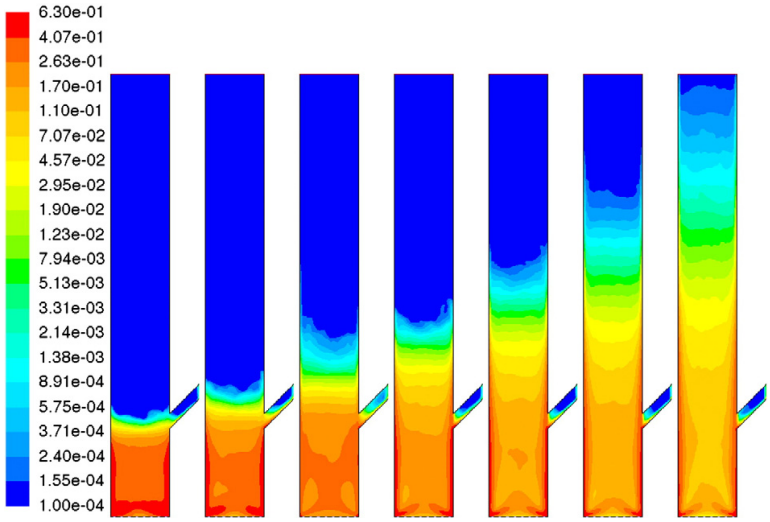

Fig. 3. Time-averaged solid volume fraction fields in simulations (from the left) 58, 59, 60, 62, 63, 64 and 65 at fluidization velocities 0.3, 0.5, 0.7, 1, 1.3, 1.6 and 2 m/s, respectively.

material properties leads to a change in bubble size and gas and solid velocities. Even in CFB conditions material properties affect the flow pattern, e.g. cluster properties, but not to the same extent as in a BFB. The low gas velocity in BFB and TFB conditions makes the processes more sensitive to the changes in material properties, since a change in the fluidization mode between BFB and TFB conditions can take place. Thus it is not equally easy to evaluate the effects of material properties at low gas velocities. Fig. 9a illustrates the effect of gas viscosity (Cases 34 and 36 in Table 1). The observed effect is negative, i.e. an increase in the viscosity leads to a lower C_{drag}. In Fig. 9b (Cases 52 and 58) the effect of gas density is shown to be small. A similar result was obtained in CFB conditions [10] and it was concluded that gas density can be omitted from the set of input parameters of a drag correction function. Fig. 10a (Cases 46 and 48) shows a positive effect of solids density while the opposite trend is observed in Fig. 10b (Cases 60 and 67). Thus solid density does not seem to have a simple independent effect on the results. Fig. 10c shows a positive effect of the particle size. The effects of the particle size and gas viscosity were evaluated only in a one case, i.e. with a single set of other operational conditions. A larger number of comparisons should be carried out to confirm whether the effects of particle size and gas viscosity are independent or affected by other flow parameters.

4. Empirical modeling

4.1. Data sampling

Since each computational cell produces one observation in the data set, the amount of data collected from each of the simulations is unnecessarily large for model development. Even after clean-up of the data and

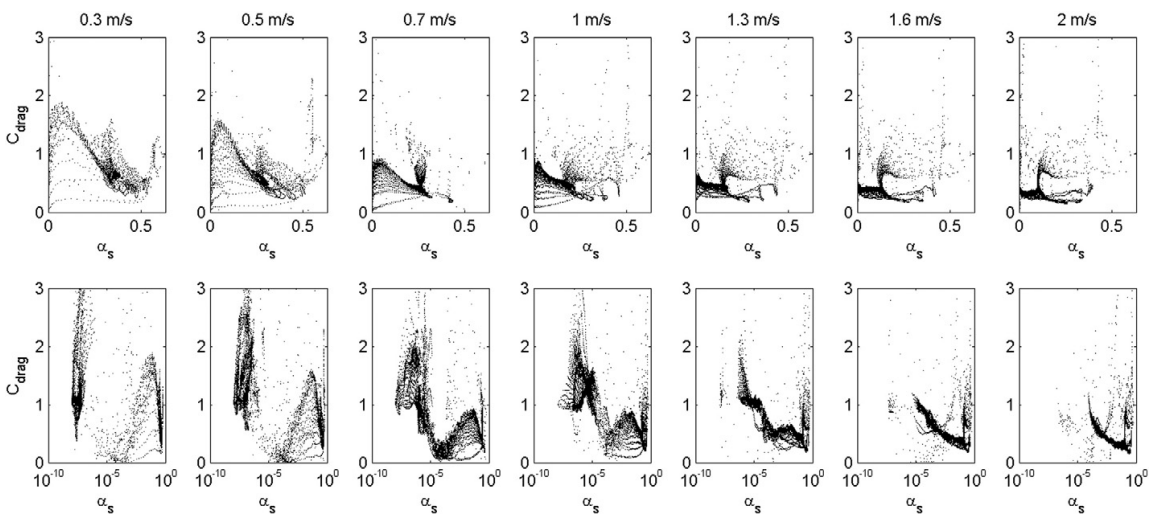

Fig. 4. Drag correction coefficient C_{drag} as a function of the solid volume fraction α_s in linear (top) and logarithmic (bottom) scales in simulations (from the left) 58, 59, 60, 62, 63, 64 and 65 at fluidization velocities 0.3, 0.5, 0.7, 1, 1.3, 1.6 and 2 m/s, respectively.

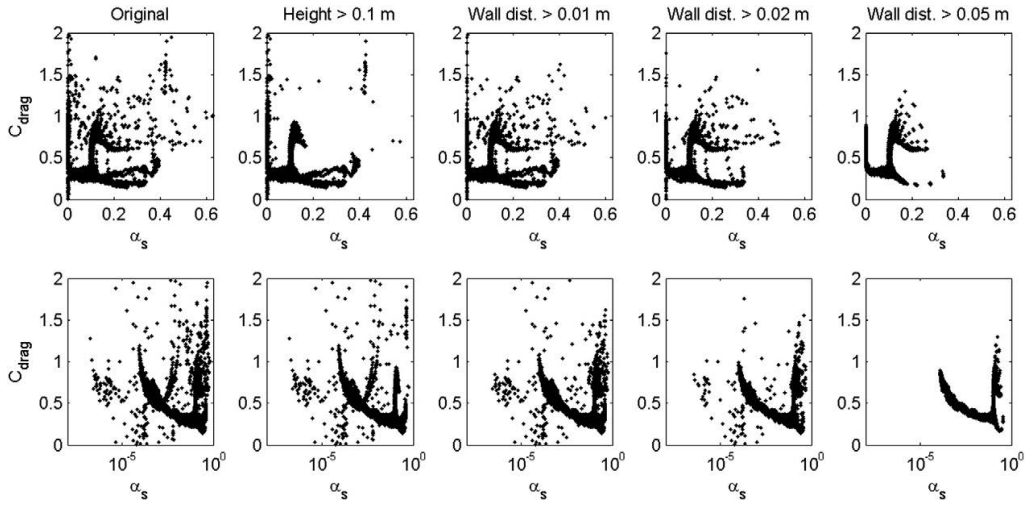

Fig. 5. Analysis of regional effects on C_{drag} in CFB conditions in Case 65 in linear (top) and logarithmic (bottom) scales. The leftmost image shows the original data and in the other images, different regions are removed from the plots. From left to right, the removed regions are: the bottom section up to 0.1 m, the wall region up to 1 cm from the wall, the wall region up to 2 cm from the wall, and the wall region up to 5 cm from the wall.

removal of data from entrance, exit and wall regions (see Section 3.2), thousands to tens of thousands of data points were collected from each of the 69 simulations. In order to reduce the amount of data to a more manageable quantity without losing relevant information, data used for modeling were randomly picked from each of the simulations. Since most of the points come from the central region of the riser, randomly picking from the entire region would mainly collect data from the central regions. In order to avoid such pre-conditioning, the simulation domain was divided into bottom, side and central regions, from which data were successively picked. A relatively larger amount of data was sampled from the dense regions at bed bottom and closer to walls, since in those zones the behavior of C_{drag} is more complex. Fig. 11 shows the picked points for Cases 59 and 65. Finally about 5000 points were included in the data set used for the empirical modeling. The full data set was used only for testing the derived correlations.

4.2. Model structure and the parameter estimation procedure

To allow the developed correlation to freely adjust to the input data, a model structure based on a combination of a number of logistic sigmoid functions was used in this work for nonlinear regression. This model structure is commonly used in neural network modeling [23]. The model can be written as

$$C_{\mathrm{drag,pred.}} = b_0 + \sum_{i=1}^{N_\sigma} b_i\, \sigma(z_i) \tag{2}$$

$$z_i = a_0 + \sum_{i=1}^{N_{\mathrm{in}}} a_i\, x_i \tag{3}$$

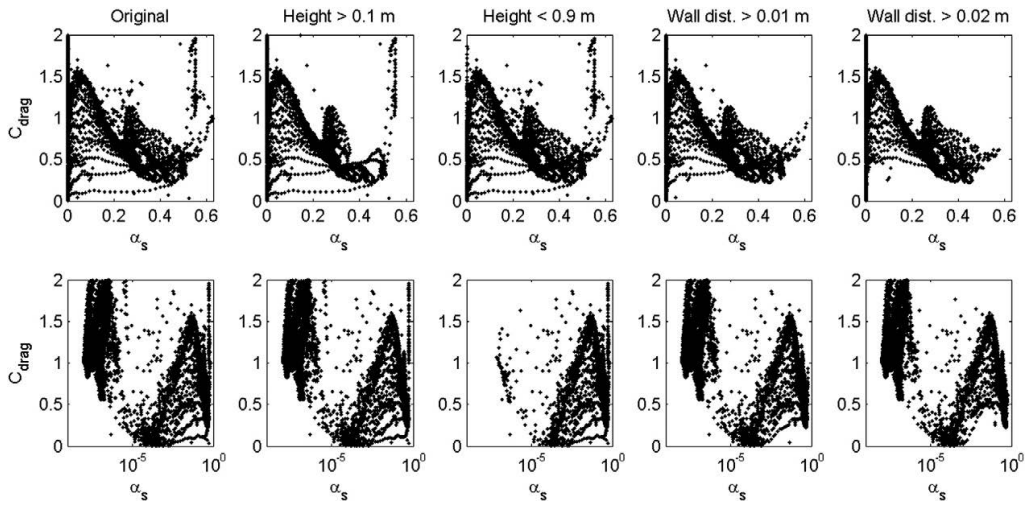

Fig. 6. Analysis of regional effects in BFB conditions in Case 59 in linear (top) and logarithmic (bottom) scales. The leftmost images show the original data and in the rest, different regions are removed from the data set. From left to right, the removed regions are: the bottom section up to 0.1 m, the freeboard region above 0.9 m, the wall region up to 1 cm from the wall, and the wall region up to 2 cm from the wall.

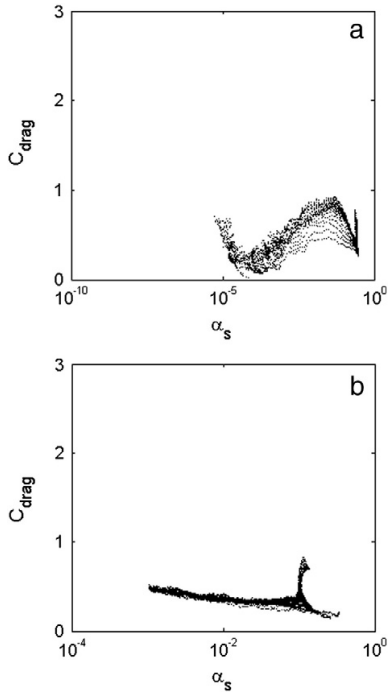

Fig. 7. Cleaned data (a) in Case 59 (BFB conditions) and (b) in Case 65 (CFB conditions).

where a_i and b_i denote model parameters and x_i the N_{in} input variables. The logistic sigmoid function that produces values between 0 and 1 is given by

$$\sigma(z_i) = \frac{1}{1+e^{-z_i}} \tag{4}$$

The input variables considered in this work were the material properties, the solid volume fraction, gas and solid velocities, the slip velocity, the distance from the wall and the elevation, which are readily available in a simulation. Instead of solid volume fraction, the logarithm

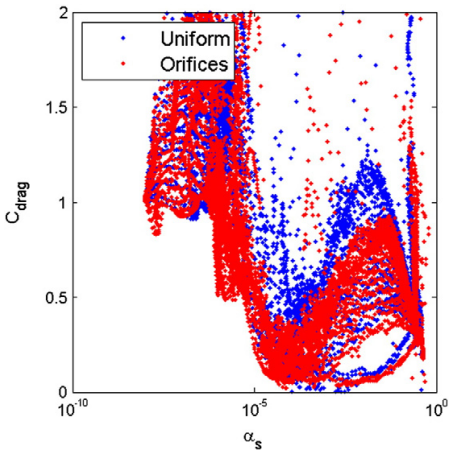

Fig. 8. Comparison of drag correction coefficient values in BFB conditions in Cases 60 (air enters through separate orifices) and 61 (a uniform gas inflow velocity at the bottom).

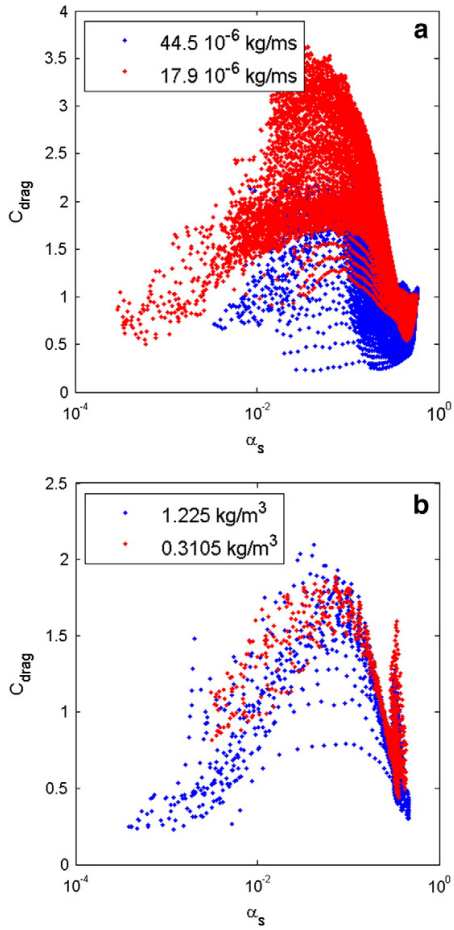

Fig. 9. Effects of (a) changed viscosity (Cases 34 and 36), and (b) changed gas density (Cases 52 and 58) in BFB conditions. From the original data set exit, entrance and wall region data have been excluded.

of solid volume fraction was used as an input parameter which makes it easier to express the steep gradients at low solid concentrations, shown in Fig. 10, with sigmoid functions.

The model parameters (a_i, b_i) were determined by minimizing the prediction error E

$$E = \sum_{k}^{N_{obs}} \left(C_{drag,obs} - C_{drag,pred} \right)^2 \tag{5}$$

Parameter search was done with the Levenberg–Marquardt [24] method. The data used as the basis for modeling were quite limited and not of optimal quality, since only very few combinations of material properties were included. Thus special attention was paid to the robustness of the correlation. The correlation should not produce excessively large or small values in the points that were excluded from the data set used for parameter estimation. Thus some interpolation capabilities were desired. Some of the parameters (a_i, b_i) were fixed to zero to reduce the complexity of the correlation and to improve its robustness. With a larger number of sigmoids and model parameters, prediction accuracy could improve for the actual data set but the correlation's ability to produce reasonable values would deteriorate in conditions that were

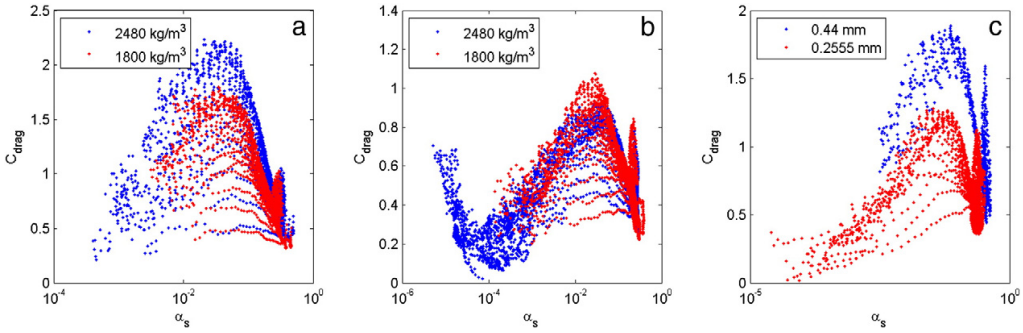

Fig. 10. Effects of changed solid density (a) in Cases 46 and 48 and (b) in Cases 60 and 67). (c) Effects of a changed particle size (Cases 57 and 58) in BFB conditions. From the original data set exit, entrance and wall region data have been excluded.

not included in the simulations carried out so far. Thus demands for robustness and accuracy need to be weighed against each other during the modeling process.

4.3. Modeling of the change from CFB to BFB conditions

As an initial test, data from 18 simulation cases with the same material properties (air at 850 ºC, solid density 2480 kg/m^3 particle size 0.255 mm) were chosen for modeling. The purpose of the test was to find the necessary parameters for describing the effect of the fluidization state. According to the initial parameter list of Kallio et al. [10], solid volume fraction, wall distance and slip velocity should suffice for the task when material properties are constant. However, a first trial made with these three input parameters did not produce a satisfactory correlation. We then introduced the height above the air distributor as the fourth variable, as the bubble size and velocity for bubbling beds are commonly expressed as a function of the height (e.g. Kunii and Levenspiel [20]). Fig. 12 shows the predicted and observed behavior in Cases 11, 16, 19, 59, 61, and 63 with the best correlation that was found based on the four input parameters. The number of parameters in the correlation was 25 and about 700 observations in the data set were picked from the 18 simulations used as the basis for modeling. The correlation was developed based on the cleaned data set (with no wall, bottom and freeboard data) but the comparisons between the observed and predicted C_{drag} values in Fig. 12 are shown for the complete data sets to evaluate the correlation's robustness and ability to extrapolate. One measure of the goodness of the fit between observed and predicted values is the correlation coefficient R (defined as the covariance of the two variables divided by the product of their standard deviations). The correlation coefficients for these cases are 0.74, 0.92, 0.94, 0.57, 0.82, and 0.69, respectively, calculated on the basis of the original data set covering the entire riser region. In BFB (Cases 59 and 61 in Fig. 12) and CFB (Cases 11, 16, and 19 in Fig. 12) conditions the fit is generally satisfactory but near the BFB surface and freeboard as well as in turbulent bed conditions a larger error is seen. The correlation has difficulties to describe the low values of C_{drag} on the surface of a bubbling bed. At similar low volume fractions in CFB conditions C_{drag} is close to unity while on the BFB surface C_{drag} approaches zero. None of the input variables seems to be able to describe the difference in the flow behavior. Despite of this setback the modeling approach can be considered successful as it produces good results in a wide range of fluidized bed conditions.

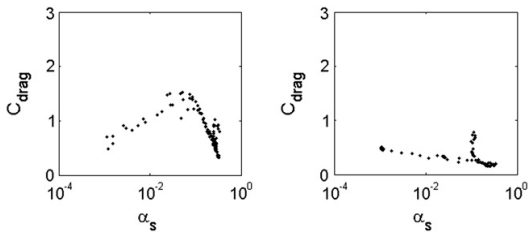

Fig. 11. Data points sampled from Cases 59 (BFB, left) and 65 (CFB, right).

Other correlations with alternative sets of input variables and a larger number of model parameters were tried but the results were not as good. Addition of complexity to the correlation showed slight improvement in the agreement between predicted and observed values but not enough to justify the increased number of model parameters, which in turn could result in a reduced robustness of the correlation.

4.4. Modeling with material properties as additional input variables

To account for changes in material properties, the data from all the 69 simulation were included for the development of the correlation. As a first tentative step, seven input variables were used, i.e. solid volume fraction, wall distance, elevation, slip velocity, gas viscosity, solids material density and particle size. All the correlations developed with these inputs encountered difficulties in reproducing C_{drag} in BFB conditions and often produced clearly false maximum C_{drag} in the bed region. The correlation between observed and predicted C_{drag} was poor ($R < 0.7$). No results obtained with this set of input parameters are shown in the present paper. We then added an eighth input variable, the local gas velocity, and the correlation improved significantly. Several different configurations of the model structure given by Eqs. (2)–(4) were tried with different numbers of sigmoids and parameters. The best developed correlation that was reasonably accurate and at the same time sufficiently robust had 71 parameters. Fig. 13 shows the observed versus predicted C_{drag} for all the points in the data set used for model development (the correlation coefficient between observed and predicted values was 0.96). The number of parameters in the model is large but not unreasonable considering that the correlation attempts to describe the effects of eight input variables, including their combined contributions. The number of observations (5000) in the data set used in the parameter estimation process is two orders of magnitude larger than the number of parameters. Thus the amount of data can be considered sufficient. However, the robustness of the correlation should still be checked by testing its behavior in conditions that were not included in those 5000 observations.

Fig. 14 compares the observed and predicted values in six different simulation cases. For qualitative assessment of the robustness of the correlation, the observations and predictions are shown for the full original data set (however, without data for the solids return duct). Fig. 14a, b, and c are for the same simulation cases (Cases 19, 59 and 63 in Table 1) as shown in Fig. 12. The predictions have deteriorated from what was obtained in Fig. 12 since the new parameters are no more optimized for the specific material property values. Correlation coefficients

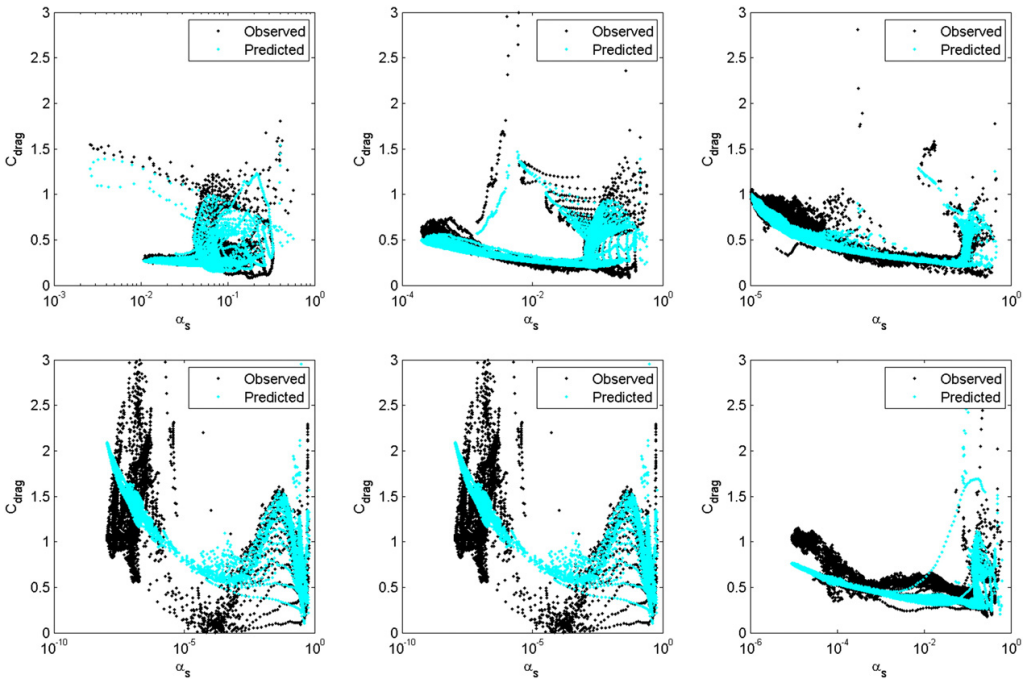

Fig. 12. The predicted and observed behavior in Cases 11 (top, left), 16, 19, 59 (bottom, left), 61, and 63 with the best found correlation based on four input parameters, i.e. the solid volume fraction, the slip velocity, the wall distance and the elevation.

calculated on the basis of the full original data sets were 0.81, 0.10, and 0.60, respectively, which all are lower than the corresponding values 0.94, 0.57, 0.69 obtained with the correlation developed in Section 4.3. Fig. 14d, e and f (Cases 6, 29 and 53 in Table 1) is for other material property values and shows a similar fit to the observed data with correlation coefficients 0.82, 0.76, and 0.02, respectively. For the BFB Cases 59 and 53, the correlation coefficients calculated on the basis of the full original data sets are very low. If the large amount of data from the dilute freeboard region ($\alpha_s < 10^{-5}$) is omitted, the correlation coefficients become 0.6728 (Case 59) and 0.87 (Case 53).

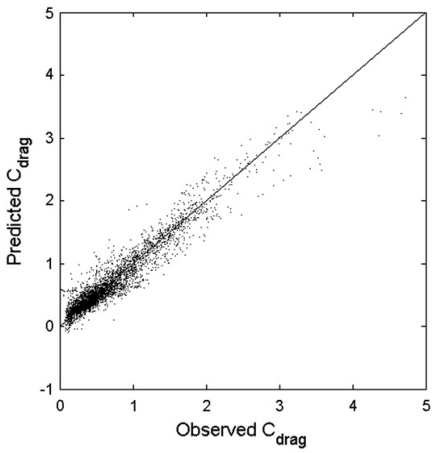

Fig. 13. The observed versus predicted C_{drag} for all the instances in the data set used for model development.

4.5. Separate correlation for the dilute CFB conditions

The correlation developed on the basis of the full range of data, discussed in the previous section, proved to be far from an optimal fit at low solids concentrations. This is probably due to the difficulties related to trying to model both BFB and CFB conditions with the same correlation. In a simulation of a CFB, dilute suspension conditions prevail in the major part of the flow domain. Thus a big error in the drag force at low values of α_s can lead to serious errors in the predicted solids velocities and concentrations in a major part of the riser. To remedy this problem, a separate correlation was developed on the basis of data collected from CFB riser simulations in regions above 1.5-m height. The set of input variables could in this case be simplified by omitting gas velocity and the elevation. Thus the correlation for the limited dilute region is based on material properties (gas viscosity, solids density, particle size), solids volume fraction, slip velocity and wall distance. Again a number of correlation structures were tried and finally a correlation with acceptable accuracy and robustness was selected. The final correlation has only 14 parameters.

Fig. 15 shows the observed versus the predicted C_{drag} for all the instances in the data set used for development of the correlation (the correlation coefficient between observed and predicted values is 0.96). As expected the predictions have significantly improved in the dilute range from what was obtained in Fig. 14, since no compromise was necessary between dilute conditions in a CFB and in the freeboard region of a BFB. In Fig. 14, this compromise led to systematically too low C_{drag} values in the dilute regions of a CFB while no such systematic error can be seen in Fig. 15. As it is, the correlation is not generally usable since it behaves poorly in dense conditions unless it is combined with a correlation that works better in the dense bottom region. Fig. 16 shows results obtained with a correlation that, by means of linear and bilinear blending functions, combines the new correlation for dilute conditions in the upper parts of a CFB with the previous correlation of

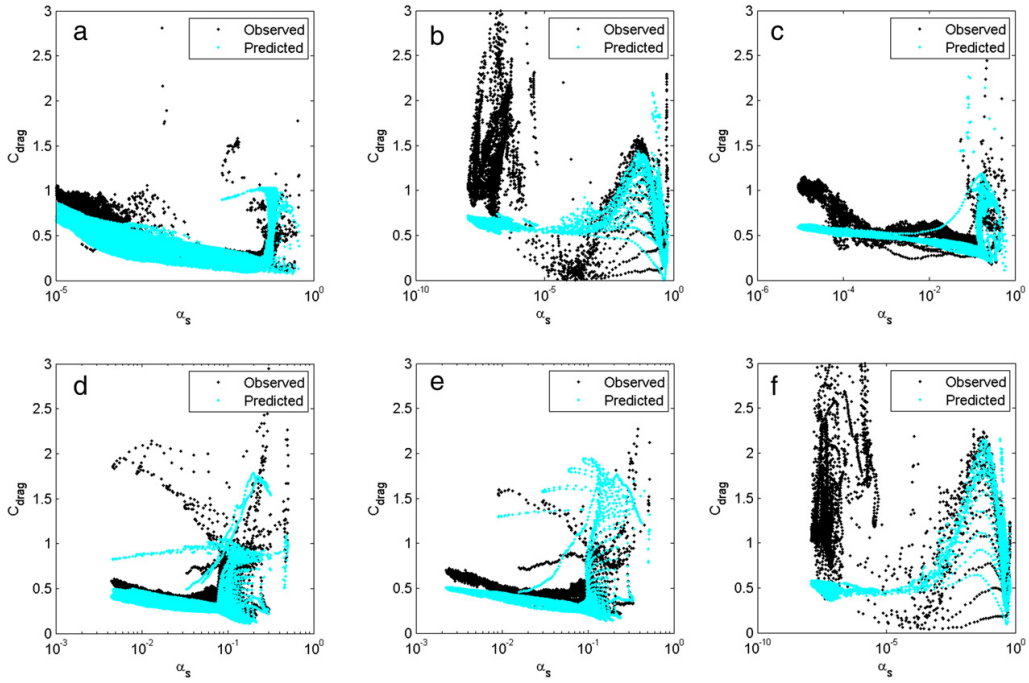

Fig. 14. The predicted and observed behavior in Cases 19 (a), 59 (b), 63 (c), 6 (d), 29 (e) and 53 (f) with the best found correlation based on eight input variables (the solid volume fraction, the slip velocity, the gas velocity, the solid density, the gas viscosity, the particle size, the elevation and the distance from the wall).

Section 4.4, which now is used only for the bottom bed and dense conditions. The two parameters that govern the switch from one correlation to the other and determine the value of the blending functions are the solid volume fraction and elevation. The blending functions are shown in Table 3.

The results shown in Fig. 16 for Cases 19, 59, 63, 6, 29 and 53 (same as in Fig. 14) are in general qualitatively correct. The correlation coefficients calculated on the basis of the full original data sets are 0.94, 0.37 (0.67 for data in the range $\alpha_s > 10^{-5}$), 0.83, 0.81, 0.77, and 0.09 (0.87 for $\alpha_s > 10^{-5}$), respectively, showing clear improvement compared to the results in Section 4.4. The values at the surface of a BFB (Fig. 16b and f) are still poorly predicted and in the dense end of the scale, large discrepancies between observed and predicted values occur in CFB conditions (Fig. 16a, d and e). However, the less well-reproduced values occur in the regions that were excluded from the data set used as basis for modeling. Thus deviations from observed values were expected. Since no order-of-magnitude errors occur in these regions, the correlation appears to be reasonably robust.

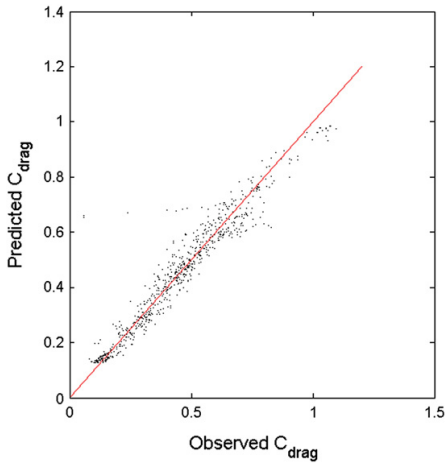

Fig. 15. Predicted versus observed C_{drag} for all the instances in the data set for dilute CFB conditions used for model development.

To illustrate the correlation's sensitivity to the changes in material properties, the observed and predicted C_{drag} values are depicted in Fig. 17 for two BFB cases with different particle sizes and in Fig. 18 for two CFB cases with different solid densities. The trends of the parametric effects are predicted correctly in Figs. 17 and 18.

4.6. Testing of the correlation

Although special attention was paid to the robustness of the derived correlations, it is useful also to compare the predicted results with observations in conditions that were not included in the data set used for derivation of the parameters. One additional case was simulated in CFB and one in BFB conditions in the 0.4 m wide geometry of Fig. 1 to test the performance of the correlation presented in Section 4.5. In both cases the material properties were as follows: particle size 0.3 mm, solids material density 2200 kg/m^3, gas density 1 kg/m^3, and solids viscosity $2.2 \cdot 10^{-5}$ kg/ms. Fluidization velocities were 3 m/s and 0.4 m/s, respectively. Since the material properties and the fluid-dynamic conditions of the two test cases fall in the middle of the range of conditions in the simulations used for the estimation of the parameters, these two simulations represent a test of the interpolation capabilities of the correlations.

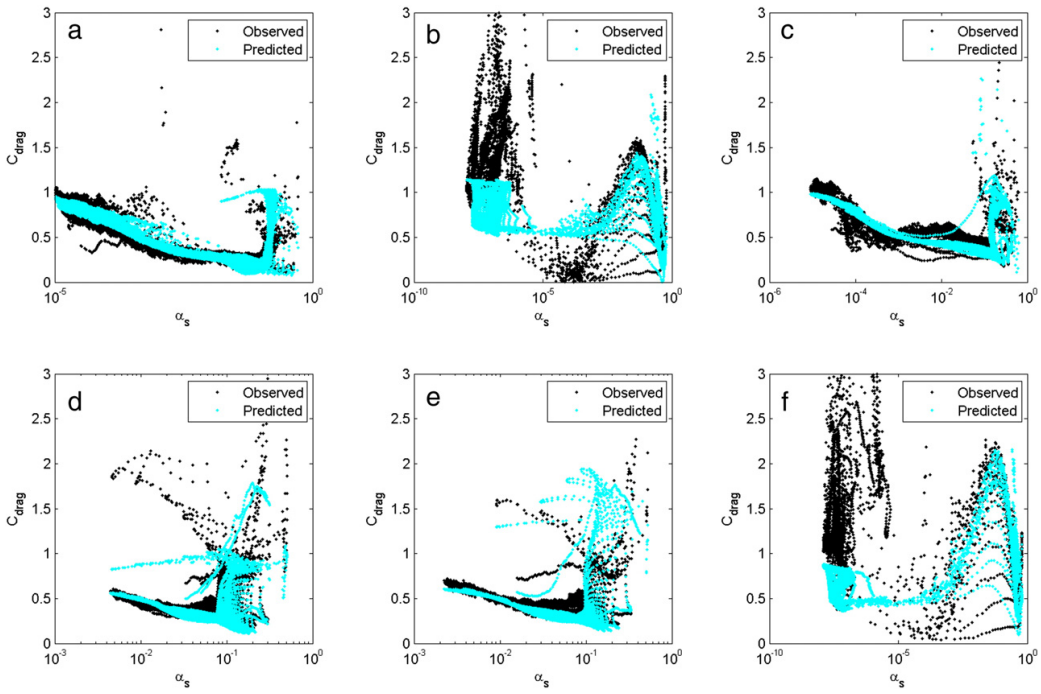

Fig. 16. Results obtained with a model that by means of blending functions combines the correlation for dilute CFB conditions with the general model, which is used for the bottom bed and dense conditions. Cases 19 (a), 59 (b), 63 (c), 6 (d), 29 (e) and 53 (f).

Fig. 19 shows a comparison between the observed and predicted C_{drag} values. Data corresponding to the air distributor region (height below 0.1 m), walls (distance from the wall less than 0.02 m), exit region (distance to the exit less than 0.5 m) and the return channel were omitted from the comparison. The freeboard region in the BFB case was also removed from the figure. The results show a good match between the observed and the predicted values, at least qualitatively. Also quantitatively the results are satisfactory, with $R = 0.84$ for the CFB case and $R = 0.96$ for the BFB case, respectively, calculated for the data points shown in Fig. 19. Thus the correlation between observed and predicted values is practically as good as what was obtained for the cases that were included in the data set used for the parameter estimation. This indicates that the correlation is robust and safe to be used for simulations in the material property and fluid-dynamic ranges included in Table 1. An extrapolation to conditions outside the range covered in this work is risky. Due to the characteristics of the logistic sigmoid function, nonlinear empirical models based on logistic sigmoids have a potential of producing steep gradients outside the range for which they are derived. Thus the behavior of the function should be carefully evaluated before using it for extrapolation outside the range from which it was derived. A safer alternative would be to carry out a small number of transient simulations in the conditions where a correlation for C_{drag} is needed and to include the new data in the data set to re-fit the model parameters.

5. Discussion

The results of the present study show that a fairly complicated drag correction function is required if the whole range from bubbling and turbulent beds to circulating fluidized beds has to be covered with a single correlation. In the present study, data from the wall and air distributor regions were omitted from the analysis. They could probably have been included in the same correlation, since the correlations developed from the reduced data set seem to be at least qualitatively capable of extrapolating to these regions. However, the flow patterns near the walls and above the air distributor are very different from the rest of the flow domain and widening the scope of a single correlation could require a larger number of parameters. Thus, separate correlations would need to be developed for the vicinity of walls and the air distributor region. The analysis of effects of the different kinds of gas-flow inlet also showed that, in bubbling bed conditions, the air distributor design can affect the drag correction needed in the entire bed area. Thus it is

Table 3
Blending function used to combine the correlation developed in Section 4.4 (denoted by f_1) with the correlation developed in Section 4.5 (denoted by f_2) to produce a continuous function f_0.

Range	Blending function
$\log \alpha_s > -1.3$ or $z < 1.3$ m	$f_0 = f_1$
$\log \alpha_s < -1.8$ and $z > 1.8$ m	$f_0 = f_2$
$-1.8 < \log \alpha_s < -1.3$ and $z > 1.8$ m	$f_0 = f_1 + \frac{f_2 - f_1}{0.5}(z - 1.3)$
$\log \alpha_s < -1.8$ and $1.3\ \text{m} < z < 1.8$ m	$f_0 = f_2 + \frac{f_2 - f_1}{0.5}(\log \alpha_s + 1.8)$
$-1.8 < \log \alpha_s < -1.3$ and $1.3\ \text{m} < z < 1.8$ m	$f_0 = 4(f_1((1.8 - x)(-1.3 - \log \alpha_s) + (1.8 - z)(\log \alpha_s + 1.8) + (z - 1.3)(\log \alpha_s + 1.8)) + f_2(z - 1.3)(-1.3 - \log \alpha_s))$

Elevation z in the blending function is given in meters.

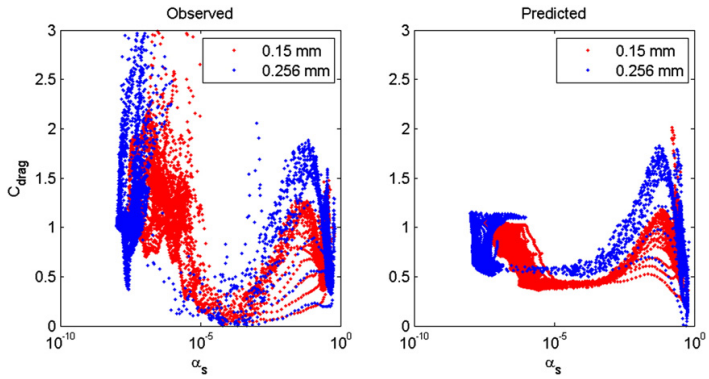

Fig. 17. Comparison of observed values and results obtained with a model that by means of blending functions combines the correlation for dilute CFB conditions with the more general model in two BFB cases with different particle sizes. Cases 57 and 58 in Table 2.

possible that a case-by-case consideration is required when choosing an appropriate correlation for different air distributor designs if high accuracy is desired.

The correlations developed in the present work are not necessarily the absolute best ones that could be developed on the basis of the data and the selected input variables. There are several possibilities to further improve the correlations. So far, only few possible configurations based on Eqs. (2)–(4) were tested. A bigger data set characterized by larger variations in the material properties would be necessary to fully take into account the possible combined effects of the different variables. This would make it possible to introduce a larger number of sigmoid functions in the correlation without reducing the correlation's robustness and interpolation capabilities.

The results also indicate that C_{drag} behaves in a clearly different way in BFB and TFB conditions. If a simulation is limited to BFB conditions, a separate correlation would most likely work better than the more general correlation developed in the present study. It is likely that a more complicated correlation with even more parameters and a larger amount of simulation data would be needed for TFB conditions. However, since a large number of parameters leads to longer computations, an efficient approach would be to have separate correlations for different purposes and different regions, like those we developed here for the dilute CFB conditions, and to combine them to a unified model with blending functions.

In some cases it could also be beneficial to use a simpler correlation with fewer parameters that could be calibrated separately for each application. For such purpose, a large set of available transient simulation data could be collected and for each application the available data closest to the actual conditions could be used to update the model parameters. This could be useful in some conditions to improve the accuracy, especially for modeling cases with constant material properties. However, in industrial processes the conditions vary and e.g. at air inlets of a CFB combustor, the gas temperature can be below 100 °C while the typical temperatures in the furnace are in the range 750 °C–950 °C. In BFB combustion the temperature variations inside the furnace are even larger. The average particle diameter at the riser bottom in a CFB combustor is typically of the order of 0.4–1 mm whereas in the upper part of the riser, the average particle size is usually in the range of 0.1–0.2 mm. Thus in fluidized bed combustors, the range of temperatures and particle sizes vary in the full range covered in the present study rendering simplification of the correlation difficult.

There is also no guarantee that the chosen set of input variables is the optimal one. Furthermore, it should be noted that the empirical approach applied in this work produces correlations instead of models since a causal relation between the different input variables and the drag correction does not necessarily exist and it is in any case not easy to prove. Thus the current work simply looks for correlations between a set of input variables and C_{drag}. When one process variable in a fluidized bed is changed, the fluidization state can considerably change which complicates the analysis of causes and effects. There could be parameters, such as e.g. the stress components and the solid acceleration rate, that allow to better describe the local conditions. Since these parameters would complicate the evaluation of C_{drag} during a steady state simulation they have not been accounted for at this stage.

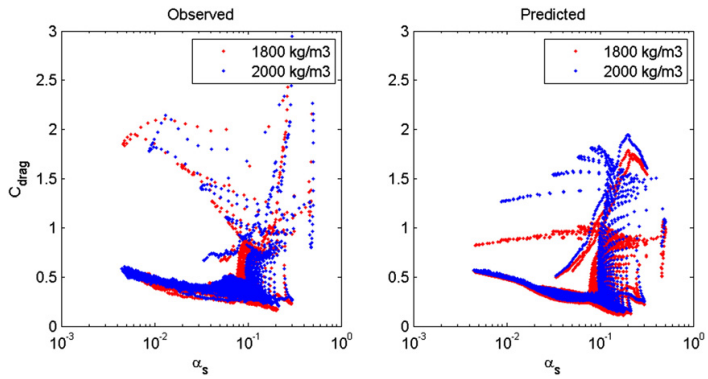

Fig. 18. Comparison of observed values and results obtained with a model that by means of blending functions combines the correlation for dilute CFB conditions with the general model in two CFB cases with different solid densities. Cases 6 and 5 in Table 2.

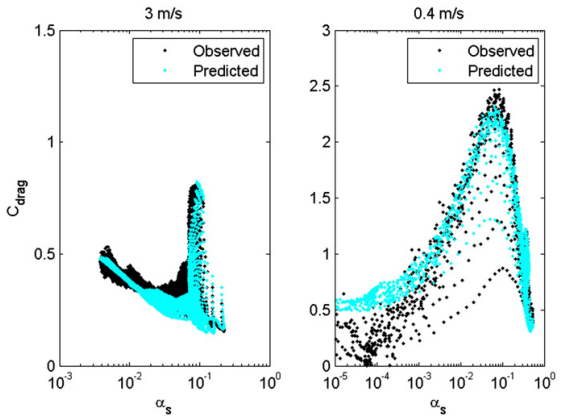

Fig. 19. A comparison between observed and predicted C_{drag} values in a CFB (left) and a BFB (right) at conditions that were not included in the data set used for derivation of the correlation for C_{drag}.

Furthermore, other important variables, like particle size distribution [25] and shape [26], which are known to have significant effects on the drag force, were also omitted from this study. At present, no data of adequate quality are available to include these variables in the correlations, but the effects of these variables should be considered in the future.

The largest uncertainty in the correlations developed here comes from the 2D simplification of the transient simulations, which compromises the accuracy of the correlations when they are applied in 3D simulations. Still, in the absence of a more reliable model, the correlations developed in this work could also be used in 3D simulations as an approximation for the gas–solid drag force. It is also possible that in TFB simulations the results suffer from the 2D simplification even more than CFB simulations because of the more significant down flow of solids in the middle portion of a TFB. In a 3D geometry, the falling clusters have more freedom to avoid collisions with rising clusters than in 2D, which renders 2D simulations inadequate for TFB studies. Thus further 2D studies of the drag correction required for TFB conditions may not be worthwhile.

Before the correlations developed in this work can be implemented in a CFD code, steps should be taken to improve their computational performance. The correlations developed here contain a large number of model parameters. Many of them may be unnecessary and a superfluous burden for the computations, but no effort has been made here to check their role in the correlation. Such an investigation should be carried out before implementation. Furthermore the correlation showed behaviors that could be problematic during numerical simulations. The correlations occasionally predicted very small and even negative values and, especially close to the air distributor, excessively high values. Hence upper and lower limits, preferably case specific, should be set for C_{drag} to avoid numerical complications. Most of the transient simulations in CFB conditions were carried out at high gas velocities which transported significant amounts of solids to the upper part of the riser. Thus the lowest solid concentrations in most of the CFD cases were far from zero, typically in the range 0.001–0.01. For example in circulating fluidized bed boilers, the local solid volume fraction in the upper part of the riser can be orders of magnitude lower. Thus the correlations need to be extended to lower solid concentrations, which can be done in the future by including more data from dilute conditions in the data set used as the basis for model development. By definition, C_{drag} should be equal to unity in the homogeneous flow conditions at very low solid concentrations and at the packing limit. The present correlations fail to correctly reproduce these limits and thus need to be modified prior to implementation in a CFD code.

In the present study, the goal was to develop a correlation for the steady-state drag force between gas and solids in a multiphase flow. In the literature, a more common approach has been to develop subgrid closures for the drag force to be used in transient CFB simulations with limited spatial resolution [27,28,29,30]. These two topics are closely related since in both the effects of the inhomogeneity of the suspension are addressed. The only difference is the choice of the temporal and spatial scales for the filtering process. In the special case where the scale of the spatial filter is larger than the transient flow structures the subgrid scale closures are identical to the steady-state closures. Thus the obtained values of the correction function and the conclusions of the present study are also indicative for sub-grid modeling, but without the added complexity of accounting for the local spatial resolution of the simulation.

6. Conclusions

The present study evaluated possible approaches to cover all fluidization states by a single drag law in steady state CFD modeling. The time-averaged drag force was expressed as a product of the drag force calculated from the traditional drag laws for homogeneous conditions and a correction function. In Kallio et al. [10], parameters that could have significant effects on the correction function in CFB conditions were identified. They were the solid volume fraction, the distance from the nearest wall, the slip velocity between the phases, the particle size, the solid density and the gas viscosity. In the present paper, the analysis is extended to TFB and BFB conditions. A larger amount of data with wider variation in material properties was collected for evaluation of the possibilities to develop an empirical drag correction function by nonlinear regression analysis of data from transient simulations.

The work showed that covering all fluidized bed conditions in a single-drag correlation is feasible. To develop an acceptable correlation that behaves well in the bed region of a BFB, two additional input variables had to be taken into account, i.e. gas velocity and the elevation above the air distributor. However, no solution was found allowing a good description of the surface and freeboard regions of a bubbling bed with a correlation that would also be applicable in CFB conditions. A more complicated correlation would be necessary to simultaneously cover the dilute conditions in the upper part of a CFB riser and in the freeboard of a BFB. Such a correlation was considered too complicated. A more reasonable approach would be to divide the correlations into separate correlations for each different region that could be combined into a single correlation by means of blending functions. This approach was demonstrated by developing a separate correlation for the dilute conditions above 1.5-m height in CFB risers. The accuracy of the correlation improved significantly in dilute CFB conditions where a much simpler correlation with six input variables could be used.

In the present work, data from 69 transient CFD simulations were used as the basis for empirical modeling. In order to derive a more accurate correlation, a larger data set would be required, especially for the evaluation of the combined effects of the material properties. The largest uncertainty in the correlations here presented arises from the 2D simplification applied in the transient simulations. In many cases, 2D simulation results significantly differ from the 3D results, which compromises the accuracy of the correlations developed from 2D data when they are applied in 3D simulations. In the absence of a more reliable model, the correlations developed in this work could be used also in 3D simulations as an approximation for the gas–solid drag force. However, before implementing the correlations in CFD software, the correlations still require refinements to reduce the possibility of numerical complications and to improve the performance in conditions outside of the data range from which the correlations have been obtained. Because of these reservations, the correlation parameters were not given in the paper and the developed correlations should only be considered as a proof of the concept. So far, no models have been presented in the literature that would cover a wide range of fluidization

conditions. Thus, besides the approximations and limitations, the modeling approach presented in this paper can serve as a promising starting point for the development of a general drag law for CFD simulation of fluidized beds.

Notation

a	parameter
b	parameter
C	correction function
d	diameter
E	error sum
e_{ss}	restitution coefficient
g	gravitational acceleration $g_{0,ss}$ radial distribution function
h	height
$\boldsymbol{I}$	unit matrix
I_{2D}	second invariant of the deviatoric stress tensor
k_{Θ_s}	diffusion coefficient of granular energy
k	index
K_{gs}	inter-phase momentum transfer coefficient
N	number of
p	pressure
R	correlation coefficient
Re	Reynolds number
u	velocity
U	time-averaged velocity
U_0	superficial velocity
v_t	terminal velocity
w	riser width
x	input variable
Δx_{mesh}	mesh spacing
Δx_{wall}	distance to the wall
z	value given by a sigma function

Greek symbols

α	volume fraction
ϕ_{gs}	energy exchange between gas and solids
η	auxiliary variable
λ_s	granular bulk viscosity
μ	viscosity
ρ	density
τ	stress Θ_s granular temperature
γ_{Θ_s}	collisional dissipation of energy

Subscripts

col	collisional
drag	related to the drag force
fr	frictional
g	gas
kin	kinetic
max	maximum
obs	observed
p	particle
pred	predicted
s	solid
t	related to the terminal velocity
y	vertical coordinate direction

Superscripts

*	calculated from time-averaged values

Acknowledgment

The authors gratefully acknowledge the financial support of Tekes, VTT Technical Research Centre of Finland, Etelä-Savon Energia Oy, Fortum, Metso Power Oy and Numerola Oy, and the support from Saarijärven Kaukolämpö Oy.

References

[1] V. Taivassalo, S. Kallio, J. Peltola, On time-averaged CFD modeling of circulating fluidized beds, Int. J. Nonlinear Sci. Numer. Simul. 13 (2012) 363–373.
[2] T.J. O'Brien, A multiphase turbulence theory for gas-solid flows: I. Continuity and momentum equations with Favre-averaging, http://dx.doi.org/10.1016/j.powtec.2014.01.030 .
[3] S. Kallio, V. Taivassalo, T. Hyppänen, Towards time-averaged CFD modelling of circulating fluidized beds, 9th Int. Conf. on Circulating Fluidized Beds, Hamburg, 2008.
[4] J. De Wilde, The generalized added mass revised, Phys. Fluids 19 (2007) 058103.
[5] J. De Wilde, G.J. Heynderickx, G.B. Martin, Filtered gas–solid momentum transfer models and their application to 3D steady-state riser simulations, Chem. Eng. Sci. 62 (2007) 5451–5457.
[6] S. Kallio, V. Poikolainen, T. Hyppänen, Mathematical modeling of multiphase flow in a circulating fluidized bed, Report 96–4, Heat Eng. Lab, Åbo akademi University, Turku, Finland, 1996.
[7] J.M. Matsen, Mechanisms of choking and entrainment, Powder Technol. 32 (1982) 21–33.
[8] C. Wen, Y. Yu, Mechanics of fluidization, Chem. Eng. Prog. Symp. Ser. 62 (1966) 100–111.
[9] D. Gidaspow, Multiphase flow and fluidization—continuum and kinetic theory descriptions, Academic Press, 1994.
[10] S. Kallio, J. Peltola, T. Niemi, Parametric study of the time-averaged gas–solids drag force in circulating fluidized bed conditions, accepted for publication, Powder Technol. 257 (2014) 20–29.
[11] D. Geldart, Types of gas fluidization, Powder Technol. 7 (1973) 285–292.
[12] T. Li, A. Gel, S. Pennala, M. Shahnam, M. Syamlal, CFD simulations of circulating fluidized bed risers, part i: grid study, Powder Technol. 254 (2014) 170–180.
[13] ANSYS Inc., ANSYS FLUENT Theory Guide. Release 14.0, Canonsburg, 2011. (2011).
[14] M. Syamlal, W. Rogers, T.J. O'Brien, MFIX documentation, Theory Guide, vol. 1, National Technical Information Service, Springfield, VA, 1993, (DOE/METC-9411004, NTIS/DE9400087).
[15] C.K.K. Lun, S.B. Savage, D.J. Jeffrey, N. Chepurniy, Kinetic theories for granular flow: inelastic particles in couette flow and slightly inelastic particles in a general flow field, J. Fluid Mech. 140 (1984) 223–256.
[16] D.G. Schaeffer, Instability in the evolution equations describing incompressible granular flow, J. Differ. Equ. 66 (1987) 19–50.
[17] S. Ogawa, A. Umemura, N. Oshima, On the equations of fully fluidized granular materials, J. Appl. Math. Phys. (ZAMP) 31 (1980) 483–493.
[18] S. Ergun, Fluid flow through packed columns, Chemical engineering progress 48 (1952) 89.
[19] S. Kallio, M. Guldén, A. Hermanson, Experimental study and CFD simulation of a 2D circulating fluidized bed, The 20th Int. Conf. on Fluidized bed combustion. May 18–20, Xi'an, China, 2009.
[20] D. Kunii, O. Levenspiel, Fluidization engineering, Butterworth-Heinemann, 1991.
[21] T. Niemi, W. Rogers, S. Kallio, Time averaged modeling of BFBs: Analysis of the terms in the momentum equations, Proceedings Fluidization XIV Conference, May 2013, Noordwijkerhout, The Netherlands, 2013, pp. 559–566.
[22] J. Leboreiro, G.G. Joseph, C.M. Hrenya, Revisiting the standard drag law for bubbling, gas-fluidized beds, Powder Technol. 183 (2008) 385–400.
[23] K. Hornik, M. Stinchcombe, H. White, Multilayer feed-forward networks are universal approximators, Neural Netw. 2 (1989) 359–366.
[24] D.W. Marquardt, An algorithm for least-squares estimation of nonlinear parameters, J. Soc. Ind. Appl. Math. 11 (1963) 431–441.
[25] R. Beetstra, M.A. van der Hoef, J.A.M. Kuipers, Drag force of intermediate Reynolds number flow past mono- and bidisperse arrays of spheres, AIChE J 53 (2) (2007) 489–501.
[26] A. Haider, O. Levenspiel, Drag coefficient and terminal velocity of spherical and nonspherical particles, Powder Technol. 58 (1989) 63–70.
[27] Y. Igci, S. Sundaresan, Verification of filtered two-fluid models for gas–particle flows in risers, AIChE J 57 (2011) (2011) 2691–2707.
[28] Y. Igci, S. Pannala, S. Benyahia, S. Sundaresan, Validation studies on filtered model equations for gas–particle flows in risers, Ind. Eng. Chem. Res. 51 (2012) 2094–2103.
[29] C.C. Milioli, F.E. Milioli, W. Holloway, K. Agrawal, S. Sundaresan, Filtered two-fluid models of fluidized gas-particle flows: new constitutive equations, 59 (2013) 3265–3275.
[30] S. Shah, J. Ritvanen, T. Hyppänen, S. Kallio, Wall effects on space averaged two-fluid model equations for simulations of gas–solid flows in risers, Chem. Eng. Sci. 89 (2013) 206–215.

PAPER VII

Analysis of the time-averaged gas–solid drag force based on data from transient 3D CFD simulations of fluidized beds

Powder Technology 274 (2015) 227–238.

Powder Technology 274 (2015) 227–238

Contents lists available at ScienceDirect

Powder Technology

journal homepage: www.elsevier.com/locate/powtec

Analysis of the time-averaged gas–solid drag force based on data from transient 3D CFD simulations of fluidized beds

Sirpa Kallio *, Juho Peltola, Timo Niemi

VTT Technical Research Centre of Finland, P.O. Box 1000, FI-02044 VTT, Finland

ARTICLE INFO

Article history:
Received 6 August 2014
Received in revised form 8 January 2015
Accepted 10 January 2015
Available online 15 January 2015

Keywords:
Drag force
Fluidized bed
Time-averaged
3D

ABSTRACT

In the present work, a qualitative analysis of the time-averaged gas–solid drag force in gas–solid fluidized beds is carried out. The analysis is based on a large number of transient Eulerian–Eulerian 3D CFD simulations of small bubbling, turbulent and circulating fluidized beds. The obtained results significantly differ from corresponding data previously obtained from 2D simulations, especially at high solid concentrations. This confirms that to accurately model the gas–solid drag force in a steady state 3D simulation, the drag model should not be based on data from transient 2D simulations. In the present work, the average drag force is expressed as the product of the drag force calculated from time-averaged velocities and volume fractions and a correction coefficient. The study shows that even when the third dimension is described in the mesh with only three nodes, the 3D character of the flow is captured in the drag correction coefficient. Thus, a large number of parametric studies could be carried out in a reasonable time frame. In the paper, the parameters affecting the time-averaged drag force are identified and the nature of the effects are analyzed. The analysis shows that solid volume fraction, particle size, solid density, gas viscosity, the slip velocity between gas and solids and the lateral distance to a wall have significant effects on the drag correction coefficient. At high gas densities typical e.g. of pressurized fluidization even the gas density has significant effects. A closure relation for the time-averaged drag force for a wide range of fluidization conditions should include these seven variables as inputs.

1. Introduction

Computational fluid dynamics (CFD) has in the past decades become a popular and efficient tool for process design. In case of multiphase processes the development has been slower than for single phase processes due to theoretical complications related to phase interactions and the greater requirements for computational capacity. Large size of industrial facilities further complicates application of multiphase CFD. Fluidized beds are no exception and only recently simulation of large industrial fluidized beds has become feasible. However, computation times in simulations with the most accurate models are still too long and hence modifications and adaptations to the modeling approaches are needed to apply them in commercial scale.

Characteristic of dense gas–solid flow is the occurrence of inhomogeneous structures like clusters and strands of particles in circulating fluidized bed (CFB) conditions and bubbles and voids in bubbling (BFB) and turbulent fluidized beds (TFB). Fluidized beds are commonly simulated in the transient mode in which the transient inhomogeneous flow patterns should ideally be resolved by the simulation. Such approach would require a fine spatial and temporal resolution which leads to a computation time that would be orders of magnitude too long in industrial applications. A solution to the problem is to decrease the resolution and include closure models that describe the effects of the unresolved sub-grid scale structures [1–3]. Largest emphasis in the development of sub-grid scale closures has so far been on the gas–solid drag force which is commonly expressed as a product of the drag force calculated from the correlations for homogeneous suspensions and a correction factor that is a function of the mesh spacing, suspension density and other parameters characterizing the flow structure such as the distance to the wall and gas-solid slip velocity [4].

As an alternative to the transient coarse mesh simulation approach, models for steady-state simulation have been developed by time-averaging the transient fluid flow equations [5,6]. The obvious benefit of this approach is that the time-consuming integration of the transient simulation results, which needs to be done to analyze average conditions in the process, is avoided. The required closure laws are similar to the closure laws needed for transient coarse mesh simulations with the difference that the closure laws for time-averaged equations are not dependent on the mesh spacing to equal extent, which simplifies modeling [7]. In a situation where the filter scale of a transient simulation is significantly larger than the inhomogeneous flow structures, the transient and time-averaged closure models are one and the same.

One of the largest terms in the time-averaged momentum equations is the gas–solid drag force. Similar to the sub-grid drag closures, the closure law for time-averaged drag can be written by means of a correction function applied on the drag force calculated assuming homogeneous conditions. In the study of Taivassalo et al. [5], correction functions

* Corresponding author. Tel.: +358 20 7224015.
E-mail address: sirpa.kallio@vtt.fi (S. Kallio).

http://dx.doi.org/10.1016/j.powtec.2015.01.029
0032-5910/

Notation

C_d	drag coefficient
d	diameter
D	depth of the bed
H	height of the riser
K_{gs}	inter-phase momentum transfer coefficient
Re	Reynolds number
u	velocity
U	time-averaged velocity
U_0	superficial velocity
v_t	terminal velocity
W	riser width
x	distance
Δx_{mesh}	mesh spacing
$\Delta x_{H,W}$	mesh spacing along width and height
Δx_D	mesh spacing in depth direction
Δx_{wall}	distance to a wall
$\Delta x_{f\ \&b}$	distance to the front wall or the back wall (minimum of the two)

Greek symbols

α	volume fraction
μ	viscosity
ρ	density

Subscripts

Ergun	Ergun drag law
g	gas
gs	gas–solid interaction
p	particle
s	solid
t	related to terminal velocity
W–Y	Wen & Yu drag law

Superscripts

*	calculated from time-averaged values

developed on the basis of transient 2D simulation data were applied. In these simple closure laws the correction was expressed as a function of solid volume fraction. Kallio et al. [8] analyzed drag data from a large number 2D simulations of CFBs to evaluate the properties that can affect the average drag force. Altogether six variables, i.e. solid volume fraction, slip velocity, distance to the wall, solid material density, particle size and gas viscosity were listed as potential input variables for a drag correction correlation, which indicates that the models used in [5] could be too simple to cover the wide range of conditions encountered in a fluidized bed. The results in the study of Kallio et al. [7] showed that on the basis of drag data collected from transient

Table 1
The models and parameters used in the simulations.

Submodel or parameter	Model or value used
Granular viscosity	Syamlal et al. [12]
Granular bulk viscosity	Lun et al. [13]
Frictional viscosity	Schaeffer [14]
Granular conductivity	Syamlal et al. [12]
Solids pressure	Lun et al. [13]
Radial distribution	Ogawa et al. [15]
Angle of internal friction	30°
Frictional and packing limit	0.61 and 0.63, respectively
Turbulence model	Standard k-ε, dispersed
Wall boundary condition, gas phase	No slip
Wall boundary condition, solid phase	Partial slip, specularity coefficient 0.001

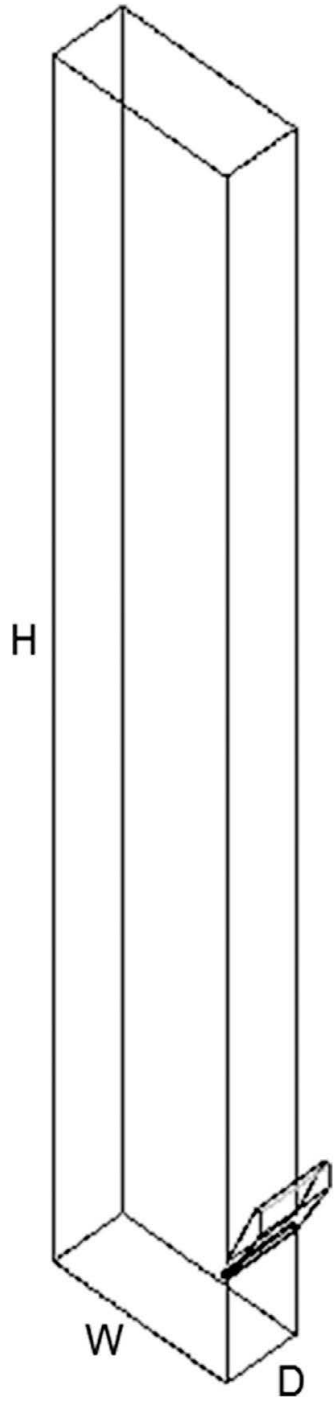

Fig. 1. The geometry of a simulated fluidized bed with depth D, width W and height H.

simulations it is possible to derive correlations that can be used in time-averaged simulations. In addition to the six parameters suggested in the study of Kallio et al. [8], height above air distributor and local gas superficial velocity were used as input parameters. The work was based on 2D simulation data covering both BFB and CFB conditions. Several comparisons of 2D and 3D CFD simulation results have been carried out in the literature [9,10]. The reported significant effects of the dimensionality imply that utilization of 2D simulation data can reduce the accuracy of the developed correlations, when they are applied in 3D simulations.

In the present paper, data from transient 3D simulations are analyzed and the results are compared with the earlier ones [7,8] obtained from 2D simulations. Like in the previous work, the present study is limited to Geldart B particles and the analysis is done only for the vertical drag force component. Due to the long simulation times of transient 3D cases, only a very limited amount of data is to date available and mainly from small fluidized beds. In the paper, the quality of the 3D simulations and the produced data is discussed. The amount of data is sufficient for the present qualitative study that presents a survey of the possibility to define the variables for an intended development of a general closure model for the drag force in fluidized bed conditions. However, more data should be included in the future if the data are to be used as the basis for development of such a general drag correlation.

2. Transient Eulerian–Eulerian 3D simulations

2.1. Methods used

The same models and numerical methods as used in the 2D studies of Kallio et al. [7,8] were used here in the 3D simulations. The simulations were carried out with the commercial code ANSYS Fluent v.14 [11] with the Eulerian–Eulerian multiphase approach based on the kinetic theory of granular flow (KTGF). The models used are listed in Table 1 and they are given in detail in the study of Kallio et al. [7].

As in the previous 2D study, the drag term was computed from the Gidaspow [16] drag model, which combines the Ergun [17] and Wen–Yu [18] drag laws. A second order discretization scheme was used for momentum and the QUICK scheme for the volume fraction equation. The time step was 0.001 s for the 10 mm and coarser meshes and 0.0005 s for the 6.25 mm and finer meshes. To validate the modeling approach, comparisons with measurements have earlier been carried out for some 2D simulations with the same models in a 0.4 m wide geometry [19]. The measurement and simulation results were in good qualitative agreement and even quantitatively the results were acceptable. On that basis the chosen approach can be considered sufficiently accurate for the present study. For each case, approximately 5 s was simulated before starting time-averaging. A further 120 s of flow time was simulated to compute the averages, which guarantees a sufficient accuracy.

2.2. The simulated cases

The 2D geometry in the study of Kallio et al.[7,8] was a simple riser with straight walls. In the present study, a similar 3D geometry, shown in Fig. 1, is used. Two alternative descriptions for air distribution were applied: a uniform gas inflow rate at riser bottom and a non-uniform distribution in which air enters through orifices placed about 5 cm apart from each other. Solids left the riser through the top edge of the simulated domain and were fed back through a return channel, the opening of which was located at 0.6–0.7 m height in the riser.

Kallio et al. [7,8] observed that simulations with mesh spacing 12 mm gave the same result for the correction coefficient for the time-averaged drag force as simulations in a finer mesh with 6 mm elements. To save computation time, most of the simulations in the present study

Table 2
Simulated cases. Inlet types marked with texts 'unif.' for uniform gas distribution and 'orif.' for air distributed through separate orifices at riser bottom.

	Inlet type	U_0	μ_g	ρ_g	ρ_s	d_p	$\Delta_{H,W}$	Δ_D	W	H	D	Average α_s	v_t	Ar	U_0/v_t
		m/s	kg/ms	kg/m^3	kg/m^3	mm	mm	mm	m	m	m	–	m/s	–	–
1	unif.	5	4.45E-5	0.3105	2480	0.255	13.3	13.3	1	7	0.4	0.0297	1.53	63.2	3.27
2	unif.	2.75	4.45E-5	0.3105	2480	0.6	12.5	12.5	0.4	3	0.0375	0.0270	4.96	824	0.55
3	unif.	0.6	4.45E-5	0.3105	2480	0.15	12.5	12.5	0.4	3	0.0375	0.0270	0.62	12.9	0.97
4	unif.	1.3	4.45E-5	0.3105	2480	0.15	12.5	12.5	0.4	3	0.0375	0.0270	0.62	12.9	2.10
5	unif.	2.75	4.45E-5	0.3105	2480	0.255	12.5	12.5	0.4	3	0.0375	0.0270	1.53	63.2	1.80
6	unif.	2.75	4.45E-5	0.3105	2480	0.255	6.25	6.25	0.4	3	0.0375	0.0270	1.53	63.2	1.80
7	unif.	1.3	4.45E-5	1.255	2480	0.255	12.5	12.5	0.4	3	0.0375	0.0269	1.20	255	1.08
8	unif.	2.75	4.45E-5	1.255	2480	0.255	12.5	12.5	0.4	3	0.0375	0.0268	1.20	255	2.30
9	unif.	2.75	1.79E-5	0.3105	2480	0.255	12.5	12.5	0.4	3	0.0375	0.0270	2.70	391	1.02
10	unif.	2.75	1.79E-5	0.3105	2480	0.255	12.5	12.5	0.4	3	0.1125	0.0269	2.70	391	1.02
11	unif.	2.75	4.45E-5	6	2480	0.255	12.5	12.5	0.4	3	0.0375	0.0267	0.81	1219	3.40
12	unif.	2.75	3.00E-5	0.3105	2480	0.255	12.5	12.5	0.4	3	0.0375	0.0270	1.99	139	1.38
13	unif.	1.3	4.45E-5	1.255	2480	0.15	12.5	12.5	0.4	3	0.0375	0.0268	0.54	52.0	2.41
14	unif.	1.3	4.45E-5	1.255	1500	0.255	12.5	12.5	0.4	3	0.0375	0.0268	0.80	155	1.63
15	orif.	1	4.45E-5	0.311	2480	0.255	10	5	0.4	3	0.015	0.0660	1.53	63.3	0.65
16	orif.	5	4.45E-5	0.311	2480	0.44	10	5	0.4	3	0.015	0.0660	3.37	325	1.48
17	orif.	2	4.45E-5	0.311	2480	0.255	10	5	0.4	3	0.015	0.0660	1.53	63.3	1.31
18	orif.	1.6	4.45E-5	0.311	2480	0.255	10	5	0.4	3	0.015	0.0660	1.53	63.3	1.05
19	orif.	1.3	4.45E-5	0.311	2480	0.255	10	5	0.4	3	0.015	0.0660	1.53	63.3	0.85
20	orif.	0.7	4.45E-5	0.311	2480	0.255	10	5	0.4	3	0.015	0.0660	1.53	63.3	0.46
21	orif.	0.5	4.45E-5	0.311	2480	0.255	10	5	0.4	3	0.015	0.0660	1.53	63.3	0.33
22	orif.	0.3	4.45E-5	0.311	2480	0.255	10	5	0.4	3	0.015	0.0660	1.53	63.3	0.20
23	unif.	1.25	1.79E-5	1.225	2480	0.255	12.5	12.5	0.4	3	0.0375	0.0666	1.86	1542	0.67
24	unif.	2.25	1.79E-5	1.225	2480	0.255	12.5	12.5	0.4	3	0.0375	0.3655	1.86	1542	1.21
25	unif.	2.75	1.79E-5	1.225	2480	0.255	12.5	12.5	0.4	3	0.0375	0.0391	1.86	1542	1.48
26	unif.	2.75	1.79E-5	1.225	2480	0.255	12.5	12.5	0.4	3	0.0375	0.0832	1.86	1542	1.48
27	orif.	1.25	1.79E-5	1.225	2480	0.255	10	5	0.4	3	0.015	0.0660	1.86	1542	0.67
28	orif.	2.25	1.79E-5	1.225	2480	0.255	10	5	0.4	3	0.015	0.0528	1.86	1542	1.21
29	orif.	2.75	1.79E-5	1.225	2480	0.255	10	5	0.4	3	0.015	0.0396	1.86	1542	1.48
30	orif.	2.75	1.79E-5	1.225	2480	0.255	5	5	0.4	3	0.015	0.0793	1.86	1542	1.48
31	orif.	2.75	1.79E-5	1.225	2480	0.255	10	5	0.4	3	0.015	0.0815	1.86	1542	1.48
32	unif.	2.5	4.45E-5	0.3105	2480	0.255	12.5	12.5	1	7	0.0375	0.0297	1.53	63.2	1.63

were carried out with a 12 mm mesh although in some runs a finer mesh was used to allow for grid sensitivity analysis. In case of 3D simulations, the computation time strongly limits the feasible mesh size. Thus, the third dimension was in the present study kept at the minimum to allow for a larger number of simulations. To analyze the effect of the small third dimension, an additional simulation with a significantly deeper bed was also carried out. In addition, simulations with varying number of elements in the third direction were done. The simulations cover the full range from bubbling to circulating fluidized bed conditions. Material property values and process conditions were varied to allow analysis of their effects. Their values were altered independently to reveal parametric effects. Thus, some of the simulated cases do not correspond to real conditions found in existing fluidized beds. In several cases, however, the gas is supposed to be air at room temperature or at around 850 °C, which is a typical CFB furnace temperature in boilers. Solid phase consists of spherical particles with restitution coefficient equal to 0.9. The simulations used as the basis for the present analysis are listed in Table 2. The average solids volume fractions given in the table are calculated from the time-averaged solids volume fraction obtained from each simulation by volume-averaging over the simulated geometry. The terminal particle velocity is estimated using the drag law of Haider & Levenspiel [20]. All the solid particles belong to the Geldart B group according to the original Geldart classification. However, if the effect of process parameters is taken into account, Cases 3, 4 and 13 are somewhat on the A-side of the A–B border [21]. Fig. 2 illustrates the solids distribution pattern obtained in Case 1, with distinct dense wall layers and a dense bottom bed.

Table 3
The transition function by Niemi et al. [20] which combines Ergun [17] and Wen–Yu [18] drag laws.

When $\alpha_g \geq 0.5$:

$$K_{gs} = K_{gs,W-Y} = \frac{3}{4} C_d \frac{\alpha_g \alpha_s \rho_g |\boldsymbol{u}_g - \boldsymbol{u}_s|}{d_p} a_g^{-2.65}$$

$$C_d = \begin{cases} \frac{24}{\mathrm{Re}}(1 + 0.15(\mathrm{Re})^{0.687}, & Re < 1000 \\ 0.44, & Re \geq 1000 \end{cases}$$

$$\mathrm{Re} = \frac{\alpha_g \rho_g |\boldsymbol{u}_g - \boldsymbol{u}_s| d_p}{\mu_g}$$

When $\alpha_g \leq 0.4$:

$$K_{gs} = K_{gs,Ergun} = 150 \frac{\alpha_s (1-\alpha_g) \mu_g}{\alpha_g d_p^2} + 1.75 \frac{\rho_g \alpha_s |\boldsymbol{u}_g - \boldsymbol{u}_s|}{d_p}$$

When $0.4 < \alpha_g < 0.5$:

$$K_{gs} = K_{gs,Ergun} + 10(\alpha_g - 0.4)(K_{gs,W-Y} - K_{gs,Ergun})$$

2.3. Time-averaging

As in the study of Kallio et al. [8], the transient data from each simulation were time-averaged to determine in each mesh point the average flow properties and the average drag force. As in the previous 2D study

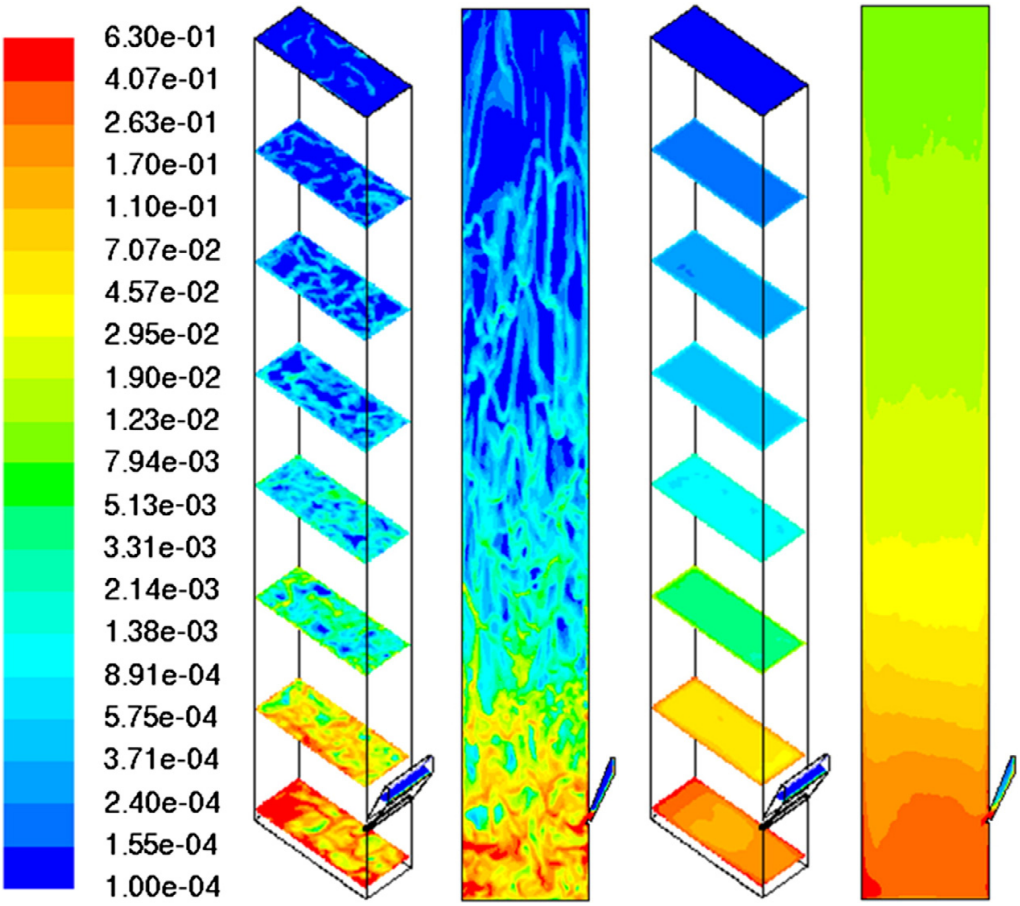

Fig. 2. Transient (left) and time-averaged (right) distribution of solid volume fraction at eight elevations and on the middle plane of the riser.

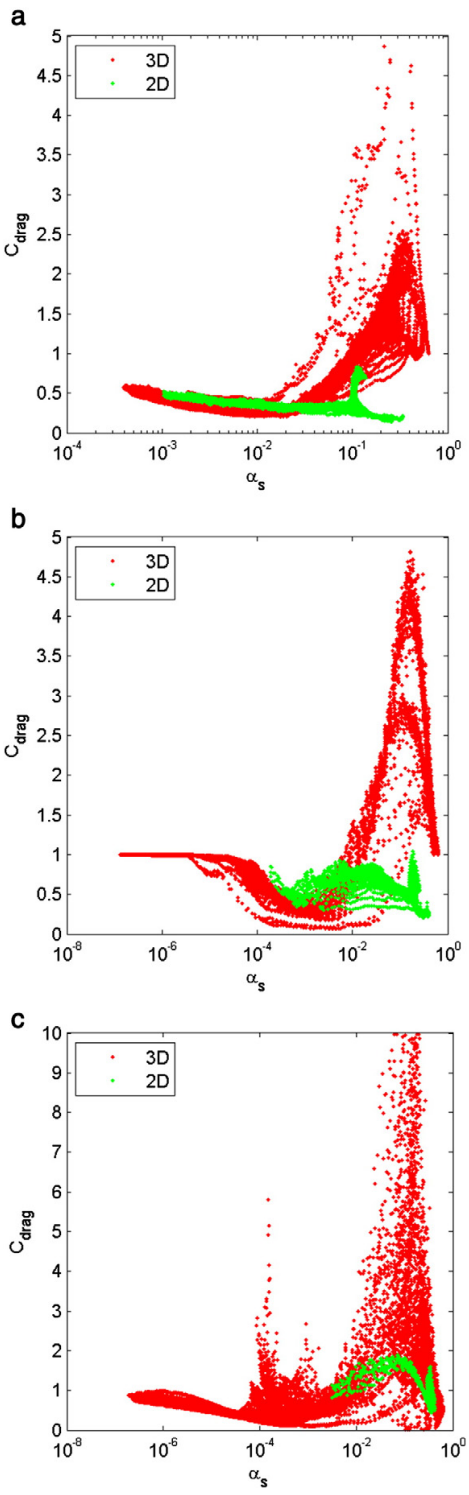

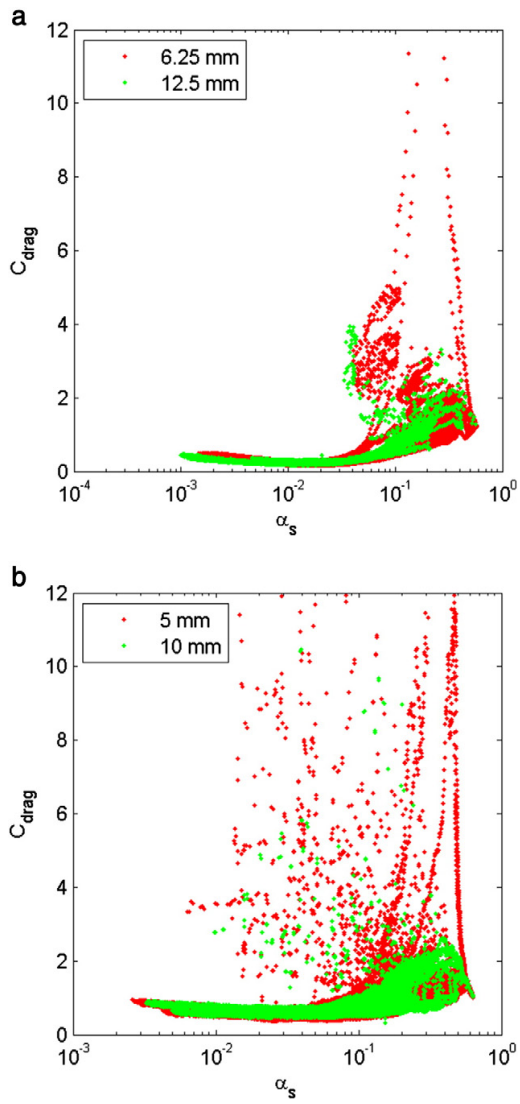

Fig. 4. Effect of mesh resolution a) in Cases 6 and 5 (mesh resolution was the same in all directions, $\mu_g = 4.45e{-}5$ kg/ms, $\rho_g = 0.311$ kg/m^3, $\rho_s = 2480$ kg/m^3, $d_p = 0.255$ mm. $U_0 = 2.75$ m/s), and b) in Cases 30 and 31, (mesh resolution in the depth direction was 5 mm in both simulations while the resolution in the other directions was altered, $\mu_g = 1.79e{-}5$ kg/ms, $\rho_g = 1.225$ kg/m^3, $\rho_s = 2480$ kg/m^3, $d_p = 0.255$ mm. $U_0 = 2.75$ m/s).

[8], the analysis is done for the dominating vertical component of the drag force. The time-averaged drag force can be written in the form

$$\overline{K_{gs}\left(u_{g,y}-u_{s,y}\right)} = C_{drag}K^*_{gs}\left(U_{g,y}-U_{s,y}\right) \quad (1)$$

where $u_{g,y}$ and $u_{s,y}$ are the instantaneous gas and solid phase vertical velocity components and $U_{g,y}$ and $U_{s,y}$ the corresponding mass-weighted

Fig. 3. Comparison of C_{drag} determined from 3D simulation results with corresponding data from earlier 2D simulations [8]: a) CFB conditions (Case 17: $U_0 / v_t = 1.31$), b) TFB conditions (Case 15: $U_0 / v_t = 0.65$), and c) BFB conditions (Case 22: $U_0 / v_t = 0.20$). $\mu_g = 4.45e{-}5$ kg/ms, $\rho_g = 0.311$ kg/m^3, $\rho_s = 2480$ kg/m^3, $d_p = 0.255$ mm.

time-averaged velocity components. K_{gs}^{*} is the inter-phase momentum transfer coefficient calculated on the basis of the time-averaged velocities and volume fractions using a similar combination of Wen and Yu [18] and Ergun [17] drag laws as in the transient simulations. However, instead of using Gidaspow's [16] drag law, a smoother transition between the drag laws, suggested by Niemi et al. [22], was used to calculate K_{gs}^{*} (see Table 3). In this model a linear transformation over a range of solid volume fractions is done between the Ergun and Wen–Yu models. The coefficient C_{drag} in Eq. (1) is a drag correction coefficient. The value of C_{drag} in each point in the flow field can be calculated from Eq. (1) by time-averaging the drag force, solid volume fraction and gas and solid velocities over the simulation time of a transient simulation.

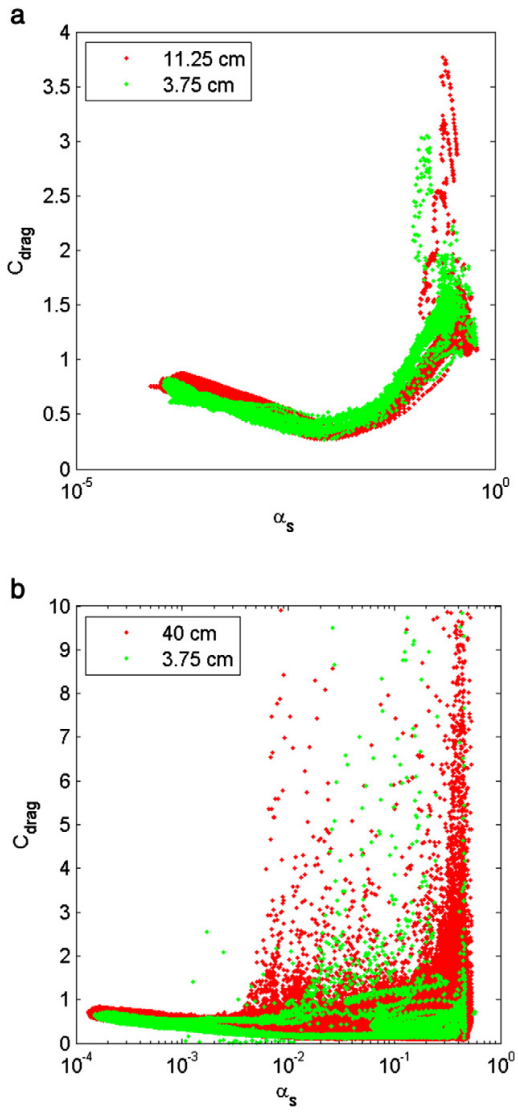

Fig. 5. Effect of the depth of the bed in different conditions: a) in Cases 10 and 9 (μ_g = 1.79e–5 kg/ms, ρ_s = 2480 kg/m^3, d_p = 0.255 mm, U_0 = 2.75 m/s, and b) in Cases 1 and 32 (μ_g = 4.45e–5 kg/m s, ρ_g = 0.311 kg/m^3, ρ_s = 2480 kg/m^3, d_p = 0.255 mm, U_0 = 5 m/s).

This kind of data was collected for each of the simulations. Filtering of the data was done at the data collection stage. For very low values of slip velocity, the computed C_{drag} can become unreasonably large or negative due to the stochastic nature of the data and the finite averaging periods. A minimum limit for the slip velocity magnitude was set at 0.001 m/s and all points with negative C_{drag} were excluded. The data for the solids return channel were also omitted at this stage from the analysis since the characteristics of the flow are there completely different. The uppermost half meter of the geometry was omitted to avoid possible exit effects.

3. Analysis of the results

3.1. Comparison with results of 2D simulations

It is fairly common to derive closure models for filtered momentum equations on the basis of results from transient 2D simulations [3,7]. However, how far the 2D results on the gas–solid drag force can be extended to 3D simulations needs to be assessed. For that purpose, several of the cases simulated in 2D in the study of Kallio et al. [7,8] were included in the present 3D analysis to allow direct comparison of the obtained C_{drag} values. Fig. 3 presents comparisons between 2D and 3D simulation results in CFB, TFB (turbulent fluidized bed) and BFB conditions. Since solid concentration is the most important variable affecting clustering and consequently also C_{drag}, the results are presented as a function of solid volume fraction α_s. Fig. 3 shows that the 2D simulations produced clearly different trends in BFB, TFB and CFB conditions. No similar significant difference between the fluidization modes can be seen in the 3D results and especially in the dense conditions of the CFB and TFB cases, the general trends in 2D and 3D results radically differ. Quantitatively, the C_{drag} values determined from 2D and 3D simulation data are similar in the dilute CFB conditions and also to some extent in BFB conditions, but in the dense bottom bed of a CFB and in a TFB the 2D results significantly deviate from the 3D results. In general, the 3D simulations produce higher C_{drag} at high solid concentrations. Thus a separate thorough 3D study of the gas–solid drag force, presented in this paper, is clearly necessary.

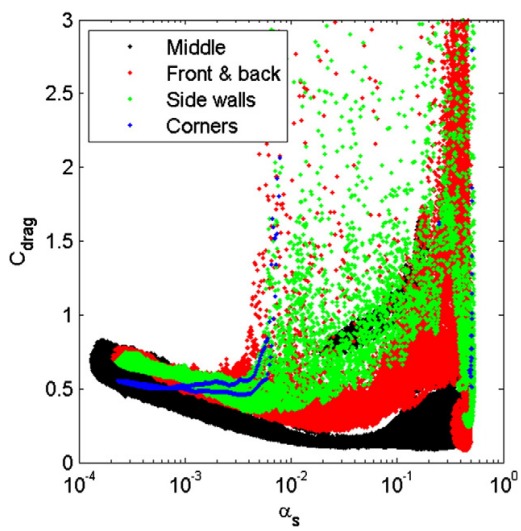

Fig. 6. C_{drag} in different geometrical regions in Case 1 (μ_g = 4.45e–5 kg/ms, ρ_g = 0.311 kg/m^3, ρ_s = 2480 kg/m^3, d_p = 0.255 mm, U_0 = 5 m/s).

3.2. Effect of mesh resolution and number of elements

To reduce computation time, the mesh resolution in the simulations of Table 2 was fairly coarse. Before analyzing effects of other parameters the possible effects of the mesh need to be evaluated. In the study of Kallio et al. [8], results obtained in 2D simulations with 25 mm, 12.5 mm and 6.25 mm mesh resolutions were compared. The two finest resolutions produced drag corrections of the same magnitude while the values obtained with the coarsest mesh were somewhat higher. A similar comparison was carried out in the 3D simulations of the present work. Fig. 4a illustrates the effect of the mesh in a simulation of a riser with a 0.4 m × 0.0375 m cross-section. With the coarser mesh, the depth direction is divided in three layers of computational elements while in the finer mesh the corresponding number of element layers is six. In the dense end of the solid concentration scale no large effect on C_{drag} can be observed. In dilute conditions the simulation with the coarser mesh produces lower C_{drag} values, which is contrary to what in general can be expected of a coarse mesh simulation. The larger number of elements in the depth direction in the finer mesh seems to reduce clustering resulting in slightly higher C_{drag}. Fig. 4b compares two simulations of a riser with 0.4 m × 0.015 m cross-section. In this mesh test, the mesh resolution was kept unchanged in the depth direction when the resolution in the other two directions was changed from 5 mm to 10 mm. No clear effect of the mesh can be observed in the bulk of the data other than an increase in the number of high C_{drag} values, especially at high α_s, which also was observed in Fig. 4a. These high values are a result of increased wall and corner effects in the finer mesh. In general we can conclude from Fig. 4 that a mesh resolution of 10–12.5 mm is sufficient to produce representative C_{drag} values. This conclusion is in agreement with the results from the earlier 2D studies [7,8]. Li et al. [23] showed that the required mesh resolution depends on the averaged variables that are considered in the analysis. Although flow structures smaller than 10–12 mm certainly exist in fluidized beds, their statistical significance for the average gas–solid drag force seems negligible which allows us to use fairly coarse mesh resolutions in the present study.

Computation time depends on the number of computational elements in the mesh. In addition to the mesh resolution, the selected geometry is also important. In the simulations analyzed in Fig. 4, the depth direction was small and the geometry corresponded to a pseudo-2D fluidized bed with a core-annular flow structure prevailing only in the width direction. Such geometries have been used in experiments to represent a 2D fluidized bed. Due to the relatively small number of cells that is required to describe a pseudo-2D fluidized bed, it would be beneficial for the present study, if the obtained C_{drag} would be representative of a 3D fluidized bed. To evaluate the applicability of this geometry, tests with different riser depths were carried out. Fig. 5 shows results from four such comparisons in different conditions. Although the results slightly change when riser depth is increased, the differences in all the two studied conditions are small. In Fig. 5b, where the differences in the depth and the number of mesh nodes in the depth direction are largest, there is clear difference in the results in the dense suspension region. This can be assumed to originate from the front and back

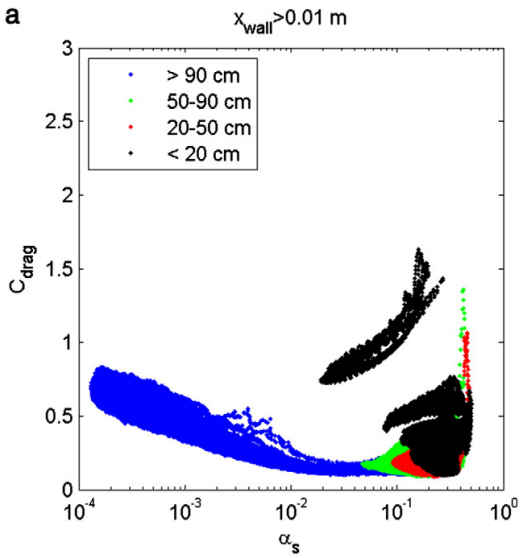

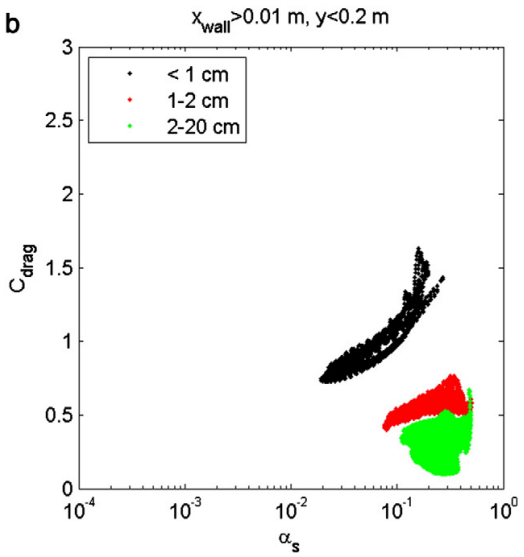

Fig. 7. C_{drag} in Case 1 in the middle section of the riser at different elevations.

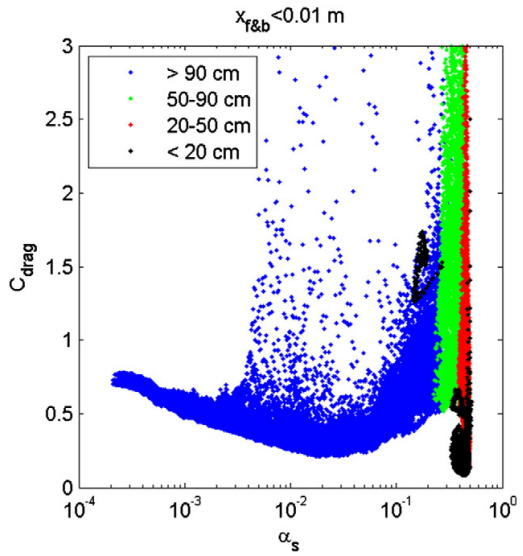

Fig. 8. C_{drag} in Case 1 in the vicinity of front and back walls at different elevations.

walls at which in the 0.4 m deep bed a dense down-flow-region is established. This is confirmed in the next section. In general, the effect of bed depth is relatively small which allows us to study parametric effects on the drag force by means of 3D simulations of pseudo-2D beds. Because of the shorter simulation time, it is thus feasible to carry out a larger number of simulations with wide variation in conditions in a reasonable time. Since the amount of data from dense suspension conditions increases with bed depth (see Fig. 5b), it would however be useful in the future to carry out more simulations in larger geometries to get a larger amount of data from conditions closer to the packing limit. Unfortunately, this could not be included in the present study. Still, enough data are available from the 32 simulations for the present qualitative analysis.

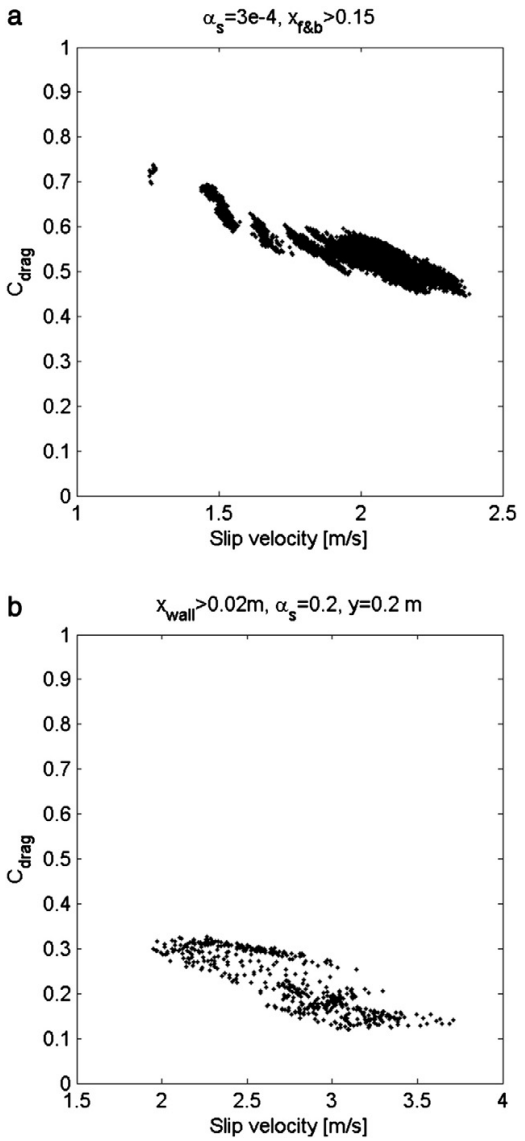

Fig. 9. Effect of slip velocity in the middle section of the riser in Case 1 a) in dilute conditions ($\alpha_s = 0.0003$) and b) at 0.2 m height in dense conditions ($\alpha_s = 0.2$).

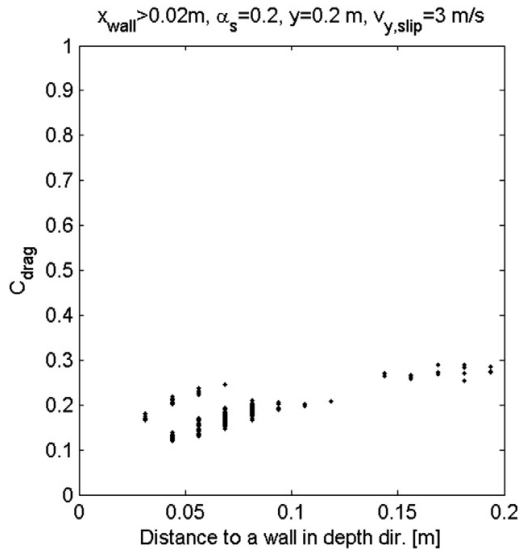

Fig. 10. Effect of the distance to a wall in the depth direction in the middle section of the riser at 0.2 m height in Case 1 when slip velocity is 3 m/s.

3.3. Regional effects

In dilute conditions, C_{drag} seems to be mainly a function of solid volume fraction if material properties are constant. In dense regions at solid volume fractions above 0.1%, there is a larger scatter in C_{drag} indicating that other variables than α_s have major effects. In earlier studies [3,4,8], the distance to the wall has been shown to be important. Of the simulations in Table 2, Case 1 with cross-section 1 m × 0.4 m offers best opportunities to evaluate the effects of the location in a fluidized bed on the drag correction coefficient.

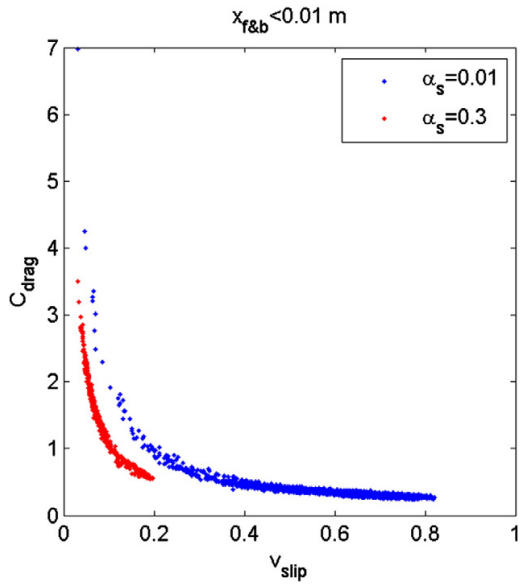

Fig. 11. Effect of slip velocity on C_{drag} at the front and back walls at solid volume fractions of 0.01 and 0.3.

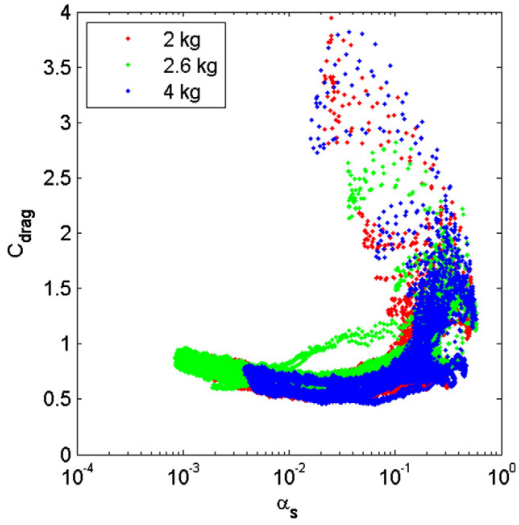

Fig. 12. Effect of solids inventory on C_{drag}. Cases 25, 24, and 26 in Table 2 ($\mu_g = 1.79e{-}5$ kg/ms, $\rho_g = 1.225$ kg/m^3, $\rho_s = 2480$ kg/m^3, $d_p = 0.255$ mm, $U_0 = 2.75$ m/s).

Fig. 6 shows C_{drag} in different regions of the CFB riser in Case 1. The riser is divided into four sections: front and back walls, side walls, corners and the middle section. Wall sections are defined as locations where the distance to the wall is below 10 mm while in the corners the distance to walls in both lateral directions is below the 10 mm limit. Close to walls, C_{drag} at solid volume fractions below 0.1 is systematically higher than in the middle region indicating that the suspension is more homogeneous close to a wall. The large scatter especially at high values of α_s needs to be analyzed further.

The data in the middle region of the riser are further split as a function of height in Fig. 7a. Fig. 7b shows that the two lower-most control volume layers at riser bottom produce clearly higher C_{drag} values than the rest of the riser volume. Both in the dilute and in the dense regions, there is a large scatter in C_{drag}, which indicates that other parameters than solid volume fraction significantly affect C_{drag}. A similar division as a function of height is presented in Fig. 8 for the wall layers at front and back walls. Significant scatter of values is also here present in the data and other parameters than α_s need to be considered.

3.4. Effect of the slip velocity and of the distance to a wall

Both slip velocity and the distance to a wall have been reported to affect the average drag force [4,8]. Fig. 9 illustrates the effect of the vertical slip velocity in dilute and dense conditions in the central region of a CFB riser. In both cases, increased slip velocity tends to reduce C_{drag}. Especially in the dense conditions, there remains a large scatter in the data even after the effects of solid volume fraction, slip velocity and elevation are removed. One possible parameter that can cause the scatter is the distance to the walls. Fig. 6 clearly showed that there is a clear difference between C_{drag} in the vicinity of a wall and C_{drag} in the central region. Whether there is an additional effect of the distance to the wall in the central region needs to be checked. Fig. 10 shows a clear effect of the distance to the front and back walls at slip velocity of 3 m/s. Interestingly, C_{drag} increases away from the wall, which means that there seems to be a minimum in C_{drag} close to the wall layer. At the wall, however, C_{drag} is according to Fig. 6. higher than in the central region.

At the wall, the slip velocity has a more pronounced effect than at riser center. Fig. 11 illustrates this effect at two solid volume fractions. The scatter in the values of C_{drag} at a specific solid volume fraction seems to be at the wall entirely caused by variations in the slip velocity. Similar to the central region in the riser, increased slip velocity reduces C_{drag}.

3.5. Effect of process conditions

Process conditions such as solids inventory, gas superficial velocity and air distributor design affect the flow patterns in a fluidized bed. They can also change the clustering tendency of the suspension and thus their effects on C_{drag} should be evaluated. Fig. 12 shows that the bed mass determines the range of solid volume fraction occurring in the fluidized bed but has no significant effect on C_{drag}. In dense conditions a small effect is visible. When bed mass increases, the location where a certain average solid volume fraction occurs will change. The differences seen in Fig. 12 at any specific value of solid volume fraction could thus, at least partly, be results of changed distance to a wall and to the air distributor.

Superficial gas velocity determines the state of fluidization for a given suspension. Fig. 13 shows the changes in C_{drag} as the gas velocity increases from 0.3 m/s to 2 m/s. At the lowest velocity the process is a BFB and at the highest velocity significant solids circulation takes place. No drastic change in the character of C_{drag} can be seen. At all velocities, reduction of the average drag force due to clustering takes place at low solid concentrations. Significant portion of the gas flow

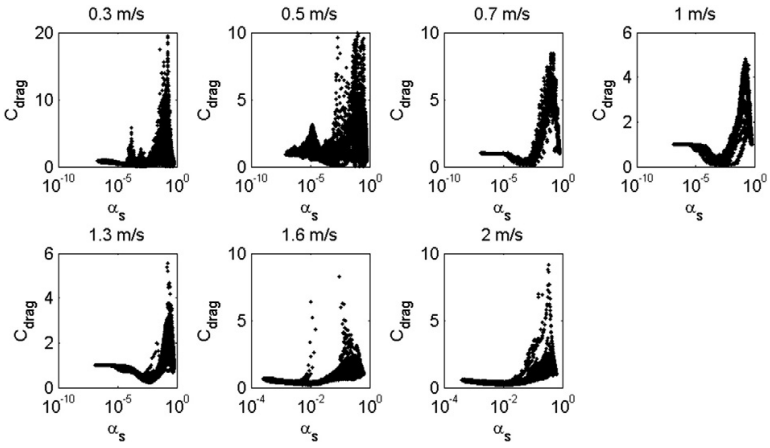

Fig. 13. Effect of superficial gas velocity on C_{drag} in Cases 17, 18, 19, 15, 20, 21, and 22, respectively ($\mu_g = 4.45e{-}5$ kg/ms, $\rho_g = 0.311$ kg/m^3, $\rho_s = 2480$ kg/m^3, $d_p = 0.255$ mm).

bypasses the clusters, which reduces the average drag force experienced by the particles. At very low solid volume fractions, C_{drag} is by definition equal to unity, which is also seen in the results. In the dense bottom and wall zones, an increase in C_{drag} above one is seen at all fluidization velocities. Although separation in dense and dilute suspension regions takes place even in the dense zones close to walls and at bed bottom, there the gas seems to travel more uniformly through both dense and dilute regions causing a significant drag force. Most particles in the bottom bed are located in the dense regions where the drag coefficient given by Ergun and Wen & Yu equations is high. Since the average drag force is by nature a volume-fraction-weighted property i.e. a Favre average, it is natural that C_{drag} can exceed unity in a dense suspension. At the packing limit the calculated values of C_{drag} are, in accordance with the definition of the drag correction coefficient, equal to unity.

Significant changes in the fluidization velocity affect the fluidization mode, which has great impact on the flow patterns and on the division of the suspension in dilute and dense suspension regions. Smaller changes in the fluidization velocity however do not affect the flow patterns in any significant way, especially in CFB conditions. Fig. 14 shows examples of effects of fluidization velocity in two cases. Even significant changes in fluidization velocities seem to be possible without any major change in C_{drag} in the dilute conditions. In the dense end of the scale the effects of the fluidization velocity are more pronounced. Fig. 14 b shows a case where the fluidization state changes from BFB to CFB as the fluidization velocity increases from 1.25 m/s to 2.75 m/s. This change is clearly visible in the results: in CFB conditions, the values of C_{drag} above unity occur at higher volume fractions than in BFB conditions.

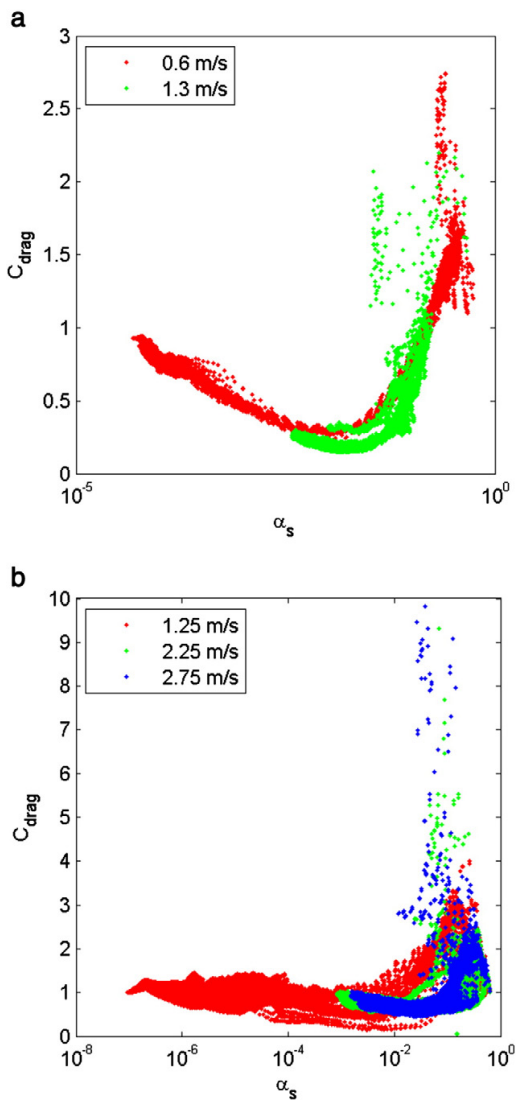

Fig. 14. Effect of fluidization velocity in different conditions: a) Cases 3 and 4 (μ_g = 4.45e–5 kg/ms, ρ_g = 0.311 kg/m^3, ρ_s = 2480 kg/m^3, d_p = 0.15 mm) and b) Cases 26, 27, and 28 (μ_g = 1.79e–5 kg/ms, ρ_g = 1.225 kg/m^3, ρ_s = 2480 kg/m^3, d_p = 0.255 mm).

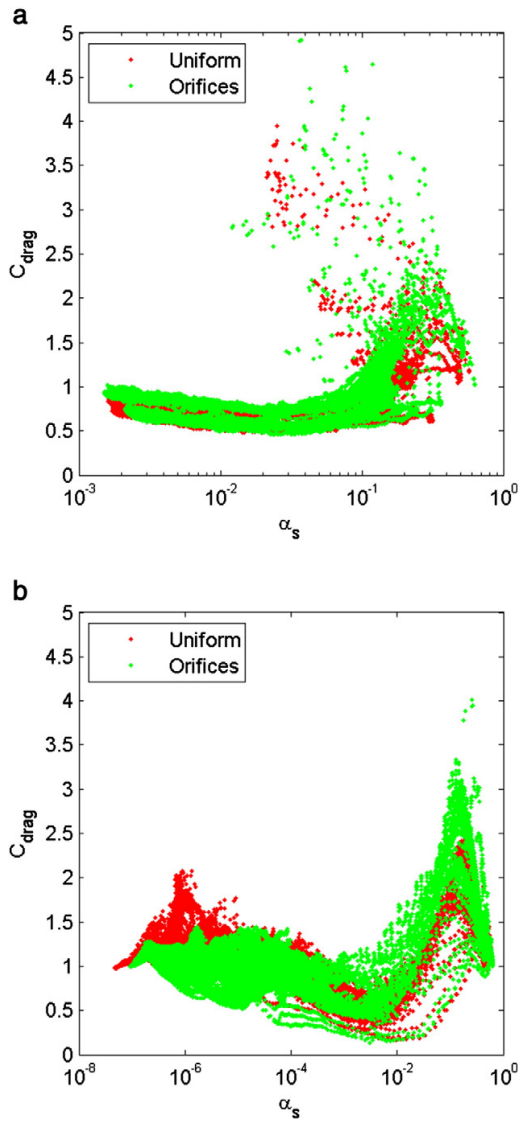

Fig. 15. Effect of orifices in different fluidization conditions: a) CFB Cases 25 and 29 (μ_g = 1.79e–5 kg/ms, ρ_g = 1.225 kg/m^3, ρ_s = 2480 kg/m^3, d_p = 0.255 mm. U_0 = 2.75 m/s), and b) in BFB Cases 23 and 27 (μ_g = 1.79e–5 kg/ms, ρ_g = 1.225 kg/m^3, ρ_s = 2480 kg/m^3, d_p = 0.255 mm. U_0 = 1.25 m/s).

Not only the fluidization velocity but also the way the air is introduced into the riser affects the flow structure. In the previous 2D analysis [7], air distribution was reported to have significant effects on C_{drag} in BFB conditions. Fig. 15 shows the effect of air distribution on C_{drag} in the 3D simulations in CFB and BFB conditions. The geometry in the simulations is a pseudo-2D bed where the orifices are assumed to reach from wall to wall in the depth direction. In CFB conditions the air distribution doesn't show any effect on C_{drag} whereas in BFB conditions C_{drag} increases when the gas flow is divided into separate nozzles. Thus air distributor design should be taken into account in drag modeling. In practice, this can be difficult in which case the possible effects of the air distributor design should be considered in the interpretation of the simulation results as a possible source of inaccuracy.

3.6. Effects of material properties

The previous 2D study [8] showed that the effects of material properties on C_{drag} cannot be described by means of a dimensionless number. Thus the effect of each material property needs to be considered separately. In the previous 2D study of the time-averaged drag force in CFB conditions [8], solid phase density and particle size were found to affect C_{drag}. Both parameters showed a positive effect, i.e. an increase in both particle size or solid material density increased C_{drag}. In BFB conditions [7] the effect of particle size was similar but the effect of density was not positive in all situations. Similar comparison on the basis of the 3D data of this study is presented in Figs. 16 and 17. Fig. 16 shows a positive effect of solid density at low solid concentrations and a negative effect in regions of high solid concentration. The effect of particle size, shown in Fig. 17, is of the same nature but even stronger. However, when reduced particle size leads to a change in the fluidization mode, like in Fig. 17b, the effect of the particle size is complicated, since the highest values of C_{drag} occur in BFBs and CFBs at different ranges of solid volume fractions, as seen in Fig. 17b.

In the earlier 2D studies [7,8], gas phase density was not found to have any significant effect on the drag correction coefficient. However, the range inside which gas density was varied was quite narrow, i.e. the range typically encountered in fluidization with air at atmospheric pressures. At elevated pressures gas density can be significantly higher. Fig. 18 shows a comparison in which gas density was changed while other parameters were kept constant. When the change in gas density is small, i.e. inside the range typical of fluidization at the atmospheric pressure, C_{drag} remains unchanged. At the higher gas density of 6 kg/m^3 in Case 11 shown in Fig. 18, significant effects on C_{drag} occur in the whole range of solid concentrations.

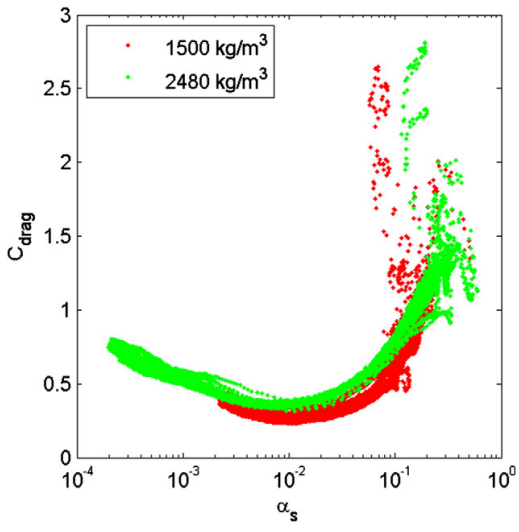

Fig. 16. Effect of solid material density on C_{drag} in different conditions: Cases 14 and 7 (μ_g = 4.45e–5 kg/ms, ρ_g = 1.225 kg/m^3, d_p = 0.255 mm. U_0 = 1.3 m/s).

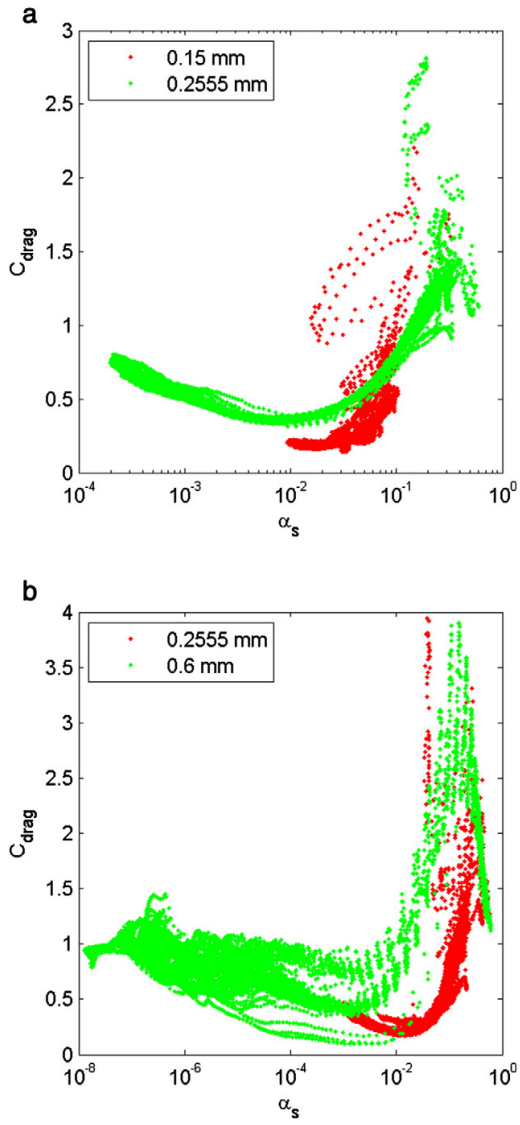

Fig. 17. Effect of particle size on C_{drag} in different conditions: a) Cases 13 and 7 (μ_g = 4.45e–5 kg/ms, ρ_g = 1.255 kg/m^3, ρ_s = 2480 kg/m^3, U_0 = 1.3 m/s), and b) Cases 5 and 2 (μ_g = 4.45e–5 kg/ms, ρ_g = 0.311 kg/m^3, ρ_s = 2480 kg/m^3, U_0 = 2.75 m/s).

The previous 2D studies [7,8] showed that gas viscosity affects C_{drag} negatively. Same qualitative conclusion can be drawn from the 3D results presented in Fig. 19.

4. Conclusions

In the present work, a qualitative analysis of the time-averaged gas–solid drag force in a fluidized bed is carried out. The average drag force is expressed as a product of the drag force calculated from the time-averaged velocities and volume fractions and a correction coefficient.

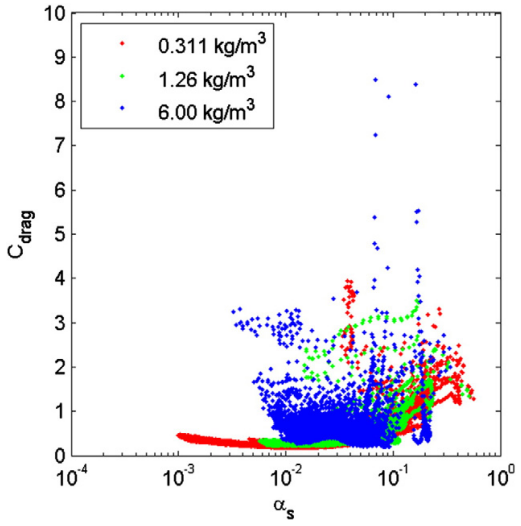

Fig. 18. Effect of gas density on C_{drag} in different conditions: Cases 5, 8 and 11 ($\mu_g = 4.45e{-}5$ kg/ms, $\rho_s = 2480$ kg/m^3, $d_p = 0.255$ mm, $U_0 = 2.75$ m/s).

The analysis is based on a large number of transient 3D simulations of small bubbling, turbulent and circulating fluidized beds. The results are compared with corresponding 2D data and the earlier parametric studies [7,8] carried out on the basis of results from transient 2D CFD simulations. Some of the trends observed in the 2D data are also seen in the 3D analysis, and especially at low solid concentrations, the results are even quantitatively close to each other. In dense regions the results of the present 3D study strongly deviate from the earlier 2D results, which confirms that to accurately model gas–solid drag force in a 3D steady state simulation, the drag model has to be based on data from 3D transient simulations.

To save computational time, most of the simulations in the present work were carried out for a small, pseudo-2D fluidized bed geometry in which the depth of the bed could be described by only three grid points. Comparisons with cases of larger dimensions were also carried out to confirm that the limited geometry didn't significantly affect the conclusions.

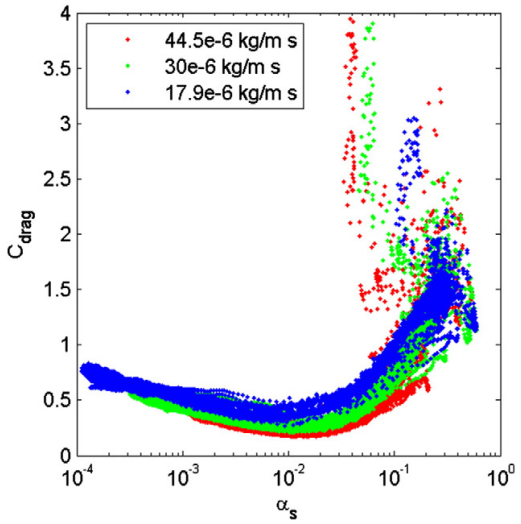

Fig. 19. Effect of gas viscosity on C_{drag} in different condition: Cases 5, 12 and 9 ($\rho_g = 0.311$ kg/m^3, $\rho_s = 2480$ kg/m^3, $d_p = 0.255$ mm, $U_0 = 2.75$ m/s).

The parametric study showed that solid volume fraction, particle size, solid density, gas viscosity, the slip velocity between gas and solids and the lateral distance to a wall have significant effects on the drag correction coefficient. At high gas densities typical of pressurized fluidization even the gas density has a significant effect. A general closure model for the time-averaged drag force in a fluidized bed should be based on these seven variables.

Acknowledgments

The authors gratefully acknowledge the financial support of Tekes, VTT Technical Research Centre of Finland, Etelä-Savon Energia Oy, Fortum, Metso Power Oy and Numerola Oy, and the support from Saarijärven Kaukolämpö Oy (Tekes Dnro 2022/31/2010).

References

[1] Y. Igci, S. Sundaresan, S. Pannala, O'brienT. , R.W. Breault, Coarse-Graining of Two-Fluid Models for Fluidized Gas-Particle Suspensions, 5th Int. Conf. on CFD in the Process Industries, CSIRO, Melbourne, Australia, 2006.
[2] D.Z. Zhang, W.B. VanderHeyden, The effects of mesoscale structures on the macroscopic momentum equations for two-phase flows, Int. J. Multiphase Flow 28 (2002) 805–822.
[3] S. Shah, J. Ritvanen, T. Hyppänen, S. Kallio, Wall effects on space averaged two-fluid model equations for simulations of gas-solid flows in risers, Chem. Eng. Sci. 89 (2013) 206–215.
[4] C.C. Milioli, F.E. Milioli, W. Holloway, K. Agrawal, S. Sundaresan, Filtered two-fluid models of fluidized gas-particle flows: new constitutive equations, 59 (2013) 3265–3275.
[5] V. Taivassalo, S. Kallio, J. Peltola, On time-averaged CFD modeling of circulating fluidized beds, Int. J. Nonlinear Sci. Numer. Simul. 13 (2012) 363–373.
[6] Zh.X. Zeng, L.X. Zhou, A two-scale second-order moment particle turbulence model and simulation of dense gas–particle flows in a riser, Powder Technol. 162 (2006) 27–32.
[7] S. Kallio, J. Peltola, T. Niemi, Modeling of the time-averaged gas–solid drag force in a fluidized bed based on results from transient 2D Eulerian–Eulerian simulations, Powder Technol. 261 (2014) 257–271.
[8] S. Kallio, J. Peltola, T. Niemi, Parametric study of the time-averaged gas–solid drag force in circulating fluidized bed conditions, Powder Technol. 257 (2014) 20–29.
[9] E. Esmaili, N. Mahinpey, Adjustment of drag coefficient correlations in three dimensional CFD simulation of gas–solid bubbling fluidized bed, Adv. Eng. Softw. 42 (2011) 375–386.
[10] T. Li, J. Grace, X. Bi, Study of wall boundary condition in numerical simulations of bubbling fluidized beds, Powder Technol. 203 (2010) 447–457.
[11] ANSYS Inc., ANSYS FLUENT Theory Guide. Release 14.0, Canonsburg, 2011. (2011).
[12] M. Syamlal, W. Rogers, T.J. O'Brien, MFIX Documentation: Volume 1, Theory Guide, National Technical Information Service, Springfield, VA, 1993. (DOE/METC-9411004, NTIS/DE9400087).
[13] C.K.K. Lun, S.B. Savage, D.J. Jeffrey, N. Chepurniy, Kinetic theories for granular flow: inelastic particles in couette flow and slightly inelastic particles in a general flow field, J. Fluid Mech. 140 (1984) 223–256.
[14] D.G. Schaeffer, Instability in the evolution equations describing incompressible granular flow, J. Differ. Equ. 66 (1987) 19–50.
[15] S. Ogawa, A. Umemura, N. Oshima, On the equations of fully fluidized granular materials, J. Appl. Math. Phys. (ZAMP) 31 (1980) 483–493.
[16] D. Gidaspow, Multiphase Flow and Fluidization — Continuum and Kinetic Theory Descriptions, Academic Press, 1994.
[17] S. Ergun, Fluid flow through packed columns, Chem. Eng. Prog. CEP 48 (1952) 89.
[18] C. Wen, Y. Yu, Mechanics of fluidization, Chem. Eng. Prog. Symp. Ser. 62 (1966) 100–111.
[19] S. Kallio, M. Guldén, A. Hermanson, Experimental study and CFD simulation of a 2D circulating fluidized bed, the 20th Int. Conf. on fluidized bed combustion, 2009. (May 18–20, Xi'an, China).
[20] A. Haider, O. Levenspiel, Drag coefficient and terminal velocity of spherical and non-spherical particles, Powder Technol. 58 (1989) 63–70.
[21] W.-C. Yang, Modification and re-interpretation of Geldart's classification of powders, Powder Technol. 171 (2007) 69–74.
[22] T. Niemi, J. Peltola, S. Kallio, Time averaged modeling of BFBs: analysis of the terms in the momentum equations, Proceedings Fluidization XIV Conference, May, Noordwijkerhout, The Netherlands, 2013, pp. 559–566.
[23] T. Li, A. Gel, S. Pennala, M. Shahnam, M. Syamlal, CFD simulations of circulating fluidized bed risers, part i: grid study, Powder Technol. 254 (2014) 170–180.

PAPER VIII

Wall effects on space averaged two-fluid model equations for simulations of gas–solid flows in risers

Chemical Engineering Science 89 (2013) 206–215.

Chemical Engineering Science 89 (2013) 206–215

Contents lists available at SciVerse ScienceDirect

Chemical Engineering Science

journal homepage: www.elsevier.com/locate/ces

Wall effects on space averaged two-fluid model equations for simulations of gas–solid flows in risers

Srujal Shah [a,*], Jouni Ritvanen [a], Timo Hyppänen [a], Sirpa Kallio [b]

[a] LUT Energy, Faculty of Technology, Lappeenranta University of Technology, P.O. Box 20, FI-53851 Lappeenranta, Finland
[b] VTT Technical Research Centre of Finland, P.O. Box 1000, FI-02044 VTT, Finland

HIGHLIGHTS

- Two-fluid model was used for numerical simulation of gas–solid flow in a riser with Geldart group B particles.
- Space averaging applied over the gas–solid drag and the convective term to analyze the subgrid-scale modeling.
- Wall effects were studied for subgrid-scale models.
- Subgrid-scale models showed dependence on distance from the wall, averaging size and solid volume fraction.
- Results obtained for Geldart group B particles clearly differ from those presented in the literature for Geldart group A particles.

ARTICLE INFO

Article history:
Received 4 June 2012
Received in revised form
15 September 2012
Accepted 16 November 2012
Available online 5 December 2012

Keywords:
Circulating fluidized bed
Computational fluid dynamics
Two-fluid model
Space averaging
Subgrid-scale models
Wall effects

ABSTRACT

For the study of gas–solid flows in a circulating fluidized bed (CFB) riser, the model based on the Eulerian description of phases is widely used. Such a description requires the usage of a fine mesh and a short time step in the numerical simulations. Due to the constraint of long calculation times with fine meshes, it becomes practical to simulate the gas–solid flow in a CFB riser with coarse meshes. This work is the continuation of formulating the subgrid-scale models for the space averaged two-fluid model equations which can be used in coarse mesh simulations of gas–solid flows in risers. In this study, the vertical component of the drag force and the convective term are analyzed and their dependence on the averaging size and solid volume fraction with the distance from the wall is presented.

1. Introduction

Multiphase flows in industrial units such as circulating fluidized beds are heterogeneous and exhibit large fluctuations over spatiotemporal scales. The modeling of gas–solid two-phase flows in a CFB riser is mainly done with the use of a two-fluid model (Anderson and Jackson, 1967; Gidaspow, 1994; Lun et al., 1984). In the two-fluid model formulation, both phases are treated as interpenetrating continua. The continuity and momentum equations are solved for both phases. The closure models for the solid phase momentum equation based on the kinetic theory of granular flow can well predict the core-annulus flow regime (Benyahia et al., 2007).

Computational fluid dynamics (CFD) simulation of gas–solid flows using a two-fluid model usually requires a very fine mesh to capture the mesoscale structures. This restricts the simulation of large scale fluidized bed units because of infeasible calculation time. For practical calculation purposes, the gas–solid flows in risers are usually simulated with coarse meshes, and as a result, the information about the mesoscale structures in the flow field is lost. This lost information about the mesoscale structures must be retrieved in the form of appropriate closure models when performing coarse mesh size simulations. Many attempts have been made by various research groups for the formulation of closures which can be used in coarse mesh simulations of gas–solid flows in risers (Agrawal et al., 2001; De Wilde, 2005; Igci et al., 2008; Wang and Li, 2007; Yang et al., 2004; Zhang and VanderHeyden, 2002).

When Reynolds averaging is applied to the Navier–Stokes equations as in the single phase flow, there is a need to model the Reynolds stresses which arise from the velocity fluctuations.

* Corresponding author. Tel.: +358 40 173 5672.
E-mail address: srujal.shah@lut.fi (S. Shah).

0009-2509/$ - see front matter © 2012 Elsevier Ltd. All rights reserved.
http://dx.doi.org/10.1016/j.ces.2012.11.020

Similarly, for two-phase gas–solid flows, the macroscopic averaging approach, also known as filtering approach, is applied over the equations. Different macroscopic averaging approaches such as ensemble phase averaging (Zhang and VanderHeyden, 2002), time averaging (Benyahia, 2008; Hrenya and Sinclair, 1997; Kallio et al., 2008) and space averaging (Igci et al., 2008; Shah et al., 2012) have been performed over the two-fluid model equations.

All these averaging approaches result for the need to develop the closure models. Kallio et al. (2008) analyzed different terms in the momentum equation to study the magnitude of the closure models by performing time averaging over the equations. In their analysis, the main terms which showed highest magnitude were the gas–solid drag force and the Reynolds stresses arising from the velocity fluctuations. Igci et al. (2008) showed in their analysis that the contribution from the Reynolds stresses is much larger than the particle phase stress and also the contribution from the drag force is much larger than the term arising from the correlation between the fluctuations in the solid volume fraction and in the pressure gradient.

During the last decade, the gas–solid drag force is the term which has received highest attention when seeking the closures for the coarse mesh simulations. For example, the approach used in the energy-minimization multi-scale (EMMS) model has concentrated only on the drag force term when performing coarse mesh simulations (Wang and Li, 2007; Yang et al., 2004). For the filtered model equations, subgrid-scale modeling of the drag force is very important. In the filtered two-fluid model equations, details about the filtered drag coefficient is presented (Igci et al., 2008). Also, in the time averaging studies by Kallio et al. (2008), the importance of correction to the drag force was presented. Coarse mesh simulation results into the loss of information about the mesoscale structures of the flow field, which leads to uniform solids concentration profiles and eventually higher solids mass flux. Thus, there is a need to correct the overestimated drag force which consequently reduces the higher solids mass flux.

Another important issue which has raised attention for the closures in the filtered two-fluid model equations is the effects caused due to the bounding walls. Igci and Sundaresan (2011) recognized the need of wall correction to the filtered drag coefficient, the filtered particle phase normal stress and the filtered particle phase shear viscosity, and formulated closure models based on the distance from the wall. Recently, Igci et al. (2012) used the idea of including the wall corrections in their simulations for different mesh sizes and obtained a reasonable agreement with experimental results. They showed that the results predicted by the filtered two-fluid model equations are nearly filter length independent. The study by Igci et al. (2012) shows the feasibility of space averaging approach in which the closure models obtained from the fine mesh simulation are applied to the coarse mesh simulation. The study of Igci and Sundaresan (2011) dealt with FCC particles belonging to Geldart group A. In the present study, a case of larger Geldart group B particles in a wider solids volume fraction range is analyzed.

In this work, the same methodology of space averaging over the two-fluid model equations as used by Igci et al. (2008) has been followed. A two-dimensional fine mesh simulation of the gas–solid flow in a CFB riser using the two-fluid model was performed in the CFD package Fluent 6.3.26. The simulation results are then space averaged over different averaging sizes to analyze the behavior of subgrid-scale models which can be used for coarse mesh simulations.

Space averaging on the two main terms, vertical component of the drag force term and the convective term, in the two-fluid model, has been performed and then the behavior of the subgrid-scale models for different averaging sizes and solid volume fraction values is analyzed. The same notations are used in this work which were defined in our prior study (Shah et al., 2012). The obtained results showed strong dependence of the subgrid-scale models on the averaging size and solid volume fraction values as a function of distance from the wall. To explain the observed behavior of the correction factor in the different averaging regions, the standard deviations of different variables were calculated to evaluate the fluctuation characteristics of the flow properties as function of the lateral coordinate.

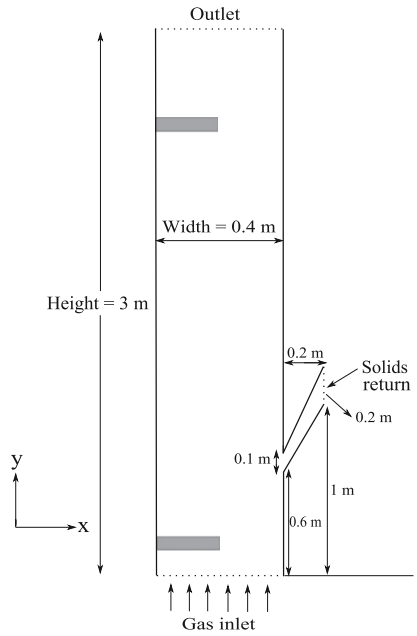

Fig. 1. Schematic drawing of the circulating fluidized bed riser and the small channel of the return leg. The selected areas seen in the lower and upper parts of the riser will be referred to later. The solid lines along the riser height and in the return leg channel represent the walls.

2. Methodology

2.1. Domain for CFD simulation

Kallio et al. (2009) give a systematic description of the experimental unit and validate the CFD modeling method by comparing measurements with results obtained from a CFD simulation, where the same models and mesh as in the present paper were used. The main components of the CFB unit include a riser, a solid separation unit, and a return leg with a loop seal. The dimensions of the CFB riser are as follows; 3 m height, 0.4 m width, and 0.015 m depth. As mentioned in Agrawal et al. (2001), ideally, 3D simulations are better than 2D simulations. In gas–solid flow systems, the qualitative analysis of heterogeneous structures can be studied by 2D simulations. In the experimental unit of our case study, we had very small depth of 0.015 m which is too small to study the fluctuations in the third direction. For this reason, our simulation was only conducted in 2D. At the bottom of the riser, an uniform gas inlet was assumed due to the difficulties in defining the computational mesh near the nozzles as located in the experiments. During the measurement, the fluidization gas velocity was 3.5 m/s and the average solids inventory in the CFB riser was about 2.5 kg. A schematic of the geometry is shown in Fig. 1.

Table 1
Governing equations and the closure models used in this study.

Gas phase (continuity and momentum equations)

$$\frac{\partial}{\partial t}(\alpha_g\rho_g)+\nabla\cdot(\alpha_g\rho_g\vec{v}_g)=0,$$
$$\frac{\partial}{\partial t}(\alpha_g\rho_g\vec{v}_g)+\nabla\cdot(\alpha_g\rho_g\vec{v}_g\vec{v}_g)=-\alpha_g\nabla p+\nabla\cdot(\bar{\bar{\tau}}_g+\alpha_g\bar{\bar{\tau}}_t)+\alpha_g\rho_g\vec{g}+K_{sg}(\vec{v}_s-\vec{v}_g).$$

Solid phase (continuity and momentum equations)

$$\frac{\partial}{\partial t}(\alpha_s\rho_s)+\nabla\cdot(\alpha_s\rho_s\vec{v}_s)=0,$$
$$\frac{\partial}{\partial t}(\alpha_s\rho_s\vec{v}_s)+\nabla\cdot(\alpha_s\rho_s\vec{v}_s\vec{v}_s)=-\alpha_s\nabla p+\nabla\cdot\bar{\bar{\tau}}_s-\nabla p_s+\alpha_s\rho_s\vec{g}+K_{gs}(\vec{v}_g-\vec{v}_s).$$

Modified $\kappa-\epsilon$ turbulence model for gas phase

$$\frac{\partial}{\partial t}(\alpha_g\rho_g\kappa)+\nabla\cdot(\alpha_g\rho_g\vec{v}_g\kappa)=\nabla\cdot\left(\alpha_g\frac{\mu_t}{\sigma_\kappa}\nabla\kappa\right)+\alpha_g\bar{\bar{\tau}}_t:\nabla\vec{v}_g-\alpha_g\rho_g\epsilon+\Pi_\kappa,$$
$$\frac{\partial}{\partial t}(\alpha_g\rho_g\epsilon)+\nabla\cdot(\alpha_g\rho_g\vec{v}_g\epsilon)=\nabla\cdot\left(\alpha_g\frac{\mu_t}{\sigma_\epsilon}\nabla\epsilon\right)+\alpha_g\frac{\epsilon}{\kappa}(C_{1\epsilon}\bar{\bar{\tau}}_t:\nabla\vec{v}_g-C_{2\epsilon}\rho_g\epsilon)+\Pi_\epsilon.$$

Granular energy equation

$$\frac{3}{2}\left[\frac{\partial}{\partial t}(\rho_s\alpha_s\Theta_s)+\nabla\cdot(\rho_s\alpha_s\vec{v}_s\Theta_s)\right]=(-p_s\bar{\bar{I}}+\bar{\bar{\tau}}_s):\nabla\vec{v}_s+\nabla\cdot(k_{\Theta_s}\nabla\Theta_s)-\gamma_{\Theta_s}+\phi_{gs}.$$

Interphase momentum exchange coefficient (Gidaspow et al., 1992)

when $\alpha_g>0.8$, $K_{gs}=\frac{3}{4}C_D\frac{\alpha_s\alpha_g\rho_g|\vec{v}_s-\vec{v}_g|}{d_s}\alpha_g^{-2.65}$,

where $C_D=\frac{24}{\alpha_g Re}[1+0.15(\alpha_g Re)^{0.687}]$ and $Re=\frac{\rho_g|\vec{v}_s-\vec{v}_g|d_s}{\mu_g}$,

when $\alpha_g\le 0.8$, $K_{gs}=150\frac{\alpha_s(1-\alpha_g)\mu_g}{\alpha_g d_s^2}+1.75\frac{\rho_g\alpha_s|\vec{v}_s-\vec{v}_g|}{d_s}$.

Phase stress–strain tensors

$$\bar{\bar{\tau}}_g=\alpha_g\mu_g(\nabla\vec{v}_g+\nabla\vec{v}_g^{\,T})-\frac{2}{3}\alpha_g\mu_g\nabla\cdot\vec{v}_g\bar{\bar{I}},\quad\text{where }\bar{\bar{I}}\text{ is the identity tensor,}$$
$$\bar{\bar{\tau}}_t=\mu_t(\nabla\vec{v}_g+\nabla\vec{v}_g^{\,T})-\frac{2}{3}(\rho_g\kappa+\mu_t\nabla\cdot\vec{v}_g)\bar{\bar{I}},\quad\text{where }\mu_t=\rho_g C_\mu\frac{\kappa^2}{\epsilon},$$
$$\bar{\bar{\tau}}_s=\alpha_s\mu_s(\nabla\vec{v}_s+\nabla\vec{v}_s^{\,T})+\alpha_s\left(\lambda_s-\frac{2}{3}\mu_s\right)\nabla\cdot\vec{v}_s\bar{\bar{I}}.$$

Turbulence exchange terms between the gas and solid phases

$$\Pi_\kappa=K_{sg}(\kappa_{sg}-2\kappa),\quad\Pi_\epsilon=C_{3\epsilon}\frac{\epsilon}{\kappa}\Pi_\kappa.$$

Covariance of the velocities of gas and solid phases

$$\kappa_{sg}=2\kappa\left(\frac{b+\eta_{sg}}{1+\eta_{sg}}\right),\quad\text{where }b=1.5\left(\frac{\rho_s}{\rho_g}+0.5\right)^{-1}\text{ and }\eta_{sg}=\frac{\tau_{t,sg}}{\tau_{F,sg}}.$$

Lagrangian integral time scale

$$\tau_{t,sg}=\frac{\frac{3}{2}C_\mu\frac{\kappa}{\epsilon}}{\sqrt{1+\frac{3}{2}(1.8-1.35\cos^2\psi)\frac{|\vec{v}_g-\vec{v}_s|^2}{\kappa}}}$$

Particle relaxation time scale

$$\tau_{F,sg}=\frac{\alpha_s\rho_g}{K_{sg}}\left(\frac{\rho_s}{\rho_g}+0.5\right).$$

Solids shear viscosity,
$\mu_s=\mu_{s,col}+\mu_{s,kin}$ (Syamlal et al., 1993) $+\mu_{s,fr}$ (Schaeffer, 1987)

$$\mu_s=\frac{4}{5}\alpha_s\rho_s d_s g_{0,ss}(1+e_{ss})\left(\frac{\Theta_s}{\pi}\right)^{1/2}+\frac{\alpha_s\rho_s d_s\sqrt{\Theta_s\pi}}{6(3-e_{ss})}\left[1+\frac{2}{5}(1+e_{ss})(3e_{ss}-1)\alpha_s g_{0,ss}\right]+\frac{p_s\sin\theta}{2\sqrt{I_{2D}}}$$

Granular bulk viscosity (Lun et al., 1984)

$$\lambda_s=\frac{4}{3}\alpha_s\rho_s d_s g_{0,ss}(1+e_{ss})\left(\frac{\Theta_s}{\pi}\right)^{1/2}.$$

Solids pressure (Lun et al., 1984)

$$p_s=\alpha_s\rho_s\Theta_s+2\rho_s(1+e_{ss})\alpha_s^2 g_{0,ss}\Theta_s.$$

Table 1 (*continued*)

Radial distribution function

$$g_{0,ss}=\left[1-\left(\frac{\alpha_s}{\alpha_{s,max}}\right)^{1/3}\right]^{-1}.$$

Diffusion coefficient for granular energy (Syamlal et al., 1993)

$$k_{\Theta_s}=\frac{15d_s\rho_s\alpha_s\sqrt{\Theta_s\pi}}{4(41-33\eta)}\left[1+\frac{12}{5}\eta^2(4\eta-3)\alpha_s g_{0,ss}+\frac{16}{15\pi}(41-33\eta)\eta\alpha_s g_{0,ss}\right],\quad\text{where}$$
$$\eta=\frac{1}{2}(1+e_{ss}).$$

Collisional dissipation of energy (Lun et al., 1984)

$$\gamma_{\Theta_s}=\frac{12(1-e_{ss}^2)g_{0,ss}}{d_s\sqrt{\pi}}\rho_s\alpha_s^2\Theta_s^{3/2}.$$

Energy exchange between the gas and solid phase

$$\phi_{gs}=-3K_{gs}\Theta_s.$$

2.2. CFD model and simulation

The two-fluid model was used for simulating the flow dynamics of the gas–solid flow in the CFB riser. There are several researchers who have performed CFD studies of the gas–solid flow in a CFB riser using the two-fluid model approach (Cabezas-Gómez et al., 2006; De Wilde et al., 2003; Hartge et al., 2009; Wang et al., 2010; Yang et al., 2004). For gas phase turbulence, a modified form of the standard $\kappa-\epsilon$ model was used with extra terms that include the interphase turbulence exchange terms. The closure models for the solid phase momentum equation are based on the kinetic theory of granular flow. In addition to the continuity and momentum equations for both phases, the granular energy equation is solved for calculating the granular temperature, which is then used to close the terms solid phase stress and solids pressure. The governing equations and the selected closure models used in this study are listed in Table 1.

The phase coupled SIMPLE algorithm was used for pressure-velocity coupling. The first order implicit for time-stepping, the first order upwind for volume fraction, and the second order upwind for the other convective terms were used as discretization schemes. The relative error between two successive iterations for each scaled residual component was below 1e−03 for most of the time steps. For the boundary conditions at the walls, the free-slip condition was used for the gas phase and Johnson and Jackson's model of the partial-slip condition with a value of 0.001 for the specularity coefficient and a value of 0.2 for the particle-wall restitution coefficient was used for the solid phase. Same values were used in Kallio et al. (2009) where a good fit to measurement data was obtained. The mass flow rate of solids at the solids return was kept the same as that at the outlet, thus maintaining the overall solid volume fraction in the riser as constant. The total simulation time was 215 s, in which the first 35 s was used to obtain the stable state operating condition, and the averaging and post-processing of the results were performed over the last 180 s. A summary of the parameters used in the CFD simulation are listed in Table 2. Although the fine mesh and short time step considered here are not highly resolved to study the smallest fluctuations in the flow field, they still capture essential features when performing the simulation. The same time step and mesh spacing were used in Kallio et al. (2011) where the simulated and measured variances of solid volume fraction showed good agreement.

3. Results and discussion

3.1. Space averaging on the drag model

In this work, a fine mesh simulation of the gas–solid flow in a CFB riser using the two-fluid model was performed. The mesh cell size used in the simulation was $0.625 \times 0.625\ \text{cm}^2$ (The aspect ratio $\delta x : \delta y$ in this simulation was 1:1). Space averaging was applied on the drag model for three different averaging sizes, $1.25 \times 1.25\ \text{cm}^2$, $2.5 \times 2.5\ \text{cm}^2$, and $5 \times 5\ \text{cm}^2$. Shah et al. (2012) studied the effect of different time step sizes in simulations and the difference was insignificant at least in the range investigated. Thus, no time averaging is considered here. The same type of notations are used here which were used in our previous study (Shah et al., 2012). For a constant time scale, the space averaging on the vertical drag force model can be mathematically given as

$$^{\Delta x}\langle {}^{\delta x}_{\delta t}(K_{gs}(v_{g,y}-v_{s,y}))\rangle = \omega K^{*}_{gs}(\tilde{v}_{g,y}-\tilde{v}_{s,y}), \tag{1}$$

where ω is the correction factor for the drag force term to be found, K^{*}_{gs} is the interphase momentum exchange coefficient calculated from averaged variables, and $\tilde{v}_{g,y}$ and $\tilde{v}_{s,y}$ are the averaged phase velocities defined accordingly as

$$\tilde{v}_{g,y} = \frac{^{\Delta x}\langle {}^{\delta x}_{\delta t}(\alpha_g v_{g,y})\rangle}{^{\Delta x}\langle {}^{\delta x}_{\delta t}\alpha_g\rangle} \quad \text{and} \quad \tilde{v}_{s,y} = \frac{^{\Delta x}\langle {}^{\delta x}_{\delta t}(\alpha_s v_{s,y})\rangle}{^{\Delta x}\langle {}^{\delta x}_{\delta t}\alpha_s\rangle}. \tag{2}$$

In this study, the mesh spacing in the transient simulation, δx, is 0.625 cm and the time step, δt, is 0.001 s. The region over which the averaging is carried out is given as Δx. On the left-hand side of Eq. (1), the transient values of the vertical drag force were calculated for the cells with size $0.625 \times 0.625\ \text{cm}^2$ for the selected areas in the lower and upper parts of the riser (see Fig. 1). These transient values of the vertical drag force are averaged over the cells which fit to the different averaging sizes (for example, 4 cells with the averaging size $1.25 \times 1.25\ \text{cm}^2$, 16 cells with the averaging size $2.5 \times 2.5\ \text{cm}^2$, and 64 cells with the averaging size $5 \times 5\ \text{cm}^2$). Thus, a transient series of the averaged vertical drag force is obtained as the left-hand side of Eq. (1). On the right-hand side of Eq. (1), the same logic has been applied for the drag force model which is calculated based on the averaged variables defined according to Eq. (2).

The correction factor ω can be written as the ratio of the averaged drag force and the drag force calculated from averaged

Table 2
Summary of parameters for the CFD simulation.

Gas density, ρ_g	1.225 kg/m^3
Gas viscosity, μ_g	1.7894×10^{-5} kg/ms
Solid particle density, ρ_s	2480 kg/m^3
Solid particle diameter, d_s	385×10^{-6} m
Fluidization gas velocity	3.5 m/s
Mesh cell size (cm^2)	0.625×0.625
Time step size (s)	0.001
Maximum packing limit, $\alpha_{s,max}$	0.63
Restitution coefficient, e_{ss}	0.9

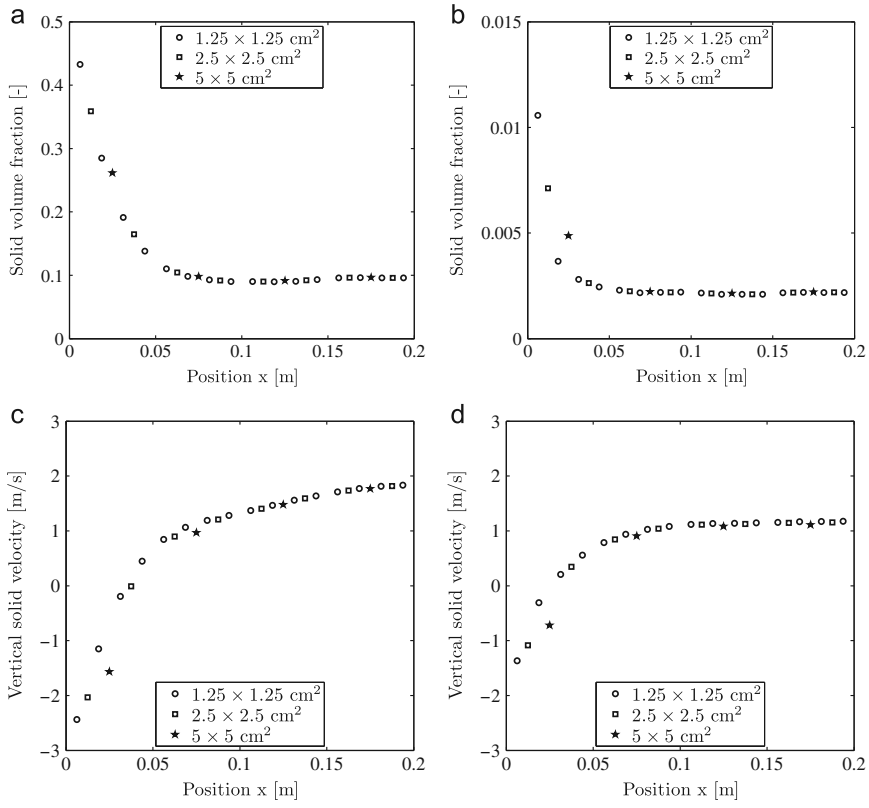

Fig. 2. Profiles of time-averaged values of solid volume fraction and vertical solid velocity for different averaging sizes. (a and c) The profiles at the height $y=0.175$ m and (b and d) the profiles at the height $y=2.475$ m.

variables. Time instant values of correction factors can be obtained for the different regions of the averaging sizes $1.25 \times 1.25\ cm^2$, $2.5 \times 2.5\ cm^2$, and $5 \times 5\ cm^2$. The statistical averages of correction factor values based on the approximate bin size of 0.008 of averaged solid volume fraction were calculated.

3.1.1. Averaged profiles in horizontal direction

To be able to interpret the results on the correction factor, it is useful to first study the horizontal profiles of the solid volume fraction and the vertical solid velocity. This is done in this section at two different heights for different averaging sizes. Fig. 2a and b shows the averaged (in time) profiles of the solid volume fraction for different averaging sizes. The profiles show similar behavior for different averaging sizes with high concentration near the walls and lower concentration towards the center of the riser. Fig. 2c and d shows the averaged (in time) profile of the vertical solid velocity for different averaging sizes calculated according to Eq. (2). From the velocity profiles, the downflow region of solids at the wall for different averaging sizes can be observed. For the averaging size of $1.25 \times 1.25\ cm^2$, the profile shows that solids flow downward within the distance of 0.0375 m in the lower part and 0.025 m in the upper part from the wall of the riser. As the size of the averaging region increases, the detailed information on the velocity and volume fraction trends in the wall region is lost. Similar loss of information on the averaged profiles is not observed in the riser center.

3.1.2. Fluctuation characteristics using standard deviation

In Igci and Sundaresan (2011) and Shah et al. (2012), the drag correction factor monotonously reduced towards the walls. Igci and Sundaresan (2011) gave as an explanation to this trend that clustering increases towards to the walls. The variation in the solid volume fraction can be used as an indicator of the level of clustering, i.e. how strongly the volume fraction is divided into dense and dilute values. In the literature, the characteristics of solid volume fraction fluctuation have been studied in experimental as well as computational analysis of gas–solid flows in CFB risers. Issangya et al. (2000) studied the standard deviation of the voidage for different solids flux and superficial air velocity conditions in a high-density CFB riser. Wang (2008) performed high-resolution Eulerian simulation and studied the solid volume fraction fluctuation using the root mean square approach. Kallio et al. (2011) presented the fluctuation characteristics of the solid volume fraction in a CFB and observed similar trends in results obtained from experimental measurements and CFD simulations. The fluctuations are, by definition, zero at zero volume fraction and at the packing limit. Fluctuations in the solid volume fraction are presented by a roughly parabolic curve as a function of the average solid volume fraction, with the peak at half of the volume fraction of a packed bed, i.e. around solid volume fraction of about 0.3. In Kallio et al. (2011) it was observed in a similar study of Geldart group B particles that at the same average volume fraction in the wall layer and in the core, the volume fraction fluctuations are stronger in the core than at the wall, which is contrary to what was stated by Igci and Sundaresan (2011).

To further study the validity of the explanation by Igci and Sundaresan (2011), the variations in the solid volume fraction and other flow properties are studied in the following. Several variables and combinations of variables were investigated of which the most interesting ones are shown here. Fig. 3 shows the variation in the standard deviations of solid volume fraction, slip velocity and drag coefficient for different averaging sizes. The analysis is here presented at the height of $y=0.175$ m where the solid volume fraction varies in a wide range. Fig. 3 clearly shows

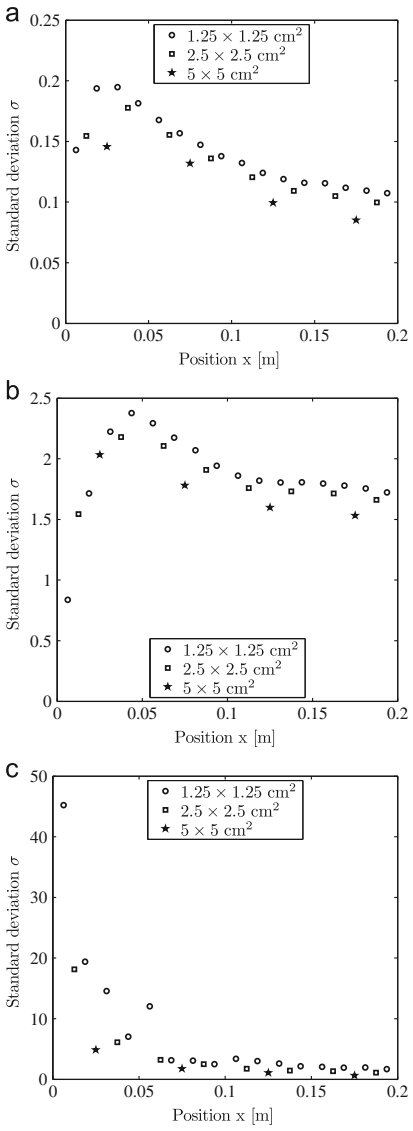

Fig. 3. Standard deviation of (a) solid volume fraction, (b) slip velocity and (c) drag coefficient for different averaging sizes. The analysis was carried out at the height $y=0.175$ m.

the dependence of standard deviation values with the averaging sizes. The standard deviation values start to decrease as the averaging size is increased. In Fig. 3a, the peak in the standard deviation profile indicates that there is the largest solid volume fraction fluctuation a couple of centimeters from the wall, where the average solid volume fraction is close to 0.3, which is in accordance with the observations in the literature. The behavior of the standard deviation of slip velocity is quite similar to the standard deviation of solid volume fraction.

It can be seen from Fig. 3 that the fluctuations of solid volume fraction and slip velocity do not give any explanation for the lower values of the correction factor near the walls. According to our analysis, the term in the drag model which gives higher

fluctuations near the walls was C_D. The mathematical model of C_D itself contains the correlation of voidage and slip velocity, which might be interpreted as the reason for higher fluctuations near the wall.

To further evaluate the reason for the low drag correction factor at the wall, the fluctuations in the slip velocity and the drag coefficient were studied for different values of solid volume fractions. Fig. 4a–c shows the standard deviation of the slip velocity for different averaging sizes. It can be seen from the figure that the variation in the slip velocity does not clearly differentiate the wall region and the center region. Fig. 5a–c shows the standard deviation of the single particle drag coefficient for different averaging sizes. Magnitude of the fluctuation of the single particle drag coefficient increases with the values of the

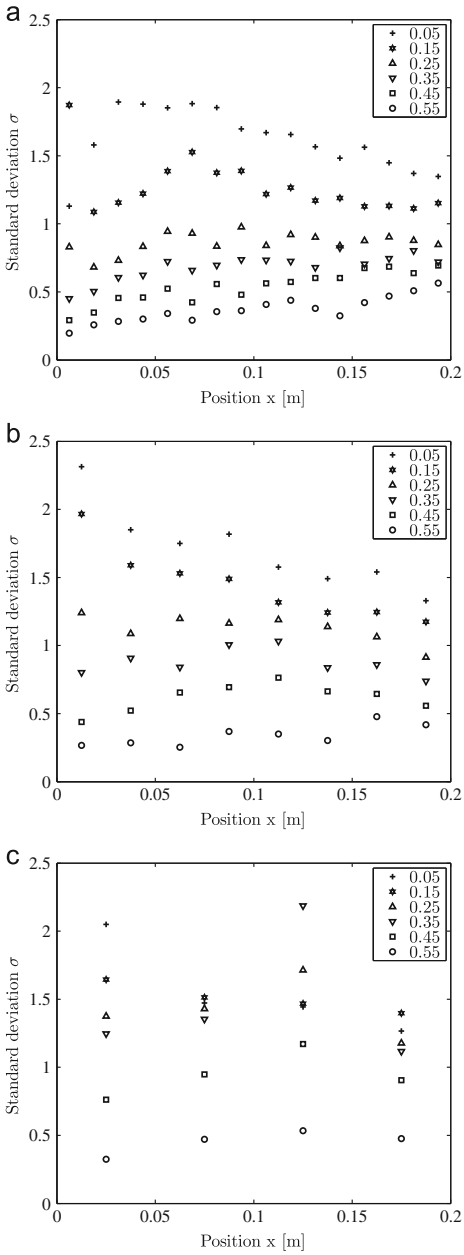

Fig. 4. Standard deviation of slip velocity for different values of solid volume fractions inside the averaging region for averaging sizes (a) 1.25×1.25 cm^2, (b) 2.5×2.5 cm^2 and (c) 5×5 cm^2. The analysis was carried out at the height y=0.175 m.

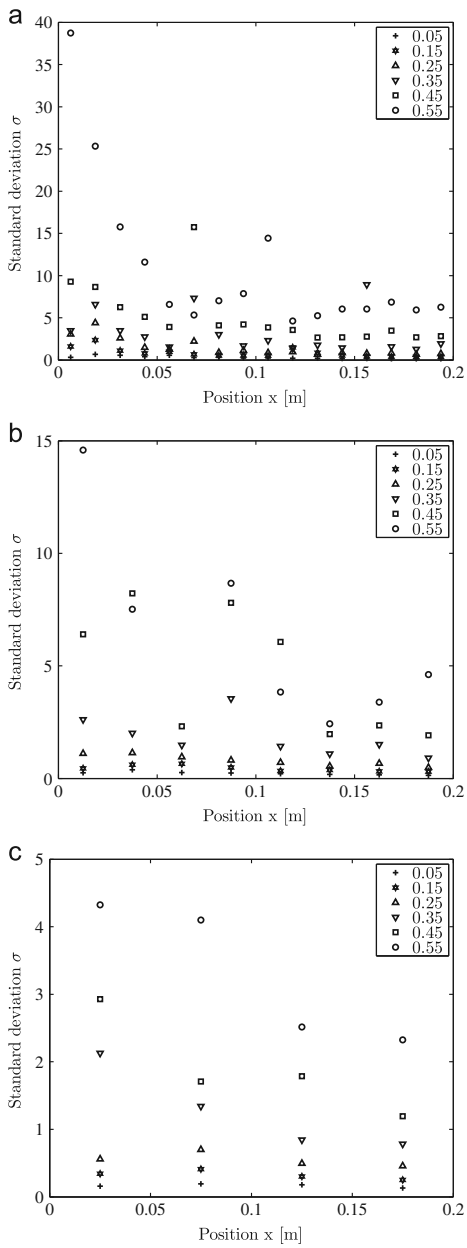

Fig. 5. Standard deviation of single particle drag coefficient for different values of solid volume fractions inside the averaging region for averaging sizes (a) 1.25×1.25 cm^2, (b) 2.5×2.5 cm^2 and (c) 5×5 cm^2. The analysis was carried out at the height y=0.175 m.

solid volume fraction. However, no uniform trend as function of the distance to the wall can be detected. For low solid volume fractions the variations in slip velocity have a tendency to increase towards the walls whereas for high solid volume fractions the fluctuations in the drag coefficient increase towards the walls. The decrease of the drag correction factor towards the walls is thus likely to be a result of complicated interactions between the primary variables and not a direct result of stronger clustering at the wall as was suggested by Igci and Sundaresan (2011).

3.1.3. Effect of solid volume fraction

In this section, we study the variation of the correction factor for different values of solid volume fractions in the averaging region as a function of the distance from the wall. The corresponding behavior of the correction factor for different values of solid volume fraction is shown in Fig. 6 for three different averaging sizes. In their analysis, Igci and Sundaresan (2011) noted that the minimum number of samples over which their statistical averages were carried out was 1000. In our analysis, for lower and moderate values of solid volume fractions, the number of samples was well above 1000. However, for higher values of solid volume fractions, the number of samples was below 1000. We want to note that the somewhat stochastic results shown in the figure for higher values of solid volume fractions may be related to not having a big enough number of samples during averaging. The general trends are still clear. At most solid volume fractions, the smallest values for the correction factor are observed in the wall layer, with a minimum at the location closest to the wall. Fig. 6a–c clearly shows the dependence of correction factor values with respect to solid volume fractions. The correction factor starts to decrease as the averaging size is increased and this observation is similar to the findings of previous works (De Wilde, 2005; Igci et al., 2008). For all the three averaging size cases, the minimum values of the correction factor lies in between the solid volume fraction values of 0.25–0.35 indicating that in this solids concentration range, a big correction to the drag force is necessary. This is understandable since this range of average solid volume fraction allows the largest local variation in the volume fractions produced by the original fine mesh simulation. The low and high average solid concentrations indicate a more uniform suspension density. In the next section, we study the more detailed behavior of the correction factor for different solid volume fraction values.

3.1.4. Effect of averaging sizes

The behavior of the correction factor for the three averaging sizes is shown in Fig. 7 for different values of solid volume fractions. The analysis was done for the selected area in the lower part of the riser so that the whole solid volume fraction range can be considered. Fig. 7a–e shows that in this moderate solid volume fraction range, there is a clear dependence of the correction factor with the averaging sizes. The correction factor decreases as the averaging size is increased. However, this type of behavior is not clearly seen for the higher solid volume fraction range and the curves represent more stochastic behavior as in Fig. 7f–h. Near the packing limit, Fig. 7i shows that the correction factor starts to tend towards unity for all the averaging sizes.

The behavior of the correction factor for three averaging sizes is shown in Fig. 8 for the selected area in the upper part of the riser. Since the suspension is dilute in the upper part of the riser, only one value of solid volume fraction, $\alpha_s = 0.005$ was considered. In the upper part of the riser also the correction factor profiles are dependent on the averaging size. In Igci and Sundaresan (2011) it was observed that the filtered drag coefficient could be normalized such that the correction as a function of the distance to the wall would become independent of averaging size and average solid volume fraction. Fig. 7 shows that the correction factors obtained in this work for Geldart group B particles in a wider solid volume fraction range cannot be expressed as a single function by normalizing the values.

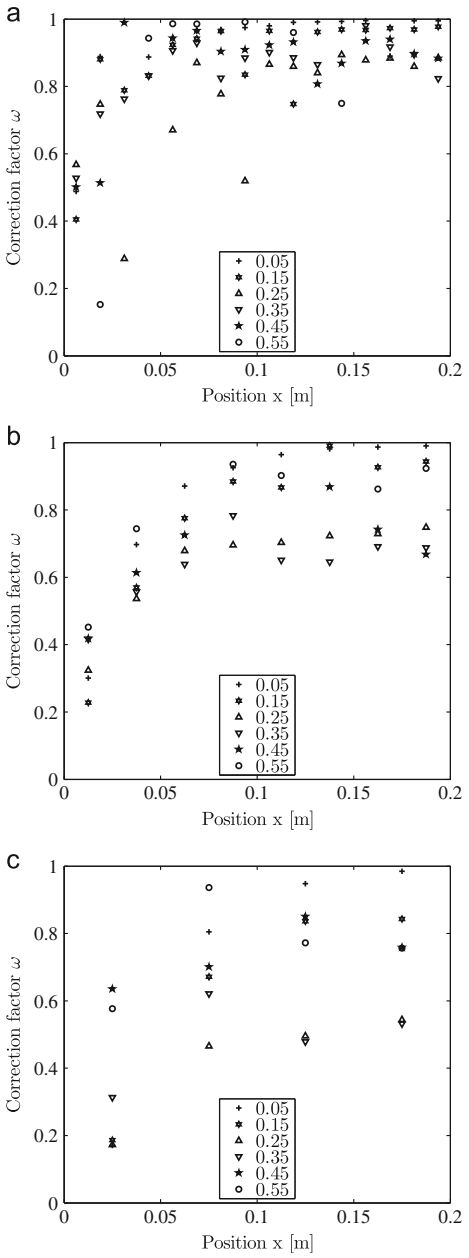

Fig. 6. Correction factor with respect to distance from the wall with different solid volume fractions inside the averaging region for averaging sizes (a) 1.25×1.25 cm^2, (b) 2.5×2.5 cm^2 and (c) 5×5 cm^2. The analysis was carried out at the height $y = 0.175$ m.

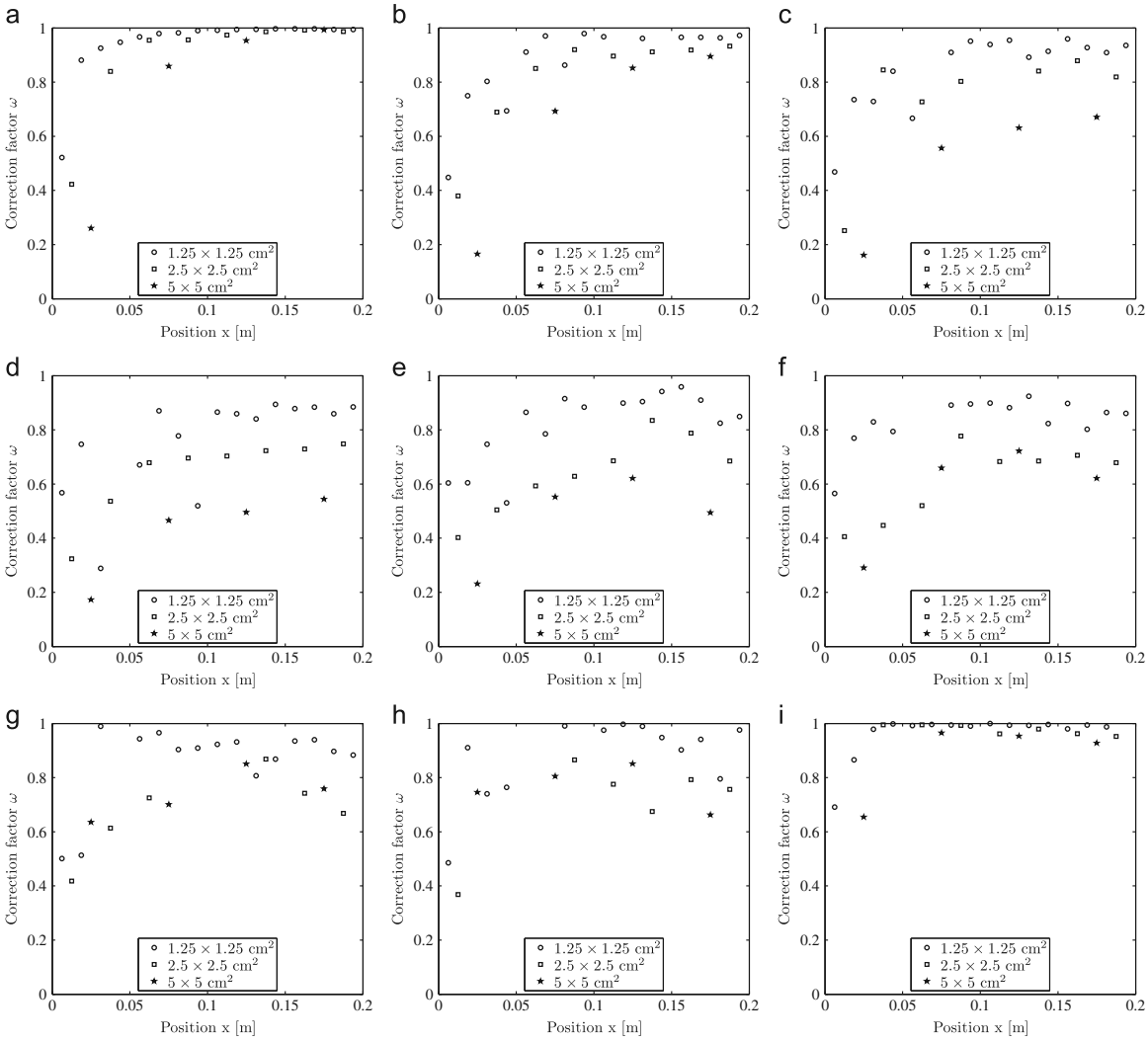

Fig. 7. Correction factor with respect to distance from the wall with different averaging sizes for solid volume fractions inside the averaging region as (a) 0.01, (b) 0.125, (c) 0.2, (d) 0.25, (e) 0.3, (f) 0.375, (g) 0.45, (h) 0.525, and (i) 0.6. The analysis was carried out at the height $y=0.175$ m.

3.2. Space averaging on the convective term

Another important term which is being analyzed in the study is the convective term. The convective term of the solid phase momentum equation is space averaged to obtain the contribution of the Reynolds stresses due to the fluctuations in the solid phase velocities. For example, in the mathematical notations, the normal Reynolds stress components can be written as,

$$^{\Delta x}\langle \tfrac{\delta x}{\delta t}(\alpha_s \rho_s v_{s,x} v_{s,x})\rangle = \overline{\alpha}_s \rho_s \tilde{v}_{s,x}\tilde{v}_{s,x} + \text{Reynolds stress}, \quad (3)$$

$$^{\Delta x}\langle \tfrac{\delta x}{\delta t}(\alpha_s \rho_s v_{s,y} v_{s,y})\rangle = \overline{\alpha}_s \rho_s \tilde{v}_{s,y}\tilde{v}_{s,y} + \text{Reynolds stress}, \quad (4)$$

where $\overline{\alpha}_s$ is the averaged solid volume fraction inside the averaging region.

The behavior of the horizontal and vertical normal Reynolds stress components for different averaging sizes is shown in Figs. 9 and 10. It is clearly seen from both figures that the behavior of the Reynolds stress components is very much dependent on the averaging size and the magnitude increases as the averaging size is increased. Similar to the correction factor for the drag force, the normal Reynolds stress component shows higher values near the walls. It is seen from the figures that the magnitude of the vertical normal Reynolds stress component is much larger than the horizontal component. The wall effects must be considered in modeling of the Reynolds stresses in such filtered model equations.

4. Conclusions

Fine mesh CFD simulations of gas–solid two-phase flow in a CFB riser with a two-fluid model are very time consuming and hence require a coarse mesh and consequently filtered model

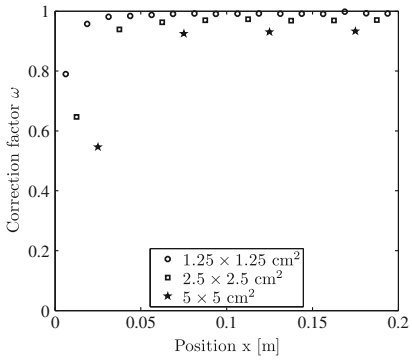

Fig. 8. Correction factor with respect to distance from the wall with different averaging sizes for the value of solid volume fraction as $\alpha_s = 0.005$. The analysis was carried out at the height $y = 2.475$ m.

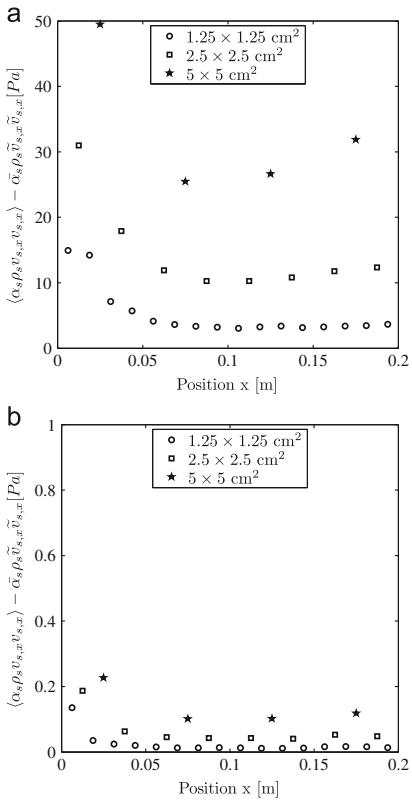

Fig. 9. Horizontal normal Reynolds stress component for different averaging sizes at two different heights: (a) $y = 0.175$ m and (b) $y = 2.475$ m.

equations. The main challenge with the filtered two-fluid model equations is the closure of the terms which result after macroscopic averaging over the equations. In this paper, a two-dimensional fine mesh simulation of the gas–solid flow in a CFB riser was performed for a case of Geldart group B particles. Space averaging on the vertical component of the drag force and the convective term was carried out in the lower and upper areas of the riser for different averaging sizes. The goal was to study the

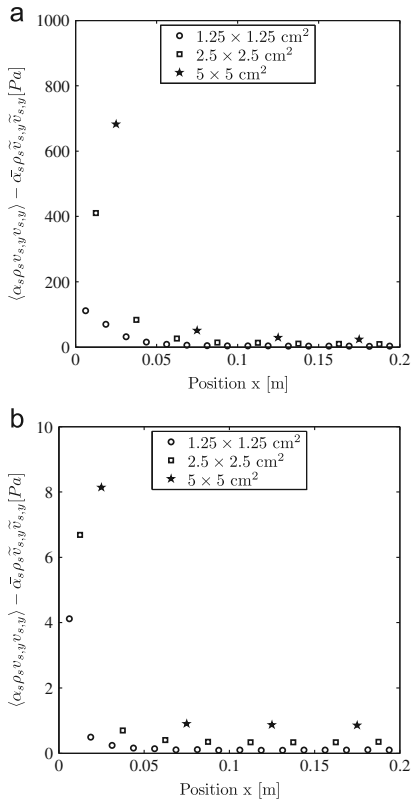

Fig. 10. Vertical normal Reynolds stress component for different averaging sizes at two different heights: (a) $y = 0.175$ m and (b) $y = 2.475$ m.

behavior of the subgrid-scale models for different averaging sizes and a wide range of solid volume fractions.

Subgrid-scale models to be applied for both the drag force and the normal components of solid phase Reynolds stress, were strongly dependent on the averaging size. Larger averaging sizes show higher magnitude in the values of the subgrid-scale models. Although the fluctuations in the solid volume fraction, related to the amount of clustering, did not always increase up to the wall, the maximum magnitude of the correction for the drag force was in all cases found at locations closest to the wall. One explanation for this observation was found in the strong fluctuation in the value of the drag coefficient in the downflow region at the wall. A clear dependence of the correction factor values of the drag force model on the distance to the wall was obtained for the lower and moderate range of solid volume fractions. At higher values of the solid volume fractions, the behavior of the correction factor was somewhat stochastic for all the averaging sizes considered here, but this could have been a result of not having a sufficient amount of data for averaging out the fluctuations in all cases. At the maximum packing limit and in very dilute conditions, the drag correction factor values were tending towards unity. In the solid phase momentum equation, the normal components of the Reynolds stress also show higher magnitude towards the walls. Thus, there is a need to formulate proper expressions for the subgrid-scale models which take into account the effects of averaging size, solid volume fraction and distance from the wall. The formulation and validation of this kind of correlations is a scope of future research activities.

Nomenclature

Symbols

$\overline{\overline{I}}$	identity tensor
$\vec{g}$	acceleration due to gravity (m/s^2)
$\vec{v}_i$	phase velocity (m/s)
$\check{v}_i$	averaged phase velocity (m/s)
C_D	drag coefficient for a particle
$C_\mu, C_{1\epsilon}, C_{2\epsilon}, C_{3\epsilon}$	constants in the gas turbulence model with values 0.09, 1.44, 1.92, and 1.2, respectively
d_i	particle diameter (m)
e_i	restitution coefficient
$g_{0,i}$	radial distribution function
I_{2D}	second invariant of the deviatoric stress tensor
K_i^*	interphase momentum exchange coefficient calculated from averaged variables, kg/m^3 s
K_i	interphase momentum exchange coefficient (kg/m^3 s)
k_{Θ_s}	diffusion coefficient for granular energy (kg/ms)
p	pressure (kg/ms^2)
Re	relative Reynolds number

Greek alphabets

α	volume fraction
$\overline{\alpha}$	averaged volume fraction
$\overline{\overline{\tau_i}}$	stress–strain tensor (kg/ms^2)
δt	time step size (s)
δx	mesh size in horizontal direction (m)
δy	mesh size in vertical direction (m)
ϵ	turbulent dissipation rate (m^2/s^3)
γ_{Θ_s}	collisional dissipation of energy (kg/m s^3)
κ	turbulent kinetic energy (m^2/s^2)
$\tau_{t,sg}$	Lagrangian integral time scale
$\tau_{F,sg}$	particle relaxation time scale
Π	turbulence exchange terms between gas and solid phases
σ	standard deviation
$\sigma_\kappa, \sigma_\epsilon$	constants in the gas turbulence model with values 1.0 and 1.3, respectively
λ_i	bulk viscosity (kg/ms)
μ_i	shear viscosity (kg/ms)
ω	correction factor
ϕ_i	energy exchange between the gas and solid phase (kg/ms^3)
ρ	density (kg/m^3)
θ	angle of internal friction
ψ	angle between mean particle velocity and mean relative velocity
Θ_i	granular temperature (m^2/s^2)

Subscripts

g	gas
i	general index
s	solid
t	turbulent

Acknowledgments

The authors from LUT Energy would like to acknowledge the financial support for this research from the Academy of Finland under Grant 124368. Srujal Shah is also grateful for the financial support for this research from the Academy of Finland under the project 'The Finnish Graduate School in Computational Fluid Dynamics'.

References

Agrawal, K., Loezos, P., Syamlal, M., Sundaresan, S., 2001. The role of meso-scale structures in rapid gas–solid flows. J. Fluid Mech. 445, 151–185.
Anderson, T.B., Jackson, R., 1967. A fluid mechanical description of fluidized beds. Ind. Eng. Chem. Fundam. 6, 527–539.
Benyahia, S., 2008. A time-averaged model for gas–solids flow in a one-dimensional vertical channel. Chem. Eng. Sci. 63, 2536–2547.
Benyahia, S., Syamlal, M., O'Brien, T., 2007. Study of the ability of multiphase continuum models to predict core-annulus flow. AIChE J. 53, 2549–2568.
Cabezas-Gómez, L., Silva, R.C., Milioli, F.E., 2006. Some modeling and numerical aspects of the two-fluid simulation of the gas–solids flow in a CFB riser. Braz. J. Chem. Eng. 23, 487–496.
De Wilde, J., 2005. Reformulating and quantifying the generalized added mass in filtered gas–solid flow models. Phys. Fluids 17, 113304.
De Wilde, J., Marin, G.B., Heynderickx, G.J., 2003. The effects of abrupt T-outlets in a riser: 3D simulation using the kinetic theory of granular flow. Chem. Eng. Sci. 58, 877–885.
Gidaspow, D., 1994. Multiphase Flow and Fluidization: Continuum and Kinetic Theory Descriptions. Academic Press, San Diego.
Gidaspow, D., Bezburuah, R., Ding, J., 1992. Hydrodynamics of circulating fluidized beds: kinetic theory approach. In: Potter, O., Nicklin, D. (Eds.), Proceedings of the 7th Engineering Foundation Conference on Fluidization. Brisbane, pp. 75–82.
Hartge, E.U., Ratschow, L., Wischnewski, R., Werther, J., 2009. CFD-simulation of a circulating fluidized bed riser. Particuology 7, 283–296.
Hrenya, C., Sinclair, J., 1997. Effects of particle-phase turbulence in gas–solid flows. AIChE J. 43, 853–869.
Igci, Y., Andrews, A.T., Sundaresan, S., Pannala, S., O'Brien, T., 2008. Filtered two-fluid models for fluidized gas–particle suspensions. AIChE J. 54, 1431–1448.
Igci, Y., Pannala, S., Benyahia, S., Sundaresan, S., 2012. Validation studies on filtered model equations for gas–particle flows in risers. Ind. Eng. Chem. Res. 51, 2094–2103.
Igci, Y., Sundaresan, S., 2011. Verification of filtered two-fluid models for gas–particle flows in risers. AIChE J. 57, 2691–2707.
Issangya, A.S., Grace, J.R., Bai, D., Zhu, J., 2000. Further measurements of flow dynamics in a high-density circulating fluidized bed riser. Powder Technol. 111, 104–113.
Kallio, S., Guldén, M., Hermanson, A., 2009. Experimental study and CFD simulation of a 2D circulating fluidized bed. In: Yue, G., Zhang, H., Zhao, C., Luo, Z. (Eds.), Proceedings of the 20th International Conference on Fluidized Bed Combustion. Xi'an, pp. 799–804.
Kallio, S., Peltola, J., Taivassalo, V., 2011. Characteristics of the solid volume fraction fluctuations in a CFB. In: Knowlton, T. (Ed.), Proceedings of the 10th International Conference on Circulating Fluidized Beds and Fluidization Technology. Sunriver, pp. 561–568.
Kallio, S., Taivassalo, V., Hyppänen, T., 2008. Towards time-averaged CFD modelling of circulating fluidized beds. In: Werther, J., Nowak, W., Wirth, K.E., Hartge, E.U. (Eds.), Circulating Fluidized Bed Technology IX. Hamburg, pp. 259–264.
Lun, C.K.K., Savage, S.B., Jeffrey, D.J., Chepurniy, N., 1984. Kinetic theories for granular flow: inelastic particles in Couette flow and slightly inelastic particles in a general flowfield. J. Fluid Mech. 140, 223–256.
Schaeffer, D., 1987. Instability in the evolution equations describing incompressible granular flow. J. Differ. Equations 66, 19–50.
Shah, S., Ritvanen, J., Hyppänen, T., Kallio, S., 2012. Space averaging on a gas–solid drag model for numerical simulations of a CFB riser. Powder Technol. 218, 131–139.
Syamlal, M., Rogers, W., O'Brien, T., 1993. MFIX Documentation: Theory Guide. Technical Report. DOE/METC-94/1004, DE94000087, Morgantown, WV.
Wang, J., 2008. High-resolution Eulerian simulation of RMS of solid volume fraction fluctuation and particle clustering characteristics in a CFB riser. Chem. Eng. Sci. 63, 3341–3347.
Wang, W., Li, J., 2007. Simulation of gas–solid two-phase flow by a multi-scale CFD approach—extension of the EMMS model to the sub-grid level. Chem. Eng. Sci. 62, 208–231.
Wang, X., Jin, B., Zhong, W., Xiao, R., 2010. Modeling on the hydrodynamics of a high-flux circulating fluidized bed with Geldart group A particles by kinetic theory of granular flow. Energy Fuels 24, 1242–1259.
Yang, N., Wang, W., Ge, W., Wang, L., Li, J., 2004. Simulation of heterogeneous structure in a circulating fluidized-bed riser by combining the two-fluid model with the EMMS approach. Ind. Eng. Chem. Res. 43, 5548–5561.
Zhang, D., VanderHeyden, W., 2002. The effects of mesoscale structures on the macroscopic momentum equations for two-phase flows. Int. J. Multiphase Flow 28, 805–822.

PAPER IX

CFD simulations of gas–solid flow in an industrial-scale circulating fluidized bed furnace using subgrid-scale drag models

Particuology 18 (2015) 66–75.

Particuology 18 (2015) 66–75

Contents lists available at ScienceDirect

Particuology

journal homepage: www.elsevier.com/locate/partic

CFD simulations of gas–solid flow in an industrial-scale circulating fluidized bed furnace using subgrid-scale drag models

Srujal Shah[a,*], Kari Myöhänen[a], Sirpa Kallio[b], Timo Hyppänen[a]

[a] Department of Energy Technology, Lappeenranta University of Technology, FI-53851 Lappeenranta, Finland
[b] VTT Technical Research Centre of Finland, FI-02044 VTT, Finland

ARTICLE INFO

Article history:
Received 5 December 2013
Received in revised form 17 April 2014
Accepted 8 May 2014

Keywords:
Circulating fluidized bed
Computational fluid dynamics
Two-fluid model
Drag correlation
Modeling

ABSTRACT

Mesoscale flow structures such as clusters and streamers of particles are characteristic features of gas–solid flow in fluidized beds. Numerical simulations of gas–solid flows for industrial-scale fluidized beds are often performed using the Eulerian description of phases. An accurate prediction of this type of flow structure using the Eulerian modeling approach requires a sufficiently fine mesh resolution. Because of the long computational time required when using fine meshes, simulations of industrial-sized units are usually conducted using coarse meshes, which cannot resolve the mesoscale flow structures. This leads to an overestimation of the gas–solid drag force and a false prediction of the flow field. For these cases, a correction must be formulated for the gas–solid drag. We have simulated a large-scale circulating fluidized bed furnace using different gas–solid drag models and compared the model results with measurements.

Introduction

Because of the advantages of circulating fluidized bed (CFB) combustion technology in the burning of different types of fuel, CFBs have been used extensively in recent decades (Gierse & Leckner, 1996). Efficient modeling tools and reliable experimental data are required to better understanding such multiphase flow systems. The flow in fluidized bed furnaces is complex, and therefore, the accurate simulation of industrial-scale units, which includes hydrodynamics, chemical reactions, and heat transfer, is challenging. An understanding of industrial-scale fluidized bed furnaces is important, and hence, many engineers and researchers have shown an interest in developing methods for their fast and accurate simulation.

Because of significant advancements in high-performance computing facilities, computational fluid dynamics (CFD) is recognized as a promising tool for understanding complex gas–solid flows in fluidized beds. In fluidized beds, the volume fraction of solids can be high (occasionally and locally up to the packing density), and thus, the flow model needs to consider particle–particle interactions. CFD modeling of such flows can be divided into three main categories: (1) Eulerian–Lagrangian collision models, (2) a hybrid Eulerian–Lagrangian approach, such as the multiphase particle-in-cell method, and (3) Eulerian–Eulerian models. The collision models can be classified into a soft- (Tsuji, Kawaguchi, & Tanaka, 1993) and hard-sphere model (Hoomans, Kuipers, Briels, & Van Swaaij, 1996). These models are based on the tracking of individual particles and their collisions. These model approaches have been used to study the small-scale fluidization phenomena, but they cannot be applied to large-scale units because of the associated high computational costs. The multiphase particle-in-cell (MP-PIC) method is based on a Lagrangian tracking of parcels of particles and an Eulerian calculation of the interaction between particles, and between particles and the gas phase (Andrews & O'Rourke, 1996). Although the number of published large-scale studies of this method is small, the MP-PIC method has also been applied to the modeling of combustion reactions (Weng, Nies, & Plackmeyer, 2011). In Ansys Fluent, the available modified MP-PIC method is termed the dense discrete phase model (Adamczyk et al., 2014). Industrial-scale CFD simulations of gas–solid flows in furnaces are typically conducted using the Eulerian description of phases. In the Eulerian–Eulerian two-fluid modeling approach, which is used in this work, both phases are treated as interpenetrating continua (Enwald, Peirano, & Almstedt, 1996; Gidaspow, 1994). Continuity, momentum, and energy equations are solved for both phases. The kinetic theory of granular flow has been used extensively for the closure models of the solid phase momentum equation in the CFD

* Corresponding author. Tel.: +358 401735672.
E-mail address: srujal.shah@lut.fi (S. Shah).

http://dx.doi.org/10.1016/j.partic.2014.05.008

Nomenclature

C_D	particle drag coefficient
d_s	solid phase particle diameter, m
e_i	restitution coefficient
$\vec{g}$	gravitational acceleration, m/s^2
$g_{0,ss}$	radial distribution function
H_d	heterogeneity index
H_i	enthalpy, J/kg
h_{sg}	volumetric heat transfer coefficient between gas and solid phases, W/(m^3 K)
I	identity tensor
I_{2D}	second invariant of the deviatoric stress tensor
K_{gs}	interphase momentum exchange coefficient, kg/(m^3 s)
K^*_{gs}	interphase momentum exchange coefficient calculated from averaged variables, kg/(m^3 s)
k_i	thermal phase conductivity, W/(m K)
k_{Θ_s}	diffusion coefficient for granular energy, kg/(m s)
Nu	Nusselt number
Pr	Prandtl number
p	pressure, Pa
Re	relative Reynolds number
T_i	temperature, K
$\vec{v}_i$	phase velocity, m/s
$\tilde{v}_i$	averaged phase velocity, m/s

Greek letters

α	volume fraction
γ_{Θ_s}	collisional dissipation of energy, kg/(m s^3)
θ	angle of internal friction
Θ_s	granular temperature, m^2/s^2
λ_i	bulk viscosity, Pa s
μ_i	shear viscosity, Pa s
$\bar{\bar{\tau}}_i$	stress–strain tensor, Pa
φ_i	energy exchange between the gas and solid phases, kg/(m s^3)
ω	correction factor
ρ_i	density, kg/m^3

Subscripts

g	gas
i	general index
s	solid

simulations (Benyahia, Arastoopour, Knowlton, & Massah, 2000; Lu, Gidaspow, Bouillard, & Wentie, 2003).

The use of the two-fluid modeling approach with the kinetic theory of granular flow-based closure models requires the calculation mesh to be fine and in the order of a few particle diameters (Andrews, Loezos, & Sundaresan, 2005; Wang, Van der Hoef, & Kuipers, 2009). In a sufficiently fine mesh, mesoscale structures such as clusters and streamers of particles in fluidized beds can be resolved accurately. The two-fluid model with kinetic theory-based closure laws is the preferred approach for small-scale fluidized beds as fine meshes can be still applied. However, for industrial-scale simulations, the requirement of a fine mesh size results in a large number of computational cells. Large-scale simulations with fine meshes are unaffordable, and simulations have to be conducted using coarse meshes. In a coarse mesh simulation, the calculation cell size is larger than the size of meso-scale structures, such as particle clusters. The model assumes a uniform solid concentration within a cell, whereas in reality the flow is non-homogeneous, and the gas flow is able to pass between the small-scale clusters of particles without interaction with the particles. The net gas–solid drag force is therefore increased, which leads to an overestimated solids circulation rate. Therefore, there is a need to formulate a suitable expression for the gas–solid drag, which can be used in CFD simulations of an industrial-scale CFB furnace with a coarse mesh. Similar problems have been encountered with the MP-PIC method (Benyahia & Sundaresan, 2012).

Many research groups have addressed the problem for the formulation of closure models that can be used for coarse mesh simulations (Agrawal, Loezos, Syamlal, & Sundaresan, 2001; Heynderickx, Das, De Wilde, & Marin, 2004; Yang, Wang, Ge, & Li, 2003; Zhang & VanderHeyden, 2002), but in general, a limited number of papers exist in the literature on the simulation of large-scale fluidized beds. One of the reasons for this is the difficulty in obtaining real measurements in commercial units for validating CFD results. The energy-minimization multi-scale (EMMS) approach has been used extensively to formulate a correction factor for the gas–solid drag force. Using the EMMS-based model, a three-dimensional (3D) full-loop industrial-scale CFB has been simulated for one (Zhang, Lu, Wang, & Li, 2010) and also for three solid phases (Lu et al., 2013). A filtering-based approach has also been presented in the literature, in which the results from the fine mesh simulations are filtered to derive constitutive correlations that can be used for coarse mesh simulations (Igci, Andrews, Sundaresan, Pannala, & O'Brien, 2008; Shah, Ritvanen, Hyppänen, & Kallio, 2012). Recently, the filtering-based approach was used to simulate large-scale bubbling and turbulent fluidized beds (Cloete, Johansen, & Amini, 2013). A one-dimensional (1D) model of a steady-state process in a fluidized bed has also been presented in the literature (Matsen, 1982) and has been used as a basis for drag closures in CFD simulations (Kallio, 2005; Vaishali, Roy, & Mills, 2008).

Different parameters have been included in the formulation of a suitable correlation for the correction factor for the gas–solid drag force applicable to coarse mesh-sized simulations. Initially, the correction factor based on the EMMS approach considered only the volume fraction (Yang et al., 2003), but later slip velocity was also included in its formulation (Wang & Li, 2007). For a filtering-based approach, the filter size was the only variable included in the correction factor (Igci et al., 2008), but later, the volume fraction (Igci & Sundaresan, 2011a) and the slip velocity (Milioli, Milioli, Holloway, Agrawal, & Sundaresan, 2013) were also included. Wall effects have also been presented in the literature (Igci & Sundaresan, 2011b; Shah et al., 2012). In addition to the above-mentioned parameters, an effort was made to analyze the effect of material properties, which proved to be important in the formulation of a correction factor for the time-averaged gas–solid drag force (Kallio, Peltola, & Niemi, 2014).

Other terms were also considered in some of the works listed above, such as the stress terms and the correlation between the fluctuations in pressure and the volume fraction. We concentrate on the drag force, which largely determines the concentration of solids at the furnace bottom and top. In the accelerating motion in the lower portion of the furnace above the bottom bed, other terms in the momentum equations can become important, and especially in the equations for the lateral velocity components, Reynolds stress terms can dominate over the drag force. Since no general correlations are available for the subgrid-scale Reynolds stress, we concentrate here on the drag force and evaluate the results of changing the drag force model only.

Various research groups have published several CFD simulations comparing different drag model closures, but most of their studies focus on small-scale apparatus. In this work, a commercial-scale CFB unit is used and a coarse mesh is applied, which provides a better basis for the comparison of different subgrid-scale models

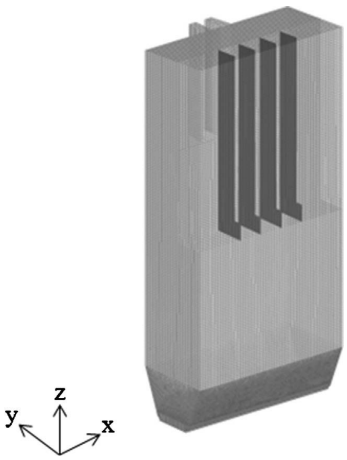

Fig. 1. Domain of the simulated CFB furnace.

for practical calculations. The same CFB unit was considered in our earlier paper (Shah, Myöhänen, Klajny, & Hyppänen, 2013), but in that work, a comparison was made only between the homogenous and space-averaged drag models. In this paper, different correlations of the correction factor for the drag model are presented as a function of volume fraction. The correlations are then applied to simulate an industrial-scale circulating fluidized bed furnace. CFD simulations with the corrected forms of the drag model are performed and compared with the homogeneous drag model.

Simulation methodology

Geometry and model description

The domain of the study is the large-scale CFB furnace, which was modeled earlier by Shah, Klajny, Myöhänen, and Hyppänen (2009). The model domain is presented in Fig. 1. The height of the furnace is ~43 m and the cross-section is 14.3 m × 6.73 m. The cell dimensions were ~0.1–0.3 m, and the number of calculation cells was ~400,000. Hexahedral and tetrahedral cells were used for most of the domain and for the tapered lower furnace section, respectively.

The model boundaries included the primary air through the grate, the secondary air through multiple secondary air nozzles and other ports, and the solid fed from the solid circulation ports. The inlet values as well as the measured pressure profile data were based on the test balance measurements by the boiler manufacturer, and the data were the same as in the earlier study by Shah et al. (2009). In large-scale CFD simulations of CFB furnaces, the reactions are often ignored and the furnace is assumed to be isothermal (e.g. Zhang et al., 2010). This is acceptable because the proportion of the gas flow because of reactions is relatively small and the temperature profile in a CFB furnace is fairly uniform. In this case, the estimated total additional gas flow because of the reactions would have been ~7% of the total inlet air flow, and thus it would not have any significant effect on the results.

A major exception to the isothermal-assumption is the temperature of the inlet gases, which is much lower than the furnace temperature. If the mass flow of the inlet gas is set correctly and the inlet temperature is set to the furnace temperature, the velocity of the gas jet, for example, at the tip of the secondary air nozzle, would be much higher than in reality, and thus the model would not simulate the real conditions. In our approach, the inlet gas temperatures were set according to the measurements (490 K), and the temperature of the solids was set to a fixed value (1150 K), which was based on the measured average furnace temperature. The heat transfer between the hot solids and the gas was included in the model to better simulate the expansion of cold inlet gases as they penetrate the furnace.

Table 1
Cumulative distribution of different particle sizes in the furnace.

Particle size (μm)	62.5	125	180	500	2000	6000
Cumulative share (%)	2.9	40.7	59.7	84.4	94.8	100

In our earlier study by Shah et al. (2009), the bed material was simulated as a mixture of two solid phases with a fine and a coarse particle size (128 and 1500 μm). The higher solid concentration at the bottom of the furnace was thus achieved with the presence of the coarse solid phase. In this study, the modeling was attempted with a single solid phase with a particle diameter of 155 μm, which corresponds with the measured average particle size of the bed. In such industrial-scale furnaces, solids have a particle size distribution, and the selection of a single particle size in the simulations is not straightforward, and can affect the results. Moreover, it is questionable whether it is possible to simulate such a system with only one particle size. However, calculations limited to one solid phase are often applied in large-scale studies to reduce the computational effort. Table 1 shows the cumulative particle size distribution in the furnace to provide a better idea of the particle size chosen in the CFD simulations. Based on the pressure profile measurements, the total bed inventory was approximately 50,000 kg, which was controlled in the model by adjusting the feed rate from the return leg chutes.

CFD simulations

CFD simulations of the gas–solid flow were performed using the commercial code, Ansys Fluent 13, by applying a two-fluid model and by using the kinetic theory of granular flow. The governing equations and the closure models are given in Table 2.

Simulations were performed for different cases and were allowed to reach stable-state conditions in which the outlet mass flow rate appears to be stable. An averaging of the result data was performed over 30 s of simulation time. A first order implicit discretization scheme was used for time-stepping and a first order upwind discretization scheme was used for the other terms. A second order upwind discretization was attempted, but it led to convergence problems. The phase-coupled SIMPLE algorithm was used for pressure–velocity coupling. The number of iterations per time step was set to 10. With these settings, the residual behavior showed an acceptable numerical convergence, and the relative error between two successive iterations for each scaled residual component was below 1×10^{-3}. The gas phase turbulence model was not used in this study and the flow was modeled as laminar flow. At the walls, a free slip boundary condition was used for the gas phase and the partial slip boundary conditions of the Johnson and Jackson (1987) model with a specularity coefficient of 0.001 and particle-wall restitution coefficient of 0.2 were used for the solid phase. The properties for the CFD simulations as used in Ansys Fluent are given in Table 3.

All the CFD simulation cases presented in this work were performed for the same set of model equations and boundary conditions, except for the correlation for the interphase momentum exchange coefficient in the drag force model, which was changed for different cases. The first one is the homogeneous drag law with the correlation proposed by Gidaspow, Bezburuah, and Ding

Table 2
Governing equations and closure models used.

Gas phase (continuity, momentum, and energy equations)

$$\frac{\partial}{\partial t}(\alpha_g \rho_g) + \nabla \cdot (\alpha_g \rho_g \vec{v}_g) = 0$$

$$\frac{\partial}{\partial t}(\alpha_g \rho_g \vec{v}_g) + \nabla \cdot (\alpha_g \rho_g \vec{v}_g \vec{v}_g) = -\alpha_g \nabla p + \nabla \cdot \bar{\bar{\tau}}_g + \alpha_g \rho_g \vec{g} + K_{gs}(\vec{v}_s - \vec{v}_g)$$

$$\frac{\partial}{\partial t}(\alpha_g \rho_g H_g) + \nabla \cdot (\alpha_g \rho_g \vec{v}_g H_g) = \nabla \cdot (k_g \nabla T_g) + h_{sg}(T_g - T_s)$$

Solid phase (continuity, momentum, and energy equations)

$$\frac{\partial}{\partial t}(\alpha_s \rho_s) + \nabla \cdot (\alpha_s \rho_s \vec{v}_s) = 0$$

$$\frac{\partial}{\partial t}(\alpha_s \rho_s \vec{v}_s) + \nabla \cdot (\alpha_s \rho_s \vec{v}_s \vec{v}_s) = -\alpha_s \nabla p - \nabla p_s + \nabla \cdot \bar{\bar{\tau}}_s + \alpha_s \rho_s \vec{g} + K_{gs}(\vec{v}_g - \vec{v}_s)$$

$$\frac{\partial}{\partial t}(\alpha_s \rho_s H_s) + \nabla \cdot (\alpha_s \rho_s \vec{v}_s H_s) = \nabla \cdot (k_s \nabla T_s) + h_{sg}(T_s - T_g)$$

Granular energy equation

$$\frac{3}{2}\left[\frac{\partial}{\partial t}(\alpha_s \rho_s \Theta_s) + \nabla \cdot (\alpha_s \rho_s \vec{v}_s \Theta_s)\right] = (-p_s \bar{\bar{I}} + \bar{\bar{\tau}}_s) : \nabla \vec{v}_s + \nabla \cdot (k_{\Theta_s} \nabla \Theta_s) - \gamma_{\Theta_s} + \varphi_{gs}$$

Diffusion coefficient for granular energy

$$k_{\Theta_s} = \frac{15 d_s \rho_s \alpha_s \sqrt{\pi \Theta_s}}{4(41-33\eta)}\left[1 + \frac{12}{5}\eta^2(4-3\eta)\alpha_s g_{0,ss} + \frac{16}{15}(41-33\eta)\eta\alpha_s g_{0,ss}\right], \text{ where } \eta = \frac{1}{2}(1+e_{ss})$$

Collisional dissipation of energy

$$\gamma_{\Theta_s} = \frac{12(1-e_{ss}^2)g_{0,ss}}{d_s\sqrt{\pi}} \rho_s \alpha_s^2 \Theta_s^{3/2}$$

Energy exchange between the gas and solid phases

$$\varphi_{gs} = -3K_{gs}\Theta_s$$

Phase stress-strain tensors

$$\bar{\bar{\tau}}_g = \alpha_g \mu_g (\nabla \vec{v}_g + \nabla \vec{v}_g^T) - \frac{2}{3}\alpha_g \mu_g \nabla \cdot \vec{v}_g \bar{\bar{I}}$$

$$\bar{\bar{\tau}}_s = \alpha_s \mu_s (\nabla \vec{v}_s + \nabla \vec{v}_s^T) + \alpha_s \left(\lambda_s - \frac{2}{3}\mu_s\right) \nabla \cdot \vec{v}_s \bar{\bar{I}}$$

Solids shear viscosity

$$\mu_s = \mu_{s,col} + \mu_{s,kin} + \mu_{s,fr}$$

$$= \frac{4}{5}\alpha_s \rho_s d_s g_{0,ss}(1+e_{ss})\left(\frac{\Theta_s}{\pi}\right)^{1/2} + \frac{\alpha_s \rho_s d_s \sqrt{\Theta_s \pi}}{6(3-e_{ss})}\left[1 + \frac{2}{5}(1+e_{ss})(3e_{ss}-1)\alpha_s g_{0,ss}\right] + \frac{p_s \sin\theta}{2\sqrt{I_{2D}}}$$

Granular bulk viscosity

$$\lambda_s = \frac{4}{3}\alpha_s \rho_s d_s g_{0,ss}(1+e_{ss})\left(\frac{\Theta_s}{\pi}\right)^{1/2}$$

Solids pressure

$$p_s = \alpha_s \rho_s \Theta_s + 2\rho_s(1+e_{ss})\alpha_s^2 g_{0,ss}\Theta_s$$

Radial distribution function

$$g_{0,ss} = \left[1 - \left(\frac{\alpha_s}{\alpha_{s,\max}}\right)^{1/3}\right]^{-1}$$

Volumetric heat transfer coefficient between gas and solid phases

$$h_{sg} = \frac{6k_g \alpha_g \alpha_s \mathrm{Nu}}{d_s^2}, \text{ where } \mathrm{Nu} = (7 - 10\alpha_g + 5\alpha_g^2)(1 + 0.7Re^{0.2}Pr^{1/3}) + (1.33 - 2.4\alpha_g + 1.2\alpha_g^2)Re^{0.2}Pr^{1/3}$$

(1992), which is a combination of the Wen and Yu (1966) model and the Ergun (1952) equation model. The other three cases considered the effect of subgrid-scale modeling. Four calculations with different drag models were performed: Model A with the drag law of the Ergun/Wen–Yu model, Model B with the space-averaged drag model, Model C with the EMMS drag model, and Model D with the macroscopic drag model as described in the following section.

Drag model correlations

The role of the interphase drag model in the CFD simulations is very important as it is one of the main parameters that characterize the behavior of the gas–solid flow in fluidized beds. In the gas and solid phase momentum equations, the drag force term is expressed as the product of the interphase momentum exchange coefficient and the slip velocity. Several correlations are available in the literature for the interphase momentum exchange coefficient. The form of the drag force correlation for a homogeneous suspension is either formulated from the experimental data (Ergun, 1952; Wen & Yu, 1966) or from numerically accurate Lattice-Boltzmann simulations (Hill, Koch, & Ladd, 2001; Hill, Koch, & Ladd, 2001; Van der Hoef, Beetstra, & Kuipers, 2005). For heterogeneous conditions, the approaches to derive drag laws are based on measurements, fine-mesh simulation, and/or theoretical considerations. We have implemented different drag models to analyze their effect on the overall gas–solid flow behavior. The comparison of the used drag models is given as a function of gas volume fraction in Fig. 2. A brief description of the used drag model correlations is presented below and its mathematical expressions are given in Table 4.

Table 3
Properties for CFD simulations in Ansys Fluent.

Gas phase	Incompressible ideal gas Molar mass = 28.872 kg/kmol $\mu = 4.37 \times 10^{-5}$ Pa s
Solid phase	Diameter = 155 μm Density = 2500 kg/m^3
Restitution coefficient	0.9
Maximum packing limit	0.63
Mesh size (m)	0.1–0.3
Time step size (s)	0.001

It has become common practice in the literature to use the notation of the heterogeneity index, H_d. This notation was first introduced for the EMMS model to compare the hydrodynamic disparity between homogeneous and heterogeneous fluidization (Wang & Li, 2007). In later studies, this notation has been used to compare the different drag correlations, and it is termed the scaling factor for the drag coefficient (Igci & Sundaresan, 2011a) or the function accounting for unresolved structures (Schneiderbauer, Puttinger, & Pirker, 2013). In all of these studies, H_d is defined as the ratio of the different drag correlations to the Wen–Yu drag model. Fig. 3 compares the heterogeneity index of the different drag models used in this work as a function of gas volume fraction.

Drag model A: Ergun/Wen–Yu model

The Ergun/Wen–Yu model is a combination of the Wen–Yu drag model and the drag model based on the Ergun equation. The combination of these two models is termed the Gidaspow or homogeneous drag model. The model was presented such that, at higher gas volume fractions, the Wen–Yu model would be used, and for

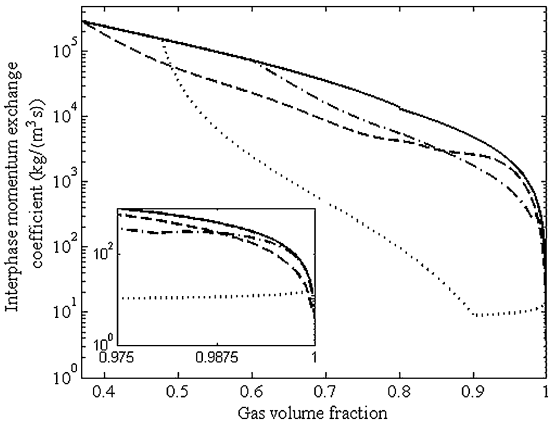

Fig. 2. Comparison of interphase momentum exchange coefficients using different models. The value of slip velocity is taken as unity. The solid, dashed, dash-dotted, and dotted lines represent the Ergun/Wen–Yu drag model, space-averaged drag model, drag from the EMMS model, and macroscopic drag model, respectively. The inset figure is used to visualize the curves more clearly at higher gas volume fraction values.

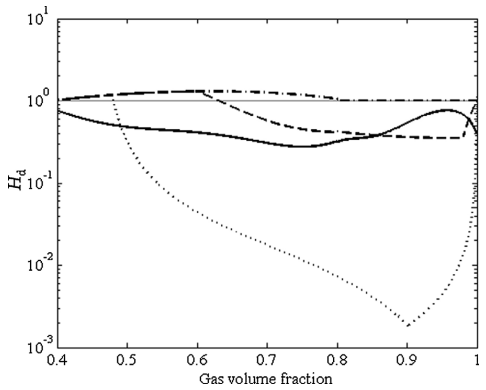

Fig. 3. Comparison of heterogeneity indices, H_d, for different drag models versus gas volume fraction. The value of slip velocity is taken as unity. ($H_d = 1$ is for the Wen–Yu drag model, the dash-dotted, solid, dashed, and dotted lines represent the Ergun/Wen–Yu drag model, the space-averaged drag model, the drag from the EMMS model, and the macroscopic drag model, respectively.)

lower gas volume fractions, the Ergun equation model would be used. Despite the discontinuity of the model at 0.8, it is commonly used in the fluidization literature.

Drag model B: space-averaged model

It is well known that CFD simulations using the two-fluid model are dependent on mesh size. Thus, a macroscopic set of equations must be formulated for coarse mesh simulations. In this approach, the space-averaging method was used to derive the subgrid-scale

Table 4
Drag model correlations used in CFD simulations.

Drag model A: Ergun/Wen–Yu model

When $\alpha_g > 0.8$,

$$K_{gs} = \frac{3}{4} C_D \frac{\alpha_s \alpha_g \rho_g |\vec{v}_s - \vec{v}_g|}{d_s} \alpha_g^{-2.65},$$

where $C_D = \frac{24}{\alpha_g Re}[1 + 0.15(\alpha_g Re)^{0.687}]$ and $Re = \frac{\rho_g d_s |\vec{v}_s - \vec{v}_g|}{\mu_g}$;

When $\alpha_g \le 0.8$,

$$K_{gs} = 150 \frac{\alpha_s (1-\alpha_g)\mu_g}{\alpha_g d_s^2} + 1.75 \frac{\alpha_s \rho_g |\vec{v}_s - \vec{v}_g|}{d_s}.$$

Drag model B: space-averaged model

When $\alpha_g > 0.8$,

$$K_{gs} = \frac{3}{4} C_D \frac{\alpha_s \alpha_g \rho_g |\vec{v}_s - \vec{v}_g|}{d_s} \alpha_g^{-2.65} \omega_{WY},$$

where $\omega_{WY} = -4055.2\alpha_g^4 + 14124\alpha_g^3 - 18404\alpha_g^2 + 10636\alpha_g - 2300.4$;

When $\alpha_g \le 0.8$,

$$K_{gs} = \omega_E \left(150 \frac{\alpha_s (1-\alpha_g)\mu_g}{\alpha_g d_s^2} + 1.75 \frac{\alpha_s \rho_g |\vec{v}_s - \vec{v}_g|}{d_s} \right),$$

where $\omega_E = 162.52\alpha_g^4 - 401.57\alpha_g^3 + 370.53\alpha_g^2 - 152.01\alpha_g + 23.809$.

Drag model C: EMMS model

When $\alpha_g > 0.60$,

$$K_{gs} = \frac{3}{4} C_D \frac{\alpha_s \alpha_g \rho_g |\vec{v}_s - \vec{v}_g|}{d_s} \omega_{EMMS},$$

where $\omega_{EMMS} = \begin{cases} 30.739\alpha_g - 29.739, & \alpha_g > 0.98 \\ 124.77\alpha_g^4 - 474.59\alpha_g^3 + 681.97\alpha_g^2 - 439.94\alpha_g + 108.15, & 0.80 < \alpha_g \le 0.98 \\ 1449.2\alpha_g^4 - 4692.4\alpha_g^3 + 5722.4\alpha_g^2 - 3117.2\alpha_g + 641.1, & 0.60 < \alpha_g \le 0.80 \end{cases}$;

When $\alpha_g \le 0.60$,

$$K_{gs} = 150 \frac{\alpha_s (1-\alpha_g)\mu_g}{\alpha_g d_s^2} + 1.75 \frac{\alpha_s \rho_g |\vec{v}_s - \vec{v}_g|}{d_s}.$$

Drag model D: macroscopic model

When $\alpha_g > 0.478$,

$$K_{gs} = \frac{3}{4} C_D \frac{\alpha_s \alpha_g \rho_g |\vec{v}_s - \vec{v}_g|}{d_s} \omega_M^{-2},$$

where $\omega_M = \begin{cases} 1, & \alpha_g > 0.9996 \\ 73.42(1-\alpha_g)^{0.5565}, & 0.901 < \alpha_g \le 0.9996 \\ 4.062 \frac{\alpha_g - 0.46}{\alpha_s \alpha_g} + \frac{0.022}{\alpha_g}, & 0.478 < \alpha_g \le 0.901 \end{cases}$;

When $\alpha_g \le 0.478$,

$$K_{gs} = 150 \frac{\alpha_s (1-\alpha_g)\mu_g}{\alpha_g d_s^2} + 1.75 \frac{\alpha_s \rho_g |\vec{v}_s - \vec{v}_g|}{d_s}.$$

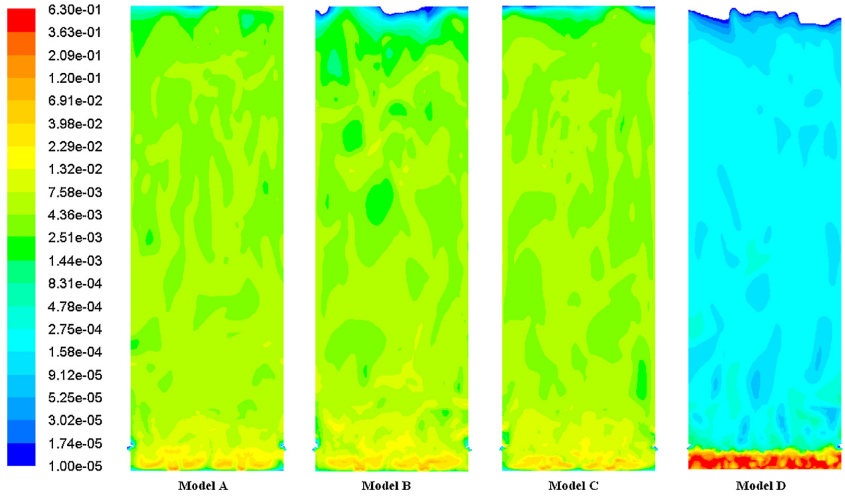

Fig. 4. Instantaneous solid volume fraction contours for different drag models used at $y = 3.365$ m. The value of solid volume fraction less than 1×10^{-5} on a logarithmic scale is colorless. (Models A, B, C, and D represent the Ergun/Wen–Yu, the space-averaged, the EMMS, and the macroscopic model, respectively.)

model for the gas–solid drag force. The fine mesh results of the vertical component of the drag force are averaged, and a correction coefficient is then written as a function of the averaged variables as shown in mathematical notation:

$$^{\Delta x}\left\langle {}^{\delta x}_{\delta t}(K_{gs}(v_{g,z} - v_{s,z}))\right\rangle = \omega K^{*}_{gs}(\tilde{v}_{g,z} - \tilde{v}_{s,z}), \quad (1)$$

where ω is the correction factor to be modeled, δt is the time step, δx is the fine mesh size, Δx is the coarse mesh size, K_{gs} is the interphase momentum exchange coefficient, K^{*}_{gs} is the interphase momentum exchange coefficient calculated from the averaged variables (Ergun/Wen–Yu model), $v_{g,z}$ and $v_{s,z}$ are the phase velocities, and $\tilde{v}_{g,z}$ and $\tilde{v}_{s,z}$ are the averaged phase velocities. We have used the same data that was generated for the previous article (Shah et al., 2012), based on the fine mesh two-dimensional (2D) simulation of the CFB riser. The principle follows that the results obtained from the fine mesh simulation with mesh size δx are averaged over the coarse averaging size Δx.

In the study by Shah et al. (2012), different averaging sizes up to 0.05 m were used, and lower correction factor values resulted as the averaging size increased. In this study, the maximum cell size is 0.3 m. Thus, even the values produced with the largest averaging size (0.05 m) may not produce small enough values of ω for this case. Using an averaging size of 0.05 m, the data generated by Shah et al. (2012) was applied to determine the correction factor as a function of the gas volume fraction. In the 2D study (Shah et al., 2012), the correction factor is affected by the distance from the wall and the slip velocity, but for this study, these effects were neglected and a correction factor was set as a function of the volume fraction only.

Drag model C: EMMS model

The EMMS model was presented in detail by Li et al. (1999), who describe the heterogeneous flow structure of a circulating fluidized bed system. The main parameter to describe the heterogeneity is the formation of clusters. According to the EMMS approach, gas and particles are considered to be in a dense or a dilute phase, and the mechanisms of the gas–solid interaction are analyzed at different scales. The set of structure parameters such as voidages and velocities is described for both dilute and dense phases resulting in a non-linear set of equations. The interphase momentum exchange coefficient is related implicitly to the structure parameters. In similar work for simulating large-scale furnaces using the EMMS model (Lu et al., 2013; Zhang et al., 2010), a correction factor was formulated as a function of slip velocity and volume fraction, and it predicted the overall fluidized bed behavior successfully. We use the correction factor of the interphase momentum exchange coefficient as a function of volume fraction only.

The correction factor for the EMMS model was generated using EMMS software obtained from the Institute of Process Engineering, Chinese Academy of Sciences. The parameters that were used to generate the correction function are given in Table 3 with a superficial fluidization velocity of 2.66 m/s and a solids flux of 5 kg/(m^2 s) corresponding to the boiler considered in this study. The superficial velocity changes along the furnace height, but fortunately the EMMS method is not very sensitive to changes in this parameter and the same correction function can be used for the whole furnace.

Drag model D: macroscopic model

The drag model described in this section is the correlation presented originally by Matsen (1982). It considers the ratio of the average slip velocity to the terminal velocity of a particle. Poikolainen (1992) used this model in a 1D analysis, and Kallio (2005) and Vaishali et al. (2008) used it as a basis for drag closure in CFD modeling. In the Matsen (1982) model, the slip velocity is approximated as the terminal velocity of a particle for very dilute suspensions. It increases as the solid concentration increases, indicating the formation of clusters. For dense phase suspensions, an equation is applied based on the bubbling theory of two-phase flows. Fig. 3 shows that the combination of these two models leads to very low values and an abrupt change in the heterogeneity index, which is not fully realistic. Matsen (1982) presented model parameters for a case of Geldart group A particles. To use the model for other conditions and Geldart group B particles, the model parameters need to be changed. In the work of the transient simulations of a CFB riser, Kallio (2005) used similar equations as formulated by Matsen (1982) and Poikolainen (1992), with the modification

that close to the packing limit, the drag force is calculated from the Ergun equation. This equation set is shown in Table 4. We consider the same type of equation set as is used by Kallio (2005). Kallio (2005) used the data for Geldart group B particles in two different cases, in addition to Matsen's parameters, to express the model parameters as functions of the Archimedes number. We have used the same expressions to calculate the coefficients for the model on the basis of material property values for the boiler considered.

The formulated equations, which were used as a basis for the above equations, were for the time-averaged description. Moreover, Matsen's correlations were based on a 1D analysis of fluidization conditions, which leads to a small overestimation of the drag correction when used locally in 2D and 3D modeling. We applied the same formulation for the drag force for the 3D transient simulation of a case that consists of a very coarse mesh applicable to industrial-scale furnaces. It can be expected that even though the mesh size is very coarse, the macroscopic steady-state drag model used here can be considered to be an extreme correction compared with the actually required value. A significant amount of temporal variations of solids velocities and voidages is produced by the transient coarse mesh simulation, leading to an overestimation of the drag correction when the steady-state, macroscopic drag model is applied. Because the macroscopic model provides the absolute limit for a coarse mesh drag closure, it is useful as a comparison and is therefore included.

Results and discussion

Solid volume fraction

The solid volume fraction is an important parameter in gas–solid flows. Fig. 4 shows the instantaneous solid volume fraction contours for different drag models used in this study. The subgrid-scale models, such as the space-averaged and EMMS models, produce similar solids distributions as the Ergun/Wen–Yu model. The macroscopic model predicts a very dense solids concentration in the lower part of the furnace and a very dilute region in the upper part of the furnace.

Fig. 5(a) compares the time-averaged simulation results for different drag models with the pressure measurements. The profiles from the simulations are plotted against the height where the measurements were taken. The pressure predicted using the Ergun/Wen–Yu model is excessively high throughout the riser height. The pressure is reduced when the space-averaged and EMMS models are used, but the results still do not match the measurements accurately. It should be noted that the modeled pressure profiles could have been adjusted to better match the measurements simply by increasing the particle size that was used in the model. However, the main purpose of this study was to compare the different model approaches when using measurement-based data. Hence, this type of sensitivity analysis was not performed. The pressure profile predicted using the macroscopic drag model is reduced significantly in the lower part of the furnace whereas in the upper part, the pressure is mainly uniform. Fig. 5(b) presents the behavior of different drag models compared with the measurements by studying the pressure gradient divided by density and gravity. In the experimental work, the solid concentration is often determined in this manner from the pressure gradient. The Ergun/Wen–Yu model predicts the lower and higher values at the bottom and upper part of the furnace, respectively. A slight improvement results when subgrid-scale drag models, such as the space-averaged and EMMS models, are used, especially in the top region, but these models do not predict accurate values. When the macroscopic model is used, an overestimated correction to the drag force results. A very dense lower and a dilute middle and upper region are predicted by using the macroscopic model.

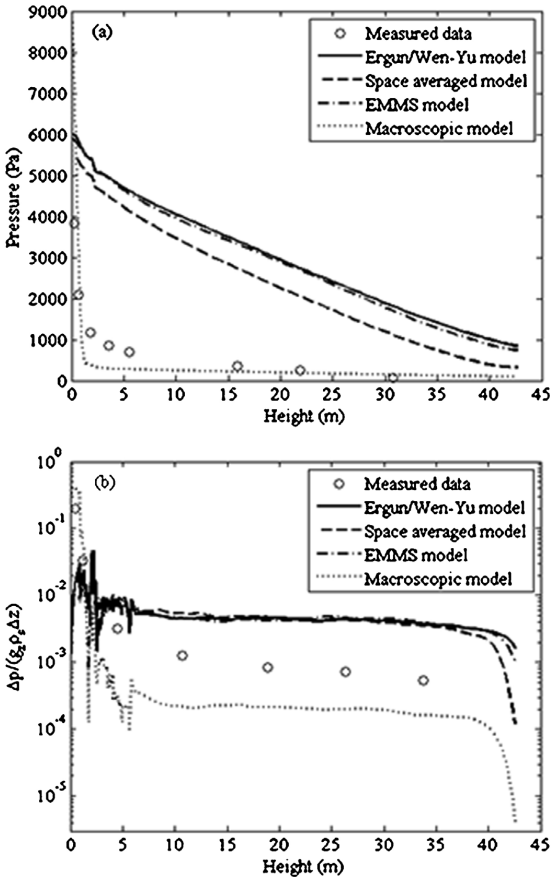

Fig. 5. Comparison of simulation results for different drag models versus furnace height with measurements for (a) pressure and (b) pressure gradient divided by density and gravity.

Solid vertical velocity

The solid velocity is also an important variable that describes how solids move in the furnace. Fig. 6 shows the Favre-averaged solids vertical velocity at different furnace heights. The profiles are plotted at the centerline of the furnace at a depth of 3.365 m. The profiles are not smooth, possibly because of the duration of the averaging time (30 s). In general, an averaging time of a few minutes would make more sense, but this was not done because of the excessive computational time requirements. The solids velocity remains mainly positive when the Ergun/Wen–Yu model is used. With the use of subgrid-scale drag models, such as the space-averaged, EMMS, and macroscopic models, a clear upflow of solids is observed at the central region and downflow occurs near the walls. This type of flow structure has often been measured in industrial-scale CFB units (Werther, 2005).

Similar profiles were plotted along the depth direction as shown in Fig. 7. The profiles are smoother in the depth direction compared

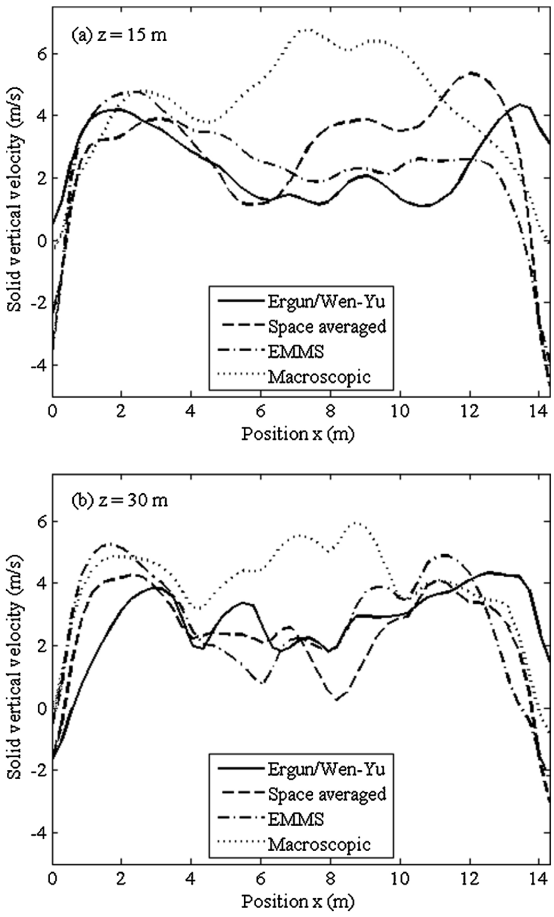

Fig. 6. Favre-averaged solid vertical velocity at different furnace heights: (a) $z = 15$ m and (b) $z = 30$ m. The results are plotted along the width direction of the furnace.

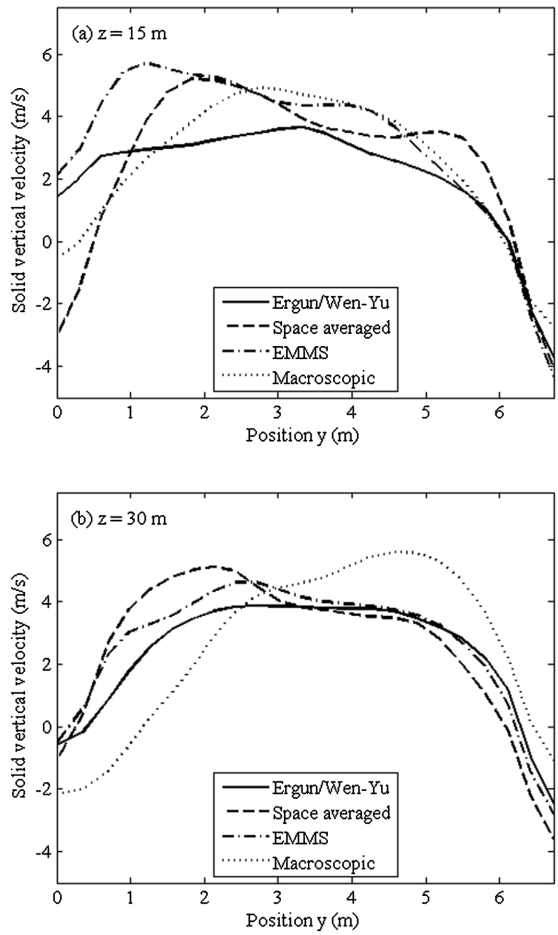

Fig. 7. Favre-averaged solid vertical velocity at two different furnace heights (a) $z = 15$ m and (b) $z = 30$ m. The results are plotted along the depth direction of the furnace.

with the width direction, because of the arrangement of feed and solid circulation ports at the bottom of the furnace, which affect the profiles in the width direction. The profiles are plotted at 3 m from the left side-wall of the furnace. Furthermore, across this direction, the solids have a higher velocity at the center and lower velocities near the walls. The velocity profiles show a down-flow of solids near the back wall for all the drag models.

Solids mass flow

An accurate prediction of solids mass flow is crucial in gas–solid flow simulations. The transient data of the solids mass flow rate at the furnace outlet has been computed and is shown in Fig. 8 for different drag models during the last 30 s of the simulations. Unfortunately, the modeled mass flows cannot be compared with the measurements because of technical difficulties related to determining the circulating mass flow in a commercial CFB.

As observed from Fig. 8, the highest solids mass flow rate is obtained using the Ergun/Wen–Yu model. With the other drag models, as expected, a decrease in the mass flow rate occurs at the outlet. The EMMS model predicts only a slightly lower mass flow rate compared with the Ergun/Wen–Yu model. It should be noted that the EMMS model also overpredicts the solids flux as the mesh size used in the simulations is coarse (Lu, Wang, & Li, 2009). The space-averaged drag model was formulated using a smaller averaging size. It can be expected that an even larger correction is needed when a coarse mesh is used, as is done in this work. Also, the formulation was conducted for 2D studies, and the resulting correlation was applied to 3D simulations. The predicted mass flow rate using the macroscopic model is very low compared with the other models.

Fig. 9 shows the averaged vertical solids mass flux profiles at different furnace heights. The profiles are plotted at the centerline of the furnace for the value in the depth direction at 3.365 m. The Ergun/Wen–Yu model predicts that the solids flux is mainly positive. With the use of subgrid-scale drag models, such as the space-averaged and EMMS models, a clear upflow of solids can be seen at the central region and a downflow of solids occurs near the walls. Using the macroscopic model, the flux is almost zero across the width direction when plotted on this scale. The predicted solids

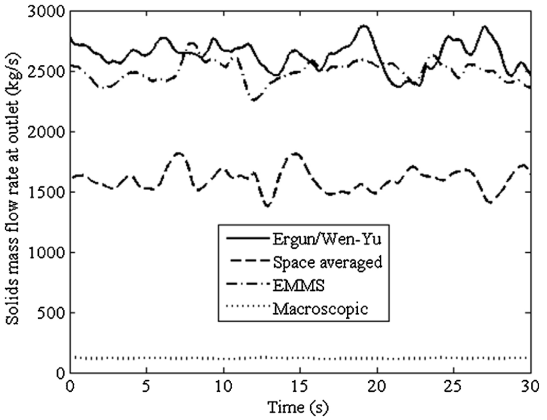

Fig. 8. Variations of solids mass flow rates with time at the outlet using different drag models.

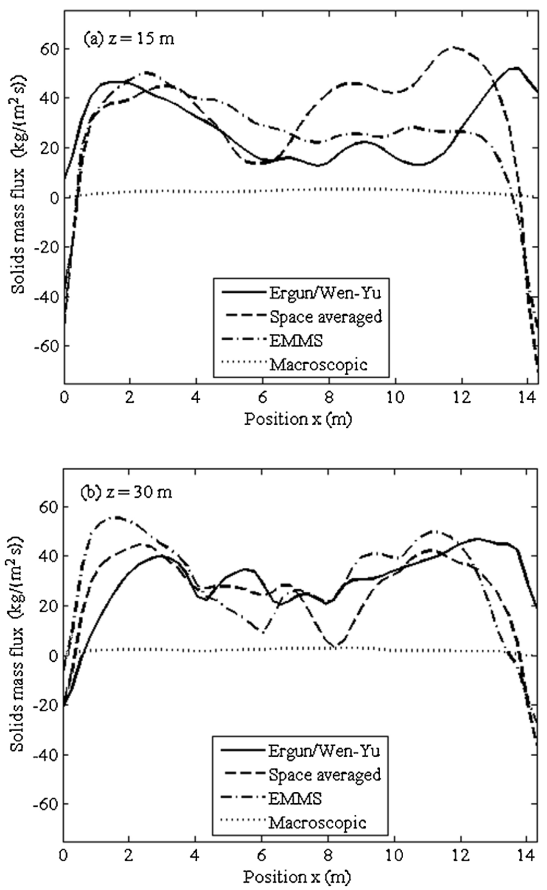

Fig. 9. Averaged vertical solids mass flux profiles along the width direction at two different furnace heights: (a) $z = 15$ m and (b) $z = 30$ m.

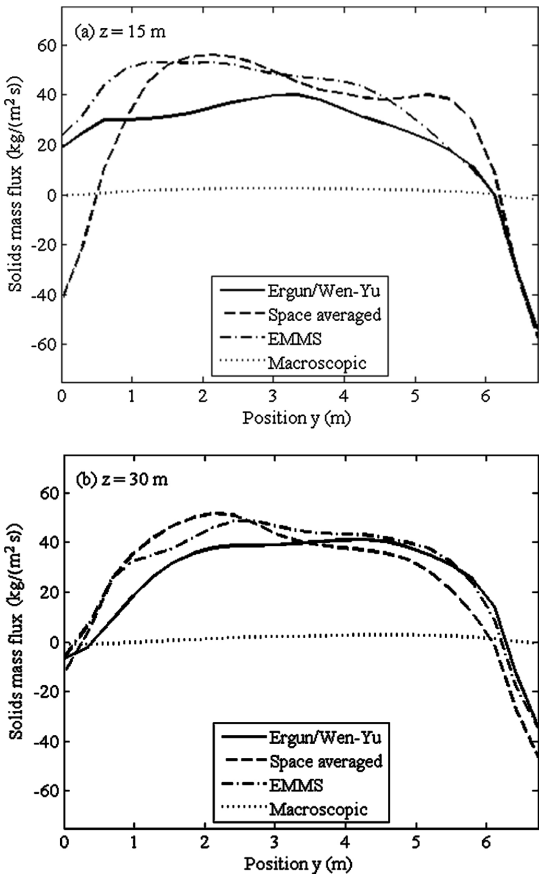

Fig. 10. Averaged vertical solids mass flux profiles along the depth direction at two different furnace heights: (a) $z = 15$ m and (b) $z = 30$ m.

concentration is low in the upper region of the furnace when it is calculated using the macroscopic model, and this explains the small flux in Fig. 9.

Fig. 10 shows the averaged vertical solids mass flux for different furnace heights in the depth direction. The profiles are plotted at 3 m from the left side-wall of the furnace. Similar profiles can be seen as for the width direction as described in Fig. 9. A clear down-flow of solids can be seen near the walls, especially at the back wall.

Conclusions

CFD simulations of an industrial-scale circulating fluidized bed furnace were performed using the Eulerian model. Different subgrid-scale drag models were applied and compared with the Ergun/Wen–Yu model. All the subgrid-scale models showed better predictions compared with the Ergun/Wen–Yu model. Although a large difference exists between the measured and predicted vertical solids distribution in the riser, the model simulates the core-annulus flow structure correctly, with qualitatively realistic down- and upflow velocities. The subgrid-scale models were based on correcting the interphase momentum exchange coefficient as

a function of volume fraction only. It is likely that other factors, such as the slip velocity, distance from the wall, material properties, and the filter size, should be included in the correction models. As an upper limit for the subgrid-scale drag model, a macroscopic model designed for steady-state simulations was also tested for comparison. As expected, the macroscopic model produced a significantly strong effect. The required correction to the drag force in very coarse meshes was found to lie between the drag corrections produced by the models in the literature and those required in steady-state modeling.

Nonetheless, more research is required in this area, particularly in the accurate matching of solids concentration profiles with measurement data and computations with coarse meshes. It should be emphasized that the simulations presented in this study were performed for one solid particle diameter, whereas solids have a wide particle size distribution in large-scale furnaces. This will be the scope of our future research work.

Acknowledgements

The authors would like to express their gratitude to Prof. Wei Wang at the Institute of Process Engineering, Chinese Academy of Sciences, for fruitful discussions and for providing assistance with the EMMS software. The authors acknowledge Foster Wheeler Energia Oy for providing the measurement data for comparison with the simulation results.

References

Adamczyk, W. P., Węcel, G., Klajny, M., Kozołub, P., Klimanek, A., & Białecki, R. A. (2014). Modeling of particle transport and combustion phenomena in a large-scale circulating fluidized bed boiler using a hybrid Euler–Lagrange approach. *Particuology*, http://dx.doi.org/10.1016/j.partic.2013.10.007

Agrawal, K., Loezos, P. N., Syamlal, M., & Sundaresan, S. (2001). The role of mesoscale structures in rapid gas–solid flows. *Journal of Fluid Mechanics*, *445*, 151–185.

Andrews IV, A. T., Loezos, P. N., & Sundaresan, S. (2005). Coarse-grid simulation of gas-particle flows in vertical risers. *Industrial & Engineering Chemistry Research*, *44*, 6022–6037.

Andrews, M. J., & O'Rourke, P. J. (1996). The multiphase particle-in-cell (MP-PIC) method for dense particulate flows. *International Journal of Multiphase Flow*, *22*, 379–402.

Benyahia, S., Arastoopour, H., Knowlton, T. M., & Massah, H. (2000). Simulation of particles and gas flow behavior in the riser section of a circulating fluidized bed using the kinetic theory approach for the particulate phase. *Powder Technology*, *112*, 24–33.

Benyahia, S., & Sundaresan, S. (2012). Do we need sub-grid scale corrections for both continuum and discrete gas-particle flow models? *Powder Technology*, *220*, 2–6.

Cloete, S., Johansen, S. T., & Amini, S. (2013). Evaluation of a filtered model for the simulation of large scale bubbling and turbulent fluidized beds. *Powder Technology*, *235*, 91–102.

Enwald, H., Peirano, E., & Almstedt, A. E. (1996). Eulerian two-phase flow theory applied to fluidization. *International Journal of Multiphase Flow*, *22*, 21–66.

Ergun, S. (1952). Fluid flow through packed columns. *Chemical Engineering Progress*, *48*, 89–94.

Gidaspow, D. (1994). *Multiphase flow and fluidization: Continuum and kinetic theory descriptions*. San Diego: Academic Press.

Gidaspow, D., Bezburuah, R., & Ding, J. (1992). Hydrodynamics of circulating fluidized beds: Kinetic theory approach. In O. E. Potter, & D. J. Nicklin (Eds.), *Proceedings of the 7th engineering foundation conference on fluidization* (pp. 75–82). New York: Engineering Foundation.

Gierse, M., & Leckner, B. (1996). Operation control of circulating fluidized bed boilers. *International Journal of Energy Research*, *20*, 839–851.

Heynderickx, G. J., Das, A. K., De Wilde, J., & Marin, G. B. (2004). Effect of clustering on gas–solid drag in dilute two-phase flow. *Industrial & Engineering Chemistry Research*, *43*, 4635–4646.

Hill, R. J., Koch, D. L., & Ladd, A. J. C. (2001a). Moderate-Reynolds-number flows in ordered and random arrays of spheres. *Journal of Fluid Mechanics*, *448*, 243–278.

Hill, R. J., Koch, D. L., & Ladd, A. J. C. (2001b). The first effects of fluid inertia on flows in ordered and random arrays of spheres. *Journal of Fluid Mechanics*, *448*, 213–241.

Hoomans, B. P. B., Kuipers, J. A. M., Briels, W. J., & Van Swaaij, W. P. M. (1996). Discrete particle simulation of bubble and slug formation in a two-dimensional gas-fluidised bed: A hard-sphere approach. *Chemical Engineering Science*, *51*, 99–118.

Igci, Y., Andrews IV, A. T., Sundaresan, S., Pannala, S., & O'Brien, T. (2008). Filtered two-fluid models for fluidized gas–particle suspensions. *AIChE Journal*, *54*, 1431–1448.

Igci, Y., & Sundaresan, S. (2011a). Constitutive models for filtered two-fluid models of fluidized gas-particle flows. *Industrial & Engineering Chemistry Research*, *50*, 13190–13201.

Igci, Y., & Sundaresan, S. (2011b). Verification of filtered two-fluid models for gas-particle flows in risers. *AIChE Journal*, *57*, 2691–2707.

Johnson, P. C., & Jackson, R. (1987). Frictional-collisional constitutive relations for granular materials, with application to plane shearing. *Journal of Fluid Mechanics*, *176*, 67–93.

Kallio, S. (2005). Comparison of simulated and measured voidage and velocity profiles and fluctuations in a CFB riser. In K. Cen (Ed.), *Proceedings of the 8th International conference on circulating fluidized beds* (pp. 105–112). Beijing: International Academic Publishers.

Kallio, S., Peltola, J., & Niemi, T. (2014). Parametric study of the time-averaged gas–solid drag force in circulating fluidized bed conditions. *Powder Technology*, *257*, 20–29.

Li, J., Cheng, C., Zhang, Z., Yuan, J., Nemet, A., & Fett, F. N. (1999). The EMMS model—Its application, development and updated concepts. *Chemical Engineering Science*, *54*, 5409–5425.

Lu, B., Wang, W., & Li, J. (2009). Searching for a mesh-independent sub-grid model for CFD simulation of gas–solid riser flows. *Chemical Engineering Science*, *64*, 3437–3447.

Lu, B., Zhang, N., Wang, W., Li, J., Chiu, J. H., & Kang, S. G. (2013). 3-D full-loop simulation of an industrial-scale circulating fluidized-bed boiler. *AIChE Journal*, *59*, 1108–1117.

Lu, H. L., Gidaspow, D., Bouillard, J., & Wentie, L. (2003). Hydrodynamic simulation of gas–solid flow in a riser using kinetic theory of granular flow. *Chemical Engineering Journal*, *95*, 1–13.

Matsen, J. M. (1982). Mechanisms of choking and entrainment. *Powder Technology*, *32*, 21–33.

Milioli, C. C., Milioli, F. E., Holloway, W., Agrawal, K., & Sundaresan, S. (2013). Filtered two-fluid models of fluidized gas-particle flows: New constitutive relations. *AIChE Journal*, *59*, 3265–3275.

Poikolainen, V. (1992). *Mathematical modeling of gas–solid fluidization with a one-dimensional hydrodynamical model* Master thesis. Finland: Lappeenranta University of Technology (in Finnish).

Schneiderbauer, S., Puttinger, S., & Pirker, S. (2013). Comparative analysis of subgrid drag modifications for dense gas–particle flows in bubbling fluidized beds. *AIChE Journal*, *59*, 4077–4099.

Shah, S., Klajny, M., Myöhänen, K., & Hyppänen, T. (2009). Improvement of CFD methods for modeling full scale circulating fluidized bed combustion systems. In G. Yue, H. Zhang, C. Zhao, & Z. Luo (Eds.), *Proceedings of the 20th international conference on fluidized bed combustion* (pp. 792–798). Beijing: Tsinghua University Press.

Shah, S., Myöhänen, K., Klajny, M., & Hyppänen, T. (2013). Numerical modeling of gas–solids flow in large scale circulating fluidized bed using subgrid-scale model. In J. A. M. Kuipers, R. F. Mudde, J. R. van Ommen, & N. G. Deen (Eds.), *Proceedings of the fluidization XIV* (pp. 575–582). New York: Engineering Conferences International.

Shah, S., Ritvanen, J., Hyppänen, T., & Kallio, S. (2012). Space averaging on a gas–solid drag model for numerical simulations of a CFB riser. *Powder Technology*, *218*, 131–139.

Tsuji, Y., Kawaguchi, T., & Tanaka, T. (1993). Discrete particle simulation of two-dimensional fluidized bed. *Powder Technology*, *77*, 79–87.

Vaishali, S., Roy, S., & Mills, P. L. (2008). Hydrodynamic simulation of gas–solids downflow reactors. *Chemical Engineering Science*, *63*, 5107–5119.

Van der Hoef, M. A., Beetstra, R., & Kuipers, J. A. M. (2005). Lattice–Boltzmann simulations of low-Reynolds-number flow past mono- and bidisperse arrays of spheres: Results for the permeability and drag force. *Journal of Fluid Mechanics*, *528*, 233–254.

Wang, W., & Li, J. (2007). Simulation of gas–solid two-phase flow by a multi-scale CFD approach—Extension of the EMMS model to the sub-grid level. *Chemical Engineering Science*, *62*, 208–231.

Wang, J., Van der Hoef, M. A., & Kuipers, J. A. M. (2009). Why the two-fluid model fails to predict the bed expansion characteristics of Geldart A particles in gas-fluidized beds: A tentative answer. *Chemical Engineering Science*, *64*, 622–625.

Wen, C. Y., & Yu, Y. H. (1966). Mechanics of fluidization. *Chemical Engineering Progress Symposium Series*, *62*, 100–111.

Weng, M., Nies, M., & Plackmeyer, J. (2011). Computer-aided optimisation of the gas–particle flow and combustion at the Duisburg circulating fluidised bed furnace. *VGB PowerTech Journal*, *91*(8), 64–69.

Werther, J. (2005). Fluid dynamics, temperature and concentration fields in large scale CFB combustors. In K. Cen (Ed.), *Proceedings of the 8th international conference on circulating fluidized beds* (pp. 1–25). Beijing: International Academic Publishers.

Yang, N., Wang, W., Ge, W., & Li, J. (2003). CFD simulation of concurrent-up gas–solid flow in circulating fluidized beds with structure-dependent drag coefficient. *Chemical Engineering Journal*, *96*, 71–80.

Zhang, D. Z., & VanderHeyden, W. B. (2002). The effects of mesoscale structures on the macroscopic momentum equations for two-phase flows. *International Journal of Multiphase Flow*, *28*, 805–822.

Zhang, N., Lu, B., Wang, W., & Li, J. (2010). 3D CFD simulation of hydrodynamics of a 150 MW_e circulating fluidized bed boiler. *Chemical Engineering Journal*, *162*, 821–828.

Series title and number

VTT Science 86

Title	**On modeling of the time- or space-averaged gas-solid drag force in fluidized bed conditions**
Author(s)	Sirpa Kallio
Abstract	Computational fluid dynamic (CFD) modeling of industrial scale fluidized beds is a challenging task due to the mismatch between a large process size and fine flow structures. In the present work, methods are developed to overcome the problems in order to make it possible to use CFD as a cost-effective tool for development of processes based on the fluidized bed concept. Two approaches to tackle the problems related to fine flow structures are discussed: 1) transient simulation using a coarse computational mesh and subgrid-scale closure relations and 2) a steady-state simulation approach that applies time-averaged transport equations for mass and momentum. The biggest benefit of the transient coarse-mesh simulation approach is that the closure laws need to describe a much smaller fraction of the total momentum transfer than what is the case in steady-state modeling. The biggest drawback is that a long simulation is required to produce the average flow field. An additional complication is that the closure laws have mesh resolution as a parameter. Steady-state simulations produce the average flow field directly and thus significantly reduce the computation time. In this work, length scales of flow patterns in fluidized beds are analyzed from experiments. Averaged transport equations for mass and momentum are presented and the terms in the equations are analyzed. It is shown that drag force is one of the main terms to be modeled. A drag correction coefficient is defined and ways to determine it from transient CFD simulation data are presented. In the work, correlations for both the space-averaged and the time-averaged drag forces are applied in riser simulations.
ISBN, ISSN	ISBN 978-951-38-8246-4 (Soft back ed.) ISBN 978-951-38-8247-1 (URL: http://www.vtt.fi/publications/index.jsp) ISSN-L 2242-119X ISSN 2242-119X (Print) ISSN 2242-1203 (Online)
Date	May 2015
Language	English, Finnish abstract
Pages	61 p. + app. 114 p.
Name of the project	
Commissioned by	
Keywords	CFD modeling, fluidized bed, gas-solid drag, cluster
Publisher	VTT Technical Research Centre of Finland Ltd P.O. Box 1000, FI-02044 VTT, Finland, Tel. 020 722 111

Julkaisun sarja ja numero

VTT Science 86

Nimeke	**Aika- ta paikkakeskiarvoistetusta kaasu-kiintoainevastusvoimasta leijupetiolosuhteissa**
Tekijä(t)	Sirpa Kallio
Tiivistelmä	Teollisen mittakaavan leijuprosessien numeerinen virtauslaskenta (CFD) on haastava tehtävä, koska prosessin koon ja hienojen virtausrakenteitten välillä on suuri epäsuhta. Tässä työssä kehitetään menetelmiä näiden ongelmien voittamiseksi, jotta virtauslaskentaa voitaisiin käyttää kustannustehokkaana työkaluna leijuteknologiaan perustuvien prosessien kehittämisessä. Työssä käsitellään kahta lähestymistapaa hienojakoisten virtausrakenteiden aiheuttamien ongelmien ratkaisuun. Nämä ovat 1) aikariippuva simulointi käyttäen karkeaa laskentahilaa ja alihilamalleja yhtälöitten sulkemiseen ja 2) tasapainotilan virtauslaskenta perustuen aikakeskiarvoistettuihin jatkuvuus- ja liikeyhtälöihin. Aikariippuvan laskennan suurin hyöty on se, että sulkemisyhtälöillä kuvataan silloin pienempi osuus liikemäärän siirrosta kuin käytettäessä aikakeskiarvoistettuja yhtälöitä. Aikariippuvan laskennan suurin haittapuoli on, että keskimääräinen virtauskenttä pitää tuottaa laskemalla pitkä ajanjakso ja laskemalla aikakeskiarvo tuloksista. Menetelmän lisärasitteena on se, että laskentakopin koon pitää olla sulkemisyhtälöissä parametrina. Tasapainotilan virtauslaskenta tuottaa keskimääräisen virtauskentän suoraan, mikä lyhentää laskenta-aikaa merkittävästi. Työssä analysoidaan leijuprosessien epähomogeenisuuksien pituusskaaloja ja esitetään keskiarvoistetut liike- ja jatkuvuusyhtälöt tiheän kaasu-kiintoainesuspension virtauksen kuvaukseen. Yhtälöitten termien suuruusluokkia arvioidaan aikariippuvien simulointien tulosten perusteella. Analyysitulokset osoittavat, että kaasun ja kiintoaineen välinen vuorovaikutusvoima on yksi tärkeimmistä mallinnettavista termeistä virtausyhtälöissä. Tälle termille määritetään korjauskerroin ja esitetään tapoja sen analysointiin ja mallintamiseen aikariippuvien simulointien tulosten perusteella. Työssä implementoidaan sekä aika- että paikkakeskiarvoistukseen perustuvat yhtälöitten sulkemismallit numeeriseen virtausratkaisijaan ja simuloidaan molemmilla menetelmillä kiertoleijuprosesseja.
ISBN, ISSN	ISBN 978-951-38-8246-4 (nid.) ISBN 978-951-38-8247-1 (URL: http://www.vtt.fi/publications/index.jsp) ISSN-L 2242-119X ISSN 2242-119X (Painettu) ISSN 2242-1203 (Verkkojulkaisu)
Julkaisuaika	Toukokuu 2015
Kieli	Englanti, suomenkielinen tiivistelmä
Sivumäärä	61 s. + liitt. 114 s.
Projektin nimi	
Rahoittajat	
Avainsanat	CFD-mallinnus, leijupeti, kaasu-kiintoainevastusvoima, klusteri
Julkaisija	Teknologian tutkimuskeskus VTT Oy PL 1000, 02044 VTT, puh. 020 722 111

On modeling of the time- or space-averaged gas-solid drag force in fluidized bed conditions

Computational fluid dynamic (CFD) modeling of industrial scale fluidized beds is a challenging task due to the mismatch between a large process size and fine flow structures. In the present work, methods are developed to overcome the problems in order to make it possible to use CFD as a cost-effective tool for development of processes based on the fluidized bed concept.

Two approaches to tackle the problems related to fine flow structures are discussed: 1) transient simulation using a coarse computational mesh and subgrid-scale closure relations and 2) a steady-state simulation approach that applies time-averaged transport equations for mass and momentum.

In this work, length scales of flow patterns in fluidized beds are analyzed from experiments. Averaged transport equations for mass and momentum are presented and the terms in the equations are analyzed. It is shown that drag force is one of the main terms to be modeled. A drag correction coefficient is defined and ways to determine it from transient CFD simulation data are presented. Correlations for both the space-averaged and the time-averaged drag forces are applied in riser simulations.

ISBN 978-951-38-8246-4 (Soft back ed.)
ISBN 978-951-38-8247-1 (URL: http://www.vtt.fi/publications/index.jsp)
ISSN-L 2242-119X
ISSN 2242-119X (Print)
ISSN 2242-1203 (Online)